Deconvolving and Improving the Spatial Resolution of Satellite Data Using the Maximum Entropy Method

by

Christopher James Jackett, B.Sc. (Hons)

A dissertation submitted in fulfilment of the requirements for the degree of Doctor of Philosophy in the CSIRO-UTAS PhD Program in Quantitative Marine Science

School of Computing and Information Systems

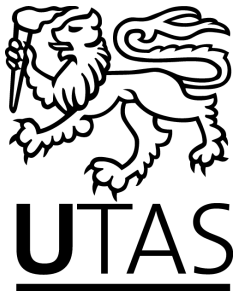

University of Tasmania

July 2013

Declaration

This thesis contains no material which has been accepted for a degree or diploma by the University or any other institution, except by way of background information and duly acknowledged in the thesis, and to the best of my knowledge and belief no material previously published or written by another person except where due acknowledgement is made in the text of the thesis, nor does the thesis contain any material that infringes copyright.

Signed: _____ Date: _____

Christopher James Jackett
PhD Candidate
Computing and Information Systems
University of Tasmania

Authority of Access

This thesis may be made available for loan. Copying and communication of any part of this thesis is prohibited for two years from the date this statement was signed; after that time limited copying and communication is permitted in accordance with the Copyright Act 1968.

Signed: _____ Date: _____

Christopher James Jackett
PhD Candidate
Computing and Information Systems
University of Tasmania

Statement of Co-authorship

The following publication contributed to the work undertaken as part of this thesis:

Jackett, C. J., Turner, P. J., Lovell, J. L., Williams, R. N., 'Deconvolution of MODIS imagery using multiscale maximum entropy', Remote Sensing Letters, Volume 2, No. 3, September 2011, Pages 179-187

C. J. Jackett was the primary author (70%). He performed the majority of the experimental work and subsequent analysis. P. J. Turner (12%) and J. L. Lovell (12%) helped guide the development and assisted in the analysis. R. N. Williams (6%) provided general support and advice. All authors provided feedback and suggestions on the manuscript.

We the undersigned agree with the above stated proportion of work undertaken for the above published manuscript contributing to this thesis.

Signed: _____ _____

Christopher James Jackett	Dr. Robert Bruce Ollington
PhD Candidate	Primary Supervisor
Computing and Information Systems	Computing and Information Systems
University of Tasmania	University of Tasmania

Date: _____ _____

Abstract

Remote sensing satellite imagery provides information about the surface of the Earth at a range of spectral bands and spatial resolutions. This information is a valuable resource for the management of terrestrial and marine environments. During the capturing process, incoming light is reflected or refracted by the instrument optics which causes a small amount of blurring. This effect is described by a mathematical operation called convolution in which the satellite input radiance field is convolved with the instrument Point Spread Function (PSF). This form of instrumental distortion has the largest impact on high-contrast scenes where bright land or clouds are adjacent to dark surfaces such as water.

This thesis investigates three mechanisms for improving the quality of recorded satellite data. An efficient convolution method was developed to minimise boundary effects, a deconvolution algorithm was used to remove instrumental distortion, and a resolution enhancement algorithm was developed to improve the spatial resolution of input images. The latter two of these problems are underdetermined and require appropriately selected constraints in order to find unique and stable solutions. An entropy-based method was chosen as the constraint element due to its heavy grounding in statistical mechanics and information theory. MODerate resolution Imaging Spectroradiometer (MODIS) Aqua images were used to quantify the improvement of these algorithms, with a focus on coastal marine and open-ocean environments.

Deconvolution is an algorithm-based process designed to reverse convolution effects with a known PSF. Multiscale Entropy deconvolution was applied to MODIS level 1A imagery to remove instrumental distortion from top-of-atmosphere radiance counts. Removing these effects at the beginning of the satellite image processing

chain reduces the propagation and amplification of errors in subsequent processing stages. Wavelet transforms were implemented to decompose images into a range of resolution levels that represent different spatial frequencies. This allows both large-scale and small-scale features to be resolved simultaneously. Multiresolution Support images were used to accurately define and target important areas within the imagery. The combination of these techniques includes two-dimensional structural information in the Multiscale Entropy calculation which results in accurate deconvolution. Validation of the Multiscale Entropy deconvolution algorithm was undertaken using in-situ measurements from the Baltic Sea and a QuickBird image of a high-contrast Antarctic ice edge.

A novel approach to the spatial resolution enhancement of MODIS imagery uses information about the optical PSF, along with the result of Multiscale Entropy deconvolution. With this information, a system of linear equations was constructed that models how high-resolution PSF convolution redistributes information over a finite area. A new method termed Multiresolution Entropy was developed to constrain the linear system and retrieve an optimal solution. The algorithm successfully improved the spatial resolution of input images and compared favourably to other interpolation-based methods. The key requirement of this technique is to obtain high-resolution PSF measurements at the same sampling frequency as the desired final output resolution.

The techniques developed and presented in this thesis contain a range of important research contributions. The combination of Fast Fourier Transform convolution with a boundary renormalisation approach produces an efficient and accurate convolution method with minimal boundary effects. A multi-detector convolution process accurately simulates the MODIS Aqua instrumentation and allows for successful deconvolution. A detector saturated estimation technique for ocean colour bands ensures the correct quantity of instrumental distortion is removed during deconvolution. The formulation of a linear system consisting of high-resolution PSF modelling and appropriate physical constraints defines the spatial resolution enhancement problem. The development of Multiresolution Entropy targets high-frequency content, constrains the linear system and results in a unique

and stable resolution-enhanced solution. The techniques developed throughout this thesis provide considerable benefit to the quality of remote sensing imagery and can substantially improve the monitoring and management of coastal zones and other marine environments.

Acknowledgements

I would like to thank Jenny Lovell and Robert Ollington for supervising this thesis. Their dedicated guidance and support was gratefully appreciated. Ray Williams and Peter Turner are also acknowledged for their supervision efforts in the early stages of this research. I would particularly like to thank Peter Turner for providing the initial inspiration for this work and outlining a worthwhile and rewarding research topic.

My gratitude extends to Thomas Schroeder, Young Je Park, Ian Grant and Edward King for reading draft manuscripts and providing useful feedback. Edward King also receives my appreciation for processing a range of MODIS scenes. Gerhard Meister, Jack Xiong and Brian Wenny generously provided the MODIS Aqua characterisation models that underpin many of the research components in this thesis. I would like to thank Susanne Kratzer for providing in-situ Baltic Sea validation measurements and making suggestions regarding the deconvolution algorithm validation. Selima Ben Mustapha and Gerald More helped facilitate the direct comparison of in-situ Baltic Sea and MODIS measurements. Petra Heil also provided high-resolution QuickBird validation data.

Finally, a special thank you to my wife Amy Jackett for always listening to my current problems, suggesting alternative strategies and being incredibly supportive.

Contents

List of Figures

List of Tables

List of Abbreviations

ABS	Australian Bureau of Statistics
AERONET-OC	AErosol Robotic NETwork Ocean Colour
AVHRR	Advanced High Resolution Radiometer
BB	Barzilai and Borwein method
CDOM	Coloured Dissolved Organic Matter
CUDA	Compute Unified Device Architecture
DFT	Discrete Fourier Transform
DSP	Digital Signal Processing
EOS	Earth Observing System
FBC	Fast Fourier Transform with Border Correction
FFT	Fast Fourier Transform
FWHM	Full-Width Half-Maximum
GCV	Generalised Cross-Validation
HR	High Resolution
HST	Hubble Space Telescope
IDL	Interactive Data Language
LR	Low Resolution

MAP	Maximum A Posteriori
MEM	Maximum Entropy Method
MERE	Maximum Entropy Resolution Enhancement
MERIS	MEdium Resolution Imaging Spectrometer
MLS	Method of Least Squares
MNB	Mean Norm Bias
MODIS	MODerate resolution Imaging Spectoradiometer
MRE	MultiResolution Entropy
PSF	Point Spread Function
REF	Resolution Enhancement Factor
RMS	Root Mean Square
SBAF	Spectral Band Adjustment Factor
SBR	Standard Convolution with Boundary Renormalisation
SeaDAS	SeaWiFS Data Analysis System
SNR	Signal-to-Noise Ratio
SSIM	Structural SIMilarity
SVD	Singular Value Decomposition
TSM	Total Suspended Matter
USGS	U.S. Geological Survey
VHR	Very High Resolution
WCLEAN	Wavelet CLEAN method

Chapter 1

Introduction

Monitoring marine environments is critical to the sustainable management of coastal regions and resources. Approximately 85% of the Australian population live within 50km of the coastline, of which a large proportion live in state capital cities that are located on or near the coast (Australian Bureau of Statistics, 2002). These regions are constantly subjected to pressure from recreational and industrial fishing, coastal population growth and urbanisation, storm water run-off, human waste management, anthropogenic climate change, and large-scale natural events including flooding, fires and other weather-related phenomena. Therefore, it is crucial to develop accurate monitoring systems that deliver frequent, high-resolution information to help manage these densely populated regions.

Remote sensing is the attainment of information about objects with which the observer has no physical contact. Remote sensing enables data to be collected in areas previously unavailable due to cost, inaccessibility or danger (Ikeda and Dobson, 1995). One form of remote sensing uses artificial Earth-orbiting satellites to record data about the surface of the Earth. Highly-sensitive satellite instruments can accurately record information about the Earth, from which products such as sea surface temperature, ocean colour, vegetation indices and global solar radiation can be derived (Baker, 1990). Some commonly used remote sensing satellite instruments include the Advanced Very High Resolution Radiometer (AVHRR) (km resolution), which senses cloud cover, surface brightness and surface temperature (NOAA, 2010); the MODerate resolution Imaging Spectroradiometer (MODIS) (250m - 1km

resolution), which measures large scale global dynamics (Justice et al., 1998); and the Landsat Thematic Mapper (30m - 100m resolution), which is a multi-spectral scanning radiometer used to detect and measure changes on the surface of the Earth (USGS, 2009). Other higher-resolution instruments capture spatially detailed information at less frequent time intervals or in targeted data acquisitions.

This thesis will concentrate on MODIS satellite instruments on-board the Earth Observing System (EOS) platform Aqua. MODIS Aqua captures data in 36 spectral bands at several spatial resolutions including 250m, 500m and 1km resolution. MODIS Aqua is calibrated to deliver over 40 standard data products such as atmospheric aerosols, snow cover, land and water surface temperature, leaf area index, sea ice extent and ocean chlorophyll concentration among many others. Aqua is fixed in a sun-synchronous, near-polar, circular orbit designed to maintain an equatorial crossing at approximately 10:30 A.M. local time each day. Aqua travels at a forward velocity of approximately 7.5km/s in low Earth orbit at an altitude of 705km. This rapid orbital path allows MODIS to provide complete global coverage every one to two days.

MODIS Aqua measures top-of-atmosphere radiance counts by reflecting the Earth-leaving light field onto an array of detectors using a rotating double-sided mirror. As the light field interacts with the instrument optics, a small amount of blurring is introduced into the recorded signal. This blurring is an inherent property of all sensor-based optical systems and is described by the mathematical operation known as convolution. That is, the existing distortion-free light field enters the instrument and becomes convolved with the instrumental spatial response function. The optical system introduces spatial distortion and attenuates the signal. The signal is then detected by sensors which add noise and have their own intrinsic gain characteristics. Calibrating the entire system to make an accurate measure of radiance is a critical issue and has been achieved by Guenther and Barnes (1996) and Xiong and Barnes (2006). Given the calibration process has been performed successfully, a correction for optical distortion can be made. Deconvolution algorithms are designed to retrieve the optimal distortion-free signal provided the instrument response function and noise level have been well

characterised. Detector-based noise is the primary factor that makes deconvolution problems ill-posed and difficult to solve. However, a unique and stable solution can be found by applying a suitable set of constraints. This thesis investigates the Multiscale Entropy deconvolution of MODIS Aqua data to accurately remove instrumental distortion and improve satellite imagery. Light detection and instrumental distortion are the last processes to occur in the light-path of the recorded signal and should therefore be the first effects that are corrected. Removing instrumental distortion errors directly after detector calibration limits the amplification of these errors at subsequent processing stages. This is a core argument that is central to the satellite image deconvolution research described in this thesis.

The convolution operator is one of the fundamental calculations performed within every iteration of the deconvolution process. Selecting the appropriate convolution boundary condition is a major concern for successful image deconvolution. A common approach is to add a zero-padded border around the convolution input image, and remove the border immediately after convolution is performed. However, image content that is redistributed into the padded border is removed with every iteration of the deconvolution algorithm, resulting in a spatially biased loss of image intensity. Fast Fourier Transforms (FFTs) are commonly applied to increase the computational speed of convolution. In this thesis, a new convolution method will be developed that combines the speed benefits attributed to FFT convolution with a boundary renormalisation approach to provide efficient and robust signal convolution.

Image spatial resolution is a fundamental measure of image quality. Methods designed to preserve or enhance spatial resolution are considered highly valuable. The natural instrumental convolution that occurs during satellite measurements is an analogue process that redistributes image content over a finite area. Using this knowledge, it is possible to improve the spatial resolution of a recorded image that has undergone a natural convolution process, provided that a high-resolution instrument response function is available. This thesis investigates an entirely novel approach to spatial resolution enhancement using high-resolution convolution modelling and a customised entropy-based linear system regularisation

method.

The data collecting capabilities provided by MODIS Aqua, and other remote sensing platforms, allow for constant and accurate monitoring of both coastal marine and open-ocean environments. This information has remarkable value, and any improvements made to the data processing chain are highly advantageous. This thesis aims to identify, explore, quantify and correct three distinct mechanisms that occur in the retrieval and processing of satellite imagery. These mechanisms include an efficient convolution correction method that can minimise boundary contamination, an operational image deconvolution algorithm implemented for MODIS Aqua ocean colour bands, and a novel spatial resolution enhancement method for optical imaging systems. These three research components will be investigated and developed with the aim of improving the monitoring and management of coastal marine and open-ocean environments.

All of the computational techniques developed throughout this thesis are implemented in the Interactive Data Language (IDL). IDL was selected because it contains a rich base of mathematical libraries that are fundamental to the algorithms developed in this thesis, and IDL is a standard programming language in the remote sensing research field.

Chapter 2 introduces relevant literature and background information concerning the three main research areas. A comprehensive review of current techniques and their limitations is explored and the necessity for further research and development is highlighted. The specific techniques developed in this thesis are general and have a wide range of application in other fields.

Chapter 3 describes a correction method for FFT convolution that limits boundary contamination artefacts resulting from convolution padding methods. The proposed correction method makes a single data-driven boundary condition assumption and only uses information contained within the original input signal to produce consistent convolution results and maintain data integrity. An analysis of the algorithm shows that it performs identically to the equivalent spatial-domain convolution approach with the only discernible differences being resolved at the level of machine rounding errors. The correction method can be applied at minimal cost

to performance and has valuable applications for scientific data processing where algorithm efficiency and data accuracy are imperative.

Chapter 4 investigates the Multiscale Entropy deconvolution of MODIS Aqua imagery which results in the removal of instrument response function effects. The implementation utilises three efficient computational methods: FFT convolution, Wavelet image decomposition and a gradient method step size estimation algorithm that together enable rapid image deconvolution. Multiscale Entropy uses Wavelet transforms to implicitly include two-dimensional structural information of an image into the entropy calculation. An evaluation using synthetic data showed that the deconvolution algorithm reduced the maximum individual pixel error from 90.01% to 0.34%, effectively removing instrumental distortion down to the level of detector-based noise. Deconvolution of MODIS data is shown to resolve all significant features and is most effective in regions with large changes in radiance such as coastal zones, contrasting land covers and cloud edges.

Chapter 5 describes the validation process of the Multiscale Entropy deconvolution of MODIS Aqua imagery using two separate validation approaches. In-situ Baltic Sea samples including surface reflectance, chlorophyll-a, total suspended matter and the diffuse attenuation coefficient were compared with MODIS Aqua overpass measurements. However, minimal scene contrast and limited in-situ spatial extent were found to insufficiently characterise the effects of deconvolution. A high-resolution QuickBird scene containing an Antarctic ice edge was spatially matched and directly compared with MODIS Aqua top-of-atmosphere radiance measurements. The results indicate that deconvolution improved the radiometric accuracy of MODIS Aqua measurements in the blue wavelengths, but did not contain a sufficient number of comparable measurements in the green or red wavelengths to reach any strong conclusions.

Chapter 6 develops a novel spatial resolution enhancement technique for satellite imagery by using high-resolution instrument response function measurements and pre-processed image deconvolution results. The resolution enhancement problem is formulated as an ill-posed system of linear equations by modelling a high-resolution convolution process and applying suitable physical constraints. This ill-

posed inverse problem can be solved using a novel variant of Multiscale Entropy regularisation, which is designed to simultaneously maximise information content and manage detector-based noise. This technique shows particular promise for single-frame imagery. Results show that this approach can moderately enhance the spatial resolution of satellite imagery, provided the instrument response function is sampled at the desired final resolution-enhanced sampling frequency.

Chapter 7 summarises each of the major research components in this thesis and discusses their original contribution. The improvement that each research topic contributes to satellite data is outlined and its impact on the monitoring and management of coastal marine and open-ocean environments is discussed. Concluding remarks for each research component are presented and an evaluation of the entire body of work is made.

Chapter 2

Background

2.1 MODIS Aqua

Containing six Earth-observing instruments, Aqua was launched on May 4, 2002 to observe and study the water cycle. The main instrumentation inside MODIS Aqua comprises a double-sided scan mirror that continuously rotates and reflects Earth-leaving radiances onto an along-track array of detectors (Figure 2.1). As the scanning mirror rotates, MODIS Aqua horizontally stripes the surface of the Earth in the scan direction while the craft travels forward in the track direction (Barnes et al., 1998). These strips of data are combined to build up a continuous image. MODIS Aqua contains a field baffle that restricts the input radiance field to a 10km field-of-view in the along-track dimension. This enables a 10-element scan to be recorded across the swath for each 1km resolution band. Similarly, the 500m and 250m resolution bands record 20 and 40-element arrays respectively. The field baffle has a strong effect on the instrument response. The spatial response of each detector in every band has a unique shape determined by the relative position of the detector with respect to the field baffle.

MODIS Aqua has a zenith angle of $\pm 55^{\circ}$ and achieves a swath width of 2330km. This translates to an unprocessed image width of 1354 pixels at 1km resolution due to the range of viewing angles of the instrument and the curvature of the Earth. The imagery retrieved from MODIS Aqua is segmented into individual datasets known as granules. Each granule consists of 5 minutes satellite time of recorded imagery and

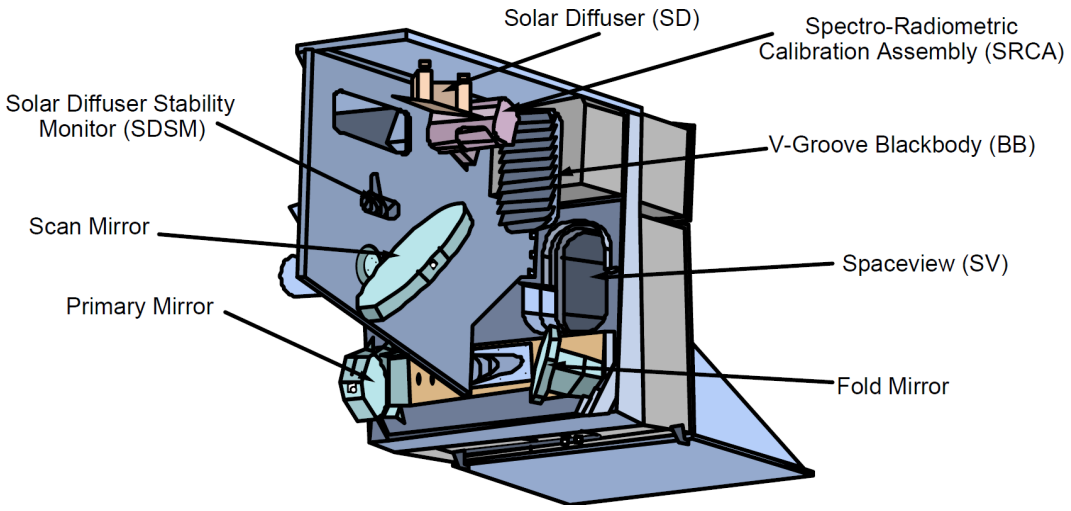

Figure 2.1: MODIS Aqua cutaway detailing the MODIS scan cavity subsystems and on-board calibrators (Xiong et al., 2005).

results in a final unprocessed image size of 1354×2040 pixels at 1km resolution. This level 0 data contains raw digital number readings from the instrument and are processed into level 1A radiance counts using NASA's SeaWiFS Data Analysis System (SeaDAS) (Fu et al., 1998; Nishihama et al., 1997). Processing the imagery to level 1B adds calibration and geolocation information to the imagery (Xiong et al., 2005). Further processing to level 2 or 3 results in individual data products, such as sea surface temperature or ocean colour, which are readily used in many scientific research fields.

The scanning-based design of MODIS Aqua results in the spatial coverage of recorded measurements increasing in both the scan and track dimensions as the instrument zenith angle increases. As the spatial coverage of MODIS measurements grow at large zenith angles, the spatial pattern of the scan takes on the shape of a bow-tie. This results in the spatial coverage of consecutive scans partially overlapping at off-nadir angles, and is known as the panoramic bow-tie effect. When MODIS data is reprojected to produce standard data products, intelligent measurement selection schemes are employed to account for these effects. Spatially duplicate measurements caused by bow-tie effects are seen in Chapters 4 and 5 and require management.

2.2 Convolution

Convolution is a mathematical process which combines two input signals to produce a third resultant output signal. Each value in the convolved output signal is equal to the sum of the point-wise multiplication of the two overlapping input signals. The first input signal is typically the data to be convolved and the second input signal is often referred to as the convolution function, impulse response function, point spread function, blurring kernel or filter kernel. Convolution is often described as the single most important technique in Digital Signal Processing (DSP) and has many applications in other fields including electrical engineering, statistics and probability (Smith, 2003; Jähne, 2002; Acharya and Ray, 2005). For a continuous system, the convolution of two signals, f and g, is described using the convolution integral (Smith, 2003):

$$(f * g)(x) = \int_{-\infty}^{\infty} f(u)\, g(x-u)\, \mathrm{d}u \tag{2.1}$$

where $*$ is the convolution operator

Discrete signals are required for digital computation to be performed. The equivalent convolution operation can be represented for discrete systems using the convolution sum (Smith, 2003):

$$O(x) = (I * K)(x) = \sum_{i=0}^{M-1} K(i)\, I(x-i) \tag{2.2}$$

$$\begin{array}{rrcl} \text{where} & O(x) & = & \text{convolved output signal} \\ & & & (N+M-1 \text{ elements}) \\ & I(x) & = & \text{input signal } (N \text{ elements}) \\ & K(x) & = & \text{convolution kernel } (M \text{ elements}) \end{array}$$

This equation describes how the convolved output signal O relates to the two input signals I and K where x is now discrete. Convolution is calculated by passing a centred convolution kernel from left-to-right over the input signal and summing

the point-wise multiplication of the two signals to produce the final convolved signal. The following mathematical properties hold for convolution (Jähne, 2002):

$$\begin{array}{rrcl} \text{Commutativity} & f * g & = & g * f \\ \text{Associativity} & f_1 * (f_2 * g) & = & (f_1 * f_2) * g \\ \text{Distributivity over Addition} & (f_1 + f_2) * g & = & f_1 * g + f_2 * g \end{array}$$

There are many applications that require convolution to be performed on two-dimensional imagery. For this purpose, Equation 2.2 can easily be extended into two-dimensional space for use in image convolution:

$$O(x, y) = \sum_{j=0}^{M-1} \sum_{i=0}^{M-1} K(i, j)\, I(x - i, y - j) \tag{2.3}$$

$$\begin{array}{rrcl} \text{where} & O(x, y) & = & \text{convolved output signal} \\ & & & ((N + M - 1) \times (N + M - 1) \text{ elements}) \\ & I(x, y) & = & \text{input signal } (N \times N \text{ elements}) \\ & K(x, y) & = & \text{convolution kernel } (M \times M \text{ elements}) \end{array}$$

The two-dimensional input signal and convolution kernel are defined to be square for simplicity. However, this is not strictly required and any sized rectangular imagery can be accommodated. In the image domain, convolution is performed by centring the two-dimensional convolution kernel over every pixel in the input signal and summing the point-wise product of the two signals, as depicted for the first data point in Figure 2.2. However, in areas close to the edge of the input signal, the convolution kernel extends beyond the boundaries of the input signal and therefore the full convolution sum cannot be calculated (Figure 2.2(c)). This problem occurs around the entire boundary of the input signal extending to approximately half the size of the convolution kernel in each dimension. The incomplete overlap here results in an intensity reduction being observed around the interior border of the convolved output. In many cases, this intensity reduction is considered a natural by-product of signal convolution, and its effects are largely ignored when performing spatial domain convolution.

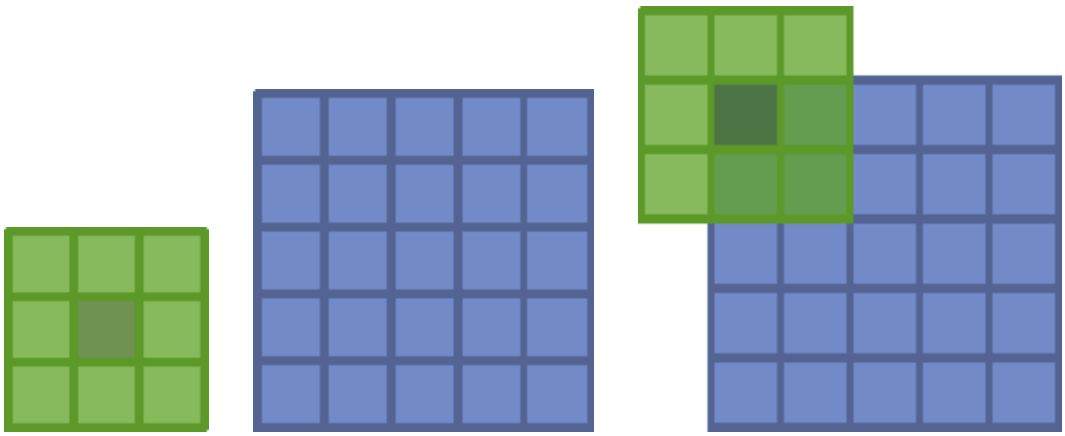

(a) (b) (c)

Figure 2.2: Two-dimensional representations of (a) the convolution kernel, (b) the data to be convolved and (c) the convolution of the first data point with the convolution kernel. Only the pixels in the convolution kernel that overlap the data will be included in the convolution sum calculation.

Since the conception of the Fourier transform, it has been well known that convolution can also be performed in the frequency domain. This capability arises from the Convolution Theorem:

$$\mathcal{F}(f * g) = \mathcal{F}(f)\mathcal{F}(g) \tag{2.4}$$

where $\mathcal{F}$ indicates a Fourier transform (Trott, 2004)

That is, the convolution of two functions in the time or spatial domain implies the multiplication of their Fourier transforms (Jähne, 2002). Reciprocally, convolution in the frequency domain can be achieved by multiplication in the time or spatial domain. The computation time required to calculate the Discrete Fourier Transform (DFT), and in turn, frequency domain convolution, is often much greater than calculating standard spatial domain convolution. A breakthrough was made with the introduction of the Fast Fourier Transform (FFT) which brought about efficient transform computation due to its radix-2 recursive architecture (Cooley and Tukey, 1965). This ushered in a new era of DSP where convolution could be readily applied to solve problems with reasonable compute time. Further research resulted in more advanced mixed-radix FFT algorithms that exploited a combination of base values

and increased the overall algorithm efficiency (Singleton, 1969). More recently, Hassanieh et al. (2012) developed an optimised technique for calculating the sparse Fourier transform which further improves on the computational complexity of the FFT and could have a significant impact on DSP, communications and digital media.

One major problem that arises when performing convolution in the frequency domain is circular convolution. This occurs when the Fourier transforms of two signals are multiplied together. When a signal is transformed into the frequency domain, by way of a DFT or FFT, a spectrum is retrieved which represents frequency, phase and amplitudinal information encoded into the component sinusoids of the signal. From the perspective of the time domain, a one-dimensional signal becomes repeated head to tail an infinite number of times. This is due to the periodicity of frequency-based analysis. When two frequency spectra are multiplied together, and convolution is performed, the information at the start of the signal will contaminate information at the end of the signal and vice-versa. This introduces an edge effect into the convolved signal that can become problematic if large discontinuities are present between the start and end of the original signal. The same problem is also encountered with two-dimensional imagery where the transformed signals become effectively repeated infinitely in both dimensions.

To minimise this edge effect, a border with a size at least half the dimensions of the convolution kernel can be added around the input signal and padded with data values. Several common techniques exist for border value padding such as zero-padding, repetition, replication and mirroring. Zero-padding simply adds a padded the border filled with the value zero (Figure 2.3(a)). This results in a convolution identical to the spatial domain intensity reduction mentioned earlier, but removes any possibility of contamination from circular convolution. Repetition repeats the edge-values of the signal to fill the border (Figure 2.3(b)). Replication repeats the input signal in the border so that the tail of the input signal is adjacent to the head of the input signal in each dimension (Figure 2.3(c)). This technique is useful in avoiding the intensity reduction seen with zero-padding, but results in the same effect encountered with circular convolution. Mirroring reflects the input signal in the border in each dimension and can be a helpful technique in avoiding severe edge

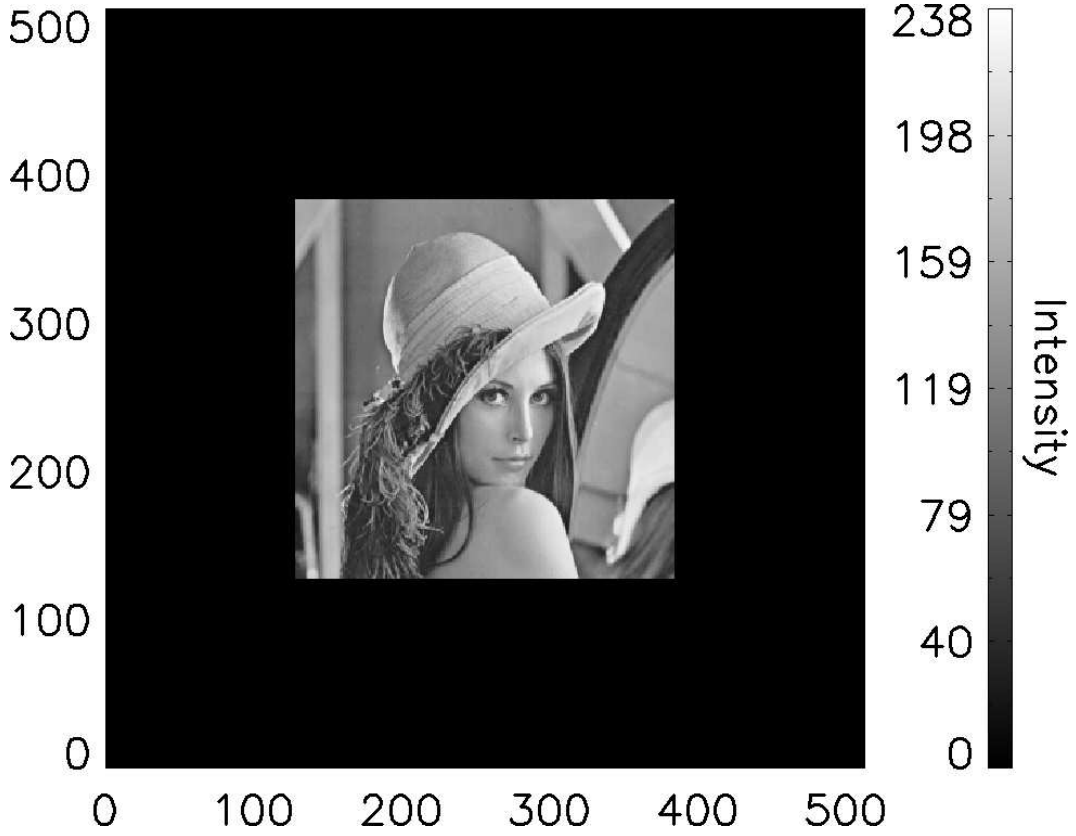

(a)

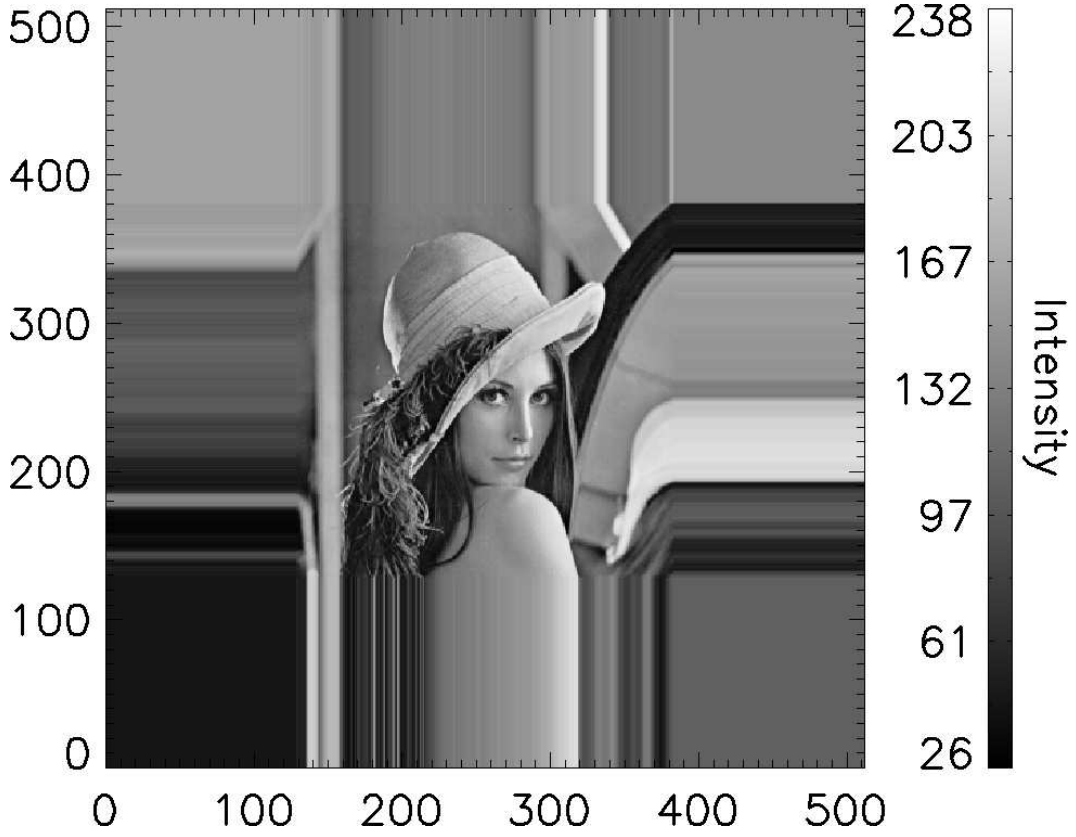

(b)

Figure 2.3: Common boundary conditions added to standard image processing test image Lena (256×256) including (a) zero-padding and (b) repetition.

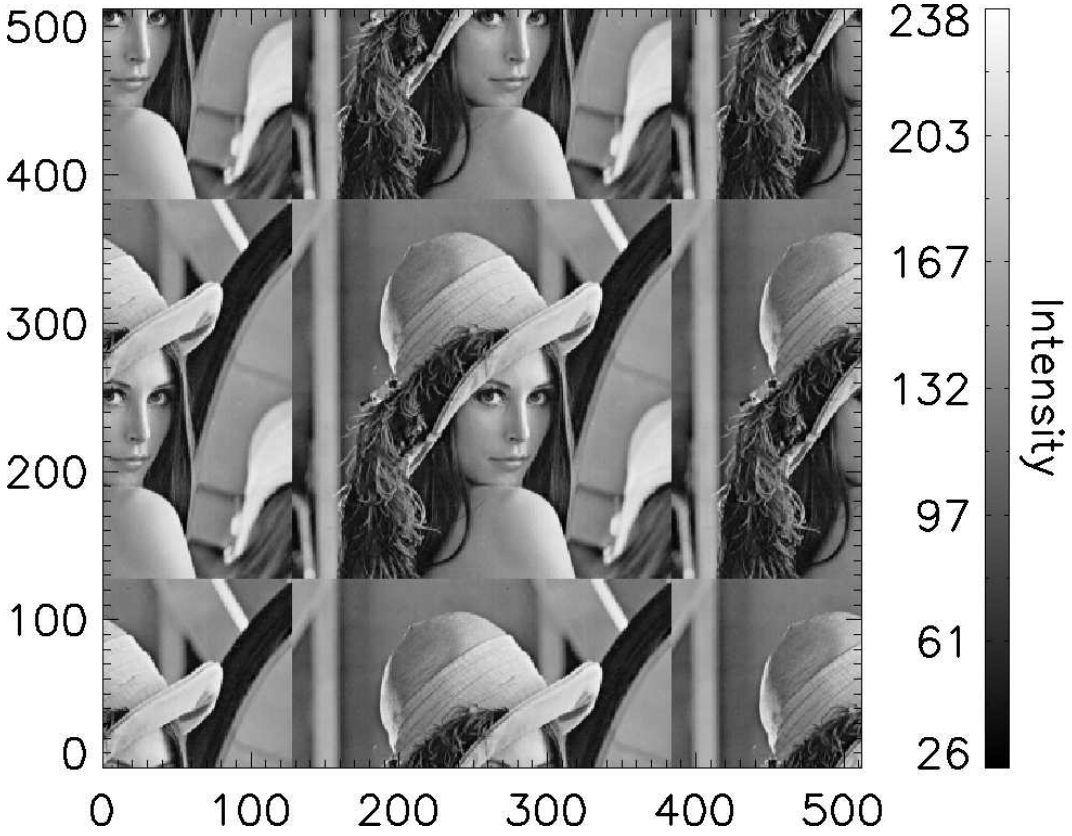

(c)

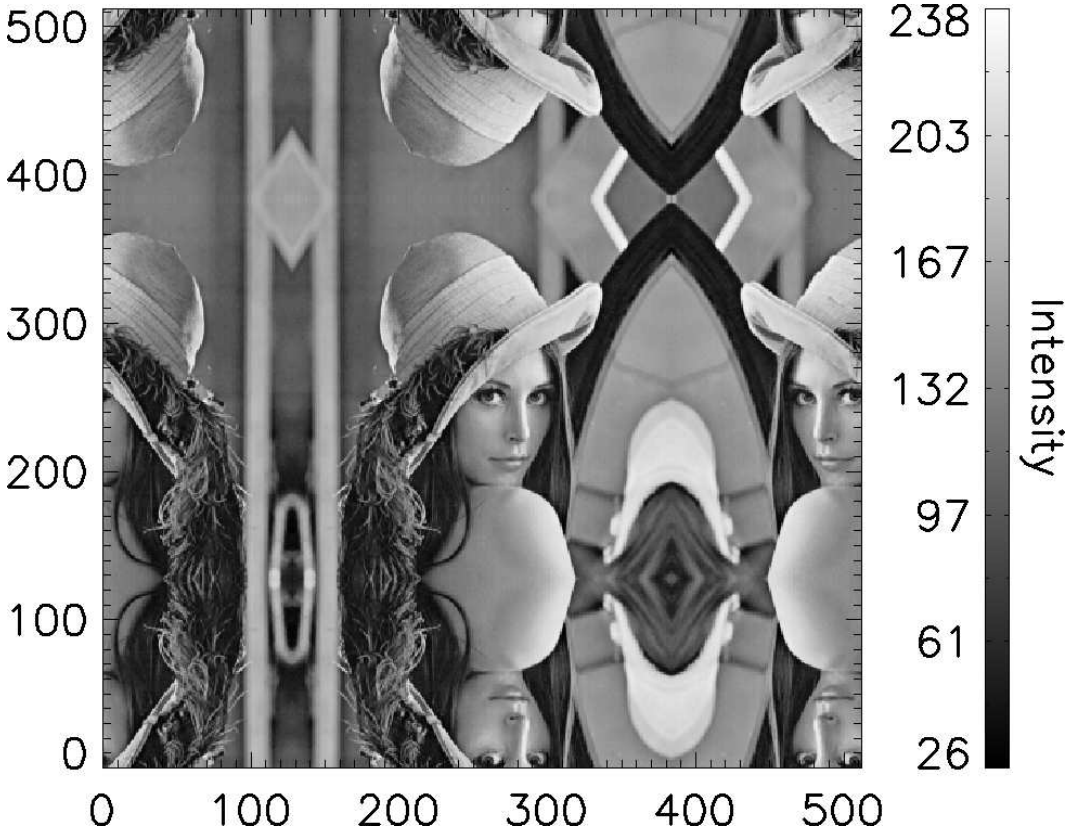

(d)

Figure 2.3 continued: Common boundary conditions added to standard image processing test image Lena (256×256) including (c) replication and (d) mirroring/reflection.

discontinuities (Figure 2.3(d)). After frequency domain convolution is performed, the result is inverse-transformed back into the spatial domain and the padded border is removed to retrieve the final convolution result. These border padding techniques provide a range of mechanisms to mitigate potential edge effects, but still introduce errors into the inner border of the convolved signal. Chapter 3 investigates an alternative boundary correction method that is applicable to frequency-domain convolution and produces results with reduced boundary artefacts.

Convolution is a process encountered in all optical systems from digital cameras to the human eye. Every optical instrument has a unique convolution kernel, which is more commonly referred to as a Point Spread Function (PSF) in the image domain. A PSF is a two-dimensional representation of the spatial response of an instrument and it describes how a point source is imaged by the optical system. The PSF of an instrument can be experimentally characterised by shining a synthetic point source through the optical system and recording the response. This process is repeated a number of times with the position of the synthetic point source being moved to cover the entire field-of-view of the instrument. In this way, a complete two-dimensional spatial response of the optical system is constructed. Meister et al. (2008) used a similar technique to derive PSFs for all 10 detectors in every 1km resolution MODIS Aqua ocean colour band. Figure 2.4 shows the MODIS Aqua band 8 (405nm - 420nm) PSF on a logarithmic scale with 1km pixel grid size. The central maximum of the PSF is the image point of the instrument and the majority of the recorded signal comes from this point. A large low response area, appearing like a platform, surrounds the central peak and this cumulative area can have a significant impact on the recorded signal.

Every optical system encounters some degree of blurring and distortion due to the quality of the imaging system and the associated environmental conditions. The PSF of an instrument strictly represents instrumental effects including optical aberration, the diffraction limit and instrumental stray light that emanates from within the field-of-view of the instrument.

Optical aberration occurs when the light from a point source does not converge into a single point upon transmission through the imaging system. Aberration

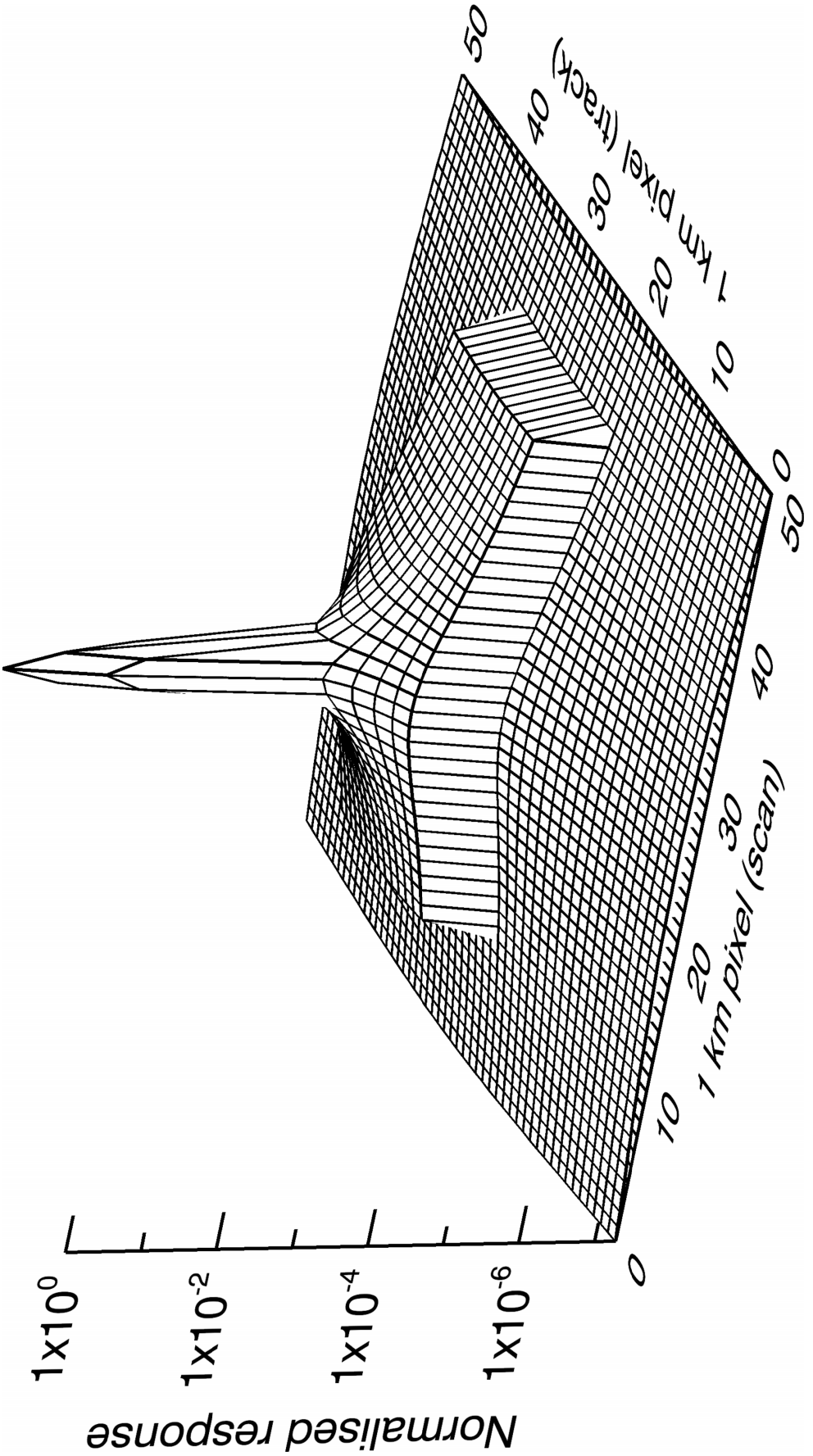

Figure 2.4: MODIS Aqua band 8 detector 5 point spread function (405nm - 420nm) on a logarithmic scale with 1km pixel grid size. The majority of the recorded signal comes from the image point of the instrument. However, the cumulative low response area surrounding the image point can have a significant impact on the recorded signal.

exists in two forms: monochromatic and chromatic. Monochromatic aberration is caused by geometric distortions in the optical lens and is encountered when light is either reflected or refracted. This form of aberration is present even when making monochromatic observations, or in other words, when the instrument is measuring narrow frequency bands as is the case in many scientific instruments. Chromatic aberration, or colour aberration, occurs when a lens-based imaging system measures large frequency bands such as the entire visible spectrum. As light passes through the optical system, the incoming wavelengths are dispersed by different quantities as determined by the refractive index of the lensing material. When this light is measured on a flat imaging plane, such as an array of detectors, the different colours become separated into their spectrum, causing the effect known as chromatic aberration (Figure 2.5(a)). This effect can be mitigated by including a secondary achromatic lens into the optical system which corrects for refraction and allows all of the wavelength of light to converge into a point at the detector (Figure 2.5(b)).

Chromatic aberration is not a common problem for satellite remote sensing because most satellite instruments compile true-colour images by combining individual narrow-band images that span the visible spectrum. However, monochromatic aberration is seen regularly in remote sensing. A classic example of this is the initial optical system of the Hubble Space Telescope (HST) launched in 1990. It was discovered shortly after deployment that the main imaging mirror contained monochromatic spherical aberration that severely blurred all recorded imagery from the HST (Figure 2.6). This was due to the main mirror being polished by a faulty device and then checked by the same faulty device, disguising the fact there were significant distortions in the instrument. Concerted effort was directed into the removal of this aberration using estimated characterisation models and the application of deconvolution methods (Hanisch and White, 1994; White and Allen, 1991). These methods proved moderately and temporarily successful until the HST received an optics upgrade during a manned servicing mission in 1993.

In the absence of other limiting factors, such as aberration and atmospheric effects, the ability of an imaging system to resolve detail is ultimately limited by diffraction. An optical system that can produce images with angular resolution equal

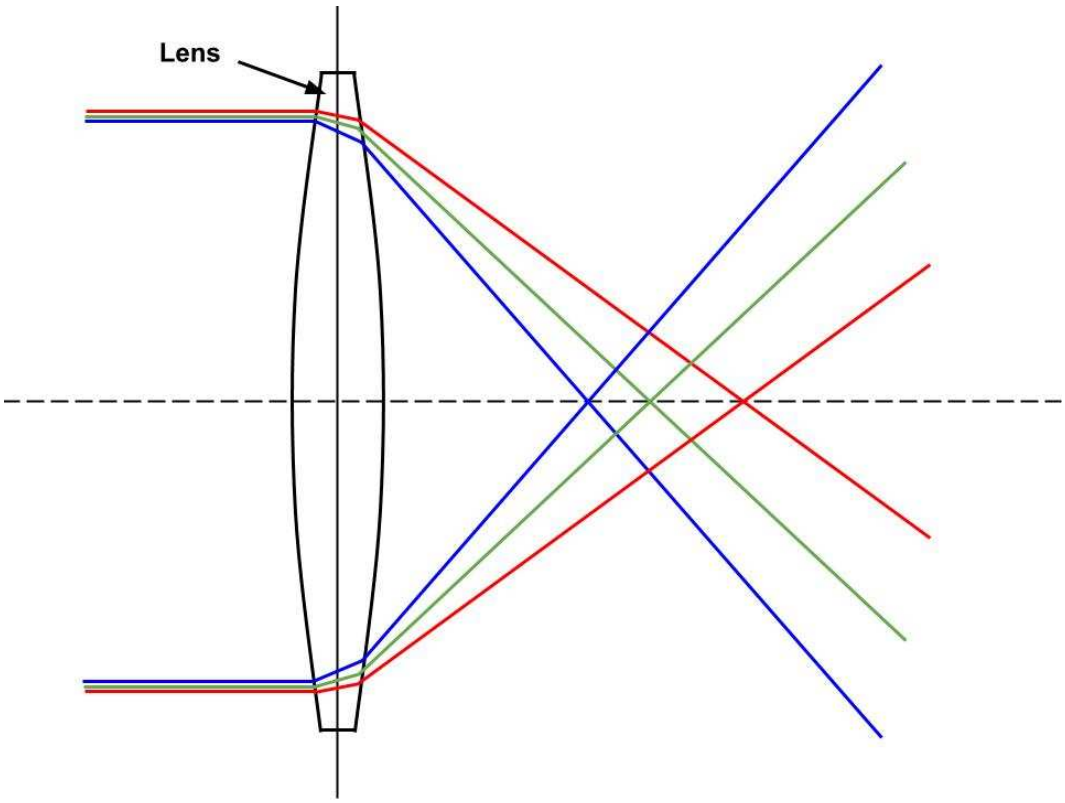

(a)

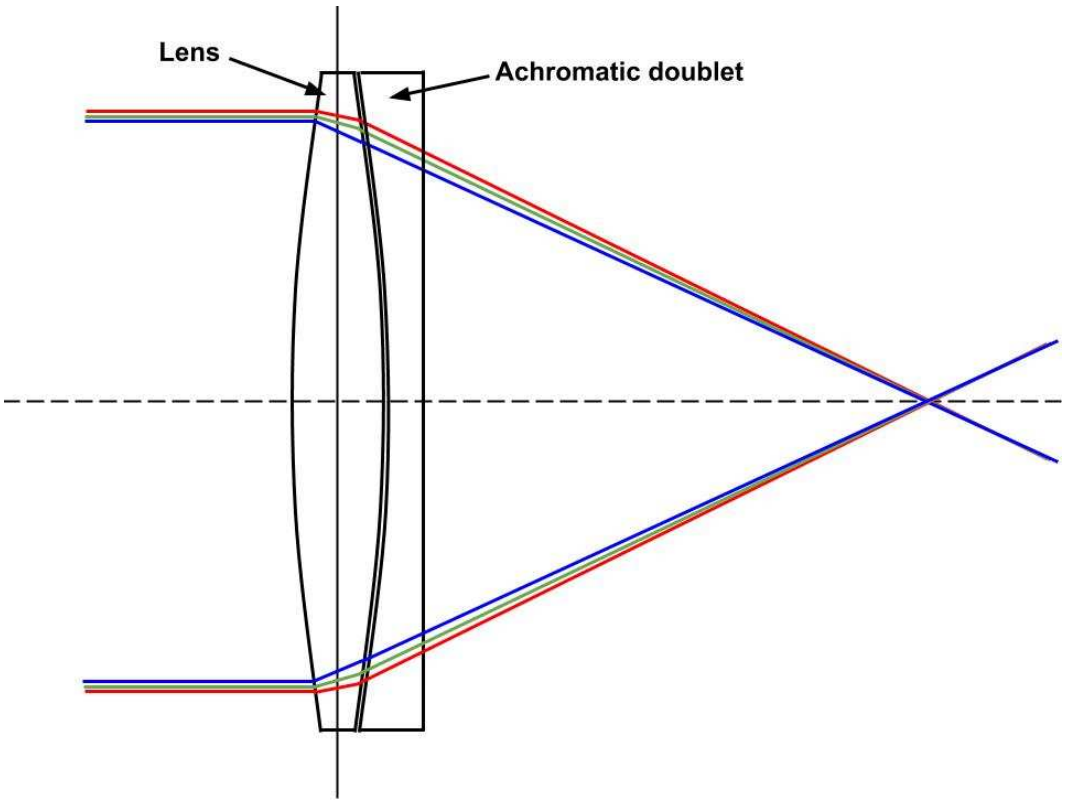

(b)

Figure 2.5: Refraction of light wavelengths through an optical lens showing (a) chromatic aberration and (b) a correction technique called achromatic lensing.

(a)

(b)

Figure 2.6: Images from Hubble's Wide Field and Planetary Camera (WFPC) of spiral galaxy M100 showing (a) the uncorrected image with spherical aberration and (b) the image after corrected optics were applied (NASA, 1993). The difference between (a) and (b) highlights the dramatic effect caused by monochromatic spherical aberration.

to the theoretical limit of the instrument is said to be diffraction limited, or operating at its diffraction limit (Bom and Wolf, 1980). Most Earth-based instruments, such as optical telescopes, are typically seeing-limited and operate at much lower resolution than their diffraction limit due to distortions introduced by the travel-path of light through several kilometres of irregular atmosphere. However, radio telescopes commonly operate close to their diffraction limit because the wavelengths they measure are suitably long so that atmospheric distortion becomes negligible. Space-based telescopes always operate at their diffraction limit as long as their optical systems do not contain any form of aberration.

When an ideal optical system, free from any imperfections in the lens or mirror, undergoes uniform illumination of the circular aperture of the instrument, the resulting diffraction response is in the form of an Airy pattern (Figure 2.7). This diffraction pattern, or instrument PSF, contains a central peak known as the Airy disk and concentric rings that are together called the Airy pattern (Airy, 1835). The Rayleigh criterion for diffraction limited systems provides a definition for the

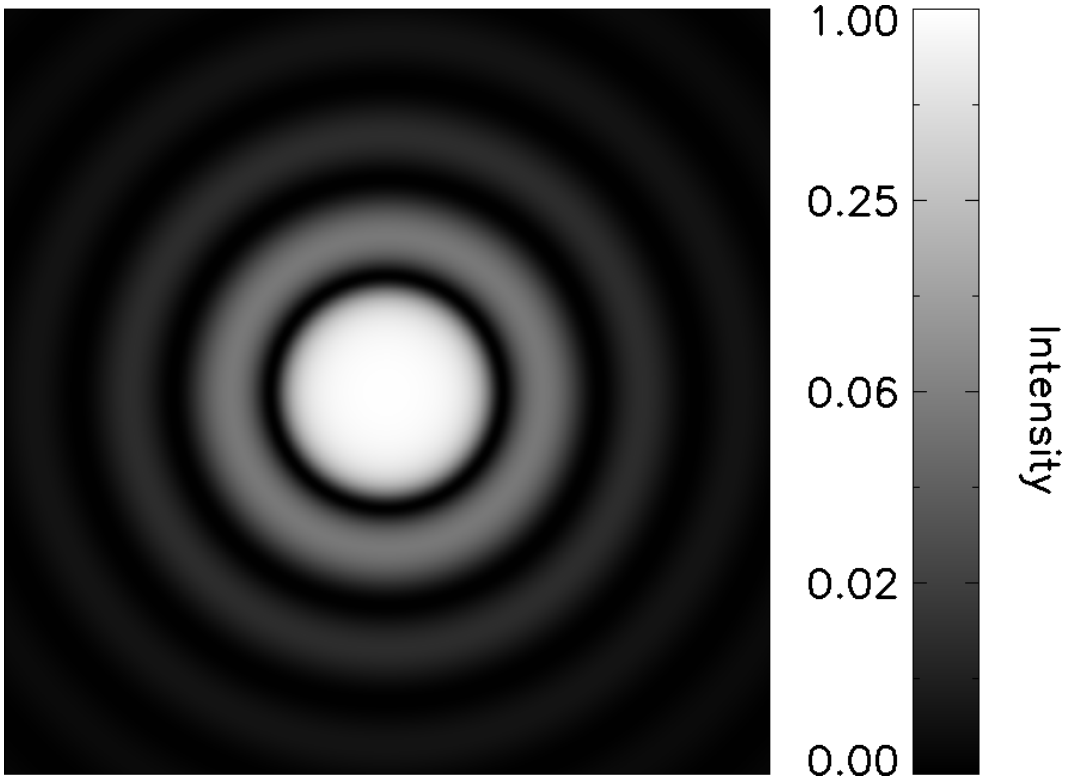

Figure 2.7: Airy pattern instrument response caused by the diffraction of light through a uniformly illuminated circular aperture.

minimum separation between two equally intense point sources that may be resolved into distinct objects. This is also known as two-point resolution and is analogous to astronomical imagery where stars are effectively point sources. As two point sources move closer together, an imaging system records the superposition of their point responses, and at some small distance it becomes impossible to detect that there were originally two separate point sources. According to the Rayleigh criterion, two point sources are barely resolved if the central peak of the diffraction pattern of one point source coincides with the first zero of the diffraction pattern of the second point source (Bom and Wolf, 1980). In other words, the Rayleigh resolution limit is determined by the distance between the central maximum and the first zero of the instrument PSF. This distance, with respect to the observed wavelength of light, is defined:

$$d = 1.22 \frac{\lambda f}{D} \tag{2.5}$$

where d = distance between the central maximum and the first zero
λ = observed wavelength of light
f = focal length
D = diameter of the aperture

As the aperture of the lens becomes larger, and/or the observed wavelength of light becomes smaller, the finer the resolution and greater the resolving power of the imaging system. The corresponding minimum angular resolution at which an object can be resolved is:

$$sin\theta = 1.22 \frac{\lambda}{D} \tag{2.6}$$

The PSF also represents instrumental stray light that can emanate from anywhere within the field-of-view of the instrument. This should not be confused with atmospheric stray light that largely comes from the molecular scattering of light outside the field-of-view of the instrument. The characterisation of instrumental

stray light is dependant on the physical attributes of the optical system and is resolved in the side-lobes of the instrument PSF. For instance, the area surrounding the image point of the MODIS Aqua band 8 PSF (Figure 2.4) describes the spatial response of how stray light sources within the field-of-view of the instrument affect the current measurement.

These three instrument-based effects – optical aberration, the diffraction limit and instrumental stray light – all have a detrimental impact on recorded imagery and therefore should ideally be removed. The effect that an instrument PSF has on recorded data can be described at point (x, y) with a convolution equation (Bracewell and Roberts, 1954):

$$I(x, y) = (O * P)(x, y) + N(x, y) \tag{2.7}$$

where $I(x, y)$ = intensity distribution (recorded image)
$O(x, y)$ = observed object (real image)
$P(x, y)$ = point spread function
$N(x, y)$ = Gaussian additive noise
and $*$ is the convolution operator

Equation 2.7 describes the physical process that occurs when an optical system observes and records information about a target. The real image $O(x, y)$, as it exists before passing through the optical system, becomes convolved with the instrument response function $P(x, y)$. This corresponds to light passing through the optical system and being reflected or refracted by the lens of the instrument. Finally, Gaussian noise $N(x, y)$ is added to the recorded signal as the incoming light is converted to digital measurements by the array of detectors in the instrument. The culmination of this entire process results in the recorded image $I(x, y)$.

2.3 Deconvolution

Deconvolution is an algorithm-based procedure that aims to reverse the effects of convolution. If the recorded signal I, the instrument response function P, and

an estimate of the detector-based noise N are all known, then deconvolution can be applied to reconstruct the original signal O (Equation 2.7). Deconvolution has attracted a significant amount of attention with the two main obstacles being the identification of a PSF cut-off frequency and the processing of detector-based noise.

Qiu et al. (2000) showed that a long-range cut-off frequency can dramatically improve the accuracy of image deconvolution, especially in high-contrast scenes such as bright clouds over dark terrain or broken snow and ice scenes. This result indicates that instrument PSFs should not be truncated to increase computational efficiency. Rather, the PSF should be preserved with the longest possible range in order to maintain the highest quality data reconstruction.

The presence of noise is the leading factor that makes deconvolution problems particularly difficult to solve. Gaussian noise is the most often assumed model, however Poisson or a combination of Gaussian and Poisson noise can also be accommodated using the Anscombe transform (Anscombe, 1948).

An efficient solution to the deconvolution inverse problem can be found by describing the convolution equation in Fourier space. Let ‘ ˆ ’ denote the Fourier transform operator (Krantz, 1999) which is equivalent to the notation defined by Trott (2004). From Equation 2.7, taking the Fourier transform leads to:

$$\hat{I}(u,v) = [O \hat{*} P](u,v) + \hat{N}(u,v) \tag{2.8}$$

The Convolution Theorem states that, under suitable conditions, the Fourier transform of a convolution is the point-wise product of Fourier transforms (Equation 2.4). Therefore, Equation 2.8 becomes:

$$\hat{I}(u,v) = \hat{O}(u,v) \cdot \hat{P}(u,v) + \hat{N}(u,v) \tag{2.9}$$

The Fourier-quotient method can be applied to isolate $\hat{O}$ and retrieve the deconvolved image:

$$\hat{\tilde{O}}(u,v) = \frac{\hat{I}(u,v)}{\hat{P}(u,v)} = \hat{O}(u,v) + \frac{\hat{N}(u,v)}{\hat{P}(u,v)} \tag{2.10}$$

where ˜ indicates an estimate

This method can be computed very efficiently. However, the primary drawback is that noise becomes amplified at frequencies close to the PSF cut-off frequency. This makes the Fourier-quotient method unsuitable for the deconvolution of data containing even small quantities of noise.

Deconvolution is generally an ill-posed problem. This means that no unique or stable solution exists. To combat this ill-posed nature, regularisation techniques must be introduced in order to constrain the solution space, promote some desirable properties and help identify a unique and stable solution.

2.3.1 Linear Regularisation Methods

The Method of Least Squares (MLS) is a standard approach to solving over-determined systems. In a linear system we have:

$$Ax = b \tag{2.11}$$

The MLS aims to find a model in which the sum of the squared residuals has the smallest value:

$$||Ax - b||^2 \tag{2.12}$$

where $||.||$ represents the Euclidean norm

Interpreting this into the deconvolution domain, the minimisation becomes:

$$||I(x,y) - P(x,y) * O(x,y)||^2 \tag{2.13}$$

This leads to the direct solution in Fourier space:

$$\hat{\tilde{O}}(u,v) = \frac{\hat{P}^*(u,v)\hat{I}(u,v)}{|\hat{P}(u,v)|^2} \tag{2.14}$$

$$\begin{aligned} \text{where} \quad \hat{P}(u,v) &\neq 0 \\ \hat{P}^*(u,v) &= \text{complex conjugate of } \hat{P} \end{aligned}$$

Again, this problem is generally ill-posed and requires the use of regularisation techniques to find a unique and stable solution. Tikhonov regularisation is one of the most commonly used regularisation methods for ill-posed problems (Tikhonov et al., 1987). From the standard approach in Equation 2.12, Tikhonov regularisation aims to give preference to a solution that shows some desirable properties using the minimisation:

$$||Ax - b||^2 + \alpha||x||^2 \tag{2.15}$$

The Tikhonov matrix α is a regularisation parameter that represents the balance between data fit accuracy and solution smoothness. The mechanism of a balancing regularisation parameter is used in many other deconvolution algorithms, as will be seen shortly. In the case of image deconvolution, the minimisation is:

$$J_T(O(x,y)) = ||I(x,y) - (P * O)(x,y)||^2 + \alpha||(H * O)(x,y)||^2 \tag{2.16}$$

$$\begin{aligned} \text{where} \quad ||I(x,y) - (P * O)(x,y)||^2 &= \text{data fit accuracy} \\ H(x,y) &= \text{high pass filter} \\ ||(H * O)(x,y)||^2 &= \text{smoothed solution} \end{aligned}$$

This can be calculated directly in Fourier space:

$$\hat{\tilde{O}}(u,v) = \frac{\hat{P}^*(u,v)\hat{I}(u,v)}{|\hat{P}(u,v)|^2 + \alpha|\hat{H}(u,v)|^2} \tag{2.17}$$

Tikhonov regularisation is capable of producing reasonable results, however it also tends to produce overly-smoothed images. This becomes a severe problem if discontinuities are contained within the original data.

Wiener deconvolution is another linear regularisation method that can be used to restore images (Dhawan et al., 1985). This method utilises the Wiener filter to minimise the impact of noise at frequencies that have a small signal-to-noise ratio (Wiener, 1949). Wiener deconvolution works by making an estimation of the spectral distribution of the desired noiseless signal. From Equation 2.7, the aim is to find some $G(x, y)$ to allow the estimation of $O(x, y)$:

$$\tilde{O}(x, y) = G(x, y) * I(x, y) \tag{2.18}$$

$$\begin{aligned} \text{where} \quad \tilde{O}(x, y) &= \text{an estimate of } O(x, y) \text{ that} \\ &\quad \text{minimises the mean square error} \\ G(x, y) &= \text{an appropriately chosen Wiener filter} \end{aligned}$$

The Wiener filter can be described in the frequency domain by:

$$\begin{aligned} \hat{G}(u, v) &= \frac{\hat{P}^*(u, v)\hat{I}(u, v)}{|\hat{P}(u, v)|^2 \hat{I}(u, v) + \hat{N}(u, v)} \\ &= \frac{\hat{P}^*(u, v)}{|\hat{P}(u, v)|^2 + \frac{\hat{N}(u,v)}{\hat{I}(u,v)}} \\ &= \frac{\hat{P}^*(u, v)}{|\hat{P}(u, v)|^2 + \frac{1}{\text{SNR}(u,v)}} \end{aligned} \tag{2.19}$$

$$\begin{aligned} \text{where} \quad \text{SNR}(u, v) &= \text{Signal-to-Noise Ratio} \\ &= \frac{\hat{I}(u,v)}{\hat{N}(u,v)} \end{aligned}$$

The spectral estimation of the desired noiseless signal is assumed to be reasonably well behaved in the frequency domain for the purpose of this method. The estimate is then compared with the original image and noise is iteratively filtered. This

method can be computed very quickly but contains some serious disadvantages, such as severe artefact creation around image features. Information about the spectral content of the noise is also required for this method to work, and this may not necessarily be well behaved in the frequency domain.

Some of the main drawbacks generally encountered with linear regularisation methods include: their inability to incorporate *a priori* information which allow negative values to exist in the solution; the formation of Gibbs oscillation around discontinuities (Gottlieb and Shu, 1997); and the degradation of resolution from using a low-pass filter as a window function. With these limitations in mind, several other approaches to image deconvolution will be investigated.

2.3.2 CLEAN

The CLEAN method is a standard approach to deconvolution that was developed specifically for astronomical images (Högbom, 1974). CLEAN assumes that all objects are a collection of point sources and attempts to decompose images by representing all significant components with δ-functions. CLEAN iteratively finds the brightest feature in the image and subtracts a fraction (loop gain) of the PSF (dirty beam) at the location of the feature. The subtracted image (residual map) is then used in the next iteration and the process is terminated when the side-lobes of the image are smaller than the noise level. The restored image (clean map) is obtained by convolving the final map of δ-functions with the addition of the ideal PSF (clean beam) and residual map. There are many examples of successful applications of the CLEAN method in astronomy (Belton and Gandhi, 1988; Deshpande, 1996; Qui et al., 2000) and several efficient implementations of CLEAN have been developed, with the most popular being published by Clark (1980). One drawback of the original CLEAN method is that it does not operate well on images containing extended structures.

Wakker and Schwarz (1988) extended the CLEAN algorithm to include Multiresolution Support images as an attempt to help deconvolve interferometric imagery. This became known as Multi-Resolution Clean and begins by defining two intermediate images: a smooth map is created by convolving the data with a

Gaussian function, and a difference map is created by subtracting the smoothed map from the original data. CLEAN is then applied to these intermediate images and the resulting recombination of the cleaned intermediate images restores the image back to full resolution.

When information is transformed into the frequency domain, the convolution operator becomes diagonalised and noise that has been amplified during the inversion process can be localised and reduced. This is acceptable when dealing with smooth images. However, Fourier basis functions are not good at representing data containing sharp spatial features. Other functions such as the Wavelet transform are better designed to handle these events (Daubechies, 1992). This has led to a second variant of the CLEAN algorithm known as the Wavelet CLEAN method (WCLEAN) (Starck and Bijaoui, 1994; Starck et al., 1998). Wavelet decomposition is a technique that divides data into separate frequency components in order to resolve each component at a resolution matched to its scale. The greatest advantage over Fourier methods is that Wavelets can efficiently model discontinuities such as sharp spikes, singularities and high-contrast edges. WCLEAN operates by applying the Wavelet transform to the original image, the PSF, and the clean beam. The CLEAN algorithm is then performed at every resolution scale of the image and PSF. The reconstructed image is then retrieved using an iterative algorithm involving the clean beam.

The three distinct waves of development seen with the CLEAN method are indicative of developments to deconvolution methods in general. The concepts of multiresolution analysis and Wavelet-based image decomposition represent significant advancements which have been replicated in other deconvolution methods. Ultimately, the CLEAN method has shown some good results under the right circumstances, however, the application of satellite remote sensing may benefit from a more uniform approach to deconvolution.

2.3.3 Bayesian Methods

To evaluate the probability of finding the original image O given the data I, the Bayesian approach of constructing a conditional probability density relationship implies:

$$Pr(O|I) = \frac{Pr(I|O)Pr(O)}{Pr(I)} \tag{2.20}$$

The $Pr(I|O)$ term is the conditional probability of finding the data I given the original image O. For maximisation purposes, $Pr(I)$ is a constant and can be ignored because it has no effect on the maximisation. From here, several different Bayesien-based approaches can be derived. If the additive noise is assumed to be Gaussian distributed, then a starting point is to inspect the probability density function of the Gaussian distribution:

$$Pr(x) = \frac{1}{\sqrt{2\pi\sigma^2}}\, e^{-\frac{(x-\mu)^2}{2\sigma^2}} \tag{2.21}$$

$$\begin{aligned} \text{where} \quad \mu &= \text{mean} \\ \sigma^2 &= \text{variance} \end{aligned}$$

For deconvolution, the maximum likelihood solution seeks to maximise the probability density function $Pr(I|O)$, and in the case of Gaussian noise, results in:

$$Pr(I|O) = \frac{1}{\sqrt{2\pi\sigma_N^2}}\, e^{-\frac{(I-P*O)^2}{2\sigma_N^2}} \tag{2.22}$$

$$\text{where} \quad \sigma_N^2 = \text{the variance of the noise}$$

Assuming that $Pr(O)$ is constant, this is equivalent to minimising:

$$J(O) = \frac{||I - (P * O)||^2}{2\sigma_N^2} \tag{2.23}$$

One method that is commonly used here is known as the Landweber method (Landweber, 1951):

$$O^{n+1} = O^n - \gamma(P^T * (I - P * O^n)) \tag{2.24}$$

where O^{n+1} = next image
O^n = current image
P^T = the transpose of the PSF
γ = step size

Another method dealing with Gaussian noise can be derived from a Gaussian Bayes model. Here, the noise is assumed to have zero mean and unit variance and this leads to the Wiener filter solution previously seen in Equation 2.19:

$$\hat{\hat{O}}(u,v) = \frac{\hat{P}^*(u,v)\hat{I}(u,v)}{|\hat{P}(u,v)|^2 + \frac{\sigma_N(u,v)}{\sigma_O(u,v)}} \tag{2.25}$$

This method is very fast to compute, but has several severe limitations as previously discussed. Alternatively, Poisson noise can also be modelled and is generally considered quite appropriate because it is analogous to photon noise recorded by the detector. Poisson noise is defined by:

$$Pr(x) = \frac{\lambda^x e^{-\lambda}}{x!} \tag{2.26}$$

Interpreting this for the purposes of deconvolution gives:

$$Pr(I|O) = \prod_{x,y} \frac{[(P * O)(x,y)]^{I(x,y)} e^{-(P*O)(x,y)}}{I(x,y)!} \tag{2.27}$$

The maximum likelihood principle can be applied here and solved by taking the logarithm and calculating its first derivative:

$$\frac{\partial \ln p(I|O)(x,y)}{\partial O(x,y)} = 0 \tag{2.28}$$

With a normalised PSF, this leads to the Richarson-Lucy method (Richardson, 1972; Lucy, 1974) which is a common technique used in astronomy:

$$O^{n+1}(x,y) = \frac{I(x,y)}{(P * O^n)(x,y)} * P^T(x,y)O^n(x,y) \tag{2.29}$$

This method calculates the most likely real image given the recorded image and PSF. Flux is preserved and the solution is always positive. If convergent, this method has been shown to produce the maximum likelihood solution for the desired image O (Dempster et al., 1977). However, it is not guaranteed that this method will converge on a solution and this can be problematic if robust deconvolution is required.

A Poisson Bayes model leads to the Maximum *A Posteriori* (MAP) solution in which the probability density function $Pr(I|O)Pr(O)$ is maximised. This is equivalent to the maximum likelihood Poisson solution provided the probability density function $Pr(O)$ is uniform. This method requires a background model $M(x,y)$ which is usually chosen to equal O^n and can be calculated using the extra probability density function term:

$$Pr(O) = \prod_{x,y} \frac{[M(x,y)]^{O(x,y)} e^{-M(x,y)}}{O(x,y)!} \tag{2.30}$$

The MAP solution to the maximisation of $Pr(I|O)Pr(O)$ now becomes:

$$O^{n+1}(x,y) = O^n(x,y) e^{\frac{I(x,y)}{(P*O^n)(x,y)} - 1 * P^T(x,y)} \tag{2.31}$$

2.3.4 Maximum Entropy Method

The Maximum Entropy Method (MEM) is a technique that aims to extract the greatest amount of information from a measurement as justified by the signal-to-noise ratio of the data (Starck et al., 2002). The MEM retains all known information about a system, subject to the applied constraints, by determining the least biased image. In this way, unknown information is approximated in an unbiased manner.

In physics, entropy is defined as a measure of disorder in a system. Mathematical entropy requires a broader definition. Shannon initially defined the field of Information Theory in his ground-breaking publication 'A mathematical theory of

communication' (1949). This gave rise to a new definition of entropy as a measure of the degree of uncertainty in a system. Shannon postulated that by applying entropy to an information source, the minimum channel capacity required to reliably transmit the source as encoded binary digits can be determined.

Entropy is a measure that assigns a positive weight to all possible configurations that are not excluded by the given information or constraints (Shannon, 1949). This form of entropy exists as:

$$S(X) = -\sum_{x} Pr(x)\, log_2\, Pr(x) \tag{2.32}$$

$$\begin{aligned} \text{where} \qquad Pr(x) &= \text{probability that } X \text{ is in state } x \\ Pr(x)\, log_2\, Pr(x) &= 0 \text{ if } Pr(x) \text{ is } 0 \end{aligned}$$

Jaynes (1957) proposed that this form of entropy could be used for radio interferometric image deconvolution and showed that the only unbiased configuration is the solution that has maximum entropy. It has further been shown that maximum entropy is the only consistent method of selecting a solution which does not introduce correlations in the image beyond those which are required by the original data (Johnson and Shore, 1980, 1983; Livesey and Skilling, 1985).

For the application of image restoration, a statistical model for the imaging process must be developed to allow the definition of an entropy measure. This requires a discrete representation of the object in terms of pixels. The object is divided into N pixels, each with area ΔA and containing a particular radiance that can be considered as a random emission of photons with energy e. If r_i is the average rate of emission of photons from the i$^{\text{th}}$ pixel, then the average radiance of the i$^{\text{th}}$ pixel is described by:

$$f_i = \frac{e}{\Delta A}\, r_i \tag{2.33}$$

The probability that a photon was emitted from the i$^{\text{th}}$ pixel, given that it was emitted from the object is:

$$Pr_i = \frac{r_i}{\sum_i r_i} = \frac{f_i}{\sum_i f_i} = \frac{f_i}{F} \tag{2.34}$$

$$\text{where} \quad F \quad = \quad \text{total intensity}$$

The entropy of the discrete probability distribution is defined as:

$$S = -\sum_{i=1}^{n} Pr_i \log Pr_i = -\sum_{i=1}^{n} \frac{f_i}{F} \log \frac{f_i}{F} \tag{2.35}$$

This model describes the uncertainty as to which pixel emitted a given photon. Described more generally, this form of entropy has been proposed alongside other definitions in the image domain, each having unique attributes and advantages under different circumstances. These include:

Burg (1975):

$$S_b(O(x,y)) = -\sum_{pixels} \ln(O(x,y)) \tag{2.36}$$

Frieden (1975):

$$S_f(O(x,y)) = -\sum_{pixels} O(x,y) \ln(O(x,y)) \tag{2.37}$$

Gull and Skilling (1991):

$$S_g(O(x,y)) = -\sum_{pixels} O(x,y) - m - O(x,y) \ln\left(\frac{O(x,y)}{m}\right) \tag{2.38}$$

$$\text{where} \quad m \quad = \quad \text{background model}$$

The major advantage of Gull and Skilling's definition is that entropy has a maximum of zero when O equals the background model m. This is the form of entropy that has achieved the most success in image deconvolution and continues to be developed in new applications.

Returning to Bayes' theorem (Equation 2.20) allows the evaluation of the probability of finding the original image O given the data I under a maximum entropy framework. $Pr(I|O)$ is the conditional probability of finding the data I given the original image O, which essentially represents the distribution of the noise. Uncorrelated Gaussian noise with variance σ^2 is given by:

$$Pr(I|O) = exp\left(-\sum_{pixels}\frac{(I - P * O)^2}{2\sigma_I^2}\right) \tag{2.39}$$

Without any knowledge of O other than it being positive, applying the maximum entropy principal leads to:

$$Pr(O) = exp(\alpha S(O)) \tag{2.40}$$

$$\begin{aligned} \text{where} \qquad \alpha &= \text{Lagrange multiplier} \\ S(O) &= \text{entropy on image } O \end{aligned}$$

Again, $Pr(I)$ is independent of O and can thus be considered a constant. After substitution and taking logarithms:

$$\ln(Pr(O|I)) = \alpha S(O) - \sum_{pixels}\frac{(I - P * O)^2}{2\sigma_I^2} \tag{2.41}$$

This consists of the entropy of the image and a quantity corresponding to χ^2 which can be used to measure the statistical distance between the data and the model prediction. The solution can be found by minimising:

$$\begin{aligned} J(O) &= \sum_{pixels}\frac{(I - P * O)^2}{2\sigma_I^2} - \alpha S(O) \\ &= \frac{\chi^2}{2} - \alpha S(O) \end{aligned} \tag{2.42}$$

$$\text{where} \quad \alpha = \text{balance between data fit and solution smoothness}$$

Skilling and Bryan (1984) developed an operational maximum entropy deconvolution algorithm that performed well, but was limited by the computational capabilities of its time. As computer hardware progressed, these methods became outdated and were replaced by more accurate and computationally complex methods. The Pyramid Maximum Entropy Method introduced the concept of multiresolution image analysis into maximum entropy deconvolution (Bontekoe et al., 1994). This was a breakthrough for the MEM as the new multiresolution interpretation allowed significant features to be resolved at different image resolutions and then recombined to produce the final image. However, the Pyramid Maximum Entropy Method suffered from some major drawbacks such as multiresolution image reconstruction, the need to determine a default background model and user-defined reconstruction parameter estimation. The Multiscale Entropy method resolved many of these issues and showed that the concept of multiresolution image analysis was indeed beneficial, but the correct mathematical tool to implement this method was the Wavelet transform (Starck, 1996).

Chapter 4 investigates the Multiscale Entropy deconvolution of MODIS Aqua ocean colour imagery and shows that instrumental PSF effects can significantly impact the quality of recorded satellite data. Wavelet transforms and optimal step size estimation are combined with customised techniques including multi-detector FFT convolution and detector-saturated radiometric correction to produce an accurate and robust MODIS deconvolution implementation.

2.4 Resolution Enhancement

There have been several studies performed on the statistical limitations for resolution enhancement using a range of different approaches. These studies set out to systematically and empirically define quantifiable limits to the statistical boundaries of how far resolution enhancement techniques can reach. The most significant early work in this area was performed by Helstrom (Helstrom C.W., 1964, 1969, 1970). In these publications, Helstrom used the Cramer-Rao inequality to derive a lower mean-square error limit for unbiased estimators of point source positions,

the radiance values for the point source objects and the distance between the point sources. Further work developed a geometrical optics field model when considering the general distribution of radiance sources and instrument PSFs for objects of inconsistent shape. Helstrom translated these results to instruments containing circular apertures and considered point source responses by applying well-reasoned simplifications and approximations to the derived optical model. These advances laid the foundations for statistical evaluations of optical system resolution.

Further work in this area was performed by Lucy with respect to statistical limitation caused by photon counts and deconvolution processes (Lucy, 1992a,b). The concept of defining limitations based on the number of detected photons is analogous to the signal-to-noise ratio of the recorded image. In both papers, Lucy redefined the concept of resolution to be the separation of two point sources that can be resolved through a deconvolution process. It was then shown that the resolution of the detected image can potentially be increased beyond the limit imposed by the Rayleigh criterion, as long as some strict conditions relating to the signal-to-noise ratio are met. This new resolution limit is termed the 'super-resolution limit'.

Bettens et al. (1999) extended Helstrom's work by further developing the Cramer-Rao lower bound to estimate the precision level attainable with respect to the distances between two point sources. This analysis assumed the instrument PSF to be Gaussian distributed and went on to derive a lower bound for the estimated two-point distance variance. More recently, Shahram (2004) presented a frequency domain approach to the two-point problem by calculating the optimal maximum likelihood estimation for the distance between the two point sources. The Cramer-Rao lower bounds were then calculated in exact and closed form. Shahram (2004) also rigorously studied a range of cases including unknown and unequal point source intensities and presented practical results detailing the specific effects that the relevant parameters have on resolution and its limitations. The major result for the case of equal intensities is that the minimum resolvable distance is proportional to $(\frac{1}{SNR})^{\frac{1}{4}}$.

Another approach to resolution was investigated by Kosarev (1990) in which Shannon's information theory was applied to the two-point resolution problem

to define a resolution limit. In this work, resolution is defined as the inverse of the minimum discernible distance between two point sources of equal brightness. Information Theory is applied to calculate a resolution enhancement limit with respect to the maximum channel capacity of a noisy transfer. In this way, a direct relationship is derived to logarithmically relate resolution to the signal-to-noise ratio.

den Dekker and van den Bos (1997) and Baker and Kanade (2002) presented detailed reviews of the different approaches that have been applied to the formulation of resolution. However, the latter of these reviews primarily deals with the case of multi-frame super-resolution.

Chapter 6 develops a novel approach to spatial resolution enhancement by utilising information contained within high-resolution PSF measurements. Super-resolution is achieved by solving a underdetermined system of linear equations with the use of a modified variant of Multiscale Entropy regularisation. Results show that a reasonable amount of high-frequency content can be extracted from the PSF, and the resolution enhanced imagery compares favourably to common interpolation techniques.

Chapter 3

Convolution

3.1 Introduction

Convolution is a formal mathematical operation which combines two input signals and produces a point response by calculating the integrated product of the two overlapping input signals. Evaluating this convolution sum at every overlapping position of the two input signals produces the resultant convolved output signal. Convolution has far-reaching applications including digital signal processing, electrical engineering, computer vision and statistics, as well as being a fundamental element in deconvolution problems (Starck et al., 2002). In a continuous system, the convolution of two signals, f and g, is described using the convolution integral (Bracewell, 2000):

$$(f * g)(x) = \int_{-\infty}^{\infty} f(u)\, g(x-u)\, \mathrm{d}u \tag{3.1}$$

where $*$ is the convolution operator

Digital computation requires data to be represented as discrete signals. The equivalent convolution operation can be calculated for discrete systems using the convolution sum (Smith, 2003):

$$O(x) = (I * K)(x) = \sum_{i=0}^{M-1} K(i)\, I(x-i) \tag{3.2}$$

$$\begin{aligned} \text{where} \quad O(x) &= \text{convolved output signal} \\ &\quad (N+M-1 \text{ elements}) \\ I(x) &= \text{input signal } (N \text{ elements}) \\ K(x) &= \text{convolution kernel } (M \text{ elements}) \end{aligned}$$

This equation describes how the convolved output signal $O(x)$ relates to the two input signals $I(x)$ and $K(x)$ from a computational perspective where x is now discrete. The results is the convolved output signal $O(x)$ containing $N + M - 1$ data points (Smith, 2003). Often, the final convolved signal is required to be the same length as the input signal. In this case, all data points that fall beyond the window of the input signal are discarded and the final convolved signal is returned with the same dimensions as the input signal. This form of convolution can be performed in one or two dimensions and, for the purposes of this chapter, will be referred to as standard convolution.

There are many convolution applications for two-dimensional imagery. To accommodate this, Equation 3.2 can be extended into two-dimensional space:

$$O(x,y) = \sum_{j=0}^{M-1}\sum_{i=0}^{M-1} K(i,j)\, I(x-i, y-j) \tag{3.3}$$

$$\begin{aligned} \text{where} \quad O(x,y) &= \text{convolved output signal} \\ &\quad ((N+M-1) \times (N+M-1) \text{ elements}) \\ I(x,y) &= \text{input signal } (N \times N \text{ elements}) \\ K(x,y) &= \text{convolution kernel } (M \times M \text{ elements}) \end{aligned}$$

The two-dimensional input signal and convolution kernel are defined to be square for simplicity. However, this is not a requirement and any sized rectangular imagery can be accommodated. Equation 3.3 is simply an extension of the one-dimensional convolution sum, and therefore all operations and results for one-dimensional data

are applicable to two-dimensional data. The computational complexities for the convolution sums in Equations 3.2 and 3.3 are:

$$\begin{aligned} \text{One-dimensional Convolution} &\Rightarrow \quad O(N) \quad = \quad N \times M \\ \text{Two-dimensional Convolution} &\Rightarrow \quad O(N \times N) \quad = \quad N^2 \times M^2 \end{aligned} \tag{3.4}$$

A worst case scenario occurs when the kernel M is the same size as the input signal. In this case, the computational complexity of standard spatial domain convolution scales with the square of the input signal. This has little impact when convolving small signals but becomes exceedingly slow for large input signal convolution.

Since the conception of the Fourier transform, it has been well known that convolution can also be performed in the frequency domain. This capability arises from the Convolution Theorem:

$$\mathcal{F}(f * g) = \mathcal{F}(f)\mathcal{F}(g) \tag{3.5}$$

where $\mathcal{F}$ indicates a Fourier transform (Trott, 2004)

That is, the convolution of two functions is equal to the inverse Fourier transform of the rectangular product of their Fourier transforms (Smith, 2003). However, the computation time required to calculate the Discrete Fourier Transform (DFT) and, in turn, frequency domain convolution, is often much greater than calculating standard convolution. The introduction of the Fast Fourier Transform (FFT) brought about efficient transform computation due to its radix-2 recursive architecture (Cooley and Tukey, 1965). For this reason, the FFT operates at optimal speed when the input signals have a data length, or a padded data length, equal to a power of 2 (Brigham, 1986). Alternatively, more advanced mixed-radix FFT algorithms have been developed that efficiently exploit a combination of base values and can be used to potentially reduce the final border padding size. For the purposes of this chapter, a simple radix-2 algorithm will be considered.

The speed advantages associated with the FFT allow frequency-domain convolution to be reduced in computational complexity:

$$\begin{aligned} \text{1D FFT Convolution} &\Rightarrow & O(N) &= N\,log_2(N) \\ \text{2D FFT Convolution} &\Rightarrow & O(N \times N) &= N^2\,log_2(N) \end{aligned} \tag{3.6}$$

This represents a significant speed improvement over standard convolution. To investigate this Computational Advantage (CA), consider the standard and FFT convolution of a one-dimensional signal of length N, with a kernel also of length N:

$$CA\,(N) = \frac{N^2}{N\,log_2(N)} = \frac{N}{log_2(N)} \tag{3.7}$$

If it is assumed that the input signal length is a power of 2 for speed purposes, i.e. $N = 2^p$:

$$\Rightarrow CA\,(p) = \frac{2^p}{log_2(2^p)} = \frac{2^p}{p} \tag{3.8}$$

Figure 3.1 shows the computational advantage of using FFT convolution. The computational advantage is significantly increased as the signal becomes larger. For instance, the convolution of a signal of length 1048576 ($p = 20$) can be calculated approximately 50 000 times faster using FFT convolution than standard convolution. In two dimensions, this is equivalent to convolving a moderate sized image of 1024×1024 pixels. This highlights the extreme computational advantage that can be obtained using FFT convolution.

FFT convolution requires that the two input signals have the same dimensions so they can be directly multiplied in the frequency domain. This can be achieved by padding the perimeter of both the input signal and the kernel to equal dimensions. However, if the input signal padding is not larger than the size of the original kernel, circular convolution will be encountered due to the inherent properties of frequency domain analysis. When a discrete signal is transformed into the frequency domain, it is represented as a periodic object. That is, the signal no longer has a start or an end; it is repeated head-to-tail an infinite number of times. When FFT convolution is performed, information at the end of the signal will contaminate the start of the

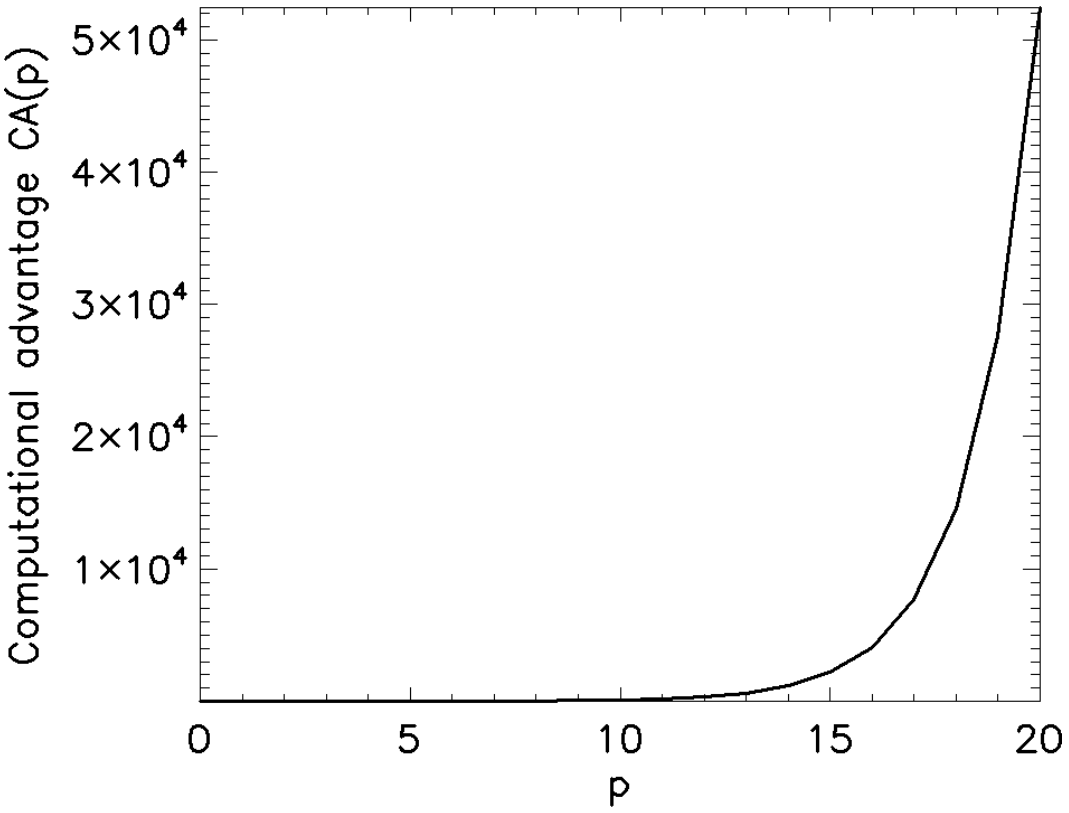

Figure 3.1: Computational advantage of FFT convolution over standard convolution.

signal and vice-versa. This is known as the 'wrap-around' effect and is a result of circular convolution.

Consequently, for FFT convolution of two-dimensional imagery, the left and right sides of the image can be considered to be connected, as can the top and bottom edges of the image. To avoid wrap-around contamination, a border must be constructed around the input signal that is larger than the length of the kernel in each dimension. In this way, the kernel will not be large enough to span the distance of the border and contaminate opposing edges in the image.

As a result, FFT convolution is burdened with the extra computational overhead of initialising and transforming padded arrays. With respect to comparing standard and FFT convolution, this overhead dominates only when the kernel size is small. Thus, a threshold exists above which it is faster to perform FFT convolution and below which it is faster to perform standard convolution (Figure 3.2). This threshold is calculated from the computational complexities defined for one-dimensional convolution in Equations 3.4 and 3.6. The jaggedness of the threshold is a result

of the computational overhead encountered by FFT convolution zero-padding to powers of 2. Additional discontinuities would be included in the threshold for more complicated mixed-radix algorithms. It is clear that standard convolution is more efficient for small kernel sizes and FFT convolution is more efficient when the kernel size becomes large, regardless of the size of the input signal.

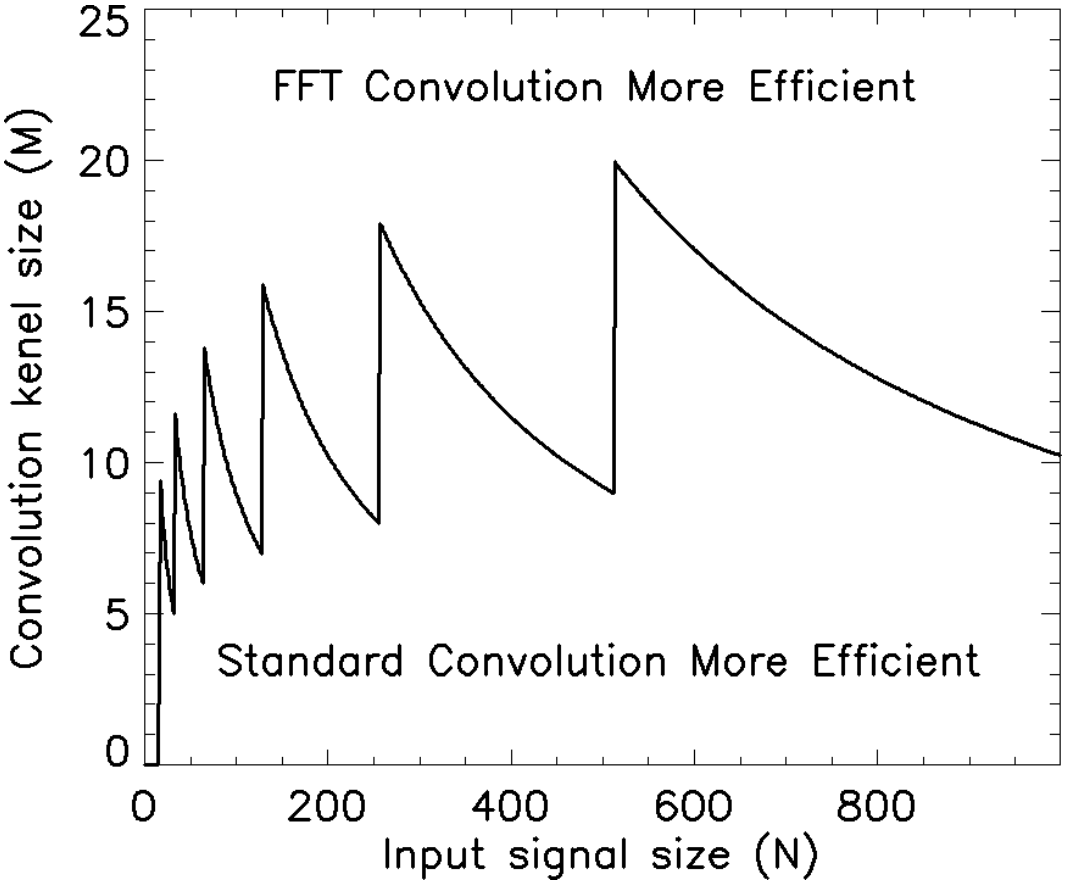

Figure 3.2: Padded convolution efficiency threshold above which it is faster to perform FFT convolution and below which it is faster to perform standard convolution.

Avoiding the circular convolution problem forces the input signals to be padded. However, the data used to pad the input will still affect the outer edges of the convolved result, as determined by the size and shape of the convolution kernel. For instance, consider the convolution of a signal that has been zero-padded. To calculate the convolved response at the left edge of the input signal, the kernel is centred on the left edge with approximately half of the kernel overlapping the input signal, while half of the kernel overlaps the zero-padded border. When the convolved response is calculated for this point it will undergo an intensity reduction

caused by the product of elements with value zero. By extending this concept, the entire boundary of the signal will exhibit an intensity reduction that decreases away from the boundary according to the size and shape of the kernel. The effect of this contamination can be seen by zero-padding and convolving a flat signal of value 1.0 with a normalised Gaussian convolution kernel (Figure 3.3). The perfect convolution of a flat signal should produce a resultant flat signal identical to the input, provided the convolution kernel is normalised. Clearly this is not the case as the zero-padded border contaminates the boundary of the convolved signal. This effect can be even greater with two-dimensional inputs where the kernel overlap at the corners of the input image will be approximately one-quarter of the kernel size.

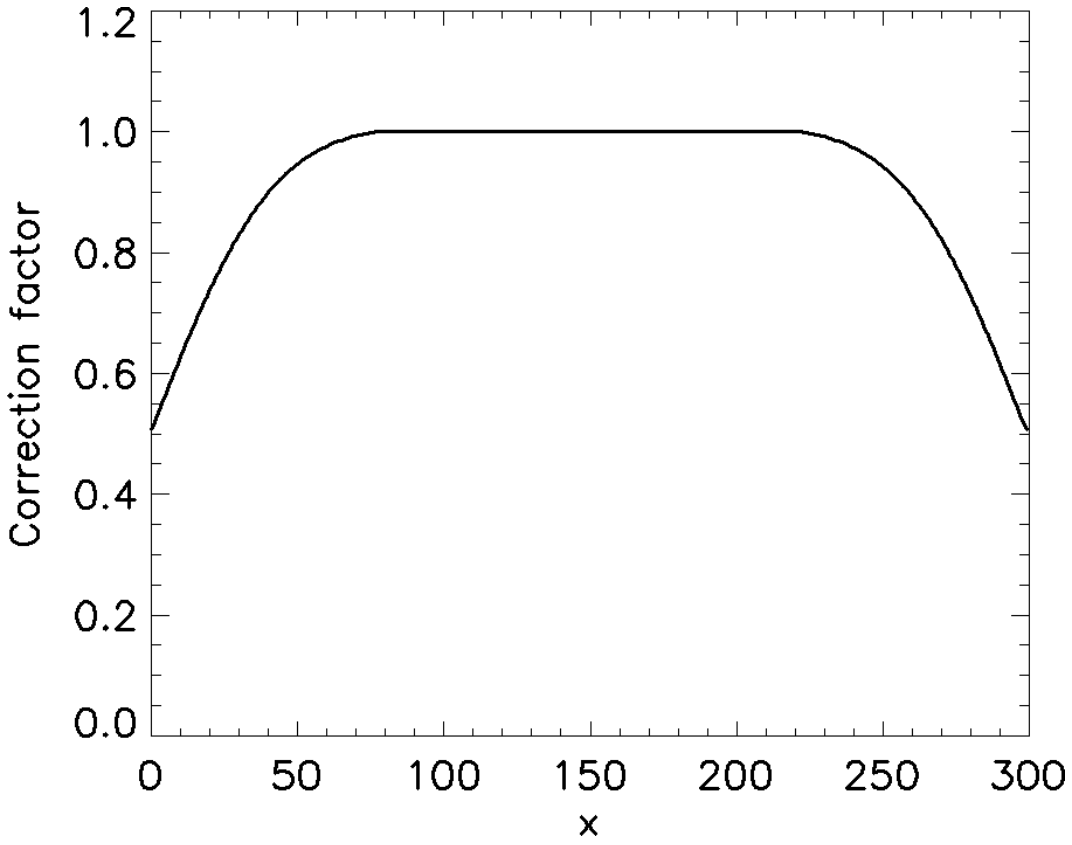

Figure 3.3: Boundary contamination encountered by convolving a zero-padded flat signal (length = 300, value = 1.0) with a normalised symmetrical Gaussian convolution kernel (length = 155, FWHM = 77).

There are several other common approaches that aim to minimise this problem by filling the border with data derived from the original input signal. These methods include replication, mirroring and repetition (Figure 3.4). Replication simply repeats the input signal in the border, while mirroring reflects the input signal in the border. Repetition copies the edge-values of the signal and repeats them to fill the border. The major advantage of the mirroring and repetition methods is that there is no discontinuity between the input signal and padded border. This reduces edge contamination when convolution is performed. All of these methods rely on generating information to fill the borders. This is not ideal because any information contained in the border will contaminate the edges of the convolved signal to some degree. One solution would be to discard the contaminated outer-boundary of the convolved signal and be left with only the perfectly convolved inner region. However, for scientific purposes this is often unacceptable due to increasing quantities of data being discarded as the size of the kernel increases. Also, processes that require multiple convolution operations progressively reduce the remaining data.

3.2 Method

A robust convolution method would make a single consistent data-based boundary assumption and also minimise the unintended intensity variation at the edges of the final convolved output. One solution is to use zero-padding and renormalise the kernel multiplication according to the area of the convolution kernel that intersects the input array for every point in the convolution sum (Equation 3.3). This increases the intensity of the contaminated border according to known localised data values while also disregarding the information contained in the border. Even though this technique can produce desirable results, it still scales with the computational complexity of spatial-domain convolution (Equation 3.4). This approach will be termed Standard convolution with Boundary Renormalisation (SBR). Smith (2003) briefly described this concept but failed to highlight its importance in conjunction with FFT convolution. Performing FFT convolution and then correcting the result using a post-convolution correction factor is proposed in this chapter as a more

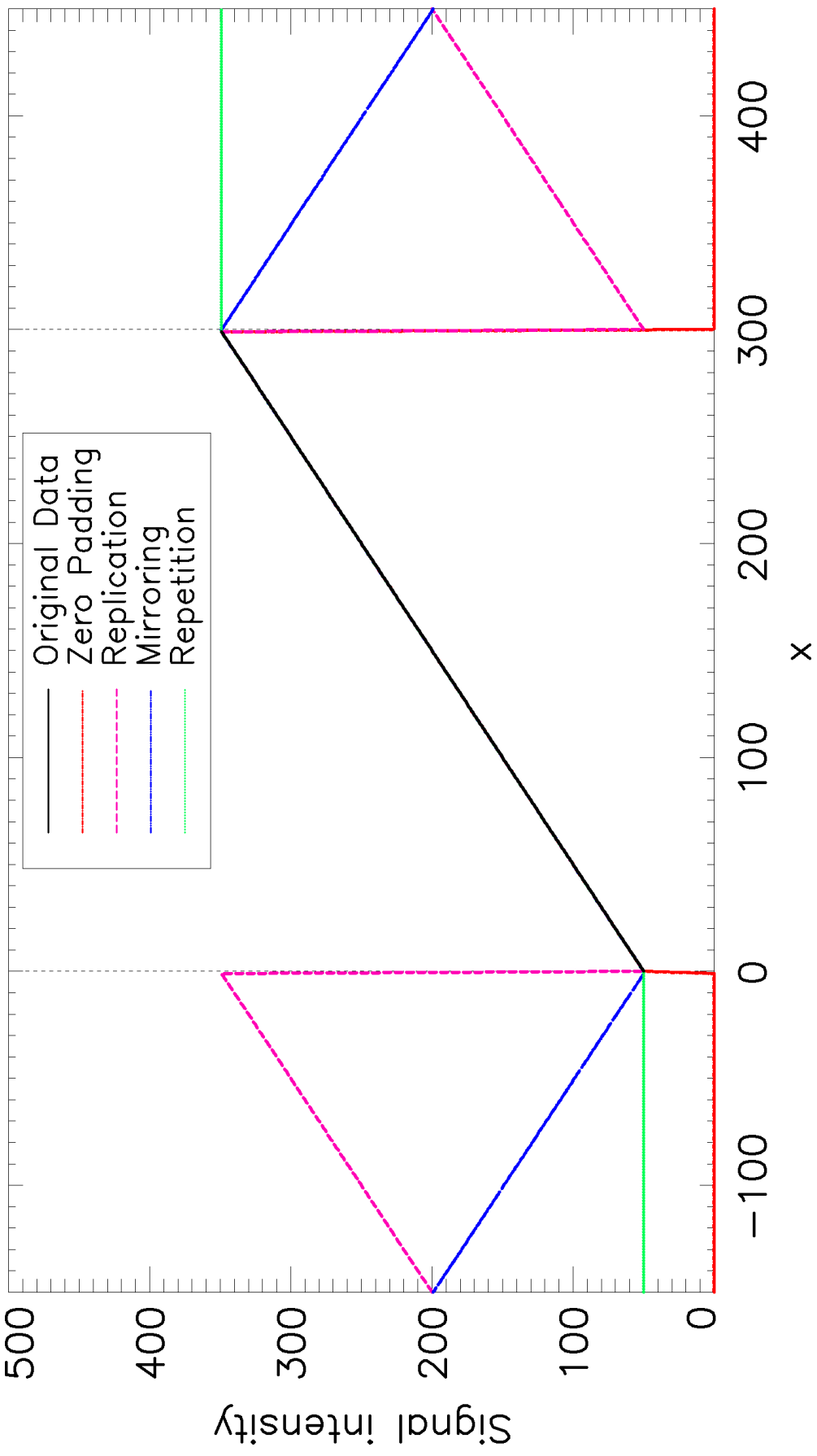

Figure 3.4: Linearly increasing signal (length = 300) with zero-padding, replication, mirroring and repetition boundary conditions (length = 150) depicted beyond the limits of the original signal.

efficient method to achieve the boundary renormalisation approach. This method will be developed in the following sections and referred to as FFT convolution with Border Correction (FBC).

The contamination seen in Figure 3.3 represents the intensity loss encountered using a zero-padded signal in convolution. Provided the border is filled with zero, the input signal can be FFT convolved and later corrected using a factor derived from the convolution kernel. Zero-padding the signal border allows the intensity loss at each data point to be accurately quantified. This is a critical element for the separability of the convolution operation and the correction factor. The correction factor can be retrieved by constructing a boolean template T of the padded signal according to the following rule:

$$T(\tilde{x}) = \begin{cases} 0 \text{ if pixel is in the border} \\ 1 \text{ if pixel is in the signal} \end{cases} \tag{3.9}$$

$$\text{where} \quad \tilde{x} \quad = \quad \text{signal length after zero-padding}$$

The template is convolved with the normalised kernel K and the correction array C is retrieved by removing the padded border from the result. These operations follow the altered convolution sum equation:

$$C(x) = \sum_{i=0}^{M-1} K(i)\, T(\tilde{x} - i) \tag{3.10}$$

Here, the result is calculated over the entire padded domain and then subset to the size of the original data to retrieve the final correction array. Having determined the correction factor, it is a simple calculation to correct the intensity loss in the FFT convolved signal. The correction factor represents the integrated response of the kernel that intersects with the input image. Therefore, the FFT convolved output is simply divided by the correction factor to correct for convolution boundary contamination:

$$O_c(x) = \frac{(I * K)(x)}{C(x)} \tag{3.11}$$

where $O_c(x)$ = corrected convolved output signal

The simplest implementation of this correction method relies on the kernel being normalised prior to operation. This naturally leads to an opportunity to increase algorithm efficiency. Depending on the size of the original input signal and the extent of the kernel, the correction factor may potentially contain a large centralised area that remains unaffected by convolution boundary contamination. This area will be represented in the correction factor by the value 1.0. Therefore, it is only necessary to apply the correction where $C(x) \neq 1.0$ and this will produce optimal computational efficiency. Alternatively, if an unnormalised kernel is used for convolution, then the central region unaffected by convolution boundary contamination will be represented in the correction factor by a single value other than 1.0. In this case, applying the correction factor requires the calculation to be performed over the entire signal domain, losing any potential efficiency optimisation.

3.3 Results

Figure 3.5 displays the responses of the different boundary condition methods from Figure 3.4 when convolved with a normalised symmetrical Gaussian convolution kernel (length = 155, FWHM = 77). The results show a wide range of edge responses for the different boundary condition methods. It is clear that the zero-padding and replication boundary conditions produce severe edge contamination for this particular signal. This is an inherent property of both boundary condition methods and is caused by large edge-discontinuities being created at the input data boundaries. The remaining three methods all produce responses similar to each other due to the input data edge values being preserved by the boundary mechanism and no severe edge discontinuities being added at the boundary of the input data. The convolved signal for the FBC method does not extend beyond the boundaries of the original input signal because the edges of the signal are corrected and the border is

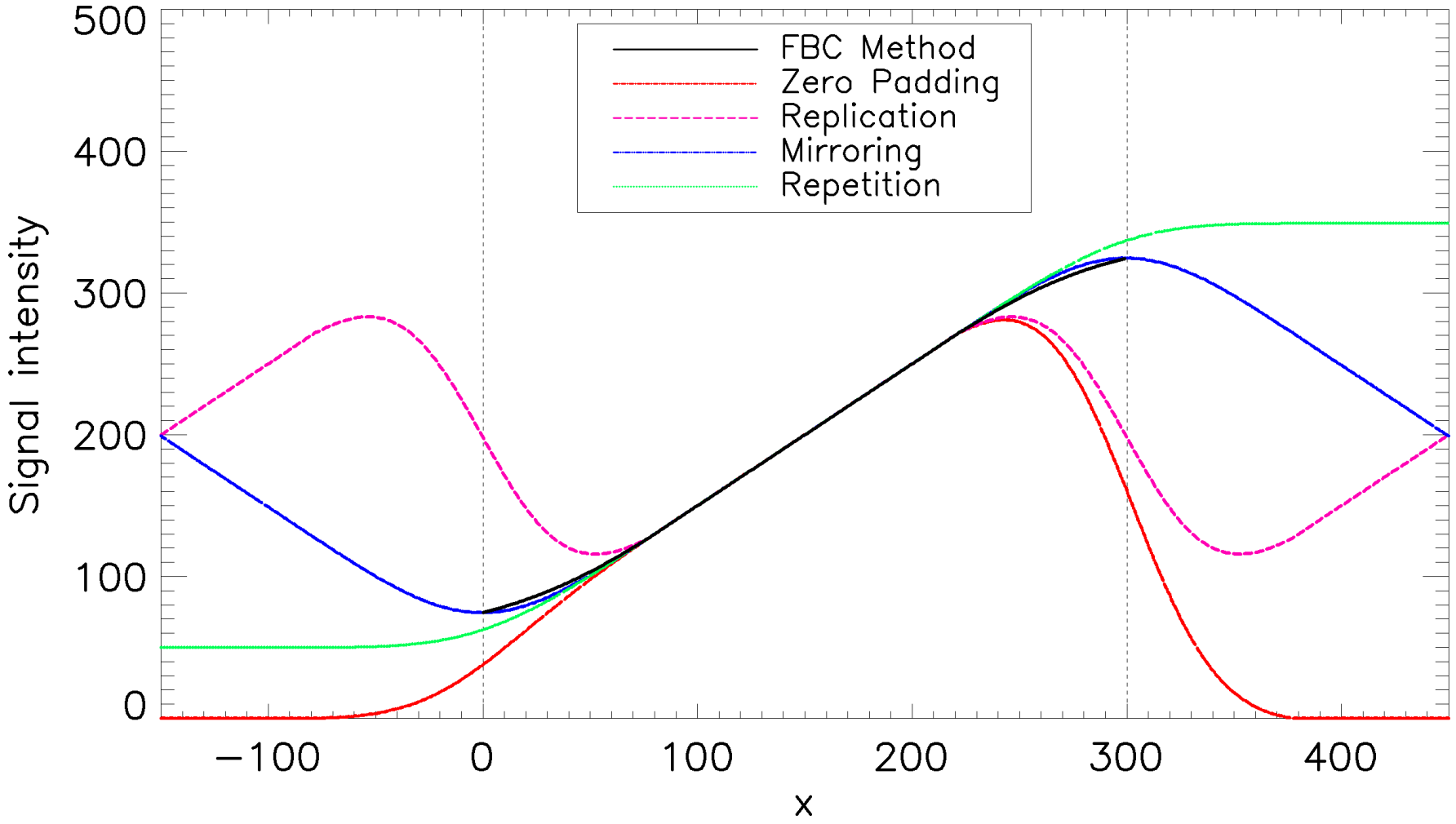

Figure 3.5: Response from convolving a linearly increasing signal (length = 300) with a normalised symmetrical Gaussian convolution kernel (length = 155, FWHM = 77) using zero-padding, replication, mirroring, repetition boundary conditions and the FBC method.

discarded.

Choice of convolution boundary condition has always been a difficult decision because information beyond the boundaries of the input data is unknown. Therefore, in making a boundary condition assumption, there will always be some form of edge degradation or contamination around the convolution output. The best option is to choose a boundary condition method that suits the input data. For the particular example shown in Figure 3.5, it is clear that the FBC method, repetition and mirroring outperform the zero-padding and replication boundary conditions. However, many real-world problems deal with data containing far less structure than that illustrated in this example. For instance, Chapter 4 implements a remote sensing deconvolution method and Chapter 6 develops a spatial resolution enhancement algorithm that both require accurate convolution operations that minimise boundary effects. In these cases, the FBC method may provide a unique and effective solution to limiting contamination that results from convolution operations by down-weighting the contribution at the edges.

To evaluate the equivalence of the SBR and FBC methods, synthetic and real test signals were convolved using both methods and the differences were analysed. These results can be directly compared because the two convolution methods perform equivalent operations. That is, SBR renormalises the intersection of the kernel with the input signal which increases the intensity of the contaminated edge values. Equivalently, the FBC method applies a correction to the convolved signal to increase the intensity of the edge values in exactly the same manner. Therefore, it is anticipated that the differences between the two methods will be very small.

Figure 3.6 shows different sized synthetic and real test signals that were used to compare the equivalence of the FBC and SBR methods. Each test signal was convolved using both methods and the residual of the resultant convolutions was calculated as the absolute value of the difference between the FBC and SBR results. The maximum values of the residuals is reported in Table 3.1 and represents the single largest difference between the two methods. For every processed test signal, the magnitude of the maximum residual difference is very small and is indicative of double precision rounding errors.

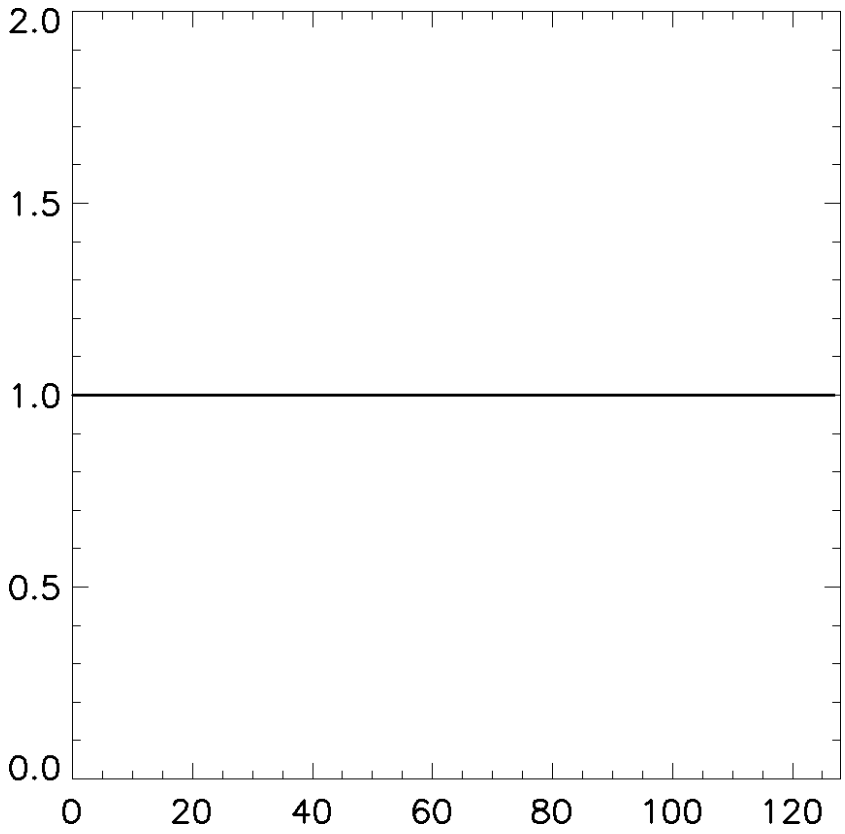

(a) Flat line

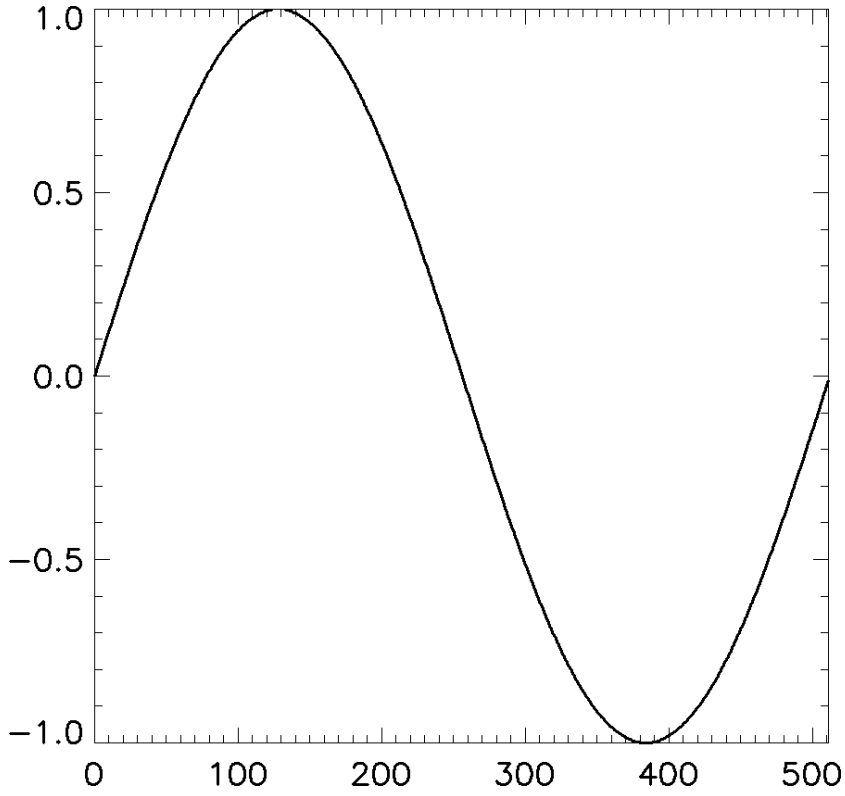

(b) Sine wave

Figure 3.6: One-dimensional test signals used to test the equivalence of the FBC and SBR methods including (a) a one-dimensional flat line and (b) a one-dimensional sine wave. These test signals are referred to in Table 3.1.

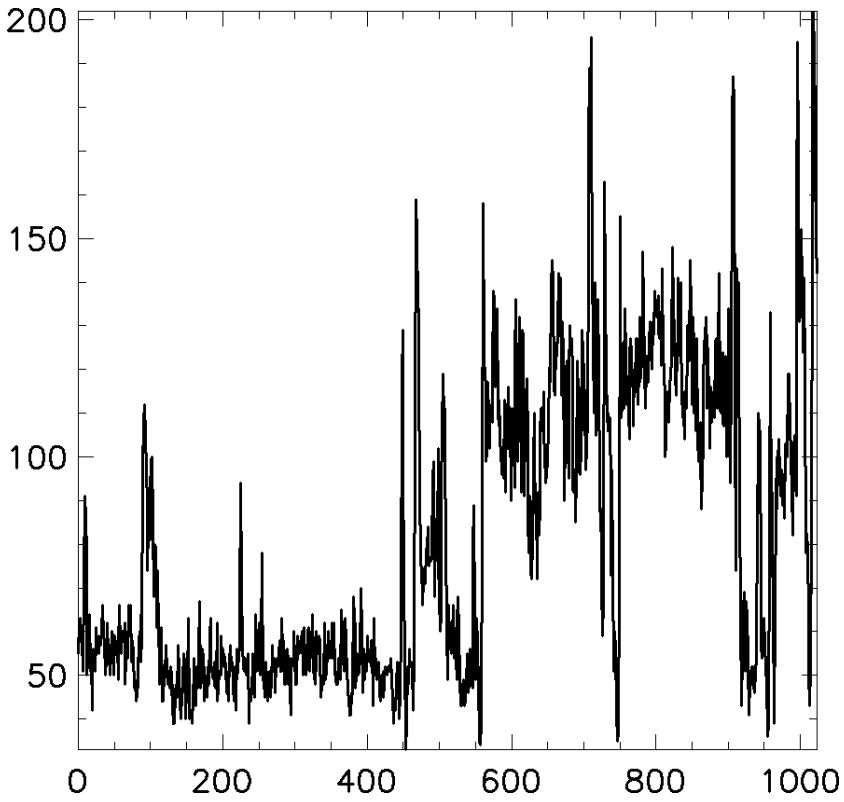

(c) Airport transect

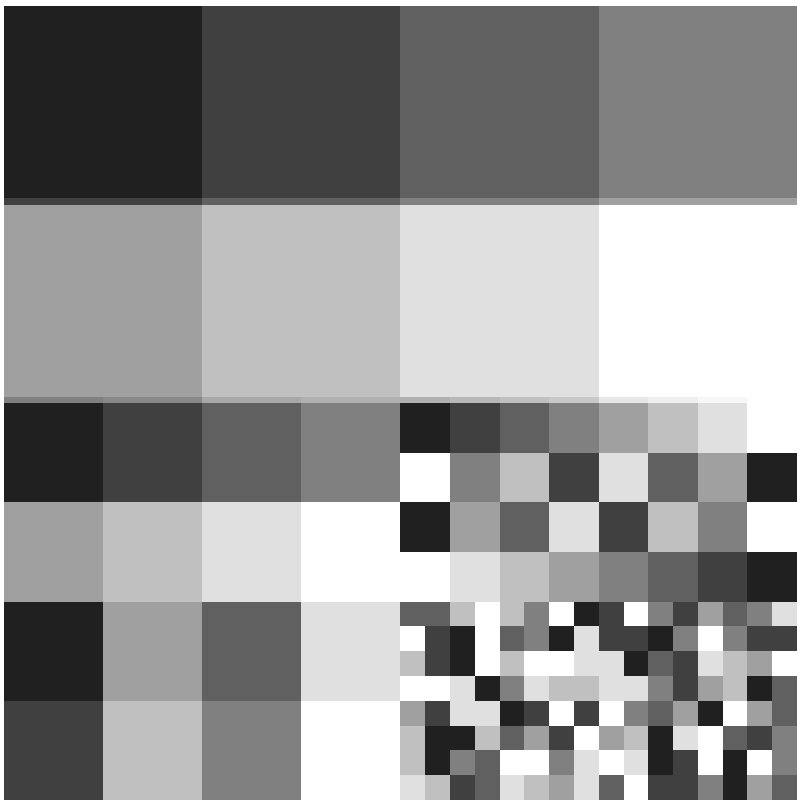

(d) USC texture mosaic #2

Figure 3.6 continued: One-dimensional and two-dimensional test signals used to test the equivalence of the FBC and SBR methods including (c) a one-dimensional airport transect and (d) the two-dimensional USC texture mosaic #2. These test signals are referred to in Table 3.1.

(e) USC texture mosaic #3

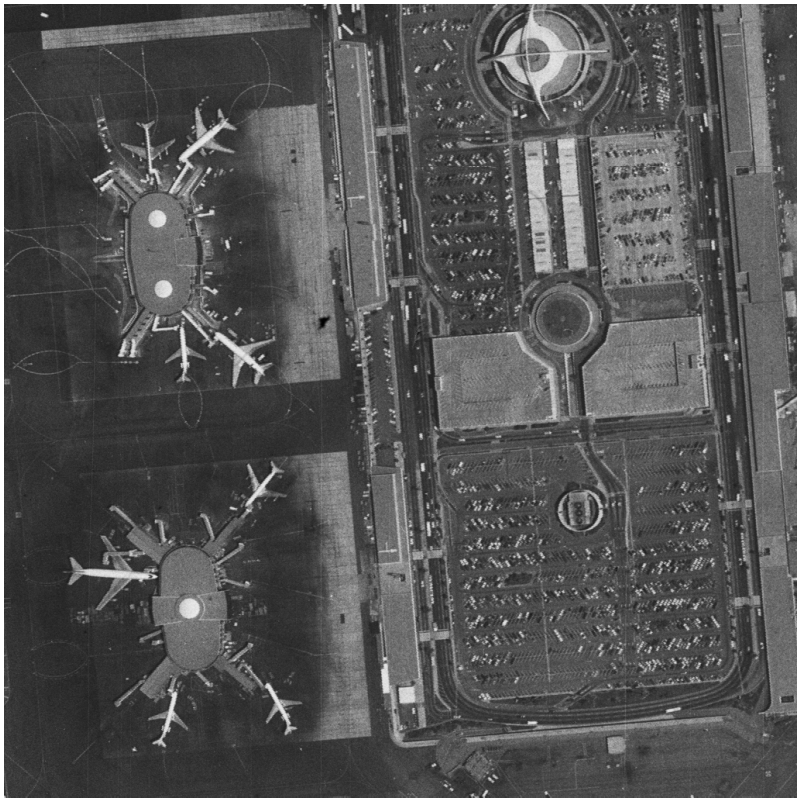

(f) Airport

Figure 3.6 continued: Two-dimensional test signals used to test the equivalence of the FBC and SBR methods including (e) the two-dimensional USC texture mosaic #3 and (f) a two-dimensional airport image. These test signals are referred to in Table 3.1.

Table 3.1: All test signals are convolved with both the FBC and SBR methods. The residual convolution result is calculated by subtracting the FBC result from the SBR result and the maximum residual difference is reported.

Test Signal	Signal Type	Dimensions	Maximum Residual Difference
(a) Flat line	Synthetic	1×128	5.55112×10^{-16}
(b) Sine wave	Synthetic	1×512	1.33227×10^{-15}
(c) Airport transect	Real	1×1024	4.61853×10^{-14}
(d) USC texture mosaic #2	Synthetic	128×128	2.58638×10^{-12}
(e) USC texture mosaic #3	Synthetic	256×256	4.47642×10^{-13}
(f) Airport	Real	512×512	4.27747×10^{-12}

These results show that the two convolution methods operate equivalently. However, with the FBC method utilising efficient FFT convolution, dramatic speed improvements can be made over using the standard convolution approach. This advantage, coupled with the conceptual design behind boundary renormalisation, may be used to provide an efficient and accurate convolution for many scientific applications.

However, there are some drawbacks associated with the FBC method. Firstly, optimal algorithm efficiency requires the kernel to be normalised before the convolution operation, which limits the usability of the FBC method for some applications. For instance, derivative and edge-detection calculations can be performed with convolution by using a kernel that contains both positive and negative components. If the FBC method is used with a normalised kernel for these applications, the positive and negative components of the kernel are rescaled in the kernel normalisation process. This results in a disruption and sensitivity reduction for any derivative or edge-detection calculation. Alternatively, an unnormalised kernel would alter the intensity of the central region of the convolution result due

to the correction factor being a value other than 1.0 in this area. Furthermore, in both cases an obvious boundary effect would be introduced from the partial renormalisation of the kernel at the boundary. Therefore, the FBC correction method may be considered unsuitable for applications where the convolution kernel has negative components.

It should also be noted that if there are any asymmetries present in the convolution kernel, the FBC method will produce subtly different boundary effects on opposing edges of the convolved output. This effect is determined by the renormalised kernel intersection and will only be as extreme as the asymmetries contained in the kernel.

3.4 Summary

Convolution of digital signals has always involved a trade-off for scientific application. FFT convolution achieves fast processing speed but can result in undesirable boundary effects. However, data accuracy is essential for scientific applications because a reduction in accuracy can lead to loss of data integrity and also detrimentally impact subsequent processing and analysis. This balance is directly caused by the choice of boundary condition used in the convolution process.

Results show that boundary renormalisation is achievable in the Fourier-domain by way of a post-convolution correction factor. The proposed correction factor adds minimal computational overhead to the FFT convolution process which results in the corrected convolution still utilising speed attributes associated with FFT convolution. As such, the FBC method employs an efficient data-based edge correction approach that is beneficial for many scientific applications.

This chapter has established a robust data-driven convolution boundary condition and examined its advantages and disadvantages for scientific applications. The main advantage of this approach is that boundary contamination effects are limited to structure contained in the input data and kernel, which in turn produces a consistent convolution result. The primary research contribution in this chapter is the novel combination of a boundary renormalisation approach with FFT

convolution to define a post-convolution correction factor and achieve accurate and efficient results.

The following chapters, specifically Chapters 4 and 6, make particular use of the FBC method to perform accurate signal convolution with minimised boundary effects. In fact, many of the small-signal convolutions that are performed in Chapter 4 do not operate successfully without some form of boundary correction and the FBC method provides an efficient and robust solution to this problem.

Chapter 4

Deconvolution

4.1 Introduction

Monitoring coastal environments is important for the sustainable management of regions affected by natural events, human activity and anthropogenic climate change. Remote sensing satellite instruments provide data at a range of spectral bands and spatial resolutions which are valuable to the monitoring of such regions. Often, however, the quality of remotely sensed data near the coast is compromised by contamination of the low signal from the ocean by high radiances from land and clouds. This contamination comes from radiance scattering in the atmosphere (Gordon, 1978) and from the instrument Point Spread Function (PSF). This chapter examines a means of removing instrumental distortion resulting from the instrument PSF.

Every satellite optical system has a unique PSF which describes the two-dimensional spatial response of the instrument. This interaction can be described at point (x, y) with a convolution equation (Bracewell and Roberts, 1954):

$$I(x,y) = (O * P)(x,y) + N(x,y) \tag{4.1}$$

where I = intensity distribution (recorded image)
O = observed object (real image)
P = point spread function
N = Gaussian additive noise
and $*$ is the convolution operator

Deconvolution is an algorithm-based procedure that attempts to reconstruct the original signal O given the recorded signal I, the spatial response function of the instrument P, and an estimate of the detector-based noise N. Deconvolution problems arise in a wide range of scientific and engineering disciplines; prominent examples occur in radio astronomy (Starck et al., 2002), microscopy (McNally et al., 1999) and seismology (Mendel, 1983).

4.2 MODIS Aqua PSF

The PSF of an instrument describes how a two-dimensional image of a point source is rendered by the optical system. This transformation can be characterised using a range of one-dimensional calibration tests performed on the instrument. Using such measurements, Meister et al. (2008) produced PSFs for all 10 detectors in every 1km resolution MODIS Aqua ocean colour band. MODIS Aqua contains a field baffle that is designed to restrict the field-of-view and reduce internal sensor-stray light. The PSF of each detector differs slightly according to its unique physical distance from the baffle. Figure 4.1 shows the PSFs for detectors 1, 5 and 10 of MODIS Aqua band 8 (405nm - 420nm) on a logarithmic scale with 1km pixel grid size. This band was chosen because the PSF is well centred and its shape is indicative of the other ocean colour bands. The peak of the PSF coincides with the image point of the instrument and shows that the majority of the recorded signal comes from this point. However, there is a large low response area surrounding and extending up to 20km from the image point. The underlying PSF is a result of the sensor optics and is spectrally

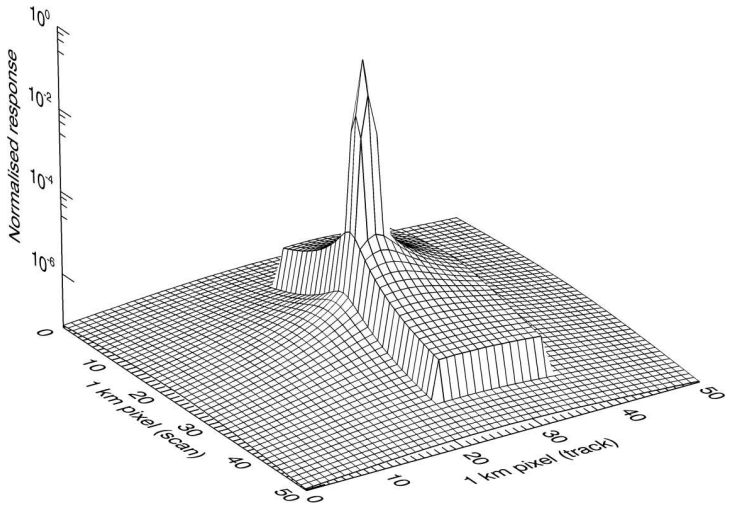

(a)

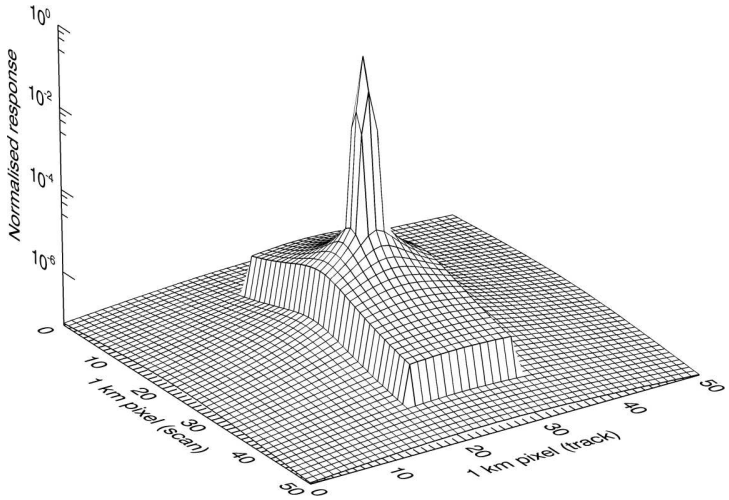

(b)

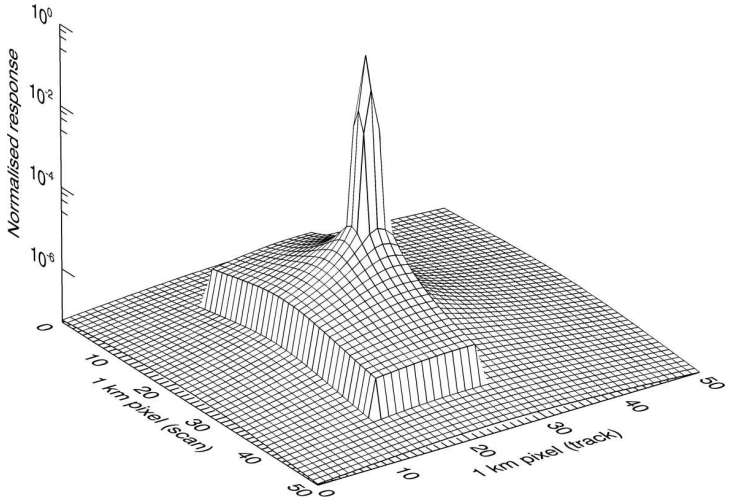

(c)

Figure 4.1: MODIS Aqua band 8 point spread functions (405nm - 420nm) on a logarithmic scale with 1km pixel grid size including (a) detector 1, (b) detector 5 and (c) detector 10. The low response area for each detector changes due to the unique position of the detector with respect the the field baffle.

independent. A truncation of the PSF occurs in both the scan and track dimensions due to the effect of the field baffle. The position of the detector relative to the field baffle determines the position of the truncation effect with respect to the centre of the PSF.

In deconvolution methods, PSFs are commonly truncated to a 3×3, 5×5 or 7×7 pixel area around the image point to reduce computing time. These cut-off levels have average integrated responses of 99.61%, 99.69% and 99.74% respectively for MODIS Aqua band 8. However, it has been shown near high-contrast edges that these approximations result in contamination, or radiance bias error, of more than 1% at distances up to 21km (Qiu et al., 2000). Scene contamination will vary from one band to another depending on the spectral reflectance of the target. Even so, all spectral bands experience some degree of contamination. Using the entire PSF throughout the deconvolution process will produce the greatest deconvolved data accuracy.

Figure 4.2 shows the effect that the MODIS Aqua band 8 PSF has on a synthetic test scene containing typical ocean reflectance of 0.5% and bright land reflectance of 30%. This synthetic scene has been designed with sharp land/ocean edges to highlight instrumental effects in coastal regions. Figures 4.2(a) and 4.2(b) clearly show the extent of contamination that can occur around sharp discontinuities. Figure 4.2(c) displays a transect of the right-hand edge of the land/ocean boundary and shows significant contamination on either side of the discontinuity. This example demonstrates an extreme case containing high contrast. It should be noted that the instrumental distortion is not symmetrical. There is a greater amount of contamination in the scan dimension, compared with the track dimension, resulting from asymmetries present in the instrument PSF.

Figure 4.3 shows the relative error introduced by the instrumental spatial response as a function of distance from a high-contrast edge. Four land/cloud reflectance values have been chosen along with a fixed water reflectance value to demonstrate the extent of contamination under different circumstances. In all cases, the first pixel from a high-contrast edge produces large errors that decrease rapidly with distance. It is evident that significant contamination errors still occur at large

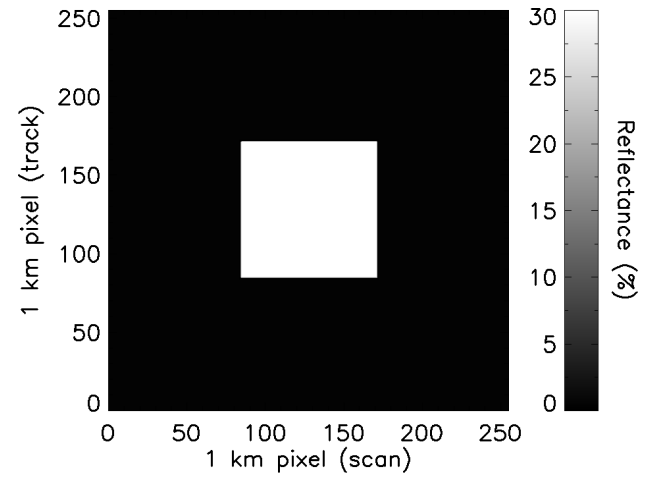

(a)

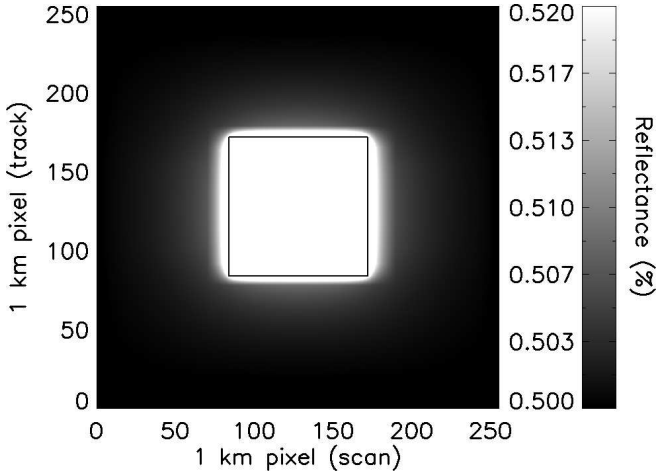

(b)

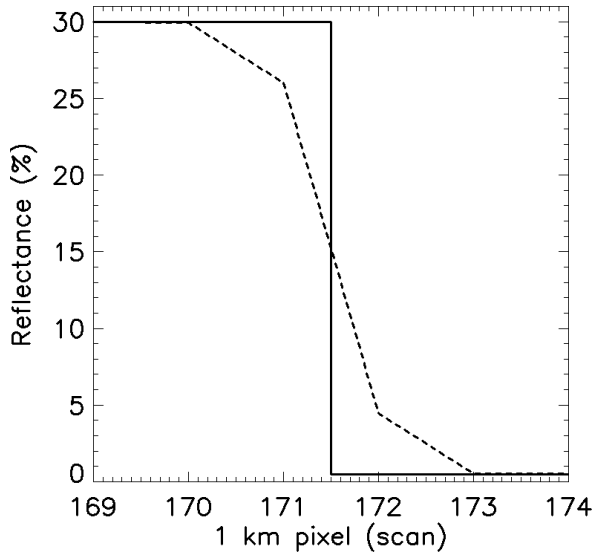

(c)

Figure 4.2: Contamination test showing (a) synthetic test scene with typical land and ocean reflectance, (b) synthetic test scene convolved with MODIS Aqua band 8 PSF with original boundary indicated and (c) comparison of original (solid) and convolved (dashed) right-hand edge transects.

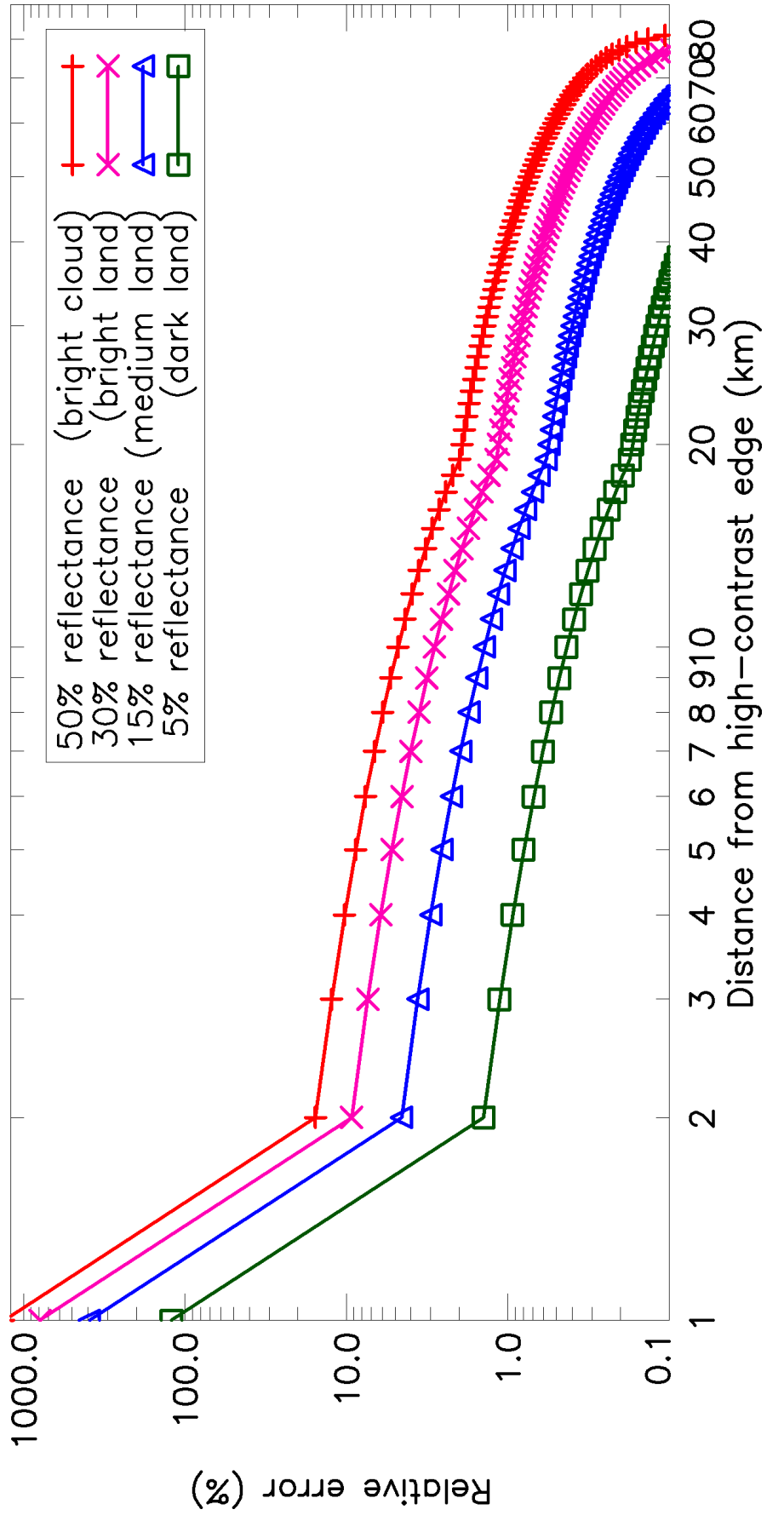

Figure 4.3: Relative contamination error caused by MODIS Aqua band 8 PSF on synthetic test scene (Figure 4.2(a)) with varying land/cloud reflectance levels.

distances from the high-contrast edge, especially with highly reflective features.

Satellite instruments measure top-of-atmosphere radiances convolved with the instrument PSF as part of the measurement process. Before the incoming light is detected by the sensors, instrumental distortion is the last effect that occurs in the light-path of the measured signal and should therefore be the first effect that is removed after calibration is performed. Removing instrumental effects at the beginning of the data processing chain, before standard MODIS processing occurs (Nishihama et al., 1997; Barbieri, 1997), results in these instrumental errors not being propagated through, or magnified by, subsequent processing stages such as atmospheric correction or chlorophyll estimation. This approach will produce optimal radiometrically corrected top-of-atmosphere images.

4.3 Multiscale Entropy Deconvolution

The Maximum Entropy Method (MEM) is a deconvolution technique that extracts the greatest amount of information from a measurement as justified by the signal-to-noise ratio of the data (Starck et al., 2002). The MEM determines the least biased image subject to applied constraints, and therefore retains all known information while unknown information is approximated in an unbiased manner. The concept of entropy originated from Shannon (1949) and is defined in Information Theory as a measure of the amount of information in a signal. This form of entropy was used to determine the minimum channel capacity required to reliably transmit encoded binary digits (Shannon, 1949). Jaynes (1957) proposed that entropy could be used for radio interferometric image deconvolution and showed that the only unbiased configuration is the solution that has maximum entropy. Furthermore, it has been shown that maximum entropy is the only consistent method of selecting a solution which does not introduce correlations into the image beyond those which are required by the original data (Johnson and Shore, 1980, 1983; Livesey and Skilling, 1985). The MEM compares favourably to other deconvolution techniques and consistently provides robust results (Madden et al., 1996).

Several major advances have been made in MEM deconvolution, from the

early operational algorithms (Skilling and Bryan, 1984) to the implementation of multiresolution image analysis (Bontekoe et al., 1994). Currently, the most advanced method is the Multiscale MEM (Pantin and Starck, 1996) which incorporates Wavelet transforms and Multiresolution Support images throughout the deconvolution process (Starck, 1995).

The Wavelet transform is similar to the Fourier transform, but rather than approximating a signal with a number of infinite sine waves, Wavelets are used to approximate the signal at several decreasing levels of resolution (Daubechies, 1992). This multiresolution paradigm makes Wavelets suitably compact and capable of effectively modelling discontinuities. The Wavelet transform procedure implemented for use in deconvolution is the discrete *à trous* [with holes] algorithm (Holschneider et al., 1989; Shensa, 1992; Starck and Bijaoui, 1994). This algorithm provides a simple method for calculating the Wavelet decomposition of an image. Using this technique, an image $O(x, y)$ can be decomposed into its Wavelet coefficients and losslessly represented by:

$$O(x, y) = c_{n_p}(x, y) + \sum_{j=1}^{n_p} w_j(x, y) \tag{4.2}$$

$$\begin{aligned} \text{where} \quad c_{n_p}(x, y) &= \text{smoothed image at the lowest scale} \\ n_p &= \text{total number of Wavelet scales (typically 4)} \\ w_j(x, y) &= \text{Wavelet coefficients at scale } j \end{aligned}$$

Each successive Wavelet scale is determined by calculating the difference between the current smoothed image and the next smoothed image. This process begins by convolving the original data with a low-pass filter, or Wavelet scaling function, ψ. For the application of image deconvolution, the B3 spline is often chosen due to its ability to represent a large range of spatial structures which is highly beneficial throughout the deconvolution process. In one dimension, the B3 scaling function is:

$$\psi = \begin{bmatrix} \frac{1}{16} & \frac{1}{4} & \frac{3}{8} & \frac{1}{4} & \frac{1}{16} \end{bmatrix} \tag{4.3}$$

This can be extended into two dimensions by convolving the B3 scaling function with the transpose of itself, producing the two-dimensional convolution mask:

$$\psi_1 = \begin{bmatrix} \frac{1}{256} & \frac{1}{64} & \frac{3}{128} & \frac{1}{64} & \frac{1}{256} \\ \frac{1}{64} & \frac{1}{16} & \frac{3}{32} & \frac{1}{16} & \frac{1}{64} \\ \frac{3}{128} & \frac{3}{32} & \frac{9}{64} & \frac{3}{32} & \frac{3}{128} \\ \frac{1}{64} & \frac{1}{16} & \frac{3}{32} & \frac{1}{16} & \frac{1}{64} \\ \frac{1}{256} & \frac{1}{64} & \frac{3}{128} & \frac{1}{64} & \frac{1}{256} \end{bmatrix} \tag{4.4}$$

The smoothed images at each resolution scale can now be iteratively calculated by convolving the original image with the first-level convolution function:

$$c_j(x,y) = \sum_{v=0} \sum_{u=0} \psi_1(u,v) c_{j-1}(x - 2^{j-1}u, y - 2^{j-1}v) \tag{4.5}$$

This is similar to a formal convolution but also includes a spacing factor of 2^{j-1} that handles the reduction in resolution at different resolution levels. The Wavelet scales, w_j, can be extracted from the smoothed images by calculating the difference between two consecutive resolution levels:

$$w_j(x,y) = c_{j-1}(x,y) - c_j(x,y) \tag{4.6}$$

Each Wavelet scale now contains structural information about the original image O at different spatial frequencies and this allows reconstruction techniques to be matched to different resolution levels. A practical implementation of Equations 4.5 and 4.6 is to perform standard convolution of the smoothed image with a Wavelet function that disperses at each subsequent resolution scale. This results in the B3 Wavelet scaling function at resolution level 2 becoming:

$$\psi_2 = \begin{bmatrix} \frac{1}{256} & 0 & \frac{1}{64} & 0 & \frac{3}{128} & 0 & \frac{1}{64} & 0 & \frac{1}{256} \\ 0 & 0 & 0 & 0 & 0 & 0 & 0 & 0 & 0 \\ \frac{1}{64} & 0 & \frac{1}{16} & 0 & \frac{3}{32} & 0 & \frac{1}{16} & 0 & \frac{1}{64} \\ 0 & 0 & 0 & 0 & 0 & 0 & 0 & 0 & 0 \\ \frac{3}{128} & 0 & \frac{3}{32} & 0 & \frac{9}{64} & 0 & \frac{3}{32} & 0 & \frac{3}{128} \\ 0 & 0 & 0 & 0 & 0 & 0 & 0 & 0 & 0 \\ \frac{1}{64} & 0 & \frac{1}{16} & 0 & \frac{3}{32} & 0 & \frac{1}{16} & 0 & \frac{1}{64} \\ 0 & 0 & 0 & 0 & 0 & 0 & 0 & 0 & 0 \\ \frac{1}{256} & 0 & \frac{1}{64} & 0 & \frac{3}{128} & 0 & \frac{1}{64} & 0 & \frac{1}{256} \end{bmatrix} \tag{4.7}$$

Further resolution levels are additionally interspersed with zero-padded rows and columns, highlighting why this method is called the *à trous* [with holes] algorithm. This implementation has the added advantage of maintaining constant image sizes throughout all resolution scales. It is more manageable to vary the size of the relatively small Wavelet function and keep the larger imagery at the same size. As the resolution levels are calculated, $c_j(x, y)$ becomes progressively smoother which results in $w_j(x, y)$ containing lower spatial frequencies while maintaining constant size. Figure 4.4 depicts the full Wavelet decomposition of a standard image processing test image (Figure 4.4(a)) through four levels of Wavelet decomposition (Figure 4.4(b), 4.4(c), 4.4(d) and 4.4(e)) and the lowest scale smoothed image (Figure 4.4(f)). Equation 4.2 details how the summation of Figures 4.4(b), 4.4(c), 4.4(d), 4.4(e) and 4.4(f) produces the original image (Figure 4.4(a)) with no loss of information. This example clearly shows how Wavelet decomposition can separate an image into a range of different spatial frequencies to be used in subsequent processing.

If the scaling function chosen for Wavelet decomposition can be broken into two one-dimensional signals, such as a vertical and a horizontal projection, then the function is said to be separable. This is certainly the case for the two-dimensional B3 spline, as it was originally created from a one-dimensional array. In this case, there is an opportunity to accelerate the convolution process by convolving the two-

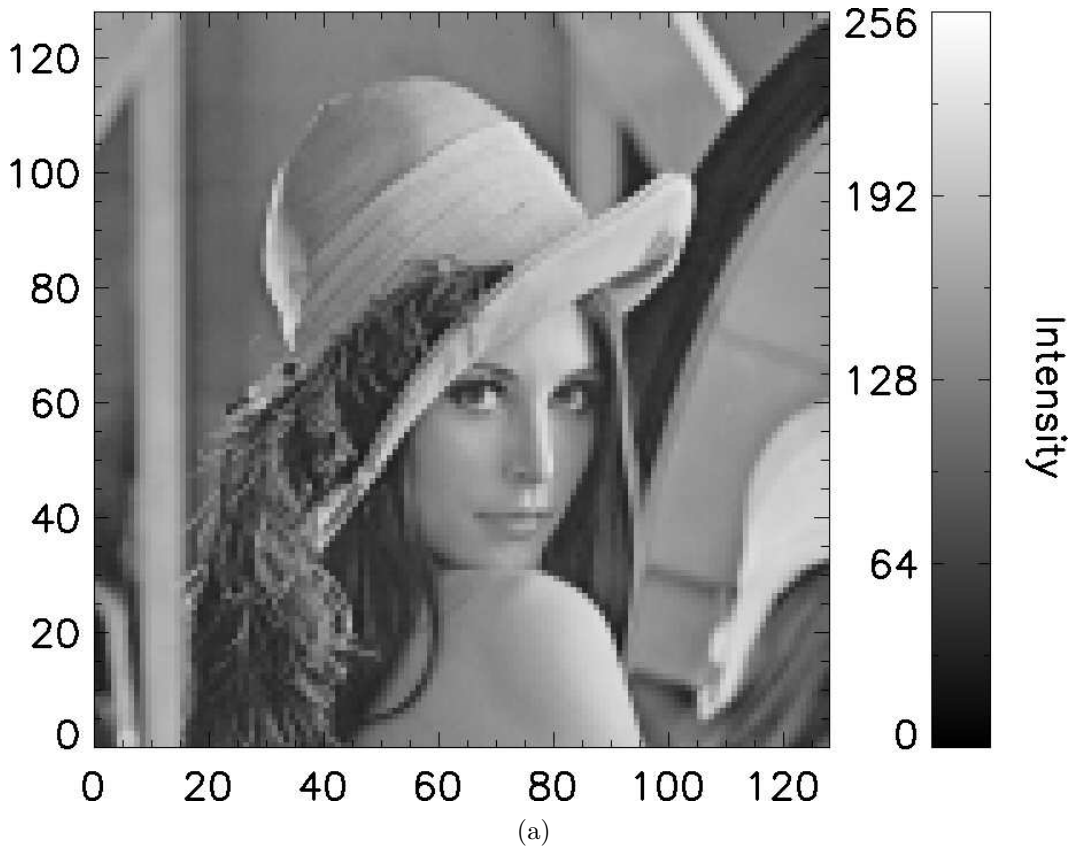

(a)

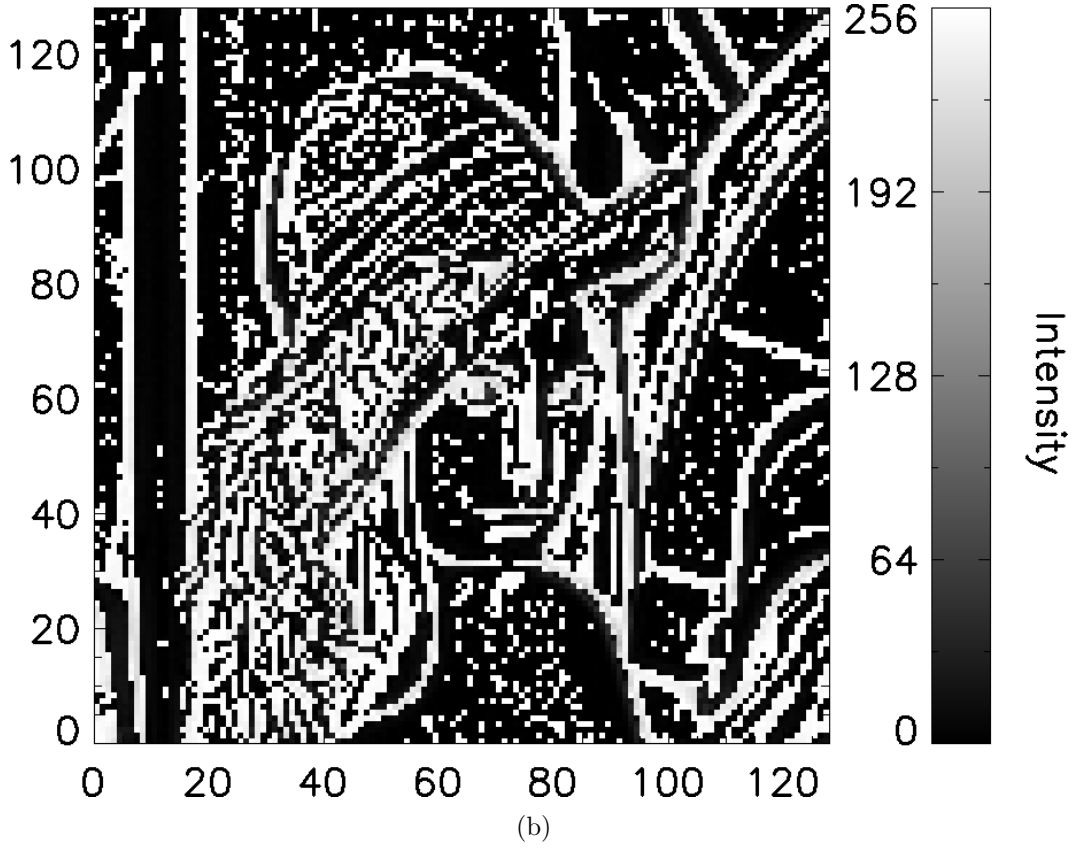

(b)

Figure 4.4: Multiresolution Wavelet decomposition depicting (a) the original test image 'Lena' and (b) the first Wavelet scale containing high-frequency content.

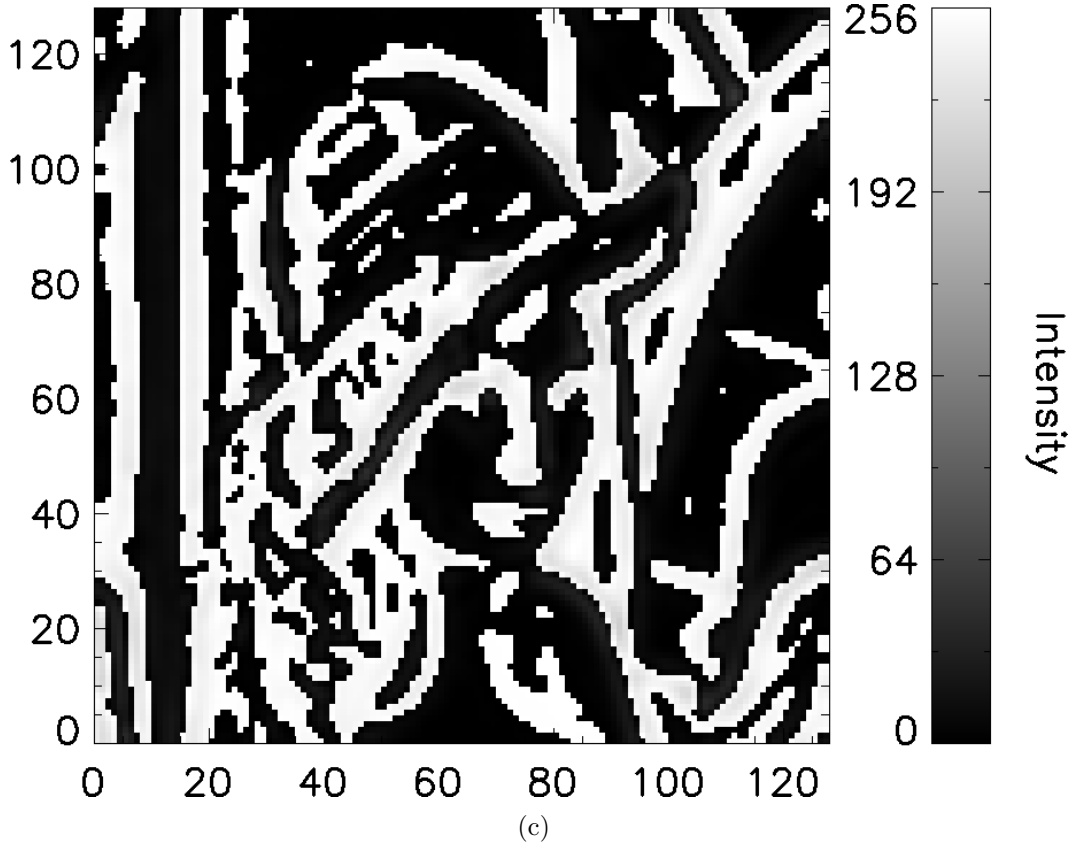

(c)

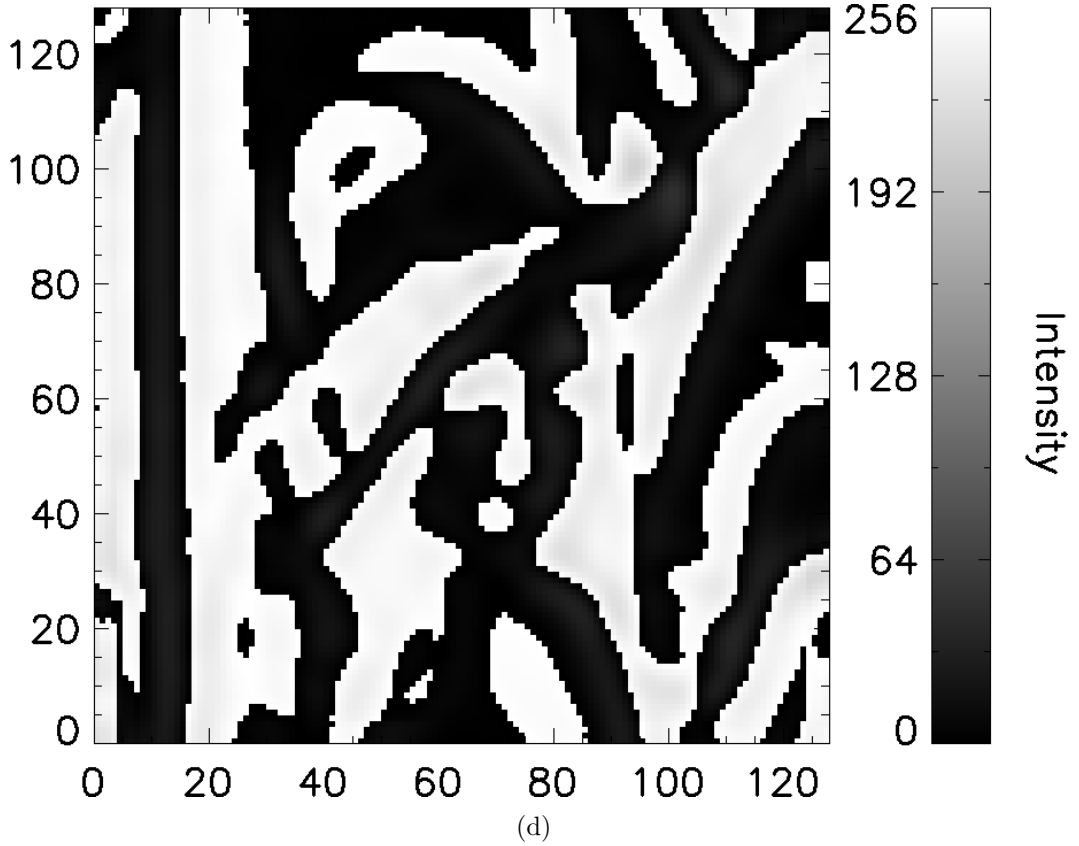

(d)

Figure 4.4 continued: Multiresolution Wavelet decomposition depicting (c) the second Wavelet scale containing moderately high-frequency content and (d) the third Wavelet scale containing moderately low-frequency content.

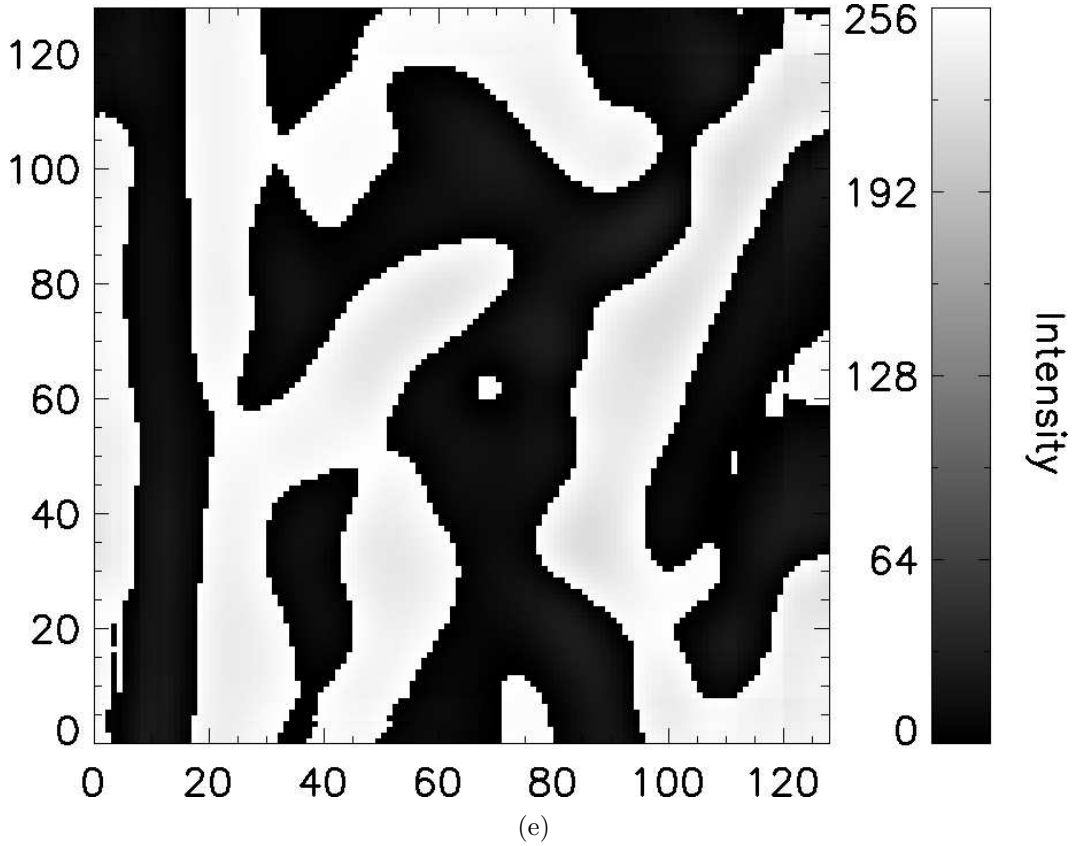

(e)

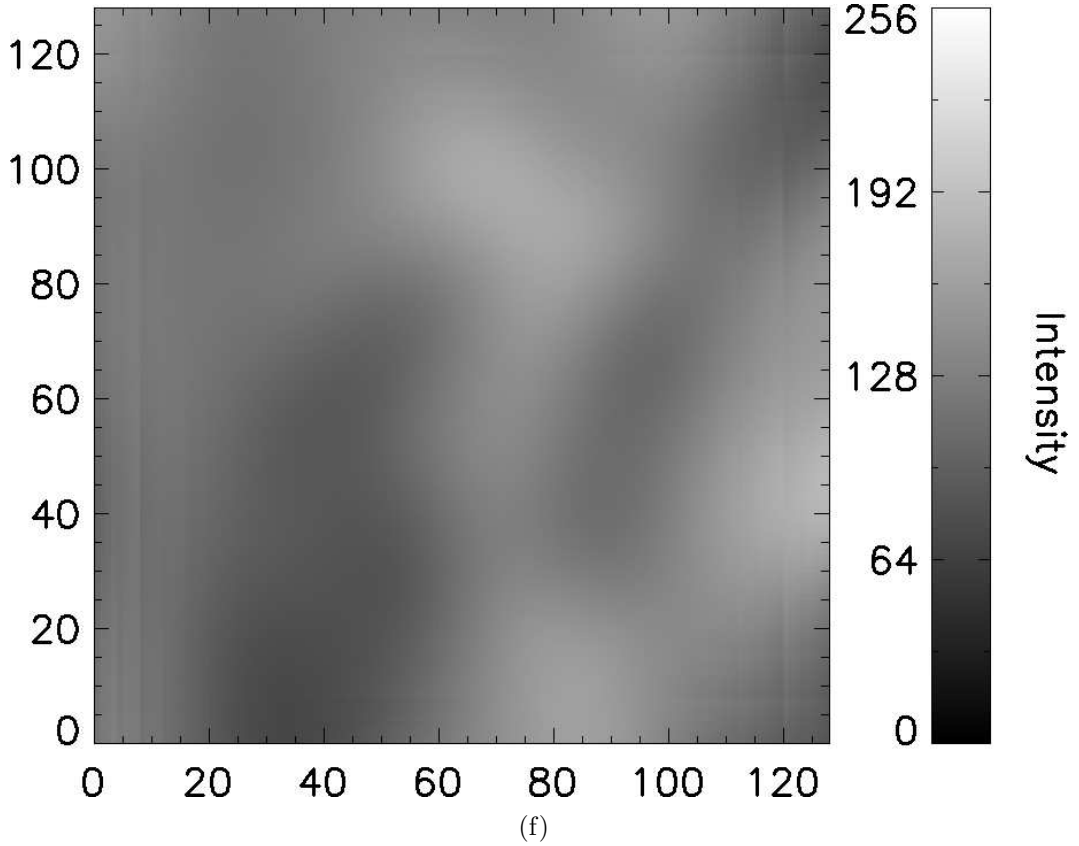

(f)

Figure 4.4 continued: Multiresolution Wavelet decomposition depicting (e) the fourth Wavelet scale containing low-frequency content and (f) the smoothed image at the lowest scale $c_{n_p}(x, y)$.

dimensional image with the one-dimensional scaling function twice. This is carried out by a row-by-row convolution with the horizontal scaling function projection, and then a column-by-column convolution with the vertical scaling function projection. This produces an identical convolution to the two-dimensional convolution case, which has previously been reported to operate with a computational complexity of N^2M^2 (Chapter 3), but can now be reduced to a computational complexity of N^2M (Smith, 2003). This technique can dramatically reduce the convolution execution time, depending on the size of the convolution function, and has been implemented for the deconvolution algorithm.

Multiresolution Support is a set of boolean images that represent significant structures at each Wavelet scale of resolution. Multiresolution Support images are calculated according to:

$$M(j,x,y) = \begin{cases} 1 \text{ if } w_j(x,y) & \geq & k\sigma_j \\ 0 \text{ if } w_j(x,y) & < & k\sigma_j \end{cases} \tag{4.8}$$

$$\begin{aligned} \text{where} \quad M(j,x,y) &= \text{Multiresolution Support images} \\ k &= \text{threshold} \\ \sigma_j &= \text{standard deviation of noise at scale } j \end{aligned}$$

The threshold k is used to distinguish between the real signal and the noise in the signal. A value of $k = 3$ is generally used to define noise with a probability of 99.7%, assuming a Gaussian distribution. The standard deviation of the noise at the various wavelet scales can be calculated by simulating a reasonably sized test image that contains only noise, applying the wavelet decomposition and calculating the resultant noise level at each wavelet scale. Figure 4.5 displays the four levels of Multiresolution Support derived from the Wavelet decomposition of Figure 4.4(a). These Multiresolution Support images separate the areas in the original image that are solely attributed to noise and allows these areas to be regularised, leaving all significant features at varying Wavelet resolutions intact.

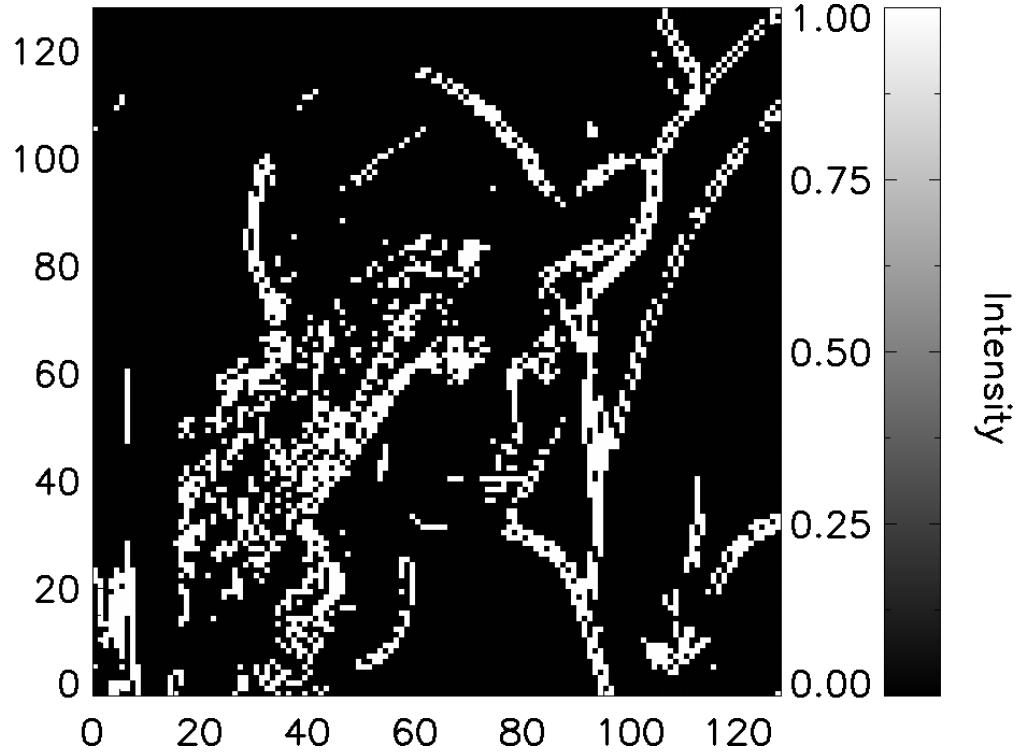

(a)

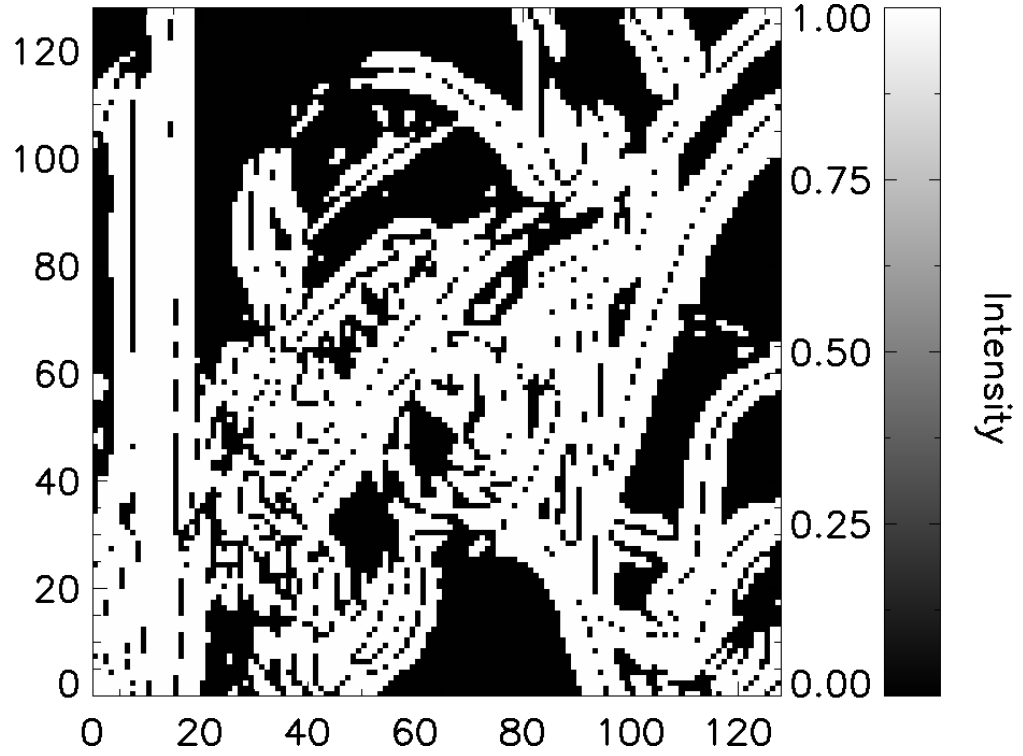

(b)

Figure 4.5: Multiresolution Support images calculated from the Wavelet decomposition of Figure 4.4(a) showing (a) level 1 support containing high-frequency content and (b) level 2 support containing moderately high-frequency content. Multiscale Entropy is calculated using the complement of these support images and this results in only the dark regions contributing to the entropy calculation.

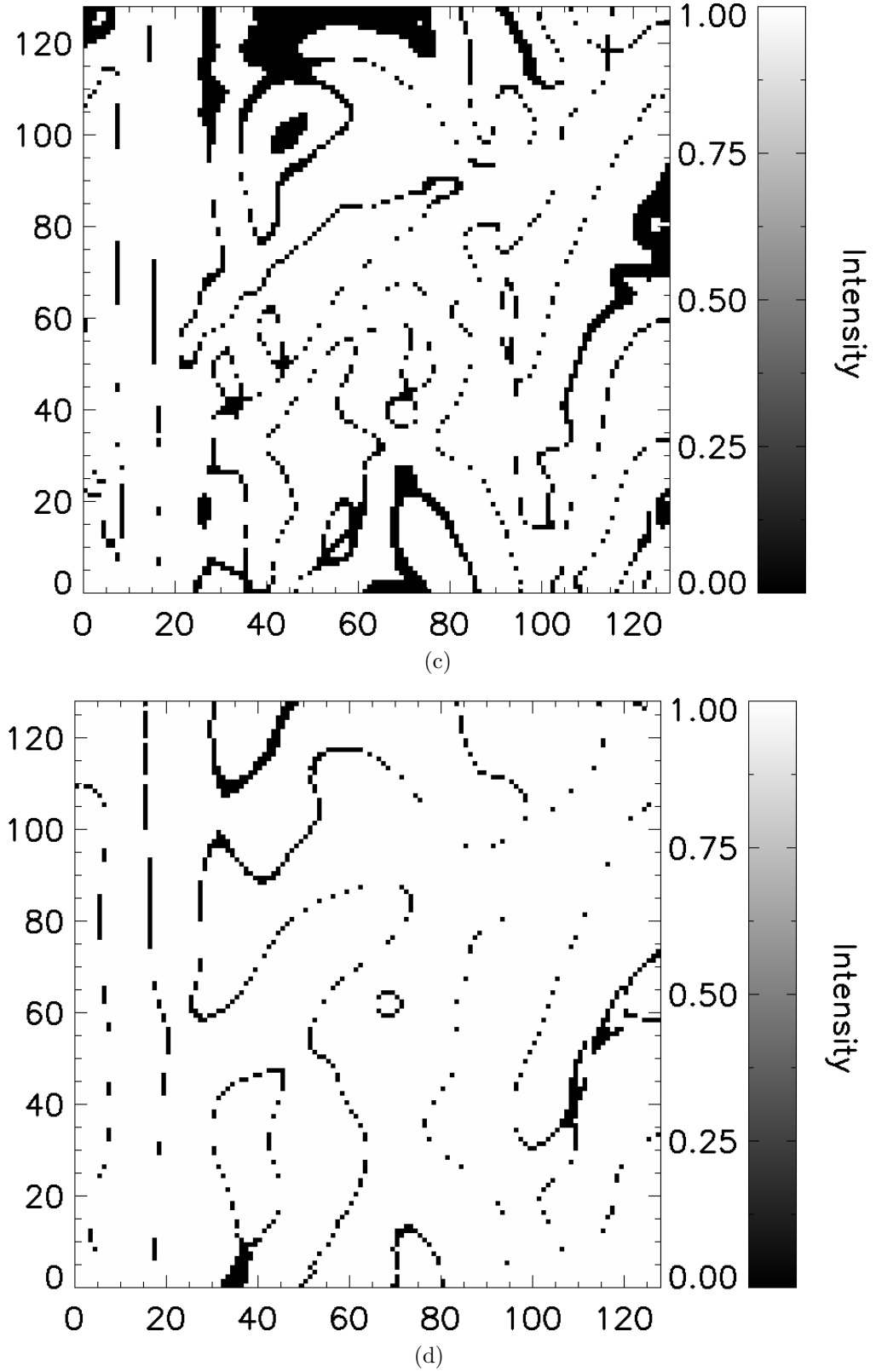

Figure 4.5 continued: Multiresolution Support images calculated from the Wavelet decomposition of Figure 4.4(a) showing (c) level 3 support containing moderately low-frequency content and (d) level 4 support containing low-frequency content. Multiscale Entropy is calculated using the complement of these support images and this results in only the dark regions contributing to the entropy calculation.

Using these new ideas, Starck (1996) developed a new definition of entropy, based on Gull and Skilling entropy (1991), that encompassed Wavelet image decomposition and Multiresolution Support:

$$S_{\mathrm{ms}}(O) = \frac{1}{\sigma_I} \sum_{j=0}^{n} \sum_{\text{pixels}} (1 - M(j,x,y)) \sigma_j (w_j(x,y) - m_j - |w_j(x,y)| \ln \frac{|w_j(x,y)|}{m_j}) \tag{4.9}$$

where

$$\begin{aligned} S_{\mathrm{ms}}(O) &= \text{Multiscale Entropy on image } O \\ \sigma_I &= \text{standard deviation of noise in image } I \\ 1 - M(j,x,y) &= \text{complement of Multiresolution Support} \\ m_j &= \text{background model at scale } j \\ &= \tfrac{\sigma_j}{100} \end{aligned}$$

By incorporating the Wavelet transform into Multiscale Entropy, the spatial structure of an image is implicitly included in the entropy calculation. In this way, the algorithm makes use of contextual information in the image throughout the deconvolution process and is able to deconvolve images based on their unique structural attributes. While Equation 4.9 collapses the entropy on image O to a single number that is used to guide the deconvolution process, Multiscale Entropy can be visualised by ignoring the second summation and inspecting the intermediate result (Figure 4.6). This shows how Multiscale Entropy responds to the information content in two-dimensional imagery. Areas in the image that were originally smooth and homogeneous result in large values of Multiscale Entropy, and areas that were originally discontinuous and turbulent result in small values of Multiscale Entropy (Figure 4.6). This example also illustrates how Multiscale Entropy preserves the two-dimensional structure of imagery at a range of resolution levels.

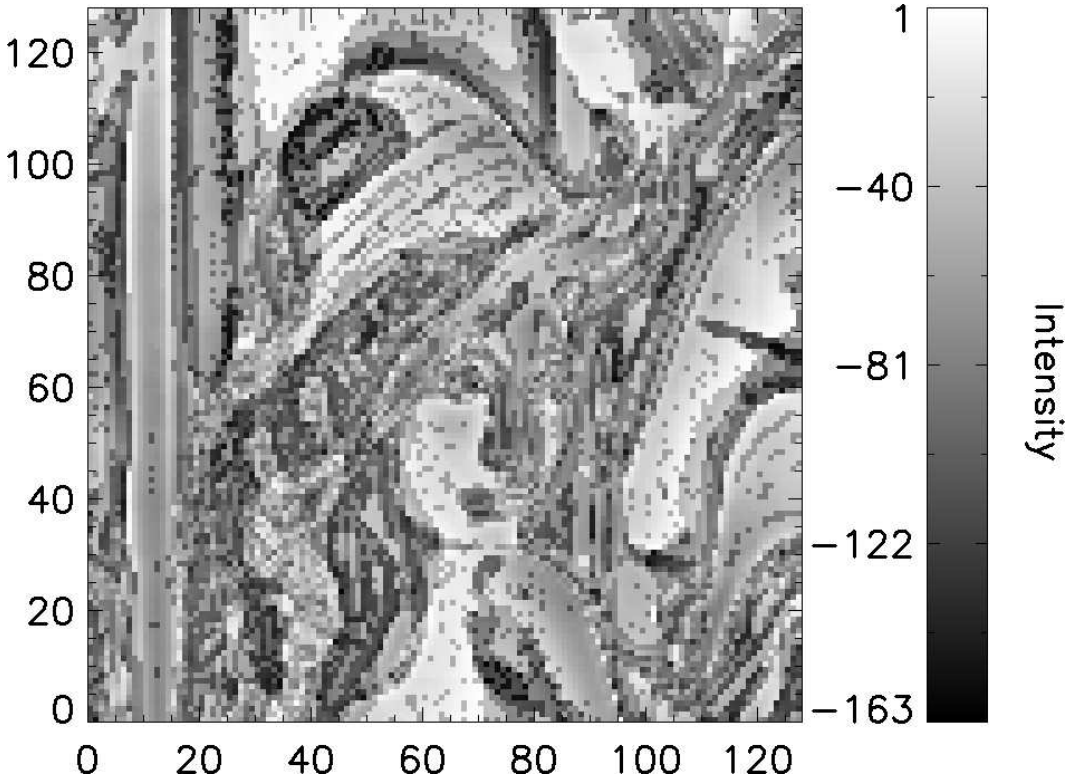

Figure 4.6: Visualisation of the Multiscale Entropy on Figure 4.4(a). The complete Multiscale Entropy response for this image is -1066222 as calculated by Equation 4.9.

Multiscale Entropy is defined on image O. The algorithm initially assumes that O is equal to the recorded image I, and proceeds to iteratively modify O until the deconvolution is successful. Starck (1996) developed the function $J(O)$ that must be minimised to retrieve the deconvolved image O:

$$J(O) = \sum_{\text{pixels}} \frac{(I - P * O)^2}{2\sigma_I^2} - \alpha S_{\text{ms}}(O) \tag{4.10}$$

where α = balance between data fit and solution smoothness

Only areas containing noise as defined by Multiresolution Support undergo regularisation and this allows the parameter α to be calculated as $\alpha = \frac{\max(\text{PSF})}{2\sigma_I}$ for all image types (Pantin and Starck, 1996). This independence significantly increases the ability of the algorithm to operate autonomously which has previously been one of the major challenges for MEM deconvolution.

Equation 4.10 can be minimised using a one-step gradient method:

$$O^{n+1} = O^n - \gamma \nabla(J(O^n)) \tag{4.11}$$

$$\begin{aligned} \text{where} \qquad O^{n+1} &= \text{next image} \\ O^n &= \text{current image} \\ \gamma &= \text{step size} \\ \nabla(J(O^n)) &= \text{search direction} \end{aligned}$$

This requires calculation of the search direction, which is the derivative of Equation 4.10:

$$\nabla(J(O)) = -P^T * \frac{(I - P * O)}{\sigma_I^2} + \alpha \frac{1}{\sigma_I} \sum_{scales j} [(1 - M(j))\sigma_j sgn(w_j^{(O)}) \ln(\frac{|w_j^{(O)}|}{m_j})] * \psi_j^T \tag{4.12}$$

$$\begin{aligned} \text{where} \qquad P^T &= \text{transpose of the PSF} \\ sgn() &= \text{signum function} \\ \psi_j^T &= \text{transpose of the Wavelet function at scale } j \\ &= \tfrac{1}{2^j}\psi(\tfrac{x}{2^j}, \tfrac{y}{2^j}) \end{aligned}$$

The Wavelet function, ψ, corresponds to the discrete *à trous* algorithm where the magnitude of the function gets smaller as its spatial coverage gets larger with each subsequent resolution level. This aids in limiting how much low-frequency content is included in the gradient calculation, otherwise the lower spatial frequencies tend to dominate the search direction.

The result of Equation 4.12 is a new image that describes the quantity in which each pixel in the deconvolving image should change in order to successfully converge. Figure 4.7 depicts the first deconvolution search direction and contains balanced edges that are the result of a convolution process. As the algorithm proceeds iteratively, the quantity and amplitude of these edges diminishes until deconvolution is achieved.

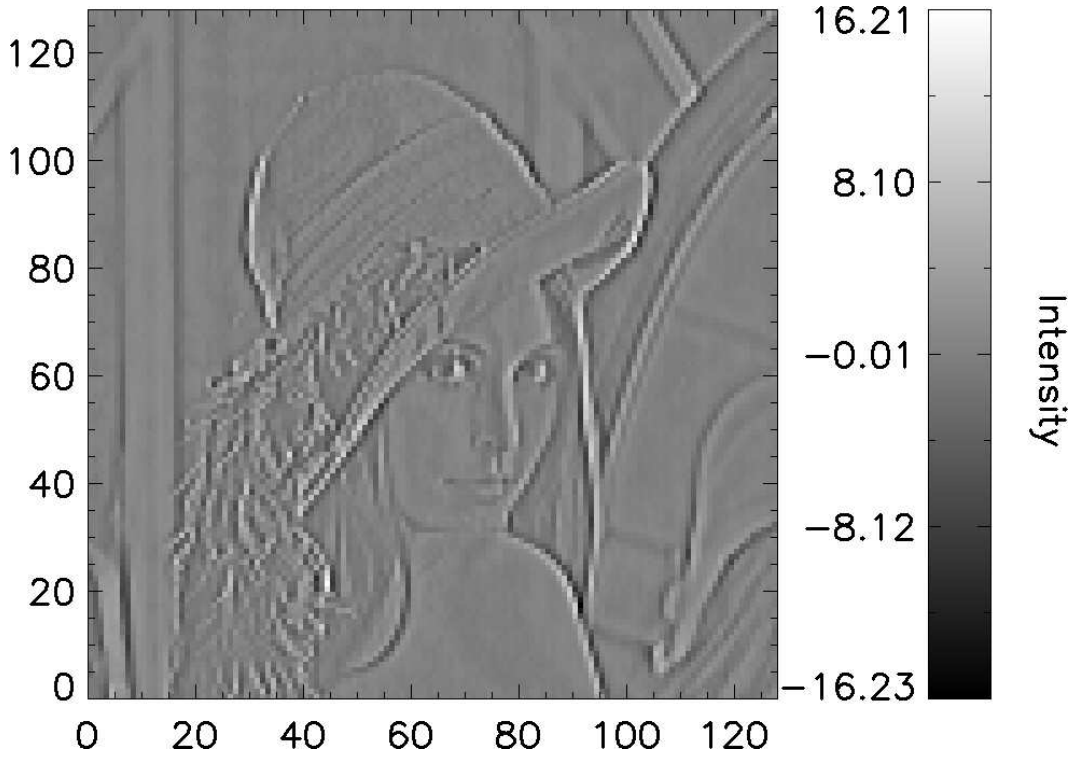

Figure 4.7: First iteration search direction for the Multiscale Entropy deconvolution of Figure 4.4(a).

Many convolution operations are required to calculate the gradient $\nabla(J(O))$ (Equation 4.12) within every iteration. The implementation developed here uses Fast Fourier Transforms (FFTs) to perform all convolutions due to the efficiency advantages of convolving two signals in the frequency domain over the spatial domain (Chapter 3). Furthermore, any convolution that involves the MODIS instrument PSF requires a composite of 10 individual convolutions, one for each of the 10 detectors in the MODIS 1km resolution ocean colour bands. MODIS builds imagery by horizontally scanning the surface of the Earth, resulting in each detector recording the information for every 10th row. The first detector in MODIS band 8 is responsible for image row numbers 1, 11, 21 and so on, the second detector is responsible for image row numbers 2, 12, 22 and so forth. It has been previously identified that each detector has a unique PSF (Figure 4.1). Therefore, accurate deconvolution requires convolutions to be individually performed with the PSF of each detector, and every 10th convolved row for each corresponding detector to be extracted to construct the final convolved response. This process adds a factor of 10 to the computation time

for each MODIS PSF convolution, but is necessary to ensure accurate deconvolution results are achieved.

A significant amount of research has been performed on step size estimation techniques for gradient methods (Shi, 2005), with a stand-out algorithm known as the BB method, which was published by Barzilai and Borwein (1988). This method has been shown to achieve super-linear convergence in finding solutions to convex quadratic problems. A dramatic reduction in processing time can be achieved using the BB method due to its optimal step size selection. This effectively reduces the algorithm compute time as the total number of iterations required to achieve successful deconvolution is substantially reduced. There are several more complicated methods that could be used for the step size estimation including the Levenberg-Marquardt method (Moré, 1978) and even an appropriately modified version of the adaptive backpropagation Rprop learning algorithm (Riedmiller and Braun, 1993). As these techniques are significantly more demanding, the BB method has been implemented for its computational efficiency and simplicity of use. The BB method calculates the ideal step size for the convergence of the one-step gradient method according to:

$$\gamma = \frac{\sum[(O^n - O^{n-1}) \times (\nabla(J(O))^n - \nabla(J(O))^{n-1})]}{\sum[\nabla(J(O))^n - \nabla(J(O))^{n-1}]^2} \tag{4.13}$$

$$\begin{aligned} \text{where} \qquad O^{n-1} &= \text{previous image} \\ \nabla(J(O))^{n-1} &= \text{previous search direction} \end{aligned}$$

This requires that the image and search direction from the previous iteration be temporarily stored to calculate the stepping distance in the search direction of Equation 4.12.

The MODIS Aqua ocean colour bands were designed to record water-based measurements and have a dynamic range specifically calibrated to target these regions. As such, land and water measurements often fall within the dynamic range of the sensors and are well rendered by MODIS. However, when MODIS measures extremely bright targets such as ice or clouds using the ocean colour bands, the real signal is often many times brighter than the maximum sensitivity of the instrument.

In this case, the recorded signal is truncated to the maximum recordable MODIS value of 4095, which is a result of 12bit quantisation of all MODIS bands. Figure 4.8 displays a scatter plot of the 500m resolution MODIS Aqua band 3 (469nm) with the 1km resolution MODIS Aqua band 8 (412nm) for a typical scene containing a range of water, land and cloud measurements. MODIS band 3 contains a wider dynamic range than the ocean colour bands and bright cloud measurements do not saturate the band 3 detectors. MODIS Aqua band 8, however, has a clear upper limit which prevents high-radiance measurements from being radiometrically accurate.

A problem arises for the deconvolution of imagery containing saturated measurements. The correct quantity of instrumental distortion is not accounted for during deconvolution due to the forced truncation of the true radiometric brightness of ice and clouds. This results in severe underestimation of instrumental effects up

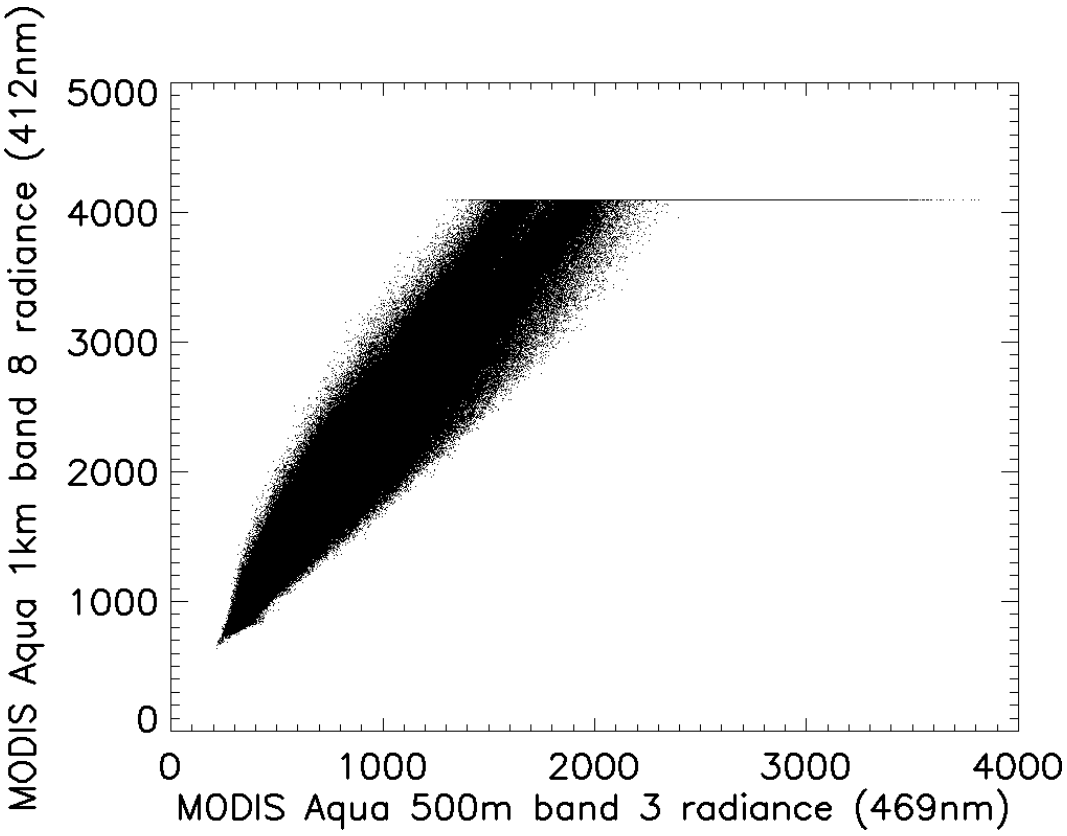

Figure 4.8: Scatter plot of 500m resolution MODIS Aqua band 3 (469nm) with 1km resolution MODIS Aqua band 8 (412nm) for a typical MODIS Aqua scene containing a range of water, land and cloud measurements. The upper limit of MODIS Aqua band 8 measurements at the value 4095 is caused by the limited dynamic range of the ocean colour detectors.

to a factor of approximately 25 for some ocean colour bands. Therefore, accurate deconvolution is unattainable in regions containing saturated measurements without applying some form of pre-deconvolution correction.

A cross-band correction method was developed to estimate the brightness of saturated ocean colour band measurements that have undergone truncation. This is achievable because other high-resolution MODIS bands contain significantly larger dynamic ranges and do not experience detector saturation. Each MODIS Aqua ocean colour band was spectrally matched to the closest 250m or 500m MODIS land/cloud band (Table 4.1). For each combination of bands, the saturated ocean colour measurements were discarded, the high-resolution matched MODIS band was appropriately downscaled, and a linear relationship was calculated (Figure 4.9). Before deconvolution was applied, all saturated ocean colour measurements were replaced with radiometric estimates using these linear relationships (Figure 4.10). While the estimated measurements appear rather unnatural, this approach provides a significantly more accurate radiometric response for bright features and reduces deconvolution inaccuracies introduced with truncated measurements. This saturated measurement correction method is crucial for removing the correct quantities of instrumental distortion from MODIS data.

Table 4.1: Spectrally matched band combinations of the MODIS ocean colour and high-resolution land/cloud bands.

MODIS ocean colour band	Matched high-resolution MODIS band
Band 8 (412nm) Band 9 (443nm) Band 10 (488nm)	Band 3 (469nm)
Band 11 (531nm) Band 12 (547nm)	Band 4 (555nm)
Band 13 (667nm) Band 14 (678nm)	Band 1 (645nm)
Band 15 (748nm) Band 16 (869nm)	Band 2 (859nm)

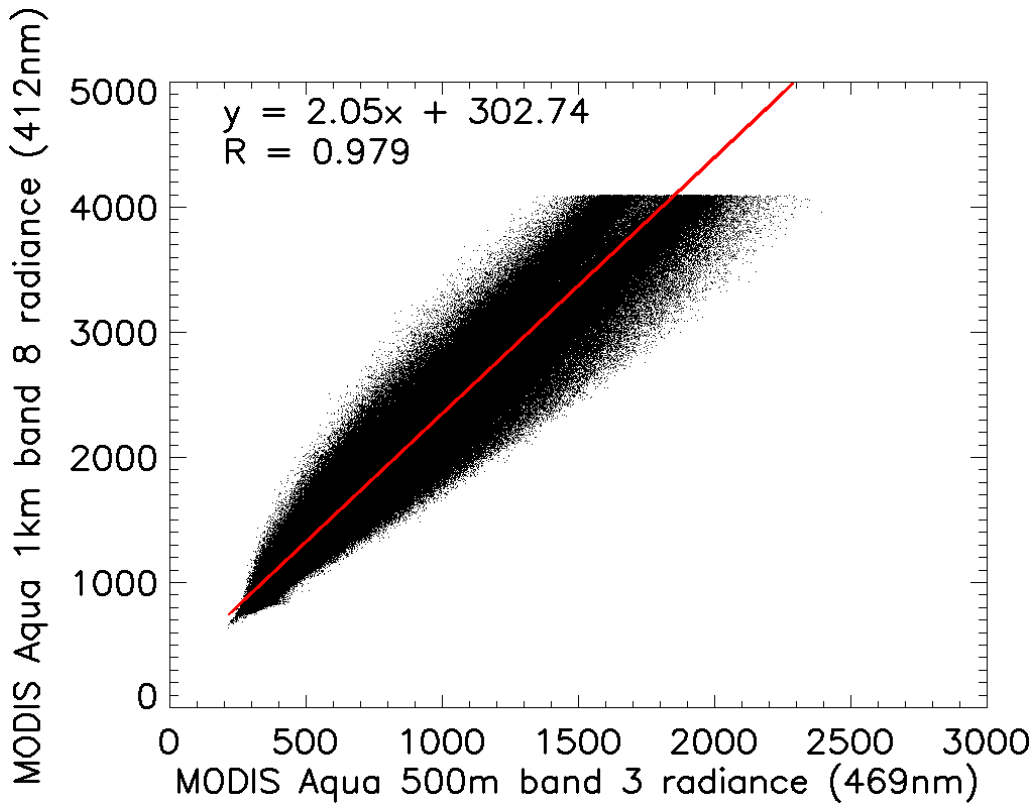

Figure 4.9: Scatter plot of 500m resolution MODIS Aqua band 3 (469nm) with 1km resolution MODIS Aqua band 8 (412nm) for a typical MODIS Aqua scene with filtered saturated measurements.

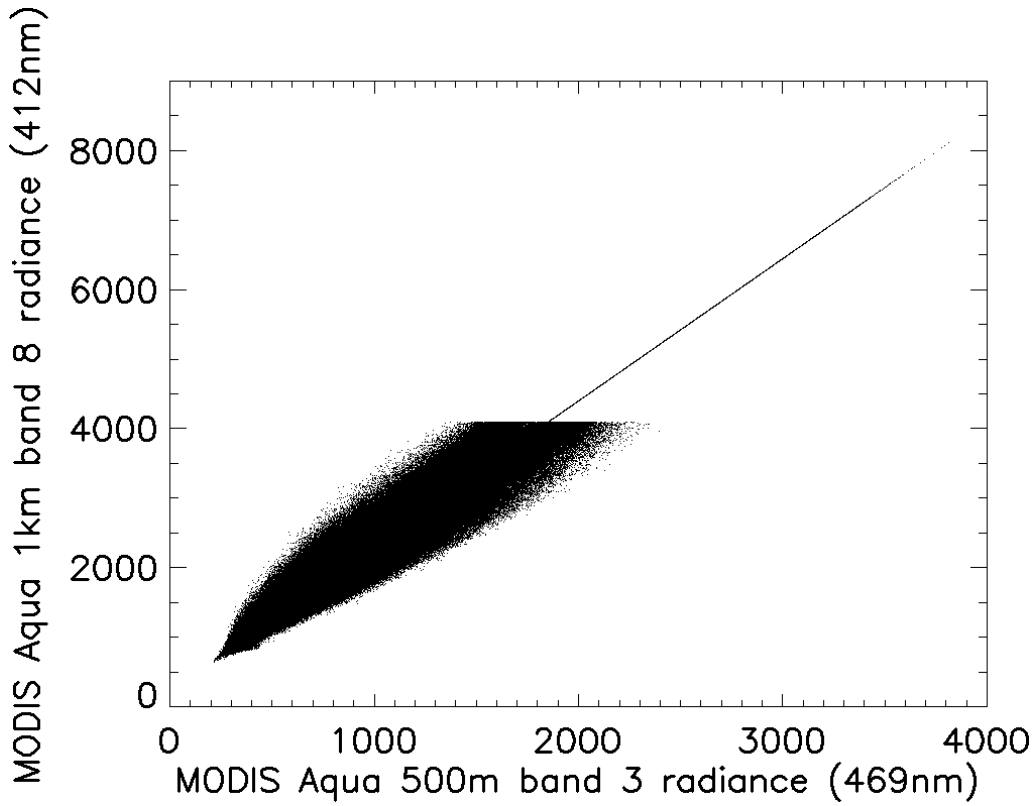

Figure 4.10: Scatter plot of 500m resolution MODIS Aqua band 3 (469nm) with 1km resolution MODIS Aqua band 8 (412nm) for a typical MODIS Aqua scene with estimated saturated measurements.

Deconvolution generally increases the brightness of bright features and decreases the brightness of dark features in regions of contrast. After deconvolution is applied, it is common for many data values to be less than 0, and there will certainly be many data values greater than 4095 after saturation correction is applied. All of these data values must be reassigned to 0 and 4095 respectively as a requirement of standard MODIS processing. The value of -1 is reserved for absent MODIS measurements which occur in 9 out of 10 MODIS granules. These values must also be replaced to allow subsequent processing stages to be successful.

4.4 Results

The accuracy of the deconvolution algorithm is evaluated by convolving a synthetic test scene, adding noise, then deconvolving the scene and analysing the differences. Initially, a standard image processing test scene (Figure 4.11(a)) is convolved with the MODIS Aqua band 8 PSF and average band 8 noise (Xiong et al., 2009) is added (Figure 4.11(b)). The difference between the original and the convolved image is displayed in Figure 4.11(c) and indicates the effect the instrument would have if the original image was rendered by MODIS Aqua band 8. This particular image contains a maximum individual pixel error of 90.01%. Figure 4.11(d) displays a frequency histogram of the pixel differences in Figure 4.11(c). The convolved image is then deconvolved using the implemented Multiscale Entropy deconvolution algorithm and the result is displayed in Figure 4.11(e). The difference between the original and the deconvolved image is displayed in Figure 4.11(f) and a frequency histogram of this difference is shown in Figure 4.11(g).

The Multiscale Entropy deconvolution algorithm removes instrument effects down to a level where no visible structures remain (Figure 4.11(f)) and the maximum individual pixel error has been reduced from 90.01% to 0.34%. The frequency histogram in Figure 4.11(g) indicates that the final pixel differences are normally distributed with a maximum magnitude of 0.18, whereas the Gaussian noise added to the original image had a maximum magnitude of 0.11. Therefore, it is clear that Multiscale Entropy deconvolution has successfully removed the instrument effects

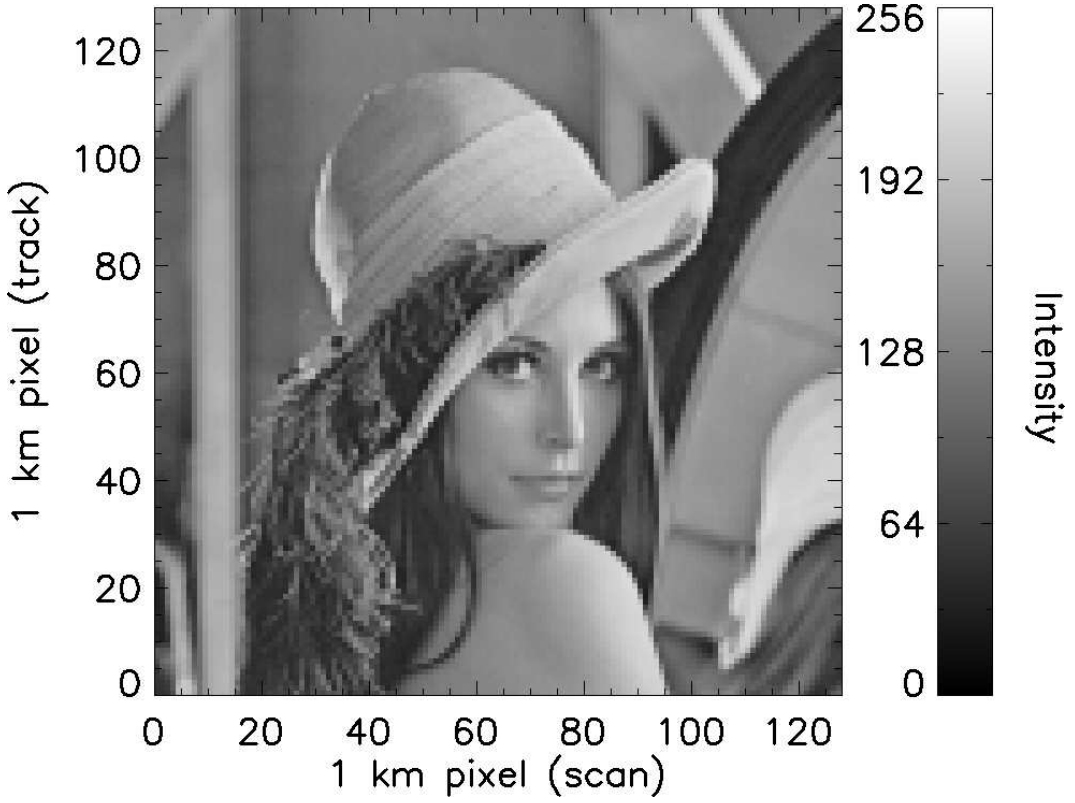

(a)

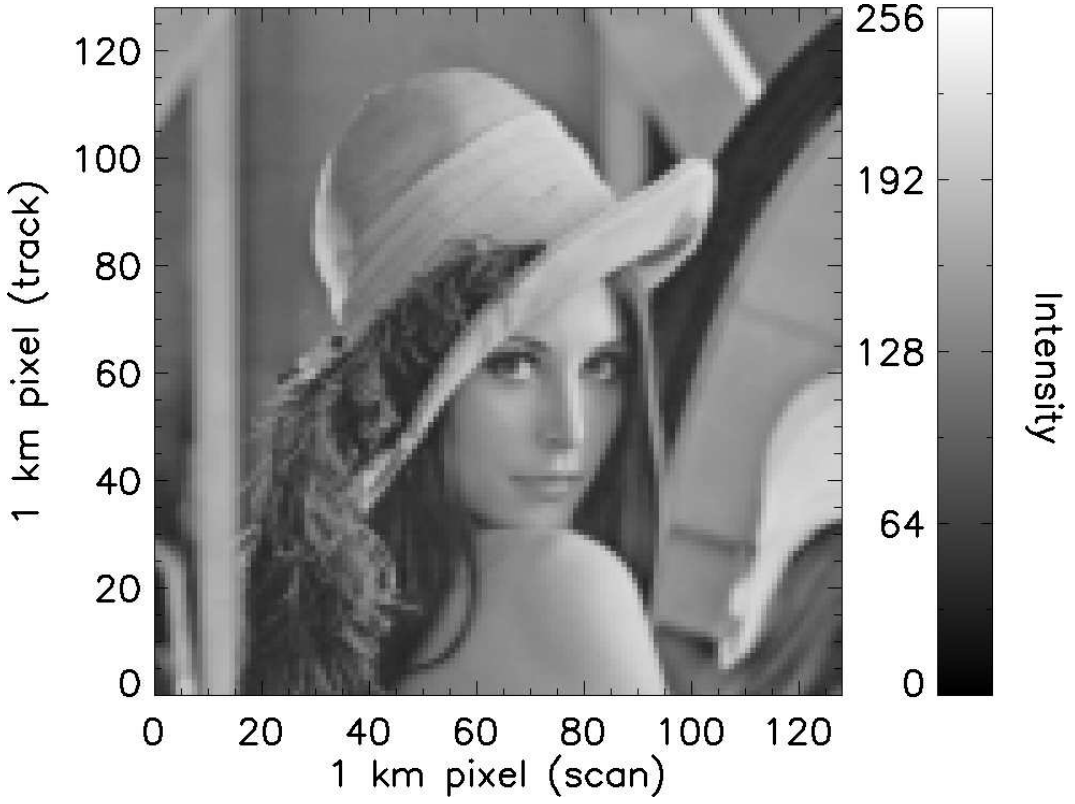

(b)

Figure 4.11: Synthetic data deconvolution accuracy test showing (a) the original image and (b) the original image convolved with MODIS Aqua band 8 PSF and average band 8 noise added.

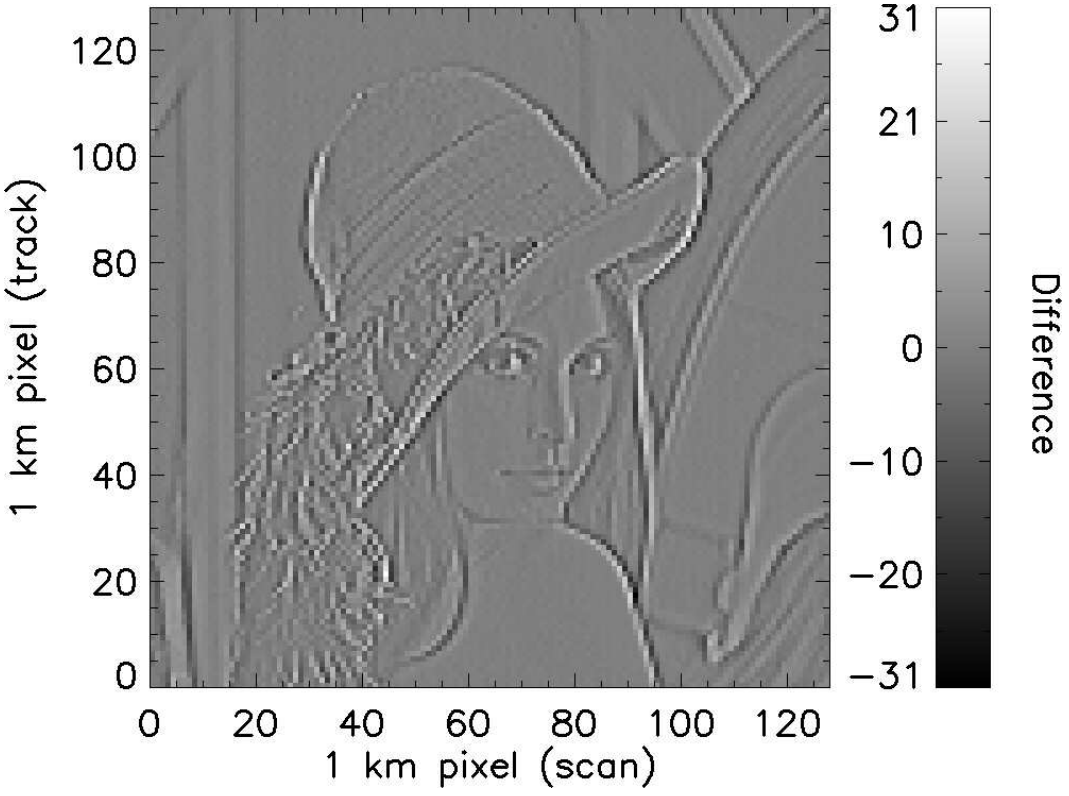

(c)

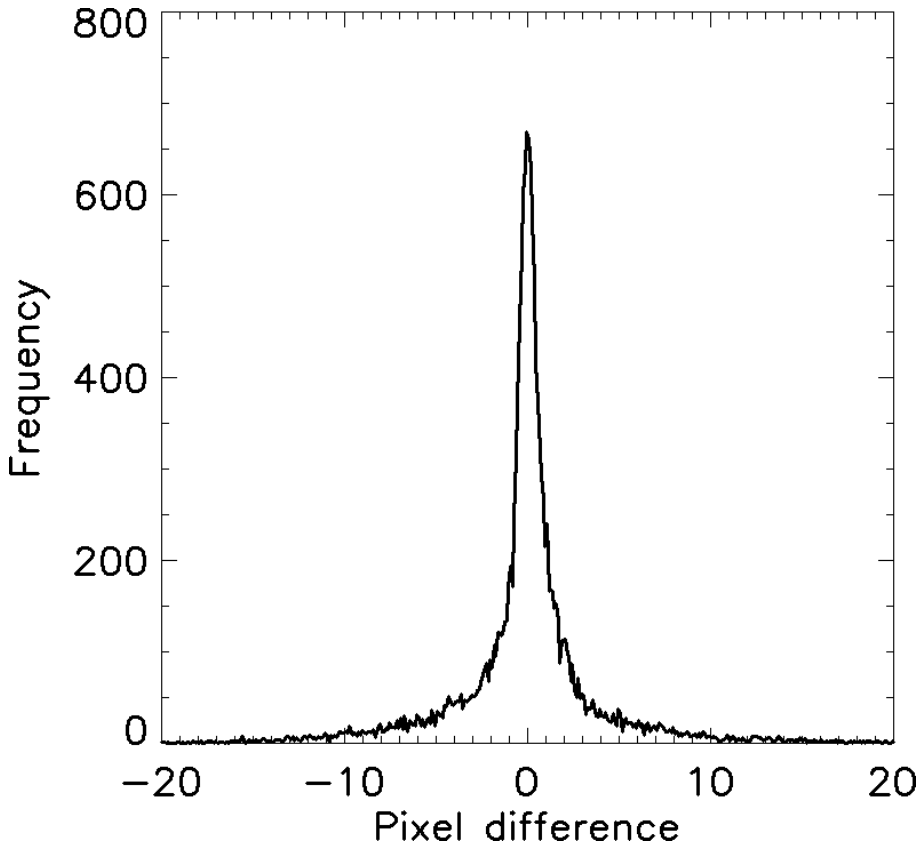

(d)

Figure 4.11 continued: Synthetic data deconvolution accuracy test showing (c) the difference between the original and convolved image and (d) a frequency histogram of (c).

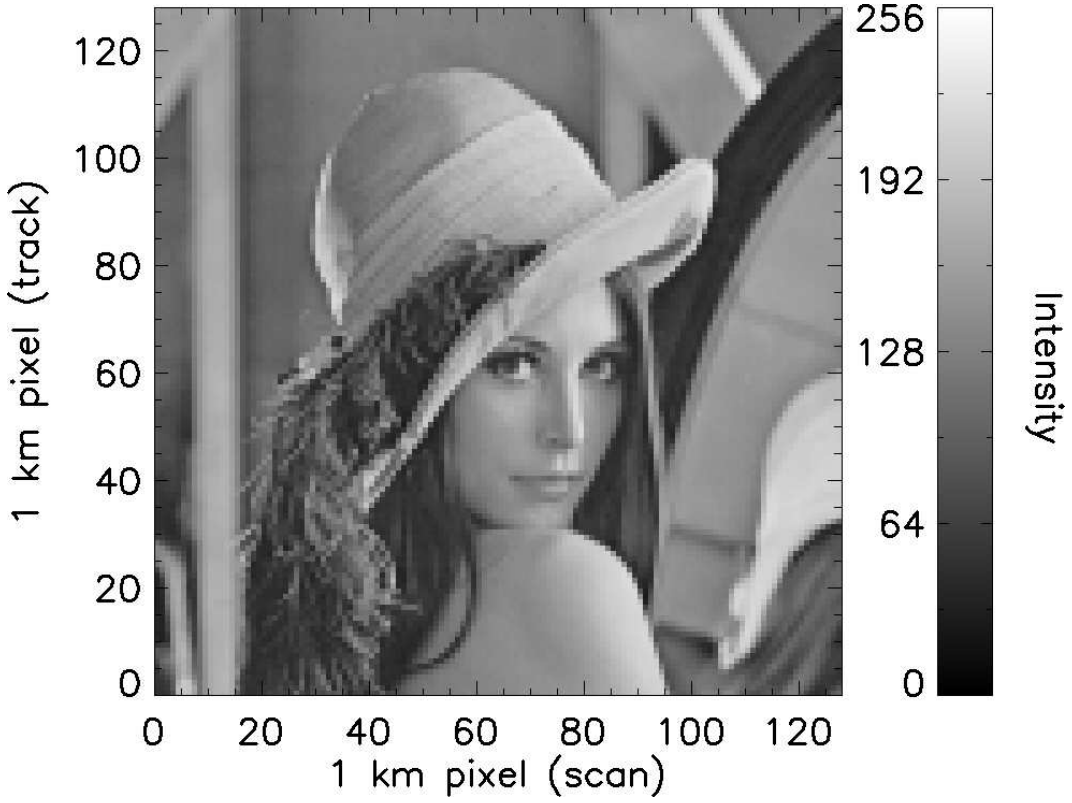

(e)

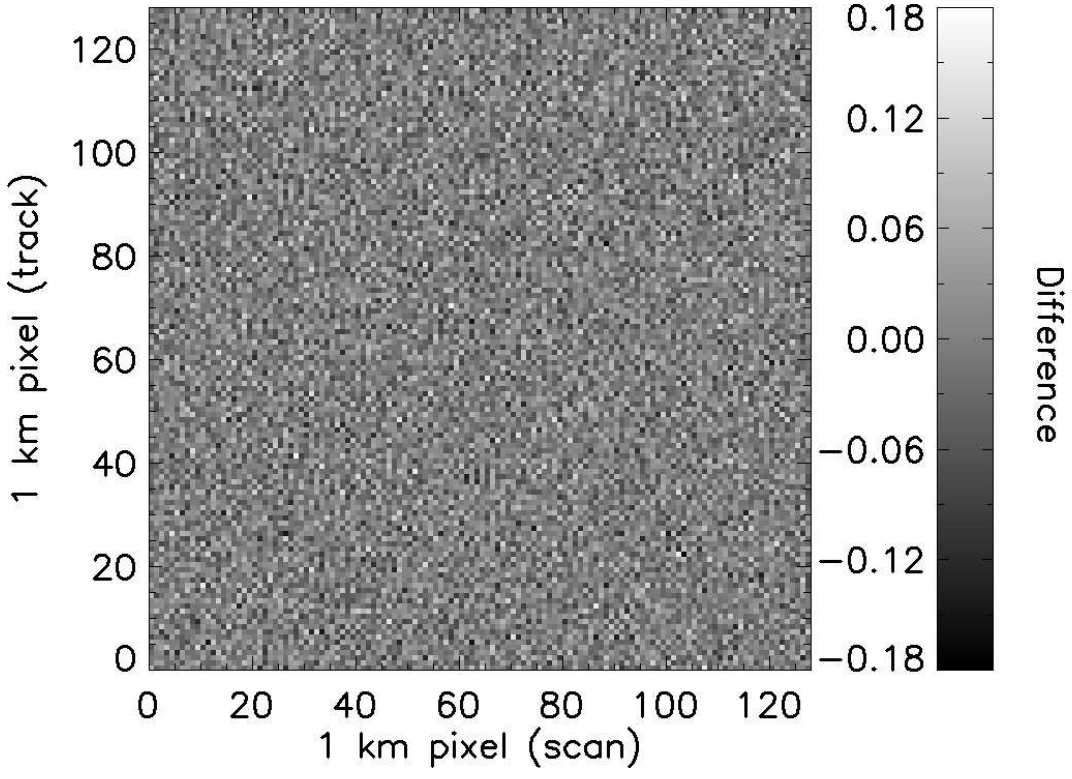

(f)

Figure 4.11 continued: Synthetic data deconvolution accuracy test showing (e) the convolved image after deconvolution with the developed algorithm and (f) the difference between the original and deconvolved image.

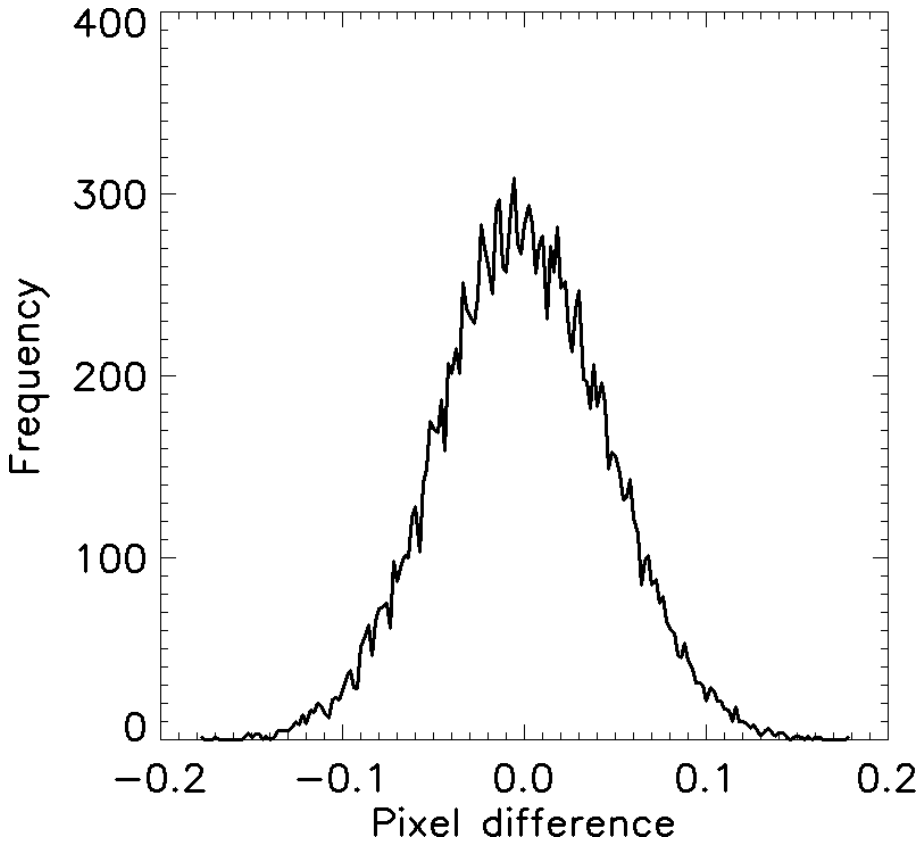

(g)

Figure 4.11 continued: Synthetic data deconvolution accuracy test showing (g) a frequency histogram of (f).

from the data with a high level of accuracy.

Figure 4.12 shows an image from MODIS Aqua band 12 (546nm - 556nm) that was chosen due to the sensitivity of coastline contrast in that waveband. The original convolved and noisy data as received from MODIS Aqua is shown in Figure 4.12(a) and the deconvolved data is shown in Figure 4.12(b). Figure 4.12(c) shows the relative pixel error with an adjusted scale and represents the instrument effects that are removed from the data. These effects are further represented with a frequency histogram in Figure 4.12(d) and have a maximum individual pixel error of 19.44% for this particular image. Considerable contamination can be seen in land regions due to large changes in radiance (Figure 4.12(c)). The coastline also contains contamination with the largest errors being produced at high radiance edges. The deconvolution process has increased the brightness of the beaches and sharp edges have been resolved.

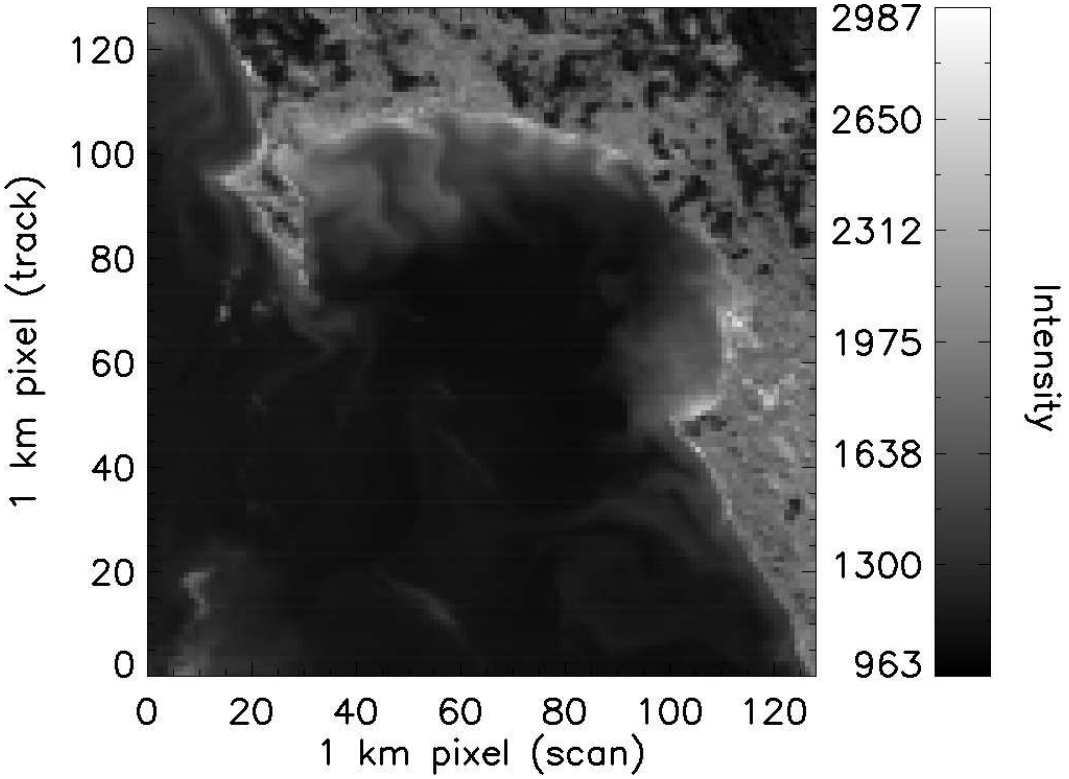

(a)

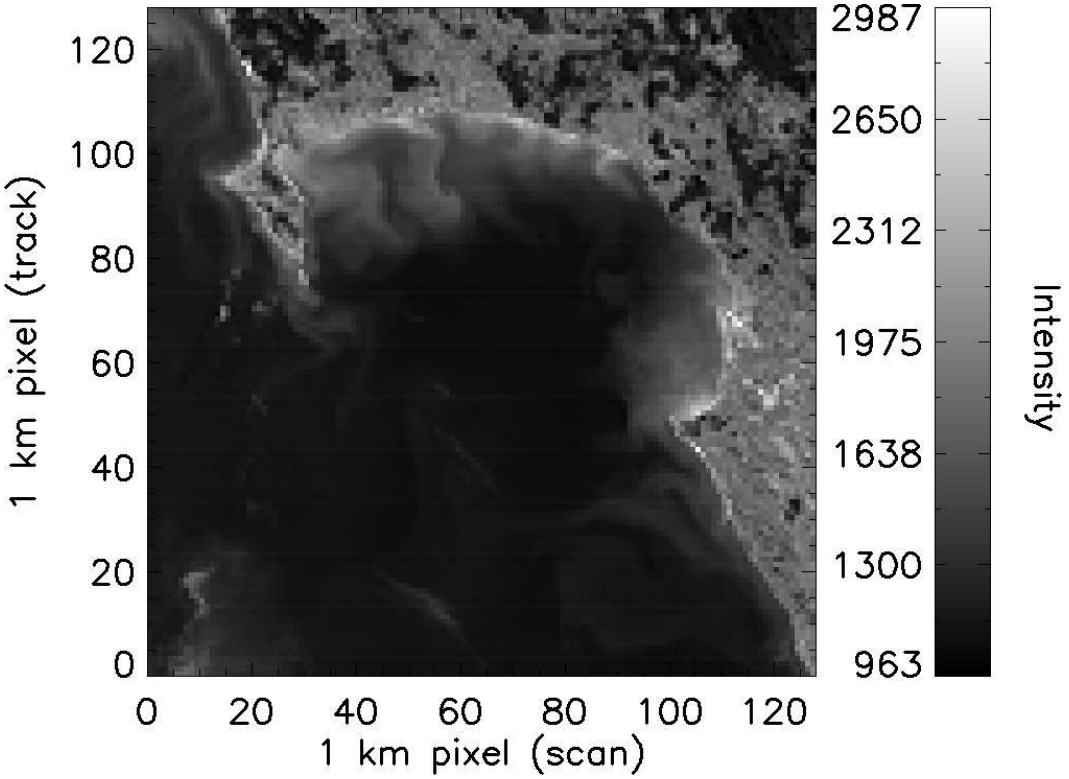

(b)

Figure 4.12: MODIS deconvolution test showing (a) the original MODIS Aqua band 12 data (convolved and noisy) and (b) the deconvolved MODIS Aqua band 12 data. Image of Hawke Bay, New Zealand (Approx. lat/long -39.44, 177.46), 06/04/2009.

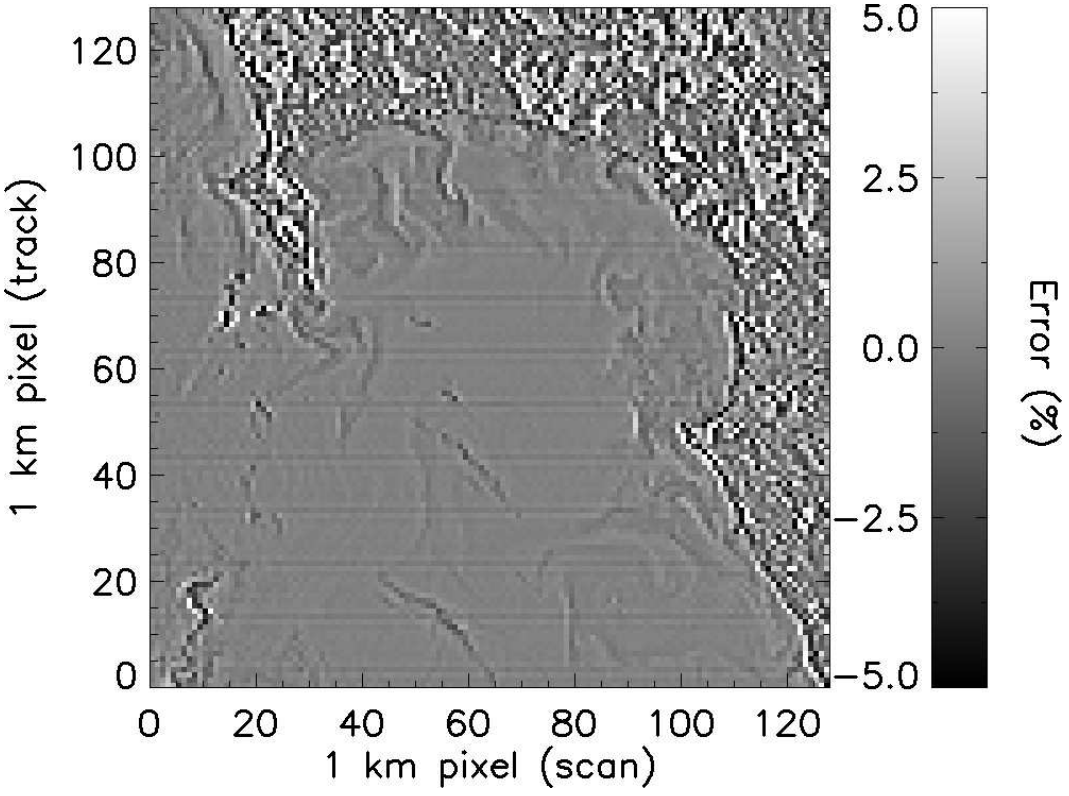

(c)

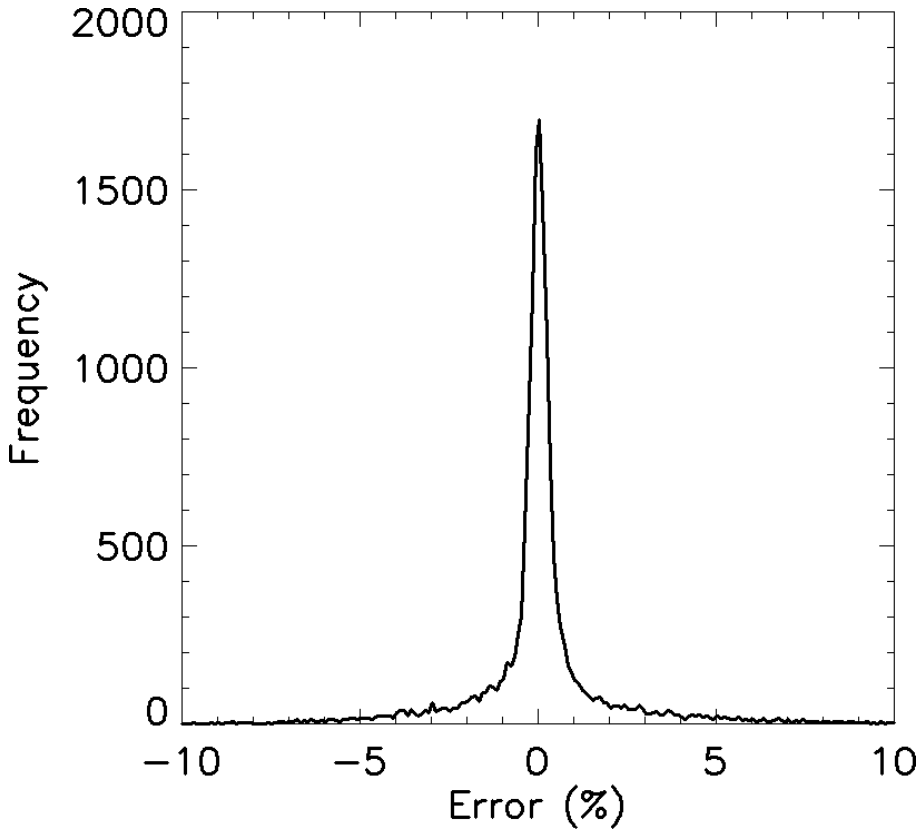

(d)

Figure 4.12 continued: MODIS deconvolution test showing (c) the rescaled relative error removed from the original data and (d) a frequency histogram of the relative error. Image of Hawke Bay, New Zealand (Approx. lat/long -39.44, 177.46), 06/04/2009.

Figure 4.13 shows the deconvolution of an open-ocean scene from MODIS Aqua band 12. This scene has undergone the same process as the previous example but highlights an extreme case where bright clouds contaminate dark ocean measurements. Figures 4.13(a) and 4.13(b) show the convolved and deconvolved MODIS Aqua band 12 images. The rescaled relative pixel error is displayed in Figure 4.13(c) and its frequency histogram is shown in Figure 4.13(d). The maximum individual pixel error for this scene reaches 114.63% which is significantly larger than the previous coastal scene example (Figure 4.12). The largest contamination errors are observed immediately around high-contrast cloud edges. However, the large spatial extent of the PSF causes water regions close to clouds, within approximately 20km, to experience moderate instrumental distortion. This contamination becomes even more severe for pockets of water that are surrounded by cloud cover. In this case, Multiscale Entropy deconvolution successfully removes instrumental distortion and restores accurate ocean measurements in high-contrast areas.

In removing the radiance contamination caused by the instrument optics, a greater quantity of ocean measurements become available for processing. Without deconvolution, ocean measurements near cloud edges are flagged for removal and do not contribute to the final data products. This reduces the spatial coverage and availability of ocean measurements and can detrimentally impact the usefulness of satellite imagery. When the instrumental distortion is removed via Multiscale Entropy deconvolution, a significant number of valuable ocean measurements are recovered and can then contribute to downstream satellite data products, which improves the spatial coverage and availability of the data.

The bow-tie effect of scanning-based satellite instruments has the potential to introduce inaccuracies into the deconvolution process. As a result of bow-tie effects, the number of spatially duplicate measurements increases towards the left and right edges of a MODIS scene. This effect is most extreme at these edges and is present in level 1A MODIS data on which the deconvolution algorithm operates. The deconvolution process can introduce radiometric inaccuracies into these areas where spatial contrast is observed due to the contribution of duplicate measurements. This effect does not occur for deconvolution at the centre of a MODIS scene where there

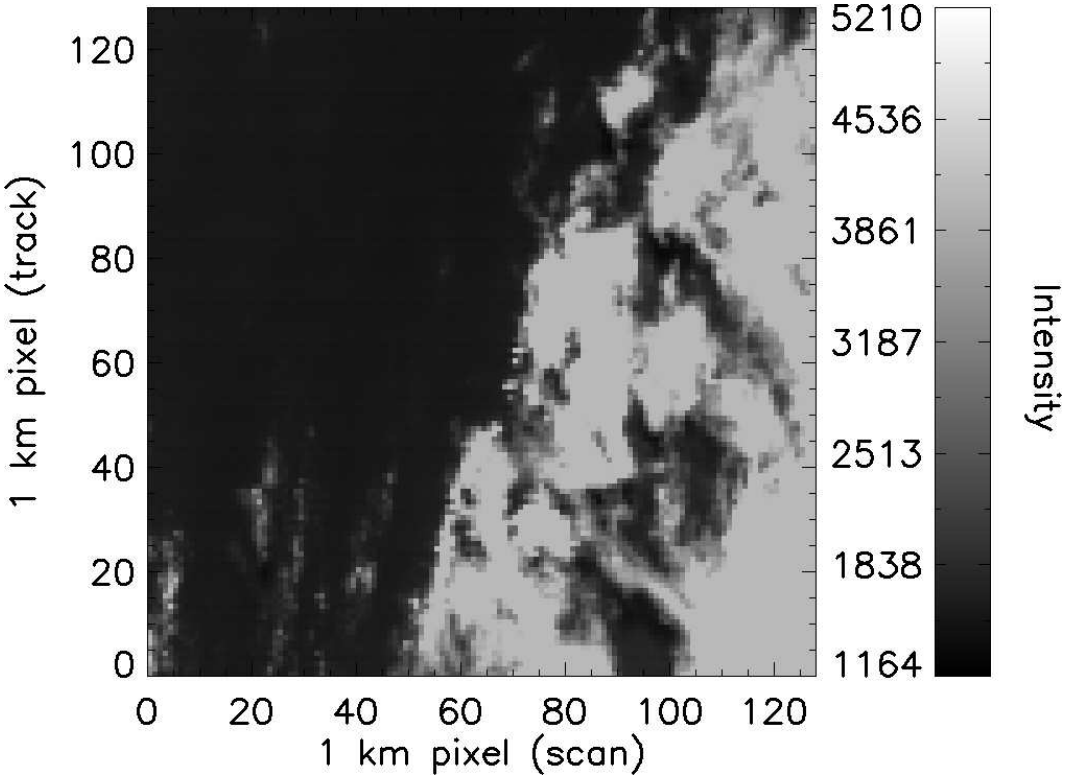

(a)

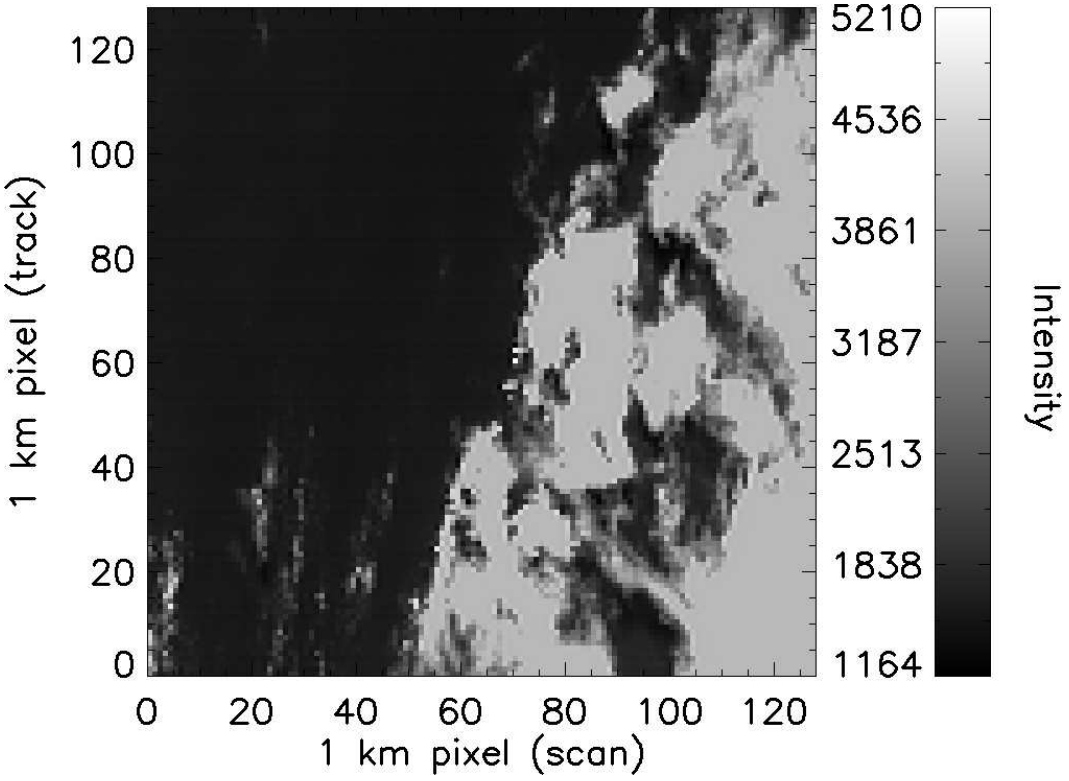

(b)

Figure 4.13: MODIS deconvolution test showing (a) the original MODIS Aqua band 12 data (convolved and noisy) and (b) the deconvolved MODIS Aqua band 12 data. Image of Southern Pacific Ocean (Approx. lat/long -45, 150), 21/04/2010.

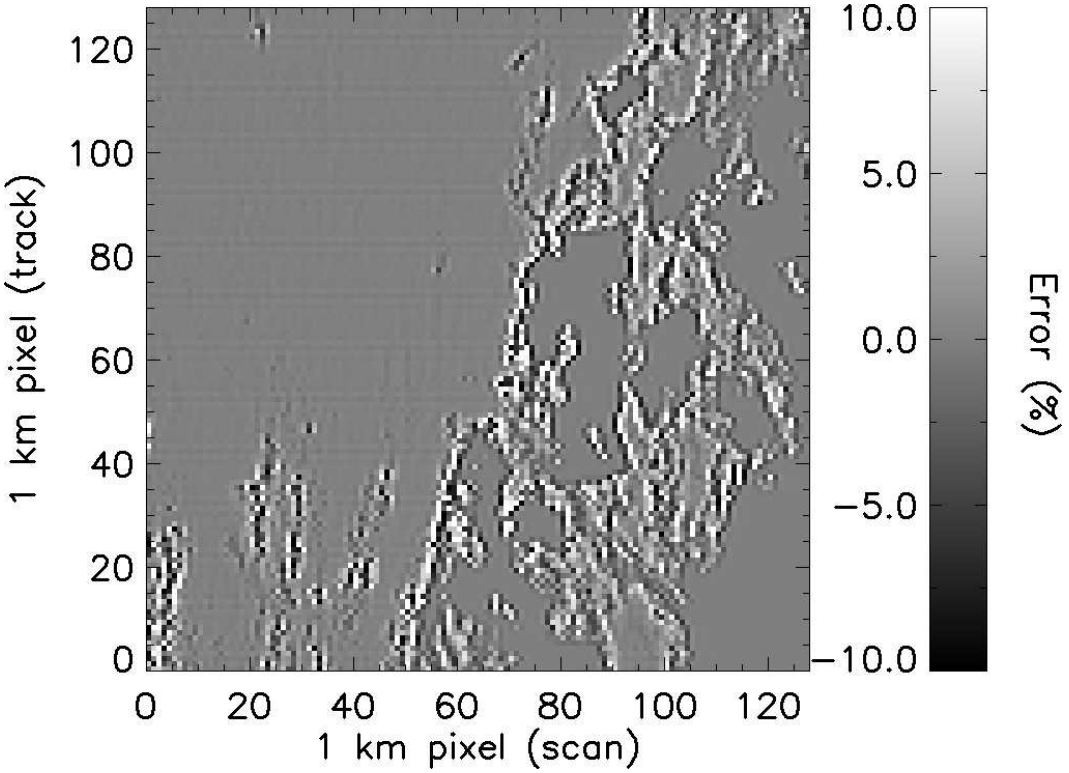

(c)

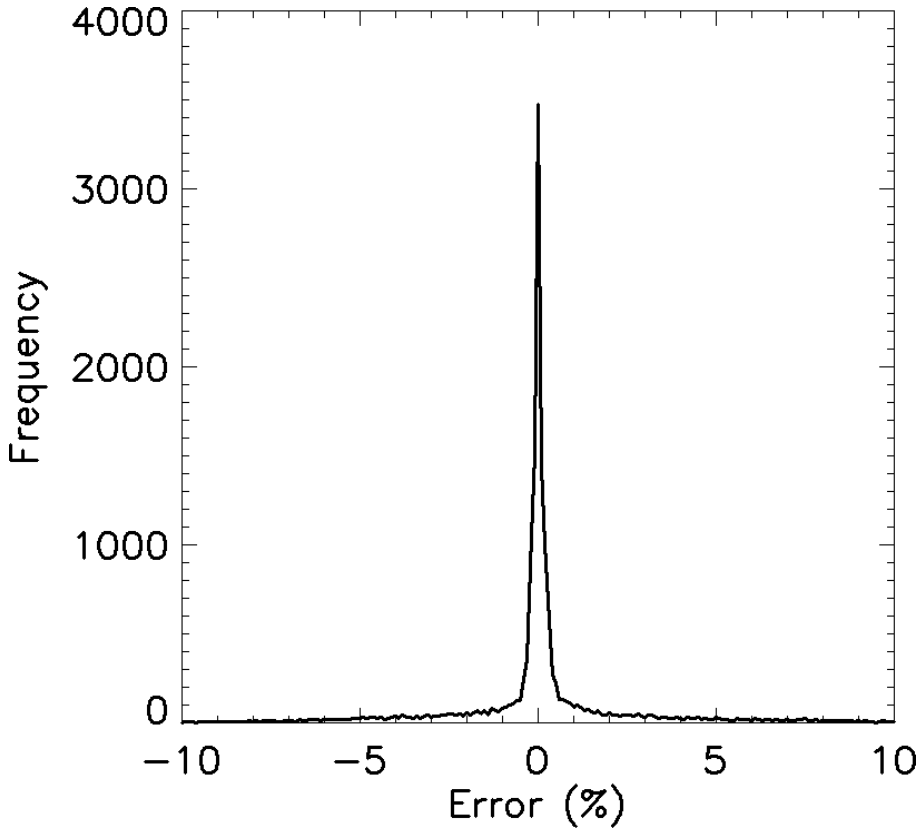

(d)

Figure 4.13 continued: MODIS deconvolution test showing (c) the rescaled relative error removed from the original data and (d) a frequency histogram of the relative error. Image of Southern Pacific Ocean (Approx. lat/long -45, 150), 21/04/2010.

are no duplicate measurements. A possible solution to this problem could employ a mask-based method to account for measurement duplication and prevent errors from being introduced during deconvolution. However, this process has not been included in the developed implementation. Wherever possible, the measurements analysed in this thesis have been taken from regions away from the edge of MODIS scene.

4.5 Summary

The deconvolution algorithm implemented throughout this chapter has the potential to autonomously and efficiently remove instrument effects from optical deconvolution problems. The removal of instrumental spatial distortion is greatly beneficial to the quality of satellite imagery because it prevents errors from being propagated and magnified by downstream processing. This process improves all MODIS ocean colour data products which are commonly used in many scientific fields.

The Multiscale Entropy deconvolution algorithm provides advantages to both terrestrial and marine environments where spatial contrast is observed. Coastal water measurements that are compromised by bright land masses receive particular improvement. This is crucial to the sustainable management of water regions in densely populated coastal zones. Open-ocean measurements containing high-radiance clouds that contrast with dark ocean also receive vast improvements in data measurement quality. This can reduce the quantity of ocean measurements that are removed due to cloud contamination and improves the spatial coverage of satellite data products.

The primary research contributions in this chapter include: a multi-detector convolution process which is fundamental to the operation of the deconvolution algorithm; a detector saturated radiometric correction method that allows MODIS measurements beyond the dynamic range of the detectors to be estimated and more accurately contribute to the deconvolution; and the development of a combination of efficient computational methods that culminate in an accurate and robust deconvolution algorithm. These components are unique and critical to the successful deconvolution of MODIS Aqua imagery.

Chapter 5

Validation

5.1 Introduction

Remote sensing data is a useful resource for the management of coastal and inland water bodies. Satellite imagery combined with physical and biological models can be used to forecast harmful algal blooms, track sediment transport and monitor general water quality (Stumpf and Tomlinson, 2005; Ruhl and Schoellhamer, 2001; Brando and Dekker, 2003). Many climate studies use remote sensing satellite products and rely on this information to be highly accurate (Behrenfeld et al., 2006; Higurashi and Nakajima, 2000; Achard et al., 2002; Kaufman et al., 2002). Remote sensing ocean colour products are becoming increasingly important for the management of water quality in coastal zones (Platt et al., 2008). As such, it is vital to quantify the accuracies and uncertainties of remote sensing products so that their use in marine research can be made with confidence. This is often achieved by comparing remote sensing products with in-situ validation measurements and, in the case of calibration, incorporating correction factors into the data processing stream.

Satellite instruments measure top-of-atmosphere radiance that comprise a combination of natural physical processes. For passive satellite sensors, the signal recorded at satellite height is the reflection of sunlight off the surface of the Earth. Light recorded at the satellite sensor is affected by atmospheric, oceanic and coupled atmosphere-ocean processes. Coastal marine measurements can additionally contain bathymetric effects where reflections occur at the surface and off the shallow

seabed. It is important to note that only approximately 10% of the recorded top-of-atmosphere signal corresponds to the water signal, with the remaining 90% being attributed to atmospheric effects (Yang and Gordon, 1997). To derive marine products, it is necessary to remove the atmospheric component of the signal using a process called atmospheric correction (Kaufman, 1989; Vermote et al., 2002; Wang, 2010). In fact, the production of ocean colour and other water-based products implicitly refers to the application of atmospheric correction methods. After atmospheric correction is applied, the remaining signal is further processed to account for variables such as solar zenith angle, Earth-Sun distance, sensor waveband response and a range of sensor transmittance processes. Once this processing is complete, one of the most important output products for marine purposes is the spectral remote sensing reflectance, $R_{rs}(\lambda)$, that describes the fraction of the incident light that is reflected from the surface of the water under consistent lighting conditions. Remote sensing reflectance is a primary data product used to derive many higher-level marine products including chlorophyll-a concentration, Total Suspended Matter (TSM) (also known as suspended solids or suspended particulate matter) and the spectral diffuse attenuation coefficient of downwelling irradiance at 490nm ($K_d(490)$). These products are readily used in marine research and will be the focus of the in-situ validation efforts in this chapter.

The optical properties of open-ocean waters are reasonably well understood and have attracted a significant amount of research (Gordon and Clark, 1980; Dekker, 1993; Lee et al., 1999). However, optically complex coastal waters provide increased signal processing difficulty due to shallow water processes and higher concentrations of in-water constituents including algal blooms, Coloured Dissolved Organic Matter (CDOM) (also known as yellow substance, or gelbstoff), suspended particulate matter, coccolithophores, detritus, and bacteria (Sathyendranath, 2000). Water is typically classified into two optical cases (Morel and Prieur, 1977; Mobley et al., 2004). Case 1 waters are predominantly affected by phytoplankton and its subsequent by-products. Open-ocean environments are generally classified as case 1 waters and behave predictably from a remote sensing standpoint. Case 2 waters contain much larger quantities of TSM and CDOM which significantly

increase their optical complexity. Many coastal zones are classified as optical case 2 waters because they often contain higher concentrations of suspended particulate matter from terrestrial run-off. This classification system is commonly used for computational modelling. Predictive bio-optical models can estimate the inherent optical properties of case 1 water such as absorption, scattering and backscattering coefficients, as well as the apparent optical properties which include reflectance and the diffuse attenuation coefficient. Chlorophyll-based bio-optical models also use this classification scheme and specialise at estimating chlorophyll concentrations from satellite measurements of ocean colour.

Instrumental distortion, which is also referred to as adjacency effects or stray light from land, occurs in high-contrast scenes where bright land or clouds contaminate the water signal. This source of contamination is an important factor for water-based measurements in coastal regions. In this chapter, instrumental distortion effects are removed from MODIS Aqua imagery using Multiscale Entropy deconvolution (Chapter 4), and the results are compared with accurate in-situ measurements. A comparison of both the original (convolved) and deconvolved MODIS products against the in-situ measurements will allow for any improvement to be quantified. Further deconvolution validation is investigated by comparing MODIS Aqua imagery with a high-resolution QuickBird image containing an Antarctica ice edge. This is a good example of a high-contrast satellite image that should substantially benefit from deconvolution.

The first area of investigation is the north-west Baltic Sea which contains unique brackish waters with low salinity due to restricted salt input water from the North Sea. It is estimated that a significant quantity of freshwater (upwards of 450km^3) contributes annually to the Baltic Sea from surrounding catchment areas (Rydén and Karlsson, 2012). The primary circulation driver is surface wind that inputs Ekman transport forces into the waterbody (Jansson, 2003). It is common for cyanobacterial blooms to become extensive in the Baltic Sea throughout the summer period. The atmospheric conditions over the Baltic Sea are typically relatively clear (Carlund et al., 2005). The Baltic Sea has particularly high CDOM concentrations which result in high absorption of short wavelengths ranging from ultraviolet to green.

Additionally, red wavelengths are heavily absorbed by water. This leads to less reflectance and a decrease in the signal-to-noise ratio in these parts of the spectrum. For this reason, accurate atmospheric correction is vital to produce good ocean colour products for the Baltic Sea region. The Baltic Sea is generally classified as optical case 2 waters due to its high CDOM content (Kratzer et al., 2003, 2008; Kratzer and Tett, 2009). This further increases the difficulty of deriving accurate marine products in this region because of the complex interaction of shallow coastal waters and high concentrations of particulate matter.

5.2 In-situ Baltic Sea

5.2.1 Method

MODerate resolution Imaging Spectroradiometer (MODIS) is a satellite instrument aboard the Earth observing system platform Aqua. MODIS Aqua captures data in 36 spectral bands with wavelengths ranging from 0.4μm to 14.4μm, and at several spatial resolutions including 2 bands at 250m, 5 bands at 500m and 29 bands at 1km resolution. MODIS is designed to deliver a wide range of ocean colour products. The validation undertaken in this chapter will concentrate on 1km resolution imagery because this is the spatial resolution for which MODIS Aqua instrument Point Spread Functions (PSFs) are available (Meister and McClain, 2010). More specifically, MODIS Aqua captures 1km resolution ocean colour imagery at centre-wavelengths of 412, 443, 488, 531, 547, 667, 678, 748 and 869nm and these wavebands must undergo individual deconvolutions using their respective unique PSFs before comparisons can be made with in-situ measurements.

The in-situ validation measurements were collected by Dr. Susanne Kratzer et al. (pers. comm., August 11, 2012) from the Baltic Sea in July 2008 using the instrumentation and techniques described by Kratzer and Vinterhav (2010) and Zibordi et al. (2012). The collection of this in-situ data was specifically designed for comparison with satellite measurements that cover extended spatial areas, as determined by resolution of the satellite instrument. The sampling stations were selected such that they form two transects (Figure 5.1). The first transect includes

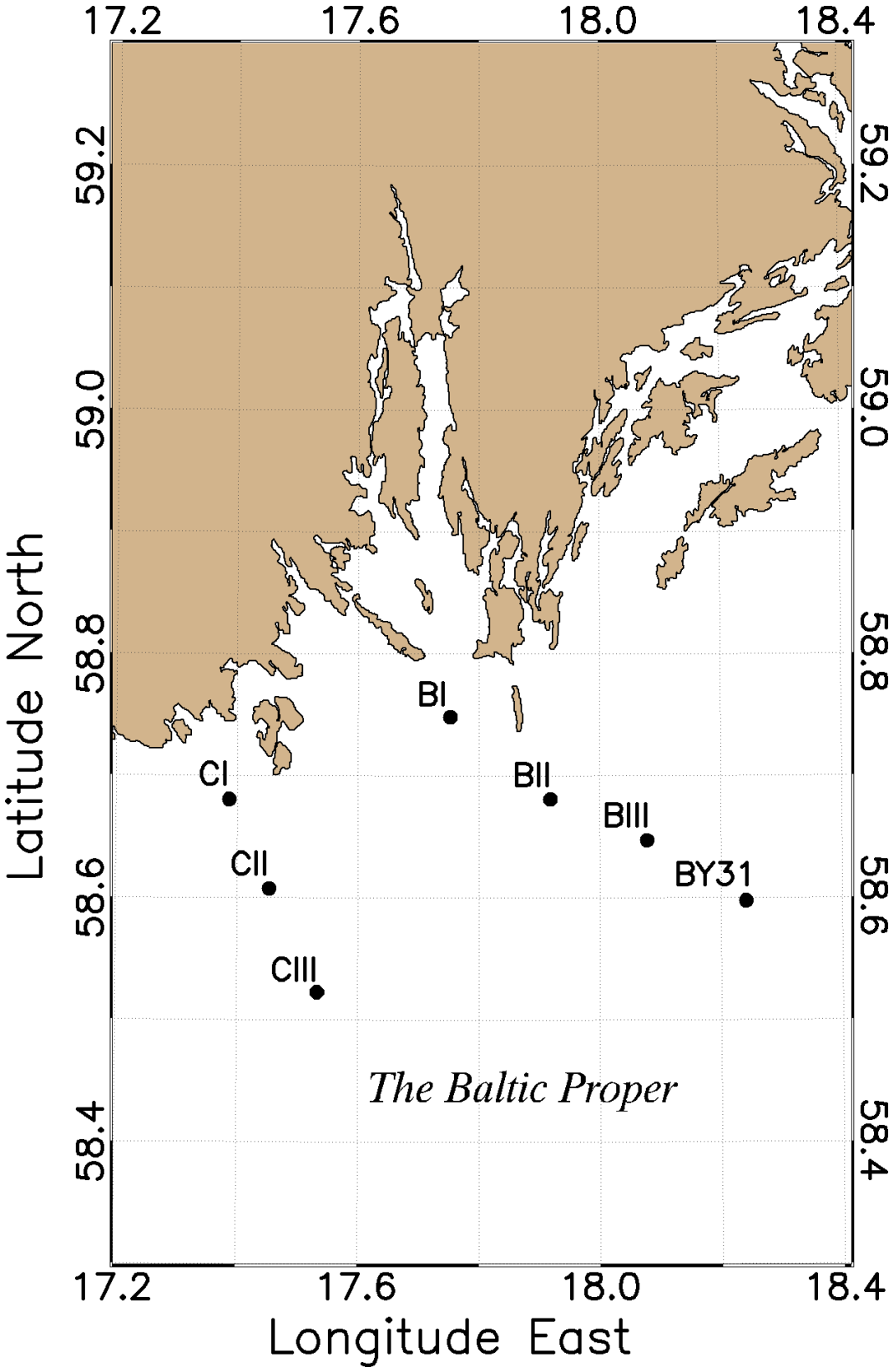

Figure 5.1: In-situ measurement stations for the July 2008 sea-truthing campaign.

stations BI, BII, BIII that were established by Kratzer and Tett (2003, 2009) and station BY31, the deepest part of the Baltic Sea (459m). The stations of the second transect include CI, CII and CIII and are positioned approximately 10km apart. They were originally selected for the evaluation of adjacency effects in the coastal zone (Vinterhav 2008). Both transects range in distance from land from 7 to 32km. The in-situ measurements were taken in 2008 over a period of eight days that experienced favourable water illumination and sea state conditions. It was noted by Kratzer and Vinterhav (2010) that all of the measurement dates offered more or less cloud free sampling conditions.

Temporally and spatially matched MODIS overpasses were collected and processed to level 2 using the SeaWiFS Data Analysis System (SeaDAS) version 6.4 for both the original and deconvolved imagery. For each in-situ measurement, a 3×3 pixel area corresponding to the position of the sampling station was extracted from the MODIS image and filtered for invalid data points. Retrieved pixel groups with at least 5 values remaining after filtering were averaged and compared with the in-situ measurements. The locations and sample times for the in-situ measurements, along with the matching MODIS overpass times are reported in Table 5.1 and true-colour images of each entire MODIS overpass are displayed in Figure 5.2.

Table 5.1: Sampling stations, sampling times and MODIS overpass times for the July 2008 sea-truthing campaign.

Date	Sampling station	Sampling time (GMT)	MODIS overpass (GMT)
24/07/2008	BY31	08:58	12:25
	BIII	10:01	
	BII	10:53	
	BI	11:37	
25/07/2008	CI	08:35	11:30
	CII	09:21	
	CIII	10:15	
31/07/2008	CIII	10:14	10:55
	CII	11:10	
	CI	12:00	

Figure 5.2: MODIS Aqua true-colour images for full Baltic Sea overpasses on (a) 24/07/2008, (b) 25/07/2008 and (c) 31/07/2008. Square boxes indicate the region that the in-situ measurements were taken and the black dots at the centre of the boxes indicates the precise location of each sampling station.

The validation undertaken in this chapter will concentrate on comparing key ocean colour quantities including the spectral remote sensing reflectance, chlorophyll-a concentration, TSM and $K_d(490)$. The in-situ remote sensing reflectance measurements are available for the wavelengths 412, 443, 490, 510, 560, 620 and 670nm, and were selected to match the wavelengths of MERIS detectors. As a result, there are discrepancies between the in-situ and MODIS measurement wavelengths. To accommodate this inconsistency, a realistic interpolation or curve-fitting method must be applied to the in-situ measurements so that reflectance values can be estimated at the appropriate MODIS wavelengths. Initially, a 6th order polynomial was fitted to the in-situ remote sensing reflectance measurements to allow MODIS-compatible values to be extracted. However, with only very few spectral in-situ data points, the fitted curves provided unsatisfactory and unrealistic results, requiring a more comprehensive fitting technique.

Every waterbody contains a unique reflectance spectrum that is affected by in-water constituents, suspended particulate matter, living micro-organisms and bathymetric topology. Ficek et al. (2011) report a range of typical Baltic Sea reflectance spectra that illustrate the spectral response with increasing quantities of CDOM (Figure 5.3). These spectra can be used to constrain the in-situ spectral curve-fitting process and provide more accurate MODIS-comparable reflectance measurements.

The aim is to use the shape of the typical Baltic Sea spectra to constrain the interpolation and allow the use of higher order polynomial fitting. Each group of in-situ reflectance measurements was matched to a suitably amplified Baltic Sea reflectance spectrum. The amplification process is justifiable because the spectra generally increase in reflectance consistently across the visible wavelengths (Figure 5.3). The in-situ reflectance measurements were then superimposed onto the matched Baltic Sea spectrum and curves were fitted to the data points. An 11th order polynomial was chosen for curve fitting because it sufficiently captured the structure and variation of the data. During the fitting process, the in-situ data points were weighted 50 times greater than the underlying typical Baltic Sea spectra. This is because, while the underlying typical spectra are required to help constrain the fitted

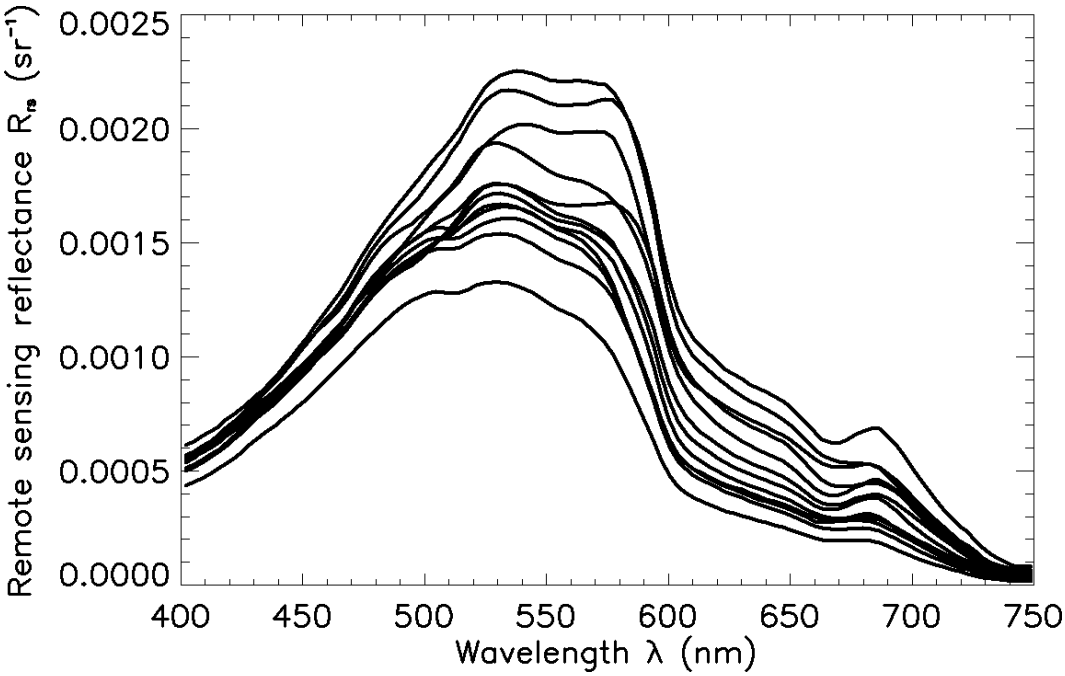

Figure 5.3: Typical Baltic Sea reflectance spectra for increasing quantities of CDOM. Data originally measured and reported by Ficek et al. (2011).

curves, the in-situ measurements are significantly more important and should be treated preferentially. Using a weighted combination of the in-situ measurements and typical Baltic Sea reflectance spectra, optimal MODIS-compatible measurements were extracted for each group of in-situ spectral samples to allow direct comparison with MODIS Aqua data. Figure 5.4 displays an underlying amplified typical Baltic Sea reflectance spectrum, the fitted weighted curve, the in-situ measurements and the MODIS-compatible measurements drawn from the fitted curve.

The in-situ measurements were designed to replicate the MERIS product of water-leaving reflectance which is defined as (Antoine and Morrel, 2005):

$$\rho_w(\lambda) = \pi \frac{L_w(\lambda)}{E_d(\lambda)} \tag{5.1}$$

where ρ_w = MERIS water-leaving reflectance (sr^{-1})

λ = observed wavelength (nm)

L_w = water-leaving radiance ($\mu W cm^{-2} nm^{-1} sr^{-1}$)

E_d = downward irradiance ($\mu W cm^{-2} nm^{-1}$)

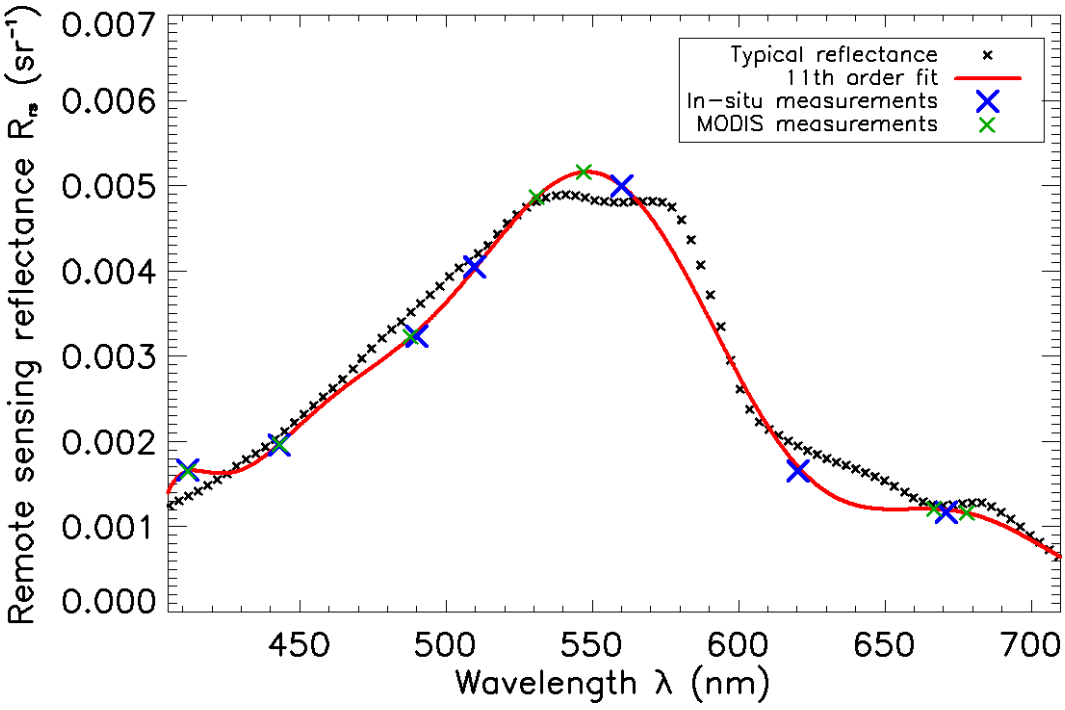

Figure 5.4: Spectral reflectance curve showing an underlying amplified typical Baltic Sea reflectance spectrum (black crosses), fitted curve weighted by in-situ measurements 50:1 (red line), in-situ measurements (blue crosses) and MODIS-compatible measurements drawn from the fitted curve (green crosses). In-situ measurements were recorded on 24/07/2008 by Kratzer and Vinterhav (2010) at sampling station BIII (Figure 5.1) in the Baltic Sea region.

In contrast, MODIS produces remote sensing reflectance, which is defined (Zibordi et al., 2010):

$$R_{rs}(\lambda) = \frac{nL_w(\lambda)}{E_0(\lambda)} \tag{5.2}$$

where R_{rs} = MODIS remote sensing reflectance (sr^{-1})

nL_w = normalised water-leaving radiance ($\mu W cm^{-2} nm^{-1} sr^{-1}$)

E_0 = mean extraterrestrial solar irradiance ($\mu W cm^{-2} nm^{-1}$) (Thuillier et al., 2003)

These two quantities are largely equivalent, except for a factor of π contained in the MERIS water-leaving reflectance product (Equation 5.1). Gordon and Voss (1999) identified that a good approximation to re-align these products is:

$$R_{rs}(\lambda) = \frac{\rho_w(\lambda)}{\pi} \tag{5.3}$$

Applying this correction allows the in-situ water-leaving reflectance values to be directly compared with the MODIS remote sensing reflectance measurements.

5.2.2 Results

MODIS-compatible reflectance values were extracted from the in-situ Baltic Sea measurements using the weighted curve-fitting method described in Section 5.2. Figures 5.5 and 5.6 display comparisons of the in-situ and MODIS spectra before and after deconvolution for each sampling station on 24/07/2008. The spectral profile of the MODIS values is reasonably well matched to the shape of the in-situ measurements, and these profiles are indicative of the spectral measurement on the other sampling dates. Even containing similar profiles, the MODIS measurements can be seen to underestimate and overestimate the in-situ truthing values. In all cases, the deconvolved reflectance values are very similar to the original MODIS values. This suggests that the deconvolution process does not have a large impact for these particular validation measurements.

Figure 5.7 displays a band-by-band breakdown of spectral measurements including those depicted in Figures 5.5 and 5.6, as well as all measurements from the other sampling dates. A perfect match between the MODIS measurements and truthing values would produce clustering around the 1:1 line, and this is clearly not the case. While some points fall close to the 1:1 line, the spread of points away from the 1:1 line indicates that MODIS is not estimating reflectance well in the Baltic Sea either before or after deconvolution. There are several possible reasons for such widespread results. The optical complexity of coastal waters makes it difficult for atmospheric correction to accurately remove the atmospheric signal and produce

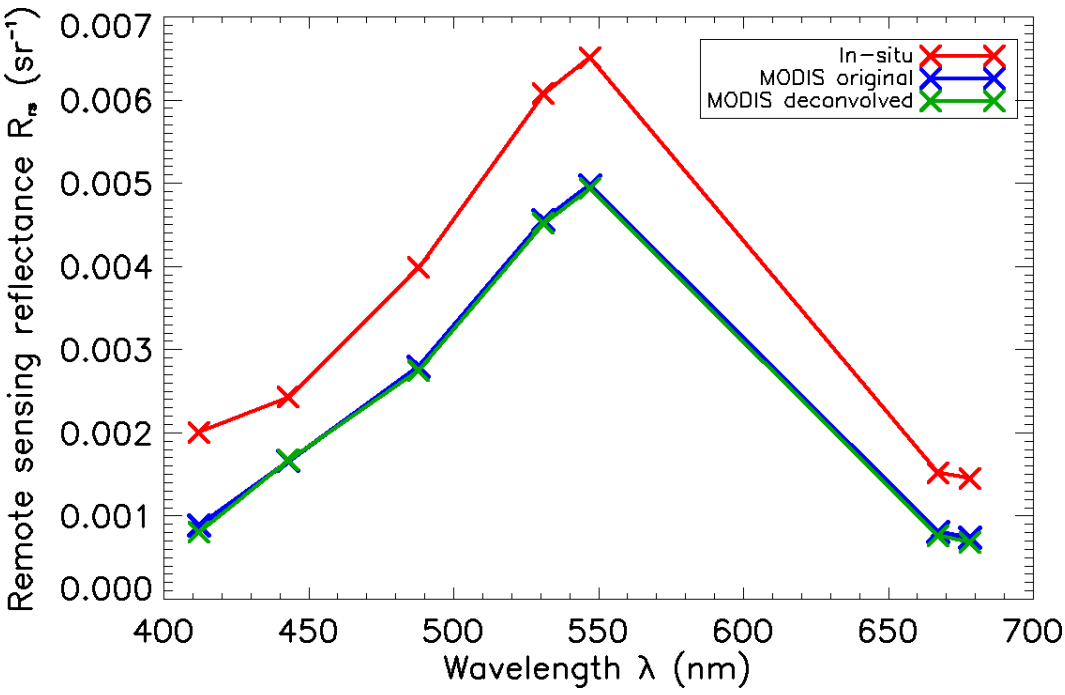

(a) BI

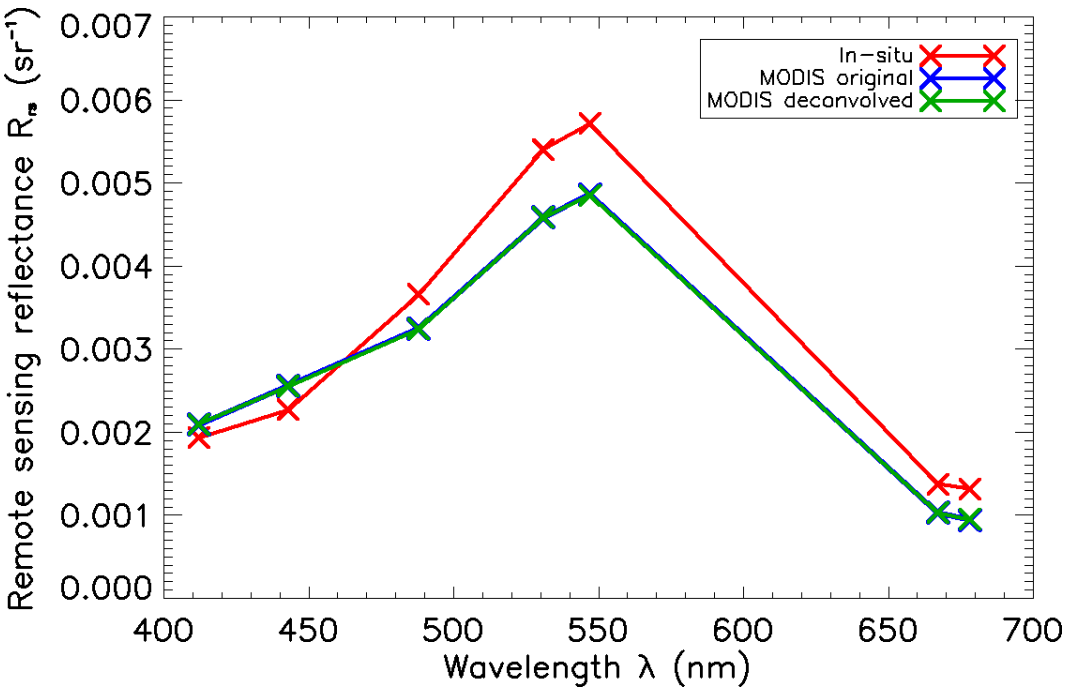

(b) BII

Figure 5.5: Direct comparison of in-situ remote sensing reflectance spectra with MODIS reflectance spectra before and after deconvolution for sampling stations BI and BII on 24/07/2008.

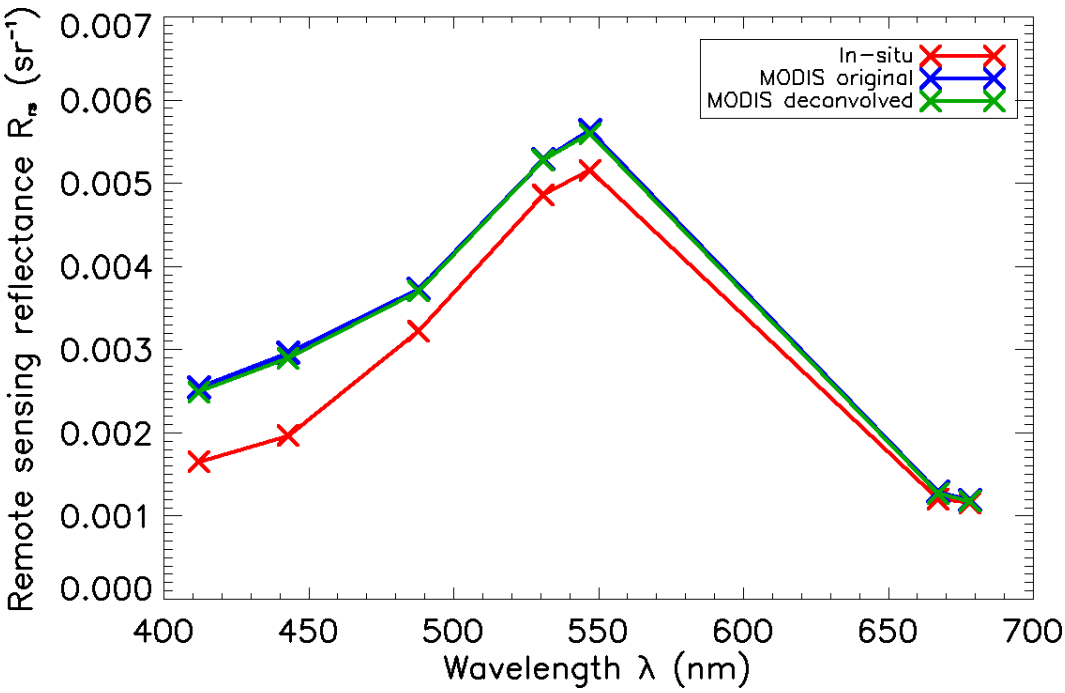

(a) BIII

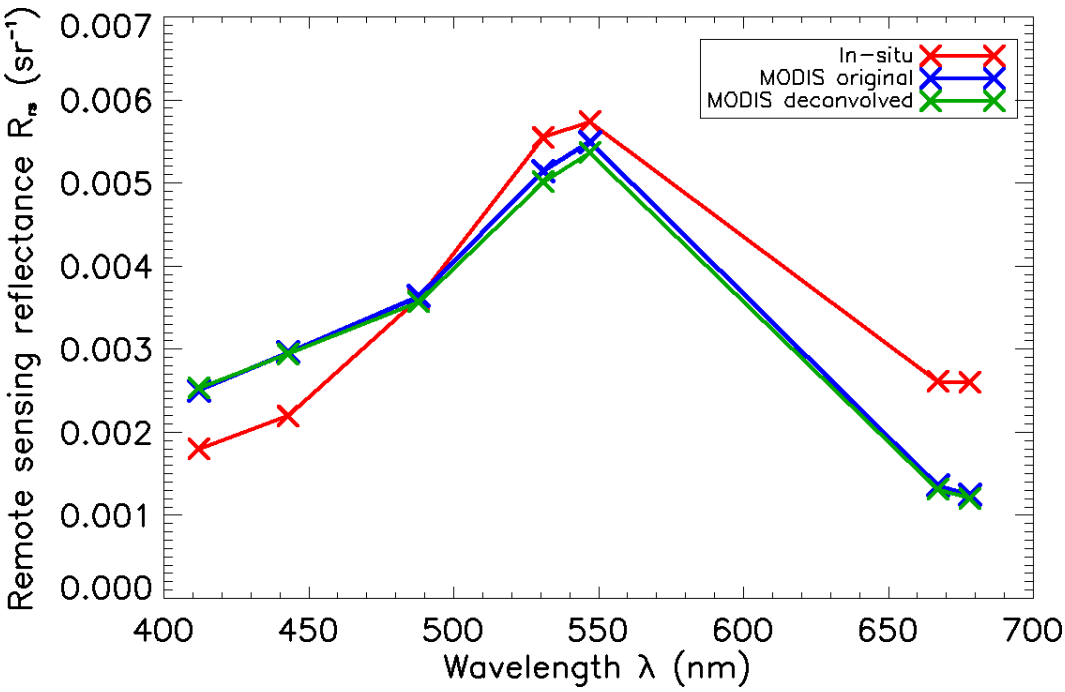

(b) BY31

Figure 5.6: Direct comparison of in-situ remote sensing reflectance spectra with MODIS reflectance spectra before and after deconvolution for sampling stations BIII and BY31 on 24/07/2008.

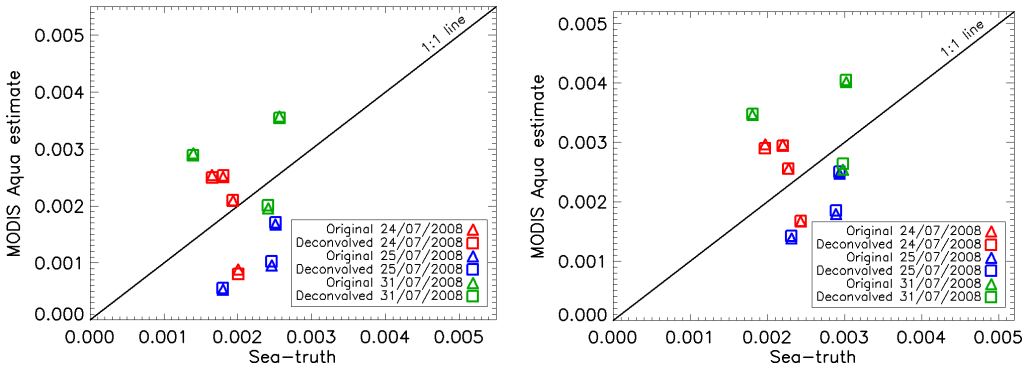

(a) R_{rs} 412nm (b) R_{rs} 443nm

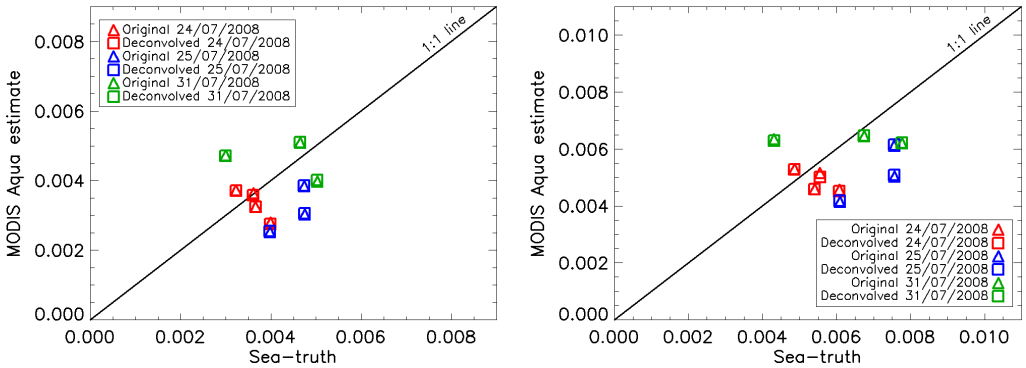

(c) R_{rs} 488nm (d) R_{rs} 531nm

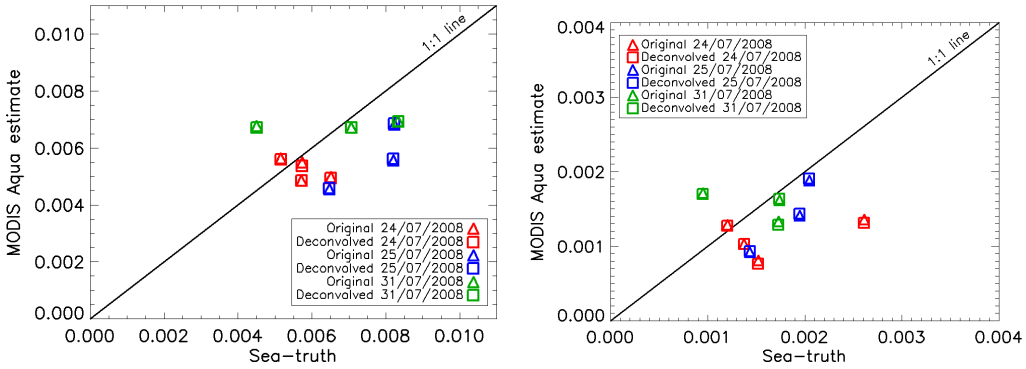

(e) R_{rs} 547nm (f) R_{rs} 667nm

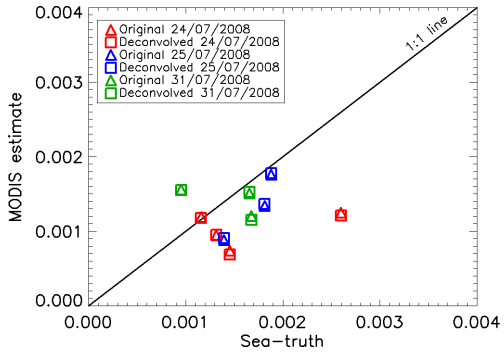

(g) R_{rs} 678nm

Figure 5.7: Individual band scatter-plot comparisons of in-situ and MODIS remote sensing reflectance measurements before and after deconvolution for the 2008 sea-truthing campaign (Kratzer and Vinterhav, 2010).

reliable water measurements. High concentrations of CDOM in the Baltic Sea also contribute to processed measurement inaccuracy, especially in the blue-green part of the spectrum where CDOM heavily absorbs and disrupts the signal. Additionally, it was recorded that extensive cyanobacterial blooms were present throughout the Baltic Sea during the 2008 sea-truthing campaign (Kratzer and Vinterhav, 2010). These cyanobacterial blooms can result in patchiness when viewed from space and may also disrupt remote sensing reflectance and subsequent products.

Comparisons can also be made with higher-level products including chlorophyll-a concentration (Chl_a), Total Suspended Matter (TSM) and the spectral diffuse attenuation coefficient for downwelling irradiance ($K_d(490)$) as seen in Figure 5.8 (a), (b) and (c) respectively. The MODIS GSM chlorophyll-a concentration shows significant deviation from the 1:1 line with deconvolution occasionally impacting the estimation (Figure 5.8(a)). Such widespread results do not inspire confidence in MODIS Aqua chlorophyll-a products in the Baltic Sea. Similar results are seen for TSM measurements where severe MODIS overestimation is apparent (Figure 5.8(b)). The MODIS $K_d(490)$ estimations are all close to the 1:1 line and compare reasonably well to the sea-truthing values (Figure 5.8(c)). $K_d(490)$ is primarily derived from MODIS Aqua bands 10 (490nm) and 4 (555nm) (Mueller, 2000). The results are consistent with Darecki and Stramski (2004) who showed that $K_d(490)$ was the most accurate MODIS product in the Baltic Sea over 25 validation datasets collected between 1993 and 2001. The $K_d(490)$ results also appear to improve on results from Lee et al. (2005). This is possibly due to an updated atmospheric correction model in SeaDAS version 6 that includes data from the AErosol RObotic NETwork Ocean Colour (AERONET-OC) stations (Zibordi et al., 2009, 2010).

In addition to visual comparisons, it is important to quantify the impact of deconvolution over all sample points. The primary measures that will be used to quantify the difference between the MODIS estimates and the in-situ measurements

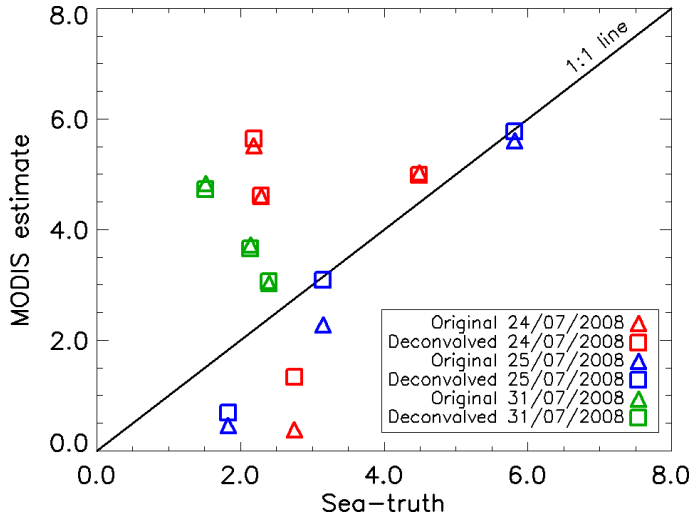

(a) Chlorophyll-a (GSM)

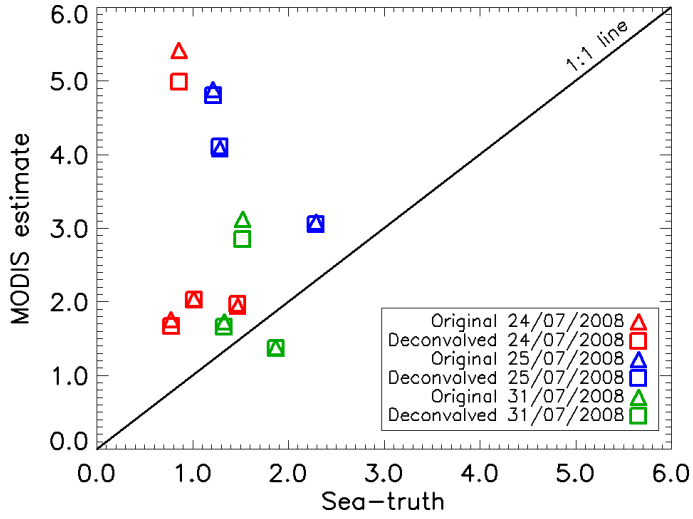

(b) TSM

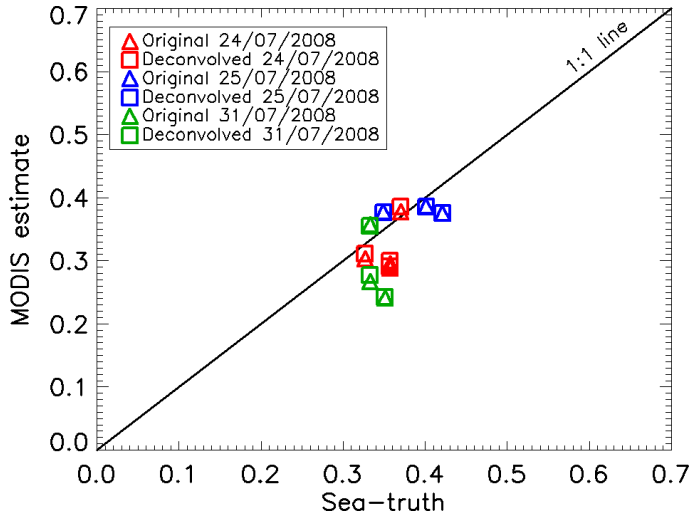

(c) $K_d(490)$

Figure 5.8: Comparisons of in-situ sea-truth and MODIS Aqua chlorophyll-a concentration (GSM), Total Suspended Matter (TSM) and the spectral diffuse attenuation coefficient ($K_d(490)$) before and after deconvolution for the 2008 sea-truthing campaign (Kratzer and Vinterhav, 2010).

are the relative Mean Norm Bias (MNB) and the relative Root Mean Square (RMS), as used in similar analyses by Cristina et al. (2009) and Kratzer and Vinterhav (2010):

$$\text{MNB} = \frac{1}{N}\sum_{i=1}^{N}\left(\frac{y_i - x_i}{x_i}\right) \times 100\% \tag{5.4}$$

$$\text{RMS} = \sqrt{\frac{1}{N}\sum_{i=1}^{N}\left(\frac{y_i - x_i}{x_i}\right)^2} \times 100\% \tag{5.5}$$

where N = number of sample points
y = in-situ measurement
x = MODIS measurement (original or deconvolved)

When calculated using all sample points, the MNB provides a measure that describes the average difference between the in-situ and MODIS measurements, including a direction bias. That is, a positive MNB indicates that the average of the measurements is overestimated and a negative MNB indicates that the average of the measurements is underestimated. It should also be noted that a MNB calculation on data evenly spread above and below the 1:1 line would produce a value of 0, effectively hiding any errors. For this reason, it is also appropriate to calculate the RMS where every difference is treated as a positive error. In this way, the RMS describes the cumulative sum of all measurement errors and can be used to determine the total magnitude of the errors.

Table 5.2 displays MNB and RMS results calculated using all sample points in each spectral band for the MODIS original and deconvolved measurements. An average is taken across all bands to provide a final impact assessment for remote sensing reflectance. MNB and RMS statistics are also derived for chlorophyll-a, TSM and $K_d(490)$ using all available sampling points. The improvement attained using deconvolution is calculated as the difference between the original and deconvolved RMS results, with positive values indicating an improvement and negative values indicating degradation. This improvement is only calculated for RMS because the bias component in the MNB would render its result misleading.

Table 5.2: MNB and RMS results for remote sensing reflectance, chlorophyll-a, TSM and $K_d(490)$ for original and deconvolved MODIS Aqua measurements. The improvement results indicate the magnitude of benefit encountered using deconvolution.

	Original		Deconvolved		Improvement
$R_{rs}(\lambda)$ (nm)	MNB (%)	RMS (%)	MNB (%)	RMS (%)	RMS (%)
412	0.99	56.13	0.25	55.32	0.80
443	0.99	56.13	0.94	55.03	1.10
488	8.18	42.32	8.77	41.58	0.74
531	-7.03	28.60	-7.20	28.28	0.32
547	-10.07	24.75	-10.30	24.46	0.29
667	-8.38	24.39	-8.73	24.00	0.39
678	-13.40	37.72	-13.90	38.05	-0.33
Spectral Average	-4.10	38.58	-4.31	38.10	0.47
Chl_a (OC3)	225.13	266.28	222.78	262.72	3.56
Chl_a (Carder)	240.11	298.06	247.49	296.69	1.36
Chl_a (Clark)	146.56	218.95	144.06	220.98	-2.03
Chl_a (GSM)	39.34	101.07	46.74	96.60	4.47
TSM	145.57	215.19	136.56	200.67	14.52
$K_d(490)$	-9.17	15.30	-8.29	14.60	0.69

The results show that MODIS Aqua remote sensing reflectance measurements are often underestimated, regardless of deconvolution. This is reflected in the spectral average MNB of approximately -4% and the spectral average RMS of approximately 38%. The improvement from deconvolution appears small but positive from spectral bands 412nm to 667nm, and negative for band 678nm. The spectral average improvement for remote sensing reflectance is 0.47% which indicates a small improvement for this particular validation data.

The different chlorophyll-a algorithms all produce overestimated concentrations for both original and deconvolved MODIS measurements. The GSM algorithm produces the smallest errors out of all of the algorithms, but is still moderately overestimated. Deconvolution improves the OC3, Carder and GSM algorithm results by between approximately 1.3% to 4.5%, but is detrimental to the Clark algorithm

adding approximately 2% RMS error to the original MODIS measurements. TSM is generally overestimated but does receive a considerable improvement of 14.52% RMS from deconvolution. The diffuse attenuation coefficient is slightly underestimated and receives a small improvement from deconvolution.

The results show no consistent significant improvement across any of the analysed MODIS products after deconvolution is applied. However, an inspection of some of the attributes of instrumental deconvolution may provide some insight on the in-situ validation results. The MODIS Aqua ocean colour PSFs contain a low-response area that extends on average up to approximately 12km from the image point of the instrument, and moderate contamination would be expected for bright features within this distance. Most of the in-situ measurement locations are considered to be open-sea sampling stations with the closest to land being approximately 7km. This means that the quantity of instrumental distortion from land would be expected to be small for the sampling points analysed in this study.

The three analysed MODIS overpasses show close to ideal sampling conditions for a typical validation process where minimal cloud cover and good sea state are optimal. However, these conditions are not sufficient to examine the full effects of instrumental distortion removal via deconvolution. In fact, such clear observing conditions are globally extremely rare. Any typical satellite scene with moderate cloud contamination would be expected to substantially benefit from instrumental deconvolution. As such, it would be expected that deconvolution would not have a large impact on imagery containing minimal contrast, such as the validation data so far analysed. This suggests that an alternative validation strategy should be investigated to comprehensively determine the accuracy and potential benefits of satellite image deconvolution.

5.3 QuickBird Southern Ocean

5.3.1 Method

A secondary validation was undertaken using a high-resolution QuickBird image of an Antarctic ice edge. QuickBird is a commercial Earth observing system launched

in 2001. It captures panchromatic imagery at 60cm resolution, and multispectral imagery at 2.4m resolution. An Antarctic ice edge QuickBird image was chosen due to its high contrast and large spatial extent compared to individual in-situ measurements. This will allow for the comparison of many MODIS data points and will provide a wider representation of the potential benefits of satellite image deconvolution. The QuickBird ice edge image used in this chapter was supplied by Dr. Petra Heil (pers. comm., March 13, 2013) and was captured at 4:27 AM UTC on 26/01/2011 with solar zenith and azimuth angles of approximately 52° and 58° respectively. The image ranges in latitude from -67.72° to -67.92° and longitude from 66.61° to 67.05° and contains 3 spectral bands, 1 for each of the blue, green and red bandpasses. Figure 5.9 shows a true-colour composite of the full extent of the QuickBird image.

The provided QuickBird image was a radiometrically corrected standard level 2 pan-sharpened data product which includes standard correction processing such as relative radiometric inter-detector response, non-responsive detector fill, and a conversion for absolute radiometry (DigitalGlobe, 2006). To make this imagery comparable to MODIS data, the QuickBird data must be converted to top-of-atmosphere spectral radiance using the following equation (Krause, 2005):

$$L(\lambda, pixel, band) = \frac{K(band) \cdot q(pixel, band)}{\Delta\lambda(band)} \tag{5.6}$$

where
$L(\lambda, pixel, band)$ = top-of-atmosphere spectral radiance image pixels ($Wm^{-2}sr^{-1}nm^{-1}$)
$K(band)$ = absolute radiometric calibration factor for a given band ($Wm^{-2}sr^{-1}count^{-1}$)
= $[0.01851735, 0.01364197, 0.01783568]$ RGB for the provided QuickBird image
$q(pixel, band)$ = radiometrically corrected detector data ($counts$)
$\Delta\lambda(band)$ = effective bandwidth for a given band (μm)
= $[0.0574, 0.0630, 0.0543]$ RGB for the provided QuickBird image

Figure 5.9: QuickBird RGB true-colour image featuring an Antarctic ice edge. Image provided by Dr. Petra Heil (ACE CRC and AAD).

After correction, the QuickBird data are now top-of-atmosphere radiance measurements, but their spectral band passes differ from MODIS and some adjustments must be made accordingly.

The closest matching MODIS Aqua overpass was captured at 9:45 AM UTC with solar zenith and azimuth angles of approximately 49° and 323° respectively. The QuickBird and MODIS capture time difference results in a small change in the solar zenith angle which is not likely to introduce significant discrepancies into the comparison. The MODIS overpass was deconvolved using the techniques developed in Chapter 4, and processed to level 2 calibrated top-of-atmosphere radiance using SeaDAS 6.4. The MODIS pixels were then located within the QuickBird scene. Initially, a small subset of the MODIS image that corresponds to the extent of the QuickBird image was retrieved by filtering all pixel coordinates not contained within this region. The latitude and longitude coordinates of the subset pixel locations are depicted with crosses in Figure 5.10. The pixel locations that lie closer to each other indicate overlapping MODIS measurements that are caused by the bow-tie effect of scanning-based remote sensing instruments.

An inspection of the MODIS data points at the locations depicted in Figure 5.10 revealed that all of the ice shelf pixels and many of the ice sheet pixels have values beyond the maximum recordable intensity of the MODIS Aqua sensors. This is due to the MODIS ocean colour bands having a precisely calibrated sensitivity and dynamic range that is optimised for water-based measurements. A pre-deconvolution correction technique was used to estimate the intensity of measurements that were truncated due to detector saturation, as discussed in Chapter 4. This allows the quantity of instrumental distortion to be more accurately defined and removed by the deconvolution algorithm. Even so, the only MODIS measurements that are appropriate for comparison are water pixels with values that lie within the dynamic range of the instrument. Therefore, all radiance measurements above the maximum intensity of the sensors are removed from the comparison for each spectral band.

MODIS Aqua captures measurements with an approximate spatial coverage of 1km × 1km at nadir, and this spatial coverage increases in both dimensions with the instrument scan angle. The MODIS instrument PSF receives more than 99% of the

Figure 5.10: Locations of MODIS Aqua data points depicted on top of the QuickBird area of interest subset.

recorded signal from a small circular region centred around the image point of the instrument. For these reasons, the spatial coverage of the MODIS measurements was estimated using appropriately dilated ellipses by taking into account the detector-based geometry (Nishihama et al., 1997). Figure 5.11 shows the spatial coverage of the final 21 MODIS measurements that are available for comparison in the blue-band. The ellipses indicate the area under which all QuickBird data points are averaged and the intensity of the filled ellipses show the values of the averaged QuickBird data points.

The provided QuickBird imagery contains singular spectrally-wide blue, green and red channels with centre wavelengths of 488nm, 543nm and 650nm respectively. In contrast, MODIS Aqua offers a range of much narrower channels (approximately 10nm bandwidths) of which 2 bands are located in each of the blue, green and red QuickBird channels. A spectral comparison of QuickBird and MODIS Aqua band passes, along with a typical rescaled blue seawater reflectance spectrum (Smith and Baker, 1981; Morel and Prieur, 1977), are displayed in Figure 5.12. Considering the spectral response of the MODIS bands in relation to the QuickBird channels and the target blue seawater spectrum, the MODIS bands must be combined in some way to produce single red, green and blue images for direct comparison with the QuickBird measurements. Appropriate spectral band weights must be calculated in order to determine the relative percentages in which to combine the MODIS bands for comparison. This is achieved by calculating Spectral Band Adjustment Factors (SBAFs) (Chander et al., 2013). The SBAF calculation involves integrating the spectral responses of the MODIS and QuickBird sensors with the spectral signature of the target at each sampled wavelength, weighted by the respective sensor. Each pair of blue, green and red MODIS SBAFs are normalised together to calculate unique band percentage compositions in which to combine the MODIS Aqua measurements. Having determined the percentage compositions of the MODIS

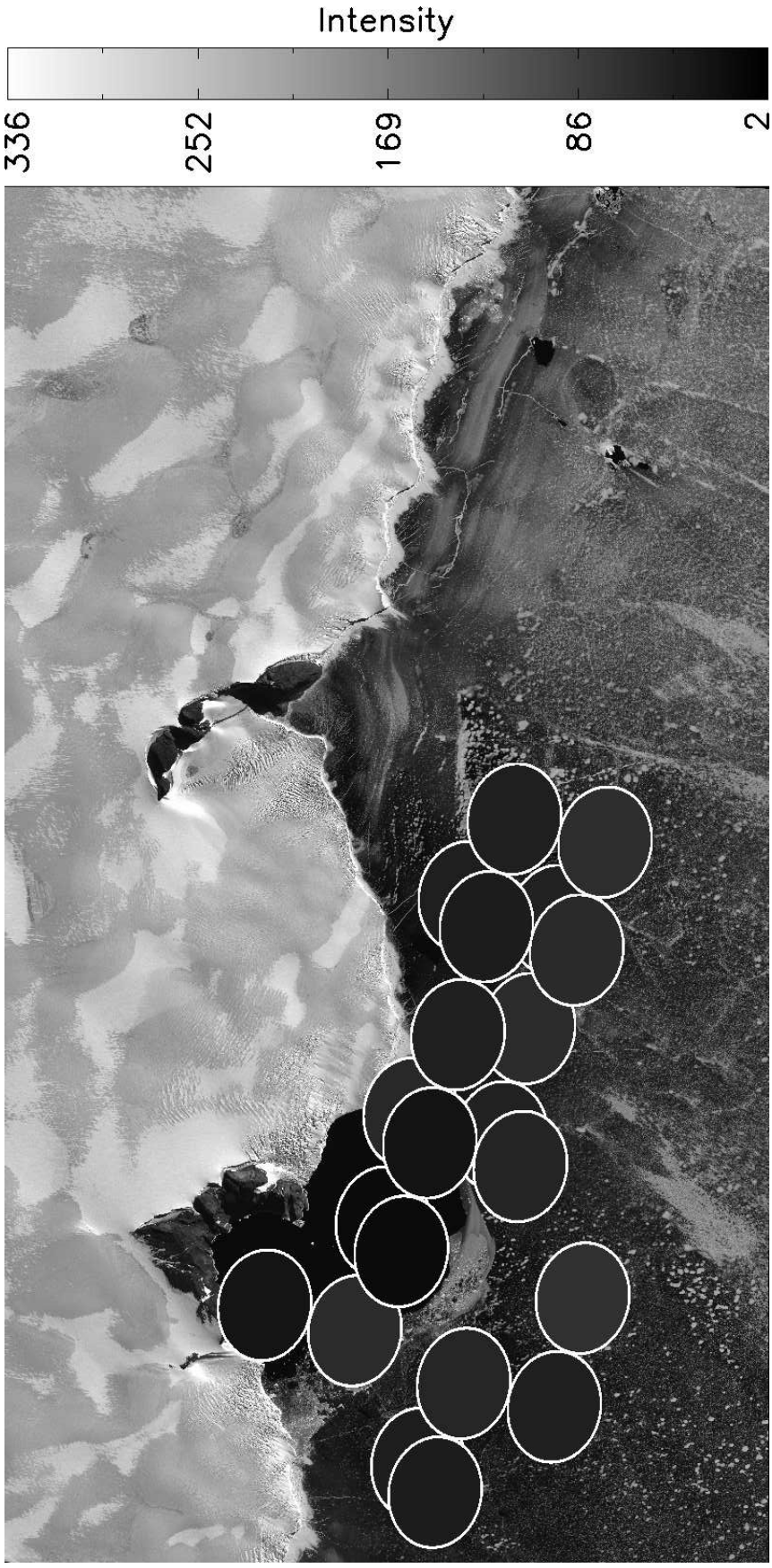

Figure 5.11: Locations and spatial coverage of the final MODIS Aqua pixels showing averaged QuickBird intensities depicted on top of the QuickBird area of interest for the blue-band.

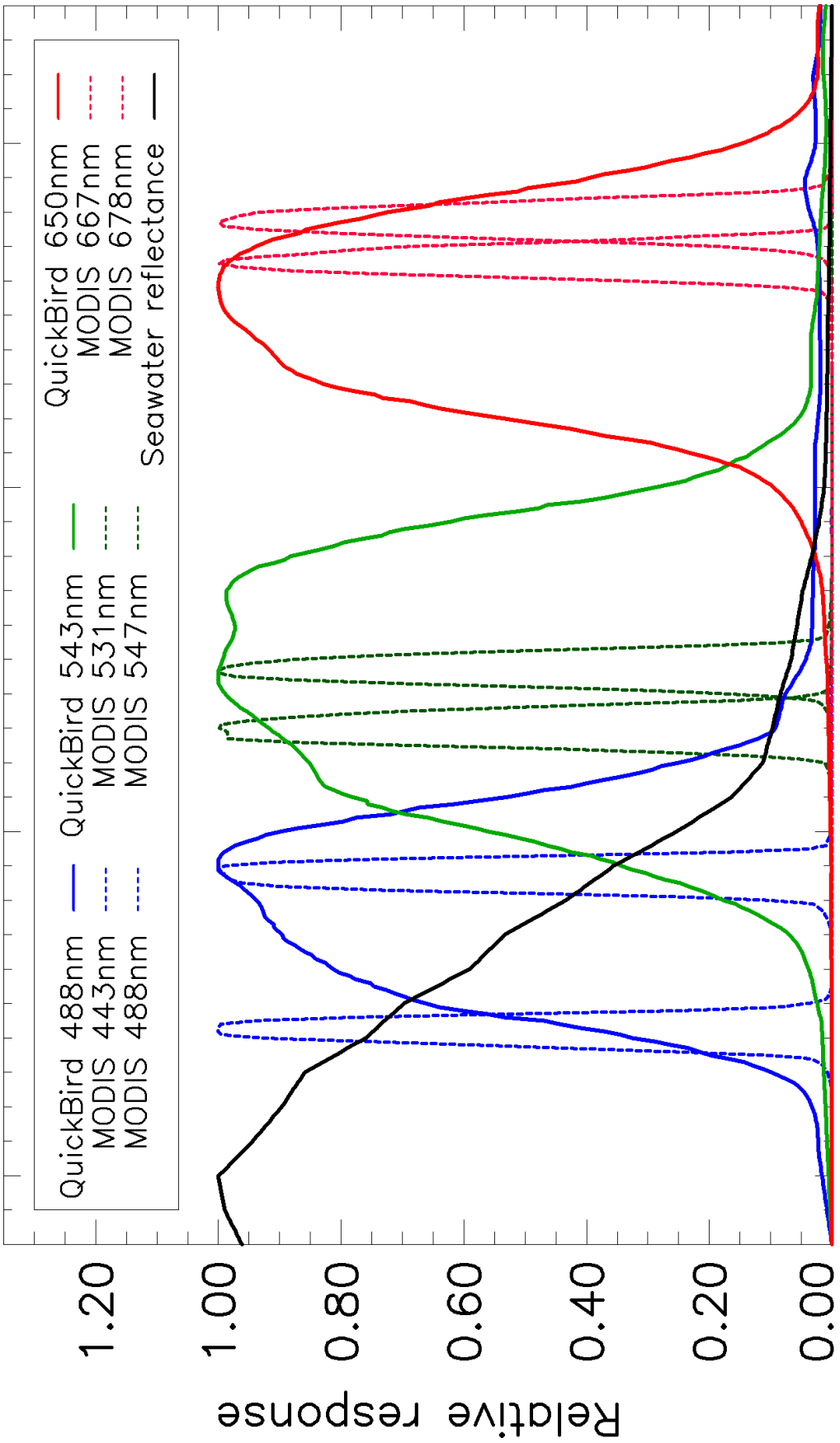

Figure 5.12: Relative spectral response of blue, green and red QuickBird channels and the 6 associated MODIS Aqua bands.

bands, the following operations were carried out to produce 3 MODIS Aqua images for direct comparison with the 3 QuickBird spectral measurements:

$$\text{MODIS}_{blue} = 0.67 \times \text{MODIS}(443nm) + 0.33 \times \text{MODIS}(488nm)$$
$$\text{MODIS}_{green} = 0.57 \times \text{MODIS}(531nm) + 0.43 \times \text{MODIS}(547nm)$$
$$\text{MODIS}_{red} = 0.54 \times \text{MODIS}(667nm) + 0.46 \times \text{MODIS}(678nm)$$

5.3.2 Results

Comparing MODIS Aqua calibrated top-of-atmosphere radiance measurements with high-resolution QuickBird imagery may help successfully validate the deconvolution process. Figure 5.13 shows the blue-wavelength down-sampled QuickBird measurements plotted against the filtered original and deconvolved MODIS Aqua data. As noted previously, many of the radiance values are beyond the sensitivity of the MODIS Aqua detectors and have therefore been removed, leaving 21 valid measurements in the blue-band comparison. Linear regression was applied to determine the line of best fit and a correlation coefficient has been calculated for each comparison. The linear regressions display reasonably similar slopes and intercepts, and their correlation coefficients suggest that the deconvolved data points are slightly more consistent with the QuickBird radiance measurements for the blue-wavelength comparison.

Equivalent comparisons are made for the green and red QuickBird channels in Figures 5.14 and 5.15. However, in both cases a significantly larger number of data points were removed due to detector intensity saturation, and only very few data points remain, especially in the red channel (Figure 5.15). With so few comparable data points, it becomes difficult to have confidence in the relationship between MODIS Aqua and QuickBird measurements. Also, comparing correlation coefficients to determine whether deconvolution is having a positive effect becomes unreliable. Therefore, nothing conclusive can be determined from the comparisons made for the green and red channels for this particular validation data.

Ultimately, the failure of comprehensively validating MODIS Aqua measurements

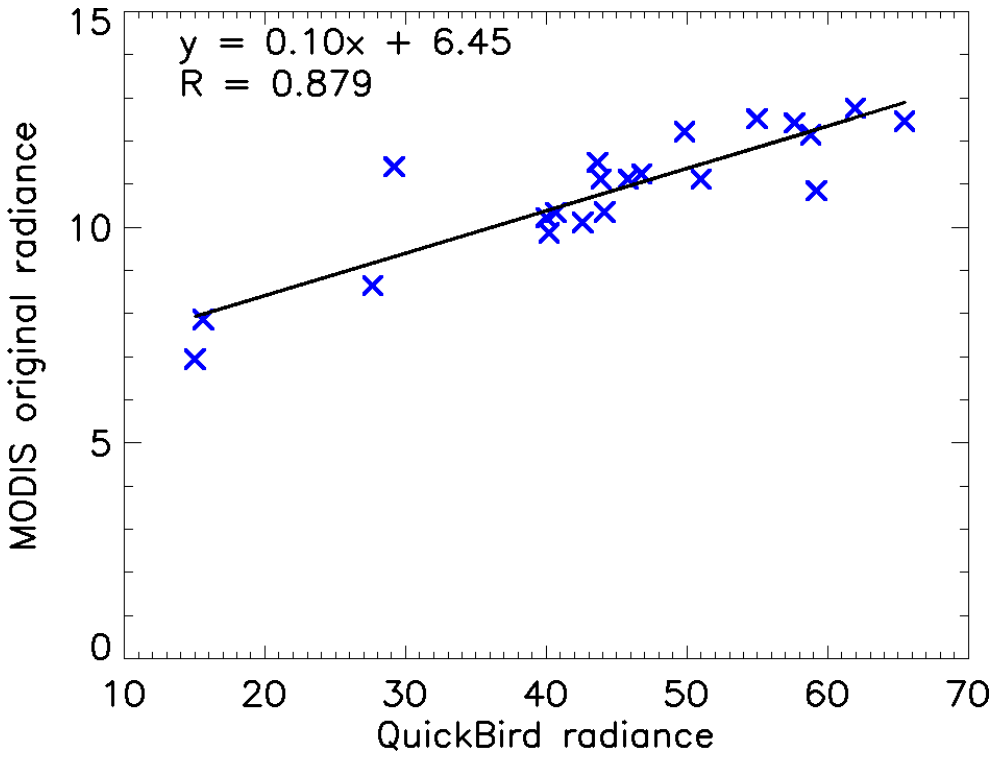

(a)

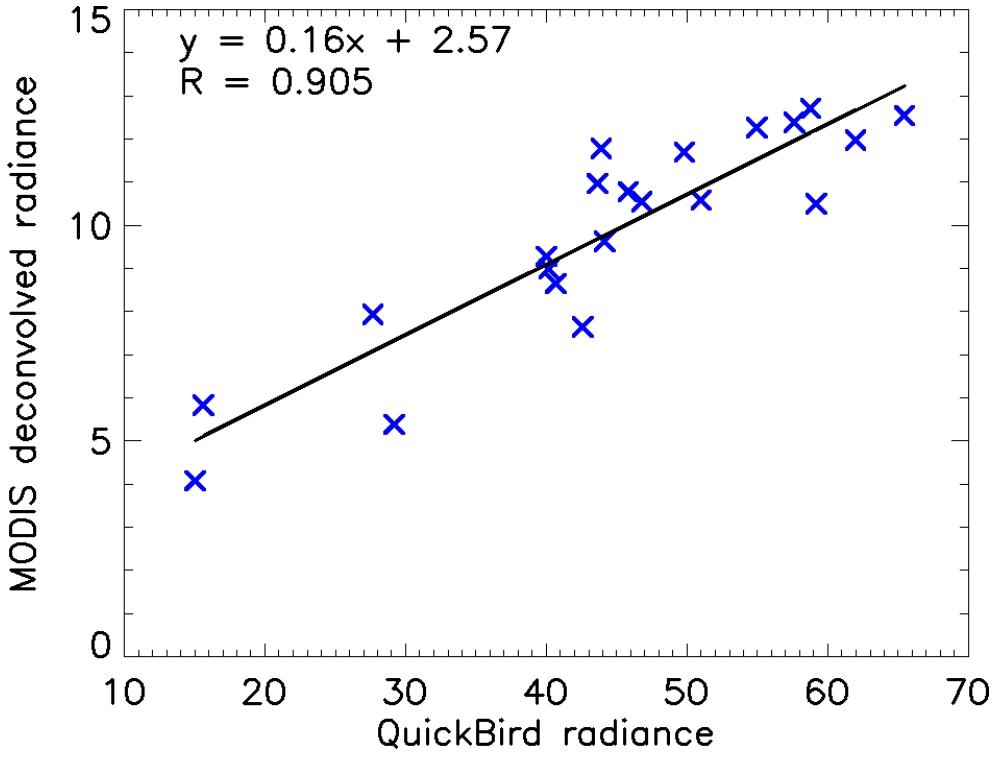

(b)

Figure 5.13: Comparison of MODIS Aqua original and deconvolved data points with down-sampled QuickBird measurements for the blue wavelengths. Linear regression is used to determine the line of best fit and the correlation coefficients indicate how well the linear fit describes the data points. A moderate number of comparable data points allows for confidence in a strong relationship between MODIS and QuickBird measurements.

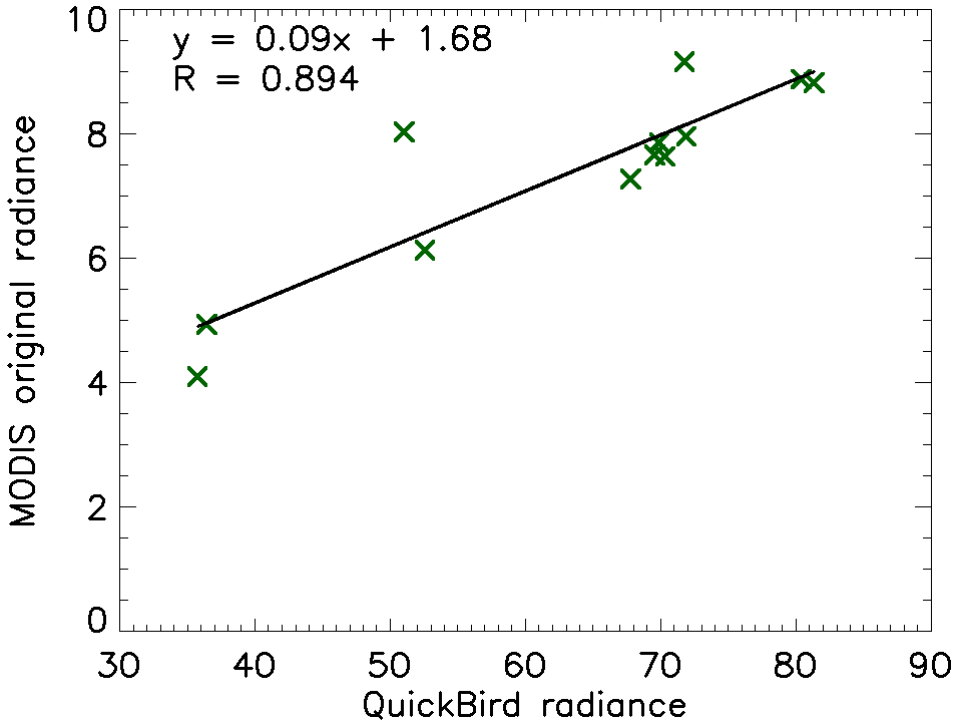

(a)

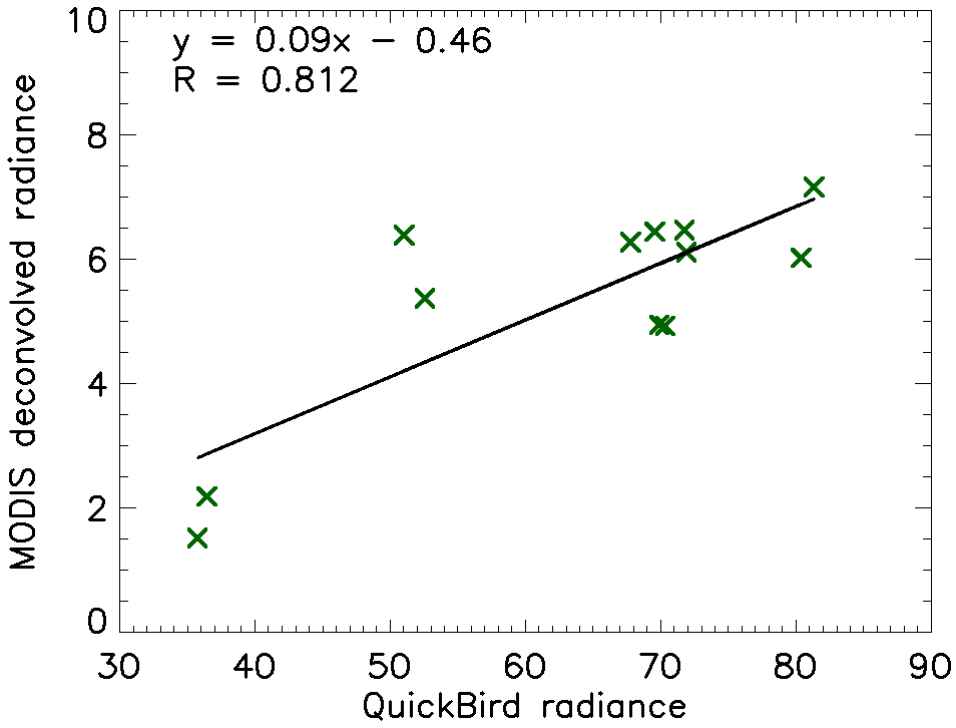

(b)

Figure 5.14: Comparison of MODIS Aqua original and deconvolved data points with down-sampled QuickBird measurements for the green wavelengths. Linear regression is used to determine the line of best fit and the correlation coefficients indicate how well the linear fit describes the data points. Few comparable data points reduce the confidence in a strong relationship between MODIS and QuickBird measurements.

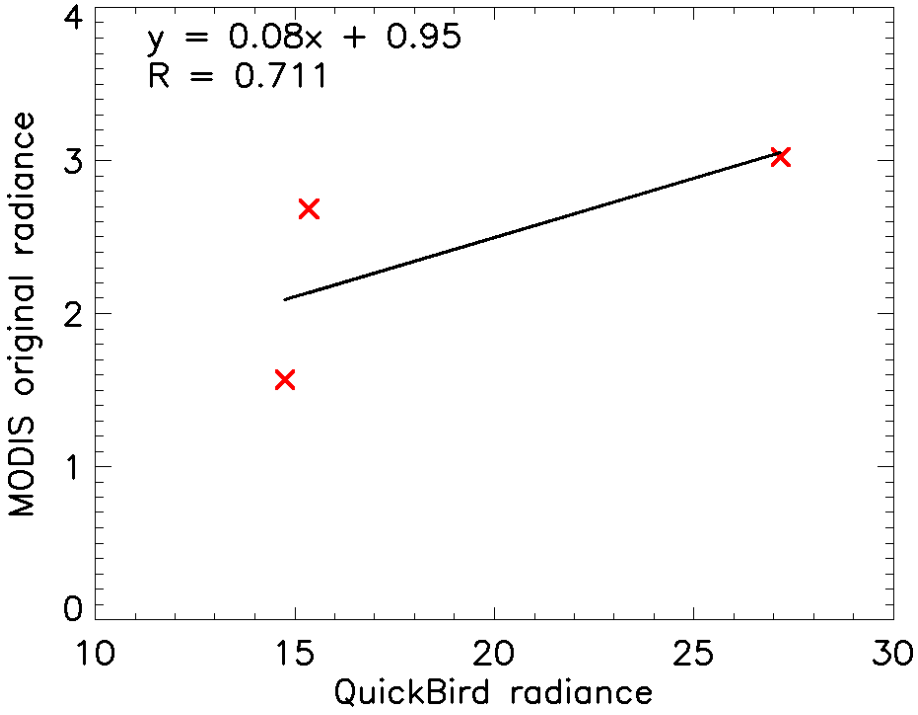

(a)

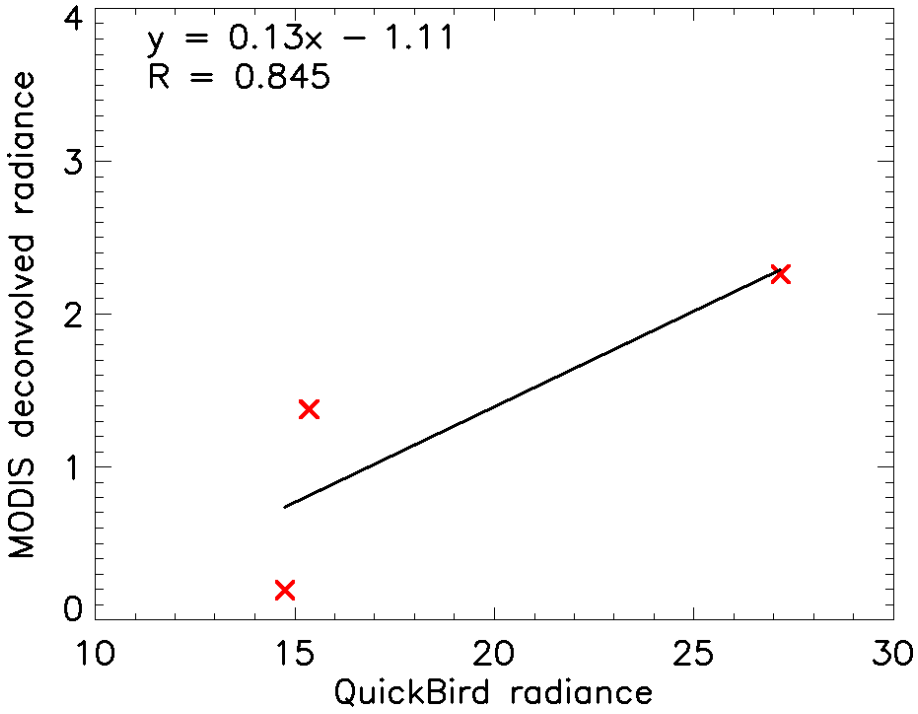

(b)

Figure 5.15: Comparison of MODIS Aqua original and deconvolved data points with down-sampled QuickBird measurements for the red wavelengths. Linear regression is used to determine the line of best fit and the correlation coefficients indicate how well the linear fit describes the data points. Very few comparable data points significantly reduce the confidence in a strong relationship between MODIS and QuickBird measurements.

using high-resolution QuickBird imagery is due to the selected scene not being ideal. Having previously determined that an in-situ validation process failed to comprehensively examine the full extent of deconvolution, it is logical to proceed with a validation technique that provides a much larger spatial coverage. For the purpose of validating a deconvolution technique, it is also logical to select a scene that contains high contrast, such as an Antarctic ice edge. However, the major downfall for the validation with the particular QuickBird scene used in this study is the lack of valid water measurements. Returning to Figure 5.9, there is only an area of approximately 3km $\times$ 3km of pure water signal uncontaminated by sheet ice. A scene that would be ideal for the purposes of validating a deconvolution method would need to contain a high-contrast feature, but also contain a large number of valid water measurements. In fact, an ice edge may indeed be contained in an ideal validation scene, but there must be many more water measurements available for comparison than in the image used for validation in this chapter.

5.4 Summary

The validation of Multiscale Entropy deconvolution of MODIS Aqua imagery was undertaken using an in-situ measurement approach and a coincident high-resolution QuickBird data comparison. The in-situ validation compared Baltic Sea reflectance, chlorophyll-a, total suspended matter and diffuse attenuation coefficient quantities against original and deconvolved MODIS Aqua data. From these products, the diffuse attenuation coefficient compared the best with a Mean Norm Bias (MNB) difference of approximately -9%, a Root Mean Square (RMS) difference of approximately 15% and a deconvolution improvement of 0.69%. Remote sensing reflectance was the next most successful comparison with approximate MNB and RMS average differences of -4% and 38% respectively and a small improvement of 0.47% from deconvolution. Chlorophyll-a and total suspended matter showed significantly larger match-up errors and appeared to have been affected by the naturally high concentrations of Coloured Dissolved Organic Matter (CDOM) in the Baltic Sea as well as extensive cyanobacterial blooms present during the sampling

period. While the atmospheric and sea state Baltic Sea sampling conditions were almost ideal for in-situ validation purposes, such low-contrast conditions do not illustrate the large potential impact of deconvolution.

The Multiscale Entropy deconvolution algorithm developed for MODIS Aqua in Chapter 4 has the most influence on high-contrast scenes that include highly reflective features such as clouds or ice, as well as low-reflectance features such as water. For this reason, a secondary validation effort was performed using a high-resolution QuickBird image featuring an Antarctic ice edge. After the appropriate calibration, product conversion and measurement location searches were performed, deconvolution was shown to slightly improve the MODIS Aqua blue wavelength measurements at 443 and 488nm. However, not enough measurements were available after valid pixel filtering to draw any strong conclusions about the green and red MODIS bands. This validation approach would greatly benefit from a more appropriate scene selection that includes significantly more valid and comparable water measurements in all frequency bands.

Two distinct research contributions were established throughout this chapter. A range of typical Baltic Sea reflectance spectra were used to constrain a high-order polynomial spectral fitting process. The development of this technique allowed in-situ samples to be directly compared with MODIS Aqua measurements and can be useful in situations where spectral measurements from different instruments do not match. A satellite measurement location mapping and coverage estimation method was developed to locate and extract comparative measurements from high-resolution QuickBird data. This technique was crucial in providing radiometric comparisons for the MODIS Aqua measurements and allows for different satellite sensors to be directly compared.

Chapter 6

Spatial Resolution Enhancement

6.1 Introduction

Digital imaging systems often aim to extract images of the highest quality from the instrumentation. One measure of image quality is image spatial resolution. Computational techniques that focus on enhancing the spatial resolution of imagery are commonly referred to as super-resolution, high-resolution image reconstruction, or simply resolution enhancement (Farsiu et al., 2004a; Park et al., 2003). Advances in these computational techniques can affect the quality of imagery without the need for costly instrumentation upgrades or replacements. Thus, resolution enhancement is generally considered to be a valuable computational technique and continues to be an extremely active research area.

Interpolation-based algorithms, such as nearest-neighbour, linear, cubic and b-spline interpolation, estimate sub-pixel information within imagery and can be considered the simplest form of resolution enhancement. These algorithms are common in the field of image processing, but tend to blur images to a severe degree (Park et al., 2003; Borman and Stevenson, 1998). This is a natural result for all interpolation methods because the interpolated data points are simply weighted averages of the surrounding data. For instance, consider doubling the size of an image in two dimensions using nearest-neighbour interpolation. The interpolated image has four times as many pixels as the original, but contains no more information than its lower-resolution original. Thus, the deterministic resolution of the image is not

affected by the change in pixel count. Much of the literature considers this property to be the image resolution, and therefore, in many circumstances deconvolution is referred to as increasing the resolution of data (Magain et al., 1998; Pijpers, 1999; Piles et al., 2009; Tao et al., 2006). However, there is great interest in increasing the spatial resolution of imagery through mechanisms that reconstruct high-frequency content and extract information that is unattainable using common interpolation-based approaches.

There are several more complicated approaches to achieve resolution enhancement, with the majority of the literature focusing on multi-frame super-resolution techniques (Park et al., 2003). This involves taking multiple, slightly offset images of the same target and combining them in such a configuration as to take advantage of the extra information contained in the difference between multiple frames. When combined correctly, this approach can produce a single higher-resolution image of the target. Many variations of multi-frame super-resolution have been shown to operate successfully and accurately (Capel and Zisserman, 2001; Irani and Peleg, 1991; Farsiu et al., 2004b). This is because the total amount of information about an object in multiple frames exceeds the amount of information contained within any single frame. The extra information obtained here comes from the sub-pixel misalignment present between multiple frames (Park et al., 2003). However, if there is too much or too little misalignment between consecutive images, then multi-frame super-resolution generally fails.

Multi-frame super-resolution techniques have been developed to achieve enhanced spatial resolution from a series of remotely sensed images (Merino and Nunez, 2007), and have also been directly applied to MODIS imagery (Shen et al., 2008). Both of these frameworks rely on images that are obtained from consecutive satellite passes over a time period of many days. Whilst multi-frame super-resolution techniques can be successfully applied to terrestrial satellite imagery, they prove to be impractical for ocean monitoring due to the comparatively rapid rate of change in marine environments.

An alternative approach to spatial resolution enhancement is to take a single image and apply specialised processing to retrieve the desired High-Resolution (HR)

image (Begin and Ferrie, 2004). These approaches are generally known as learning-based methods or dictionary leaning methods (Yang et al., 2008, 2010). For the application of ocean-based satellite imagery, there is great interest in techniques that achieve resolution enhancement from single images because, in most cases, multiple images of the same target are not available within a reasonable time frame. Learning-based resolution enhancement techniques attempt to reconstruct the unknown HR image using rules derived from a set of training prior (Freeman et al., 2000). In most cases, it is assumed that the PSF has been characterised and the training examples are generated using this known PSF. Learning-based algorithms will then typically undergo some validation testing that encompasses processing synthetically degraded images not included in the training data. This form of spatial resolution enhancement has seen rapid development and has achieved remarkable improvement in image quality at reasonable computational cost (Sun et al., 2003; Bishop et al., 2003; Wright and Huang, 2008). The major disadvantage of learning-based methods is that the accuracy of the algorithm relies directly on how well the input Low-Resolution (LR) image matches the training samples (Lin et al., 2008). Ocean-based remote sensing data can potentially contain an extremely large class of signals. Consequently, this approach would require an impractical quantity of training data where every possible pixel configuration is represented. This requirement effectively renders learning-based resolution enhancement approaches unsuitable for the application of ocean-based satellite imagery.

An alternate training strategy, known as image hallucination, has seen recent development and adds another constraint to which image resolution enhancement can be achieved (Sun et al., 2003; Liu et al., 2007). The idea is that some prior information about the image signal class is known, for example facial portraits, and a set of training priors is included to further constrain the resolution-enhanced solution. In this case, superior resolution-enhanced results can be achieved under consistent lighting conditions. However, this technique can only be applied to a single well-defined image class at any time. Again, this resolution enhancement approach would be ineffective for the application of ocean remote sensing due to its extremely large signal class size.

Another approach to single-frame resolution enhancement is to enhance the spatial resolution of an image within the deconvolution process (Zhang and Cham, 2008). This approach is categorised as a reconstruction-based method in which sub-pixel information is initially estimated using interpolation, and then iteratively adjusted until the resultant resolution-enhanced image complies with the applied constraints. Zhang and Cham (2008) developed a blind deconvolution algorithm under a Maximum *A Posteriori* (MAP) framework to achieve this form of spatial resolution enhancement and produced effective results. With the use of a Bayesian inferencing prior, the MAP framework induces a regularised version of the maximum likelihood solution for image deconvolution while the instrument PSF is solved simultaneously. The drawback with blind deconvolution techniques is that the instrument response function is often assumed to be Gaussian distributed. This results in an inferior deconvolution when applied to instruments that are not Gaussian distributed, due to the inaccurate reconstruction of the instrument PSF. In most cases, it is highly beneficial to use measured instrument response functions for deconvolution. Dorband and Hollis (1992) briefly described a similar technique for spatial resolution enhancement that involves a maximum entropy constraint. However, these single-frame inter-deconvolution techniques are not well documented and have not been followed up with significant published research.

This chapter focuses on a new approach to single-frame spatial resolution enhancement in which sub-pixel information is extracted from a HR PSF convolution process. The key to successful operation of this technique is to obtain HR PSF measurements at the same sampling frequency as the desired final output resolution.

6.2 Problem Formulation

When an optical system captures an image of a scene, the underlying instrument convolution process can be described by the following convolution equation:

$$I(x,y) = (O * P)(x,y) + N(x,y) \tag{6.1}$$

where I = intensity distribution (recorded image)
O = observed object (real image)
P = Point Spread Function (PSF)
N = Gaussian additive noise
and $*$ is the convolution operator

This equation relates the recorded image to: the image that exists before being rendered by the optical system (real image); the PSF which represents the inherent physical properties of the optical instrument; and the detector-based noise level of the optical system. This relationship is thoroughly examined in Chapters 2, 3 and 4. The reversal of this convolution process is achieved by applying a deconvolution technique, as discussed in detail in Chapters 2 and 4. This chapter develops a methodology for using information concerning how data is redistributed over a finite area during convolution to improve the spatial resolution of the recorded imagery. This is only possible because the instrumental convolution taking place in the satellite optical system is an analogue process. The difference between the representation of audio on vinyl records and compact discs provides a good analogy here. Vinyl records have audio waveform scratched into the surface of the record, resulting in a resolution and frequency that is limited only by the waveform inscription quality. Alternatively, compact discs represent audio as a binary digital sampling of the original waveform which significantly limits the resolution and frequency of the waveform. Thus, there is considerably more information in a vinyl record than a digital compact disc. Similarly, digital convolution is performed with discrete signals and has a specific resolution, whereas the natural convolution process occurring in the optical system does not have the same imposed limitation. Natural convolution can be considered to occur at an extremely high resolution, limited only by the frequency of light passing through the instrument and the atomic precision of the optical system. This implies that the natural instrument PSF responsible for the convolution process is effectively a continuous signal, and the natural convolution

process itself is an operation involving continuous signals. Therefore, there is an opportunity to extract information from signals that have undergone a natural convolution process, simply because this process occurs at a spatial resolution much greater than the discrete objects recorded by the imaging system. However, this is only possible if the instrument PSF is sampled at the desired final resolution-enhanced sampling frequency, which allows the redistributed HR signal intensities to be accurately modelled.

To formalise the problem using a small example, the original recorded image, I, is defined as a 5×5 pixel array (Figure 6.1(a)) and a Resolution Enhancement Factor (REF) of 2 in both dimensions will be used for simplicity. Suppose at the original LR, a deconvolution technique is applied using I, P and N to retrieve O (Chapter 4). Now, let $\uparrow O$ be initially defined as a HR nearest-neighbour interpolation of O at twice its resolution in both dimensions, making a 10×10 pixel array (Figure 6.1(b)), and $\uparrow P$ be a HR PSF sampled at the same frequency as $\uparrow O$ (Figure 6.1(c)). $\uparrow I$ can be constructed from the original recorded data, I, also using nearest-neighbour interpolation, so now I, P, O, $\uparrow I$, $\uparrow P$ and a starting point for $\uparrow O$ have all been defined. The bold grid in Figure 6.1(b) represents the spatial coverage of single data points in I (Figure 6.1(a)) and the faint grid represents the new HR data points in $\uparrow O$. The use of nearest-neighbour interpolation implies that every HR pixel in each four pixel group of $\uparrow O$ contains the same value as the corresponding single pixel in O.

Consider how an individual point convolution is performed at the higher resolution with respect to its equivalent lower-resolution operation. A single point convolution now becomes the composite of four distinct point convolutions where $\uparrow P$ is centred on each pixel in every HR upscaled group of four pixels (Figure 6.2). Figures 6.2(a), 6.2(b), 6.2(c) and 6.2(d) show four point convolutions at HR that make up the equivalent lower-resolution single point convolution and Figure 6.2(e) depicts the composite convolution attained by spatially combining the previous four single point convolutions.

This concept of a HR composite convolution is further described in Figure 6.3 where each subfigure has been reformed into one dimension. Figures 6.3(a), 6.3(b),

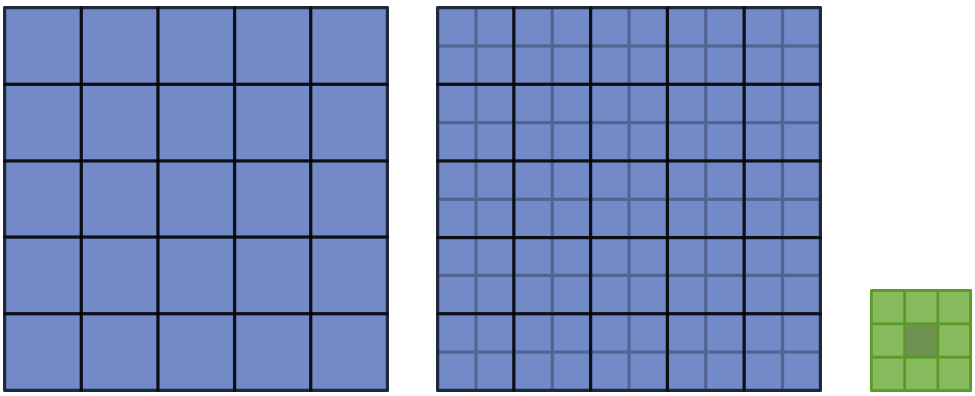

Figure 6.1: Two-dimensional representations of (a) the original recorded image I (5×5), (b) the nearest-neighbour interpolation of O (5×5) producing $\uparrow O$ (10×10), and (c) a high-resolution point spread function (3×3) sampled at the same frequency as $\uparrow O$.

6.3(c) and 6.3(d) directly correspond to Figures 6.2(a), 6.2(b), 6.2(c) and 6.2(d) respectively. Only the overlapping points of $\uparrow O$ and $\uparrow P$ are considered in the reformation and the data points that do not overlap are discarded. When $\uparrow P$ does not completely overlap with $\uparrow O$, the truncated $\uparrow P$ points will result in a loss of power caused by discarding some elements and the remainder of $\uparrow P$ not being normalised. In fact, combining the four individual point convolutions in Figures 6.2(a), 6.2(b), 6.2(c) and 6.2(d) into a single HR composite convolution, $\uparrow P_c$, will most likely result in an un-normalised composite convolution function. Therefore, as with the convolution technique developed in Chapter 3, it is important to renormalise the HR composite convolution function to 1.0. In this way, image power will be conserved and any potential boundary effects will be minimised. Figure 6.3(e) shows how the four point convolutions are combined spatially to form a single composite convolution function, equivalent to the two-dimensional representation in Figure 6.2(e).

When the composite convolution operation is performed, information contained in the overlapping region will be redistributed according to the distribution of $\uparrow P_c$. That is, every overlapped pixel in $\uparrow O$ will have some of its information encoded into the upscaled group of four convolved pixels during the convolution process. In this example, a small 3×3 PSF is used for simplicity, but typically the PSF will have a significantly larger extent. This would result in a much larger number of

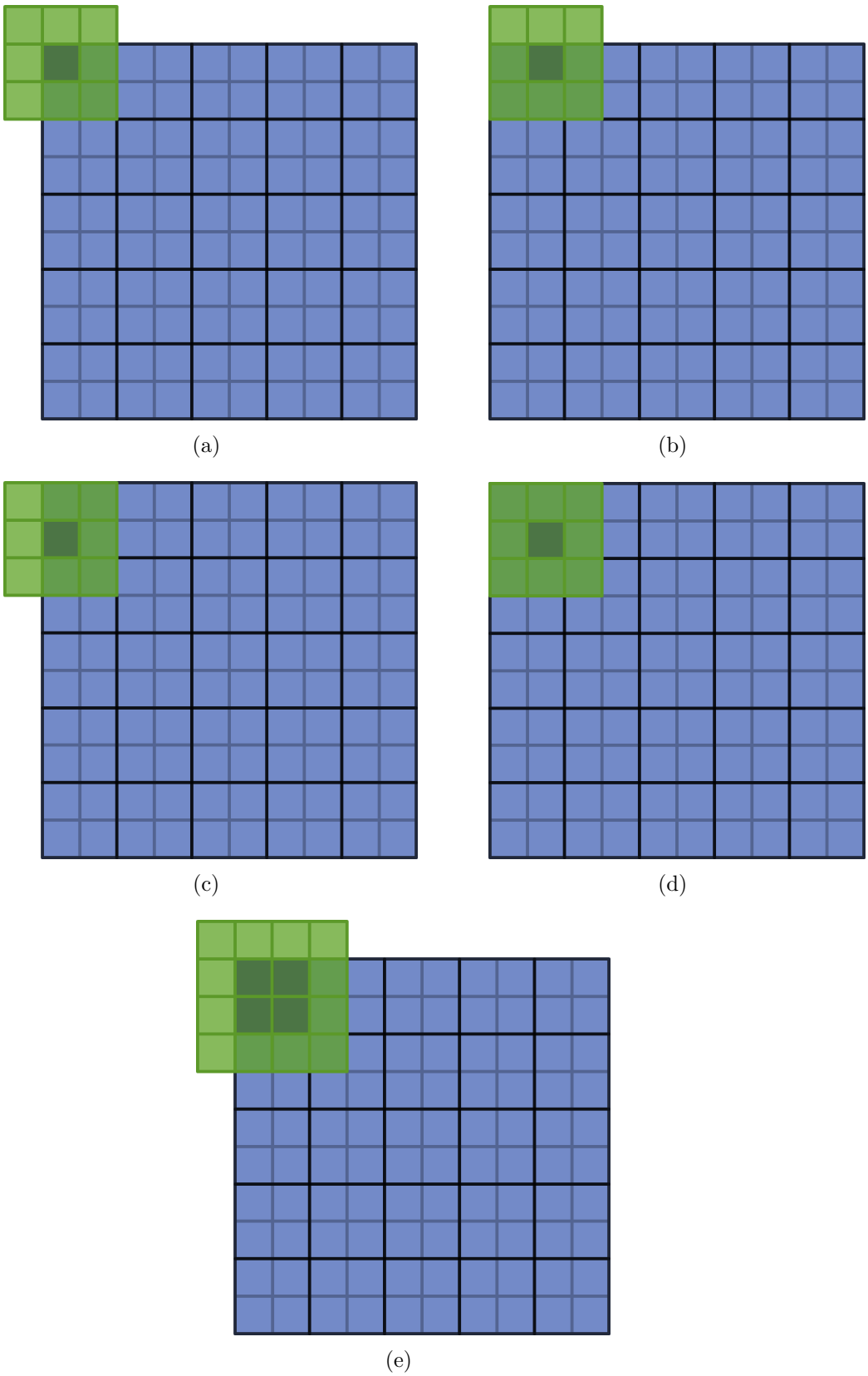

Figure 6.2: Two-dimensional representations of (a), (b), (c) and (d) the four point convolutions at high resolution that make up the equivalent single lower-resolution point convolution and (e) the composite convolution achieved by spatially combining the four individual point convolutions in (a), (b), (c) and (d). The dark pixels in $\uparrow P$ indicate the central peak of the point spread function.

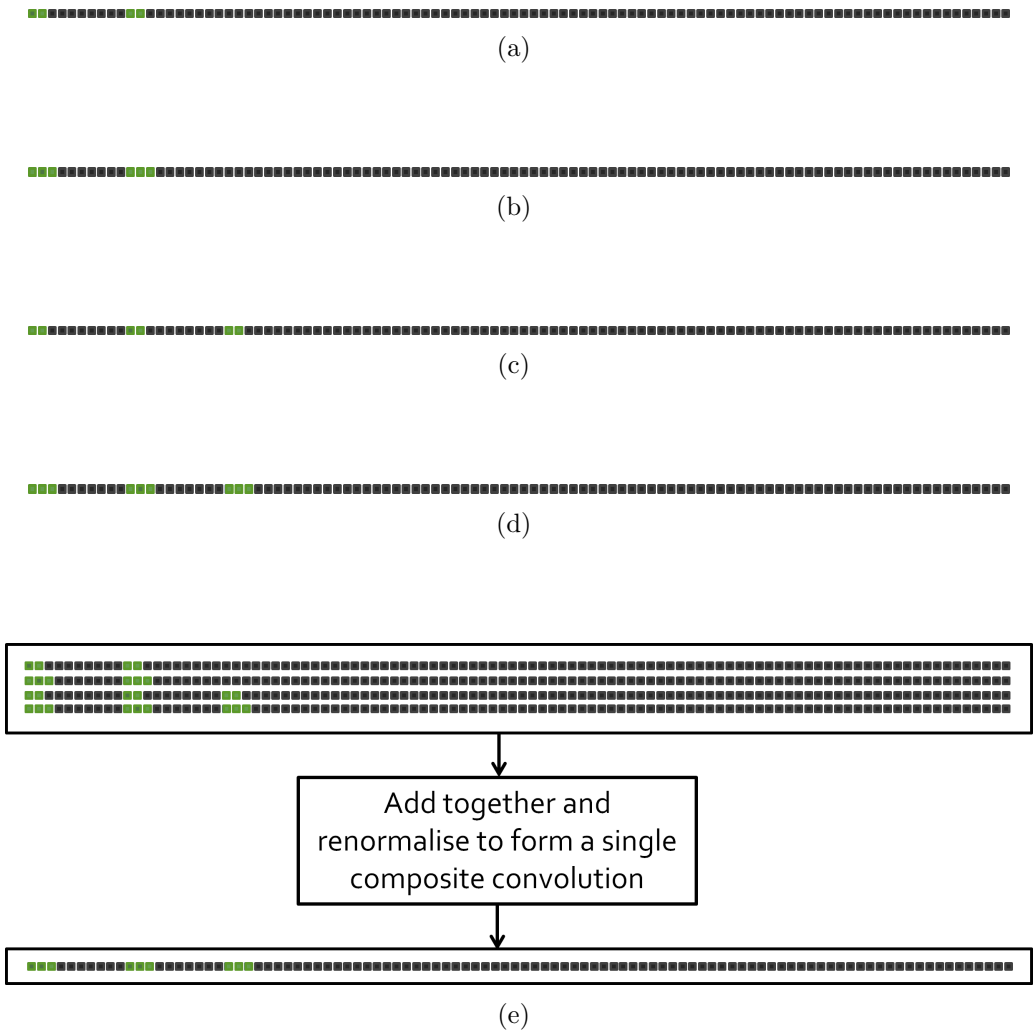

Figure 6.3: One-dimensional representations of (a), (b), (c) and (d) the four point convolutions including only overlapping data points in $\uparrow O$ and (e) the composite convolution achieved by spatially combining and renormalising the four individual point convolutions. Dark data points indicate areas with no overlap, resulting in values of zero. Light data points represent overlapping areas with non-zero values and dark-centred light data points indicate the position where the individual convolution functions, and in turn, composite convolution function are centred.

pixel overlaps occurring and therefore the information encoded at convolution will be significantly increased.

Now, consider the entire convolution of $\uparrow O$ with $\uparrow P_c$. For every HR group of four pixels, an equation can be constructed that relates the recorded data values in $\uparrow I$ to the surrounding pixels in $\uparrow O$ using the HR PSF $\uparrow P_c$. The number of constraint elements for each equation is determined by how many HR pixel overlaps occur, which in turn is determined by the size of $\uparrow P$. The result of each equation is equal to the corresponding value in the original convolved data I (Equation 6.1). This process can be formulated as a system of linear equations:

$$Ax = b \tag{6.2}$$

where A = matrix $(M \times N)$ with each row containing HR composite convolution modelling reformed into one dimension in row major order

x = column vector (M) representing every HR data point in row major order

b = column vector (N) containing the resultant composite convolution values (I) in row major order

The construction of this system of linear equations is depicted in stages in Figures 6.4 and 6.5. Figure 6.4 spatially describes the entire convolution of $\uparrow O$ with $\uparrow P_c$. Figures 6.4(a), 6.4(b), 6.4(c), 6.4(d) and 6.4(e) show the first 5 individual convolutions with the HR composite convolution function. Figures 6.4(f), 6.4(g), 6.4(h) and 6.4(i) depict the remainder of the complete convolution of $\uparrow O$ with $\uparrow P_c$ where 5 individual HR composite convolutions for each upscaled row have been combined for illustrative purposes. Figure 6.5 shows how the linear system is constructed in stages by taking the HR spatial composite convolutions in Figure 6.4, discarding any non-overlapping data points and reforming into one dimension. Figure 6.5(a) shows the first 5 composite point convolutions depicted in Figures 6.4(a), 6.4(b), 6.4(c), 6.4(d) and 6.4(e). Figures 6.5(b), 6.5(c), 6.5(d) and 6.5(e) show the remainder of the complete convolution previously illustrated in Figures 6.4(f),

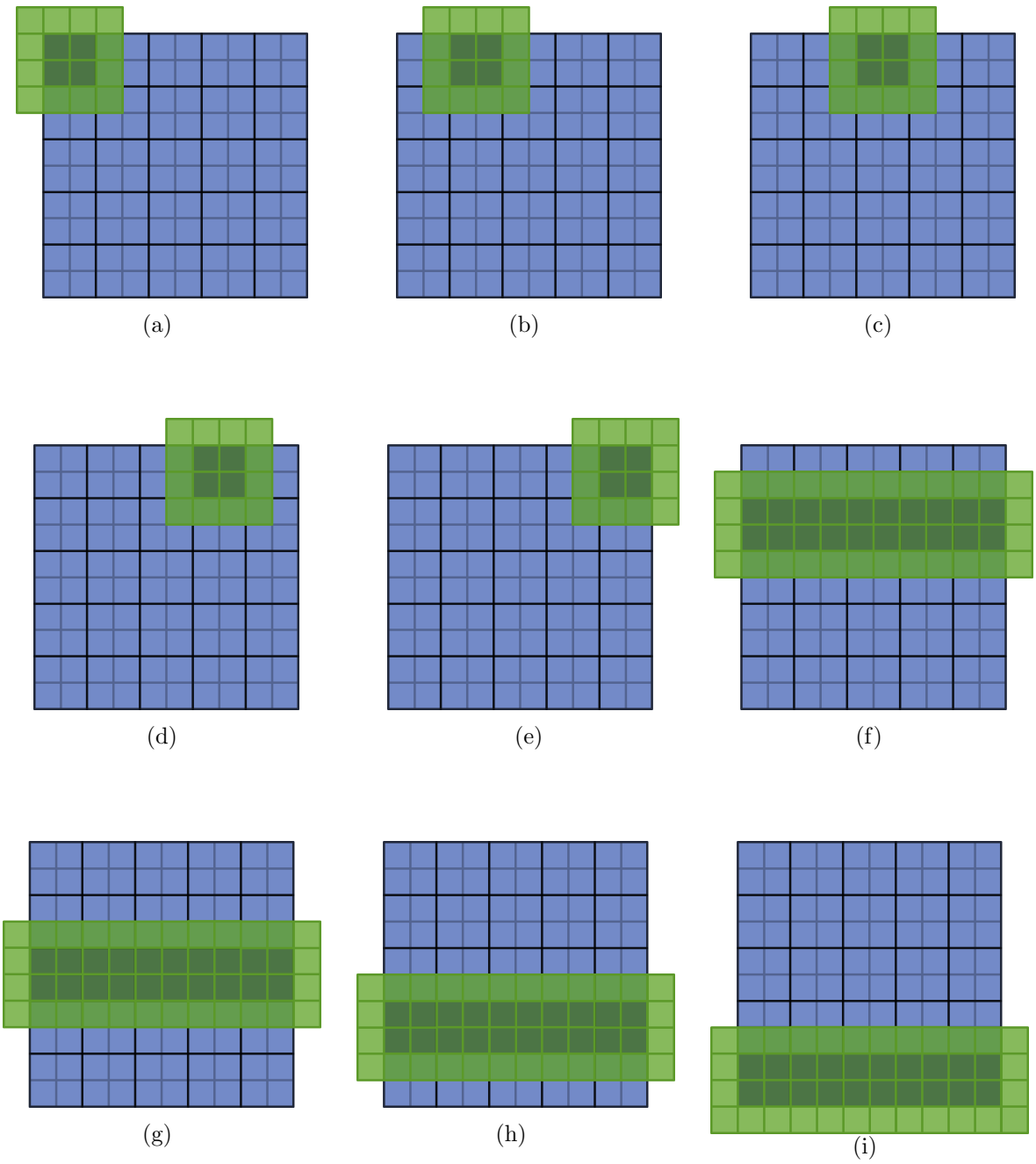

Figure 6.4: Two-dimensional representations of the complete convolution of $\uparrow O$ with $\uparrow P_c$ showing (a), (b), (c), (d) and (e) composite individual high-resolution point convolutions and (f), (g), (h) and (i) five combined composite individual high-resolution point convolutions. Figures (a), (b), (c), (d) and (e) relate directly to Figure 6.5(a) and Figures (f), (g), (h) and (i) relate directly to Figures 6.5(b), 6.5(c), 6.5(d) and 6.5(e) respectively. The dark points in $\uparrow P_c$ indicate the central peak of the composite convolution function.

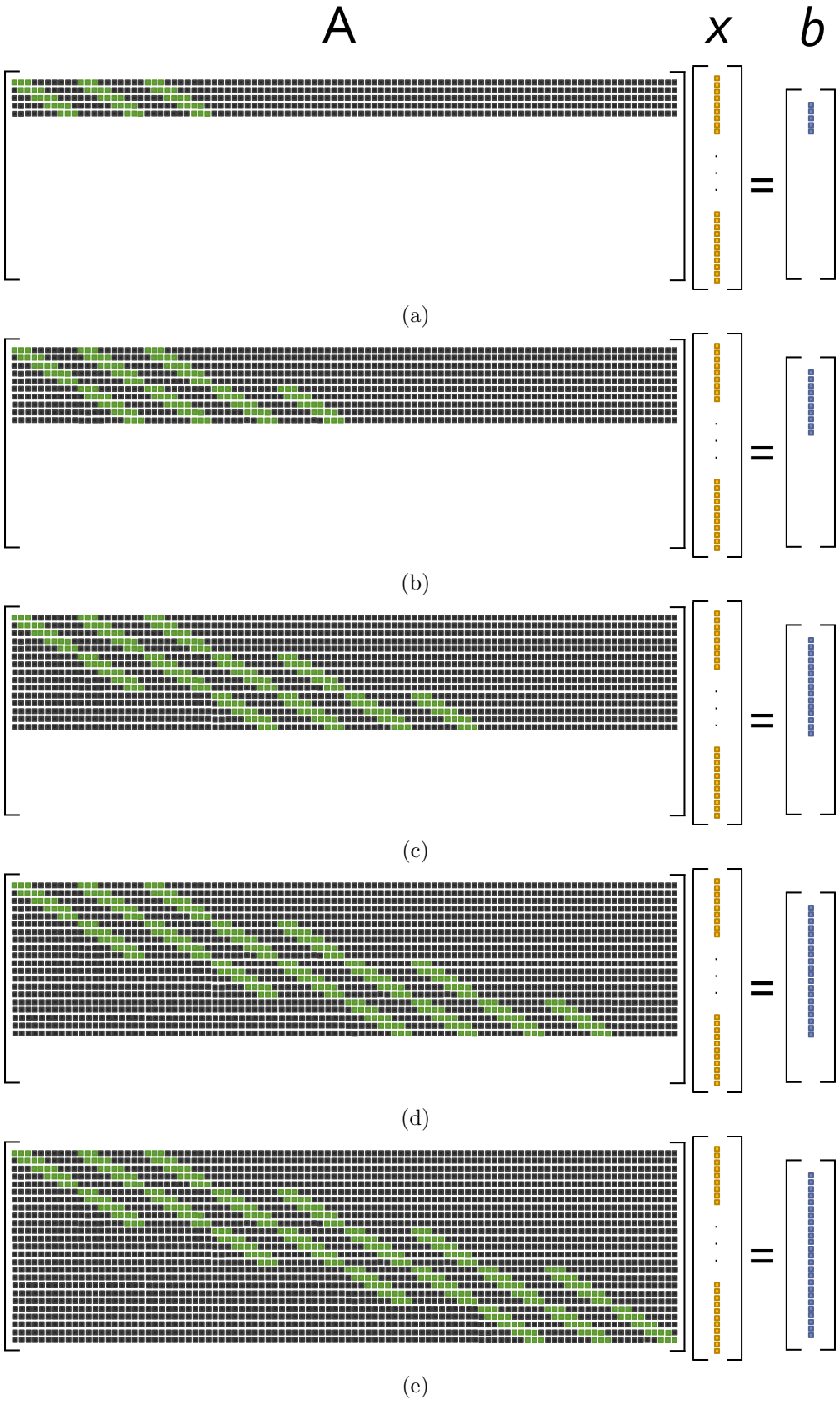

Figure 6.5: One-dimensional representation of the cumulative construction of the linear system with (a) corresponding to Figures 6.4(a), 6.4(b), 6.4(c), 6.4(d) and 6.4(e), and (b), (c), (d) and (e) corresponding to Figures 6.4(f), 6.4(g), 6.4(h) and 6.4(i) respectively. Dark points represent elements with value zero and light points represent elements with non-zero values.

6.4(g), 6.4(h) and 6.4(i). The one-dimensional response of the HR PSF modelling results in a diagonal pattern in the linear system (Figure 6.5(e)). This pattern of non-zero elements becomes more widespread as the instrument PSF size increases. If the input imagery is significantly larger than the instrument PSF, then the linear system will be sparse and predominantly contain elements of zero value.

These equations represent the HR PSF modelling component of the linear system. However, a power-conserving constraint can also be useful to limit intensity variability of any individual HR data point in every group of four pixels. This is achieved by adding a single equation for every upscaled group of four pixels. At the lower resolution, a single pixel of information represents the average radiance value reflecting from a specific area on the surface of the Earth and striking the detector. If one lower-resolution data point is to become four higher-resolution data points after resolution enhancement, each higher-resolution data point should contain a unique value while still conforming to the average radiance value at the lower resolution. From the perspective of energy conservation, the average of the four higher-resolution data points should be equal to its single lower-resolution counterpart. Therefore, a single equation can be constructed that relates each of the four pixels in every HR group, weighted evenly with a value of $\frac{1}{\text{REF}^2}$, to its result, being the original deconvolved data O. Figure 6.6 depicts the complete linear system with the bottom half of the A matrix representing the power-conserving constraint. Each of the non-zero elements in the power-conserving component of A contain the static value of 0.25 for the example involving a REF of 2. The results of these equations are represented in the bottom half of the b vector and contain values from the original deconvolved data O reformed into one dimension in row major order. The addition of a power-conserving constraint restricts the resolution-enhanced solution so that it conforms to the LR deconvolution result while also maintaining enough freedom to deliver high-frequency content to the final resolution-enhanced solution.

This particular linear system has twice as many unknown data values to be reconstructed (M) as it has equations (N) and is therefore underdetermined. More generally, the number of unknown data values (M) is equal to the REF multiplied by the number of constraint equations (N). This implies that the A matrix has a

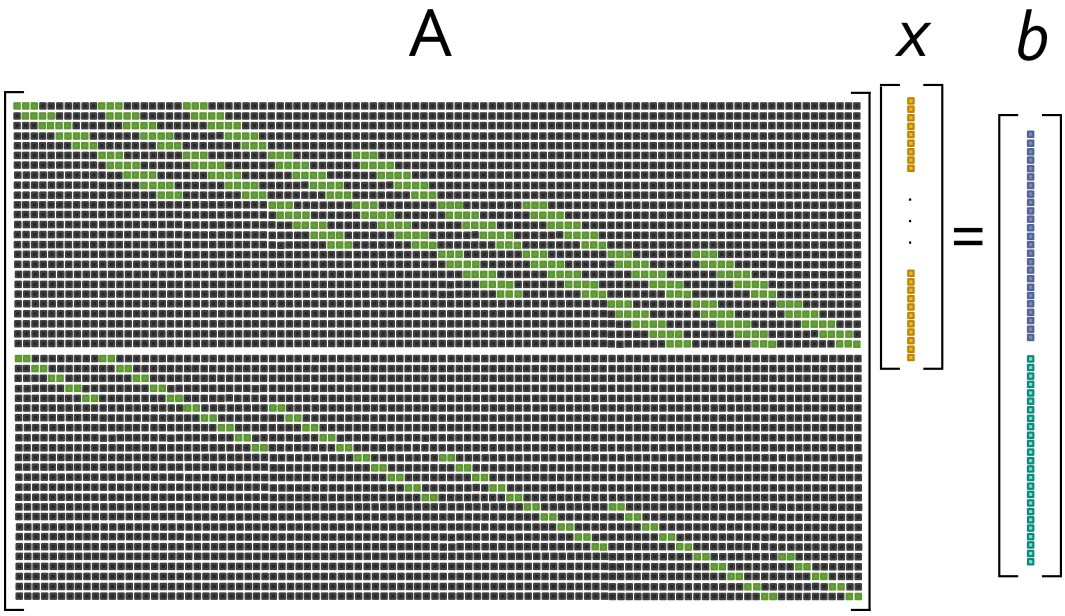

Figure 6.6: One-dimensional representation of the complete linear system including a power-conserving constraint. Dark points represent elements with value zero and light points represent elements with non-zero values.

large condition number and the overall problem is ill-conditioned. From this system of equations, a resolution-enhanced solution can be found by selecting the optimal configuration of pixels that would result in the individual pixel values changing by the quantities observed in the LR deconvolution process (Equation 6.1). However, appropriate regularisation constraints must be applied to the linear system in order to retrieve such a result.

6.3 Linear System Regularisation

The constructed linear system is designed to combine all of the available information about the original LR convolved and deconvolved signals, as well as the HR PSF distribution. Further regularisation constraints are required to determine a unique and stable solution to the ill-posed linear system. Multiscale Entropy regularisation is chosen for its ability to maximise information content, mitigate instrumental detector-based noise and select maximally unbiased solutions (Pantin and Starck, 1996; Starck, 1995). However, the standard Multiscale Entropy algorithm used for deconvolution requires appropriate customisation to allow the fundamental physical

intricacies between resolution levels to be managed. The original Multiscale Entropy method is defined for deconvolution as:

$$S_{\text{ms}}(O) = \frac{1}{\sigma_I} \sum_{j=0}^{n} \sum_{\text{pixels}} (1 - M(j,x,y)) \sigma_j (w_j(x,y) - m_j - |w_j(x,y)| \ln \frac{|w_j(x,y)|}{m_j}) \tag{6.3}$$

where

$$\begin{aligned} S_{\text{ms}}(O) &= \text{Multiscale Entropy on image } O \\ \sigma_I &= \text{standard deviation of noise in image } I \\ 1 - M(j,x,y) &= \text{complement of Multiresolution Support} \\ \sigma_j &= \text{standard deviation of noise at scale } j \\ w_j(x,y) &= \text{Wavelet coefficients at scale } j \\ m_j &= \text{background model at scale } j \\ &= \tfrac{\sigma_j}{100} \end{aligned}$$

Multiscale Entropy is designed to decompose the input signal into a succession of different resolution levels that represent different signal frequency ranges. Calculations are then performed on the decomposition, including an entropy metric, and this approach has proven remarkably successful for image deconvolution. Spatial resolution enhancement requires some fundamentally different outcomes, while still retaining the underlying Multiscale Entropy approach. Therefore, it is necessary to modify Multiscale Entropy in a few distinct ways. This new version of entropy will be termed MultiResolution Entropy (MRE) and the overall resolution enhancement approach will be termed Maximum Entropy Resolution Enhancement (MERE).

Firstly, the complement of Multiresolution Support is designed to apply regularisation to areas in the image that do not contain significant signals, as specified by its Wavelet decomposition. This is done because any areas in the image that are void of significant signals are assumed to contain only noise, and it is therefore appropriate to apply regularisation and smoothing to these areas. However, when enhancing spatial resolution, the most important areas to reconstruct are areas that contain large signals. This is where the greatest quantity of high-frequency information is under-represented and restoration is most important. For this reason,

the complement of Multiresolution Support can simply be replaced with the standard Multiresolution Support term, $M(j,x,y)$. This alteration has a significant impact on the MRE calculation and results in the regularisation favourably concentrating on high-frequency content. The MRE quantity, S_{mr}, now becomes:

$$S_{\text{mr}}(O) = \frac{1}{\sigma_I} \sum_{j=0}^{n} \sum_{\text{pixels}} M(j,x,y)\sigma_j(w_j(x,y) - m_j - |w_j(x,y)| \ln \frac{|w_j(x,y)|}{m_j}) \quad (6.4)$$

A cost function requiring minimisation can be defined to retrieve a unique and stable solution to the linear system:

$$F(x) = ||Ax - b||^2 + \lambda^2 S_{\text{mr}}(x) \quad (6.5)$$

where	$F(x)$	=	cost function
	$\|\|.\|\|$	=	Euclidean norm
	λ	=	regularisation parameter
	$S_{\text{mr}}(x)$	=	Multiresolution Entropy reformed into one dimension in row-major order

This cost function is similar to the approach taken for deconvolution in Chapter 4. The $||Ax - b||^2$ component is the Euclidean distance from the statistically ideal solution and is often called the data fit, or data fidelity term. This is a standard approach known as ordinary least squares. It aims to minimise the residuals, but is incapable of independently finding a stable solution because the problem is underdetermined. $S_{\text{mr}}(x)$ is traditionally the regularisation component that smooths the solution. However, this has been replaced with an entropy method designed to reconstruct high-frequency content for the application of spatial resolution enhancement. The regularisation parameter λ manages the balance between data fit and high-frequency reconstruction. Only by combining the data fit approach with some form of regularisation can a valid and stable solution be found for the linear system. Actively solving the linear system requires the minimisation of the cost function (Equation 6.5) using a gradient method. Therefore, it is necessary to

calculate the cost function derivative at each iteration of the gradient method:

$$\begin{aligned}\nabla F(x) &= \nabla||Ax-b||^2 + \lambda^2 \nabla S_{\text{mr}}(x) \\ &= 2A^T(Ax-b) + \lambda^2 \frac{1}{\sigma_I} \sum_{\text{scalesj}} [M(j)\sigma_j sgn(w_j^{(O)}) \ln(\frac{|w_j^{(O)}|}{m_j})] * \psi_j^T \end{aligned} \tag{6.6}$$

$$\begin{aligned} \text{where} \quad sgn() &= \text{signum function} \\ \psi_j &= \text{Wavelet function at scale j} \\ &= \tfrac{1}{2^j}\psi(\tfrac{x}{2^j}, \tfrac{y}{2^j}) \end{aligned}$$

Multiscale Entropy, and in turn MRE, is designed to operate on two-dimensional imagery. This is due to the Wavelet decomposition process extracting the spatial structure contained within the input imagery, and using this information to guide the reconstruction. Building the system of linear equations requires the two-dimensional imagery to be reformed into one dimension. However, retrieving an appropriate solution to the linear system requires the calculation of the MRE derivative in two-dimensional space, as defined in Equation 6.6. Therefore, within each gradient descent iteration it is necessary to temporarily reform x into two dimensions, calculate $\nabla S_{\text{mr}}(x, y)$, and then reform the result back into one dimension to continue the reconstruction.

Within the calculation of the gradient function (Equation 6.6), it is also important to match the Wavelet function, ψ, to the task of resolution enhancement. In deconvolution methods, the Wavelet function is typically the B3 filter:

$$\psi_{B3} = \begin{bmatrix} \frac{1}{16} & \frac{1}{4} & \frac{3}{8} & \frac{1}{4} & \frac{1}{16} \end{bmatrix} \tag{6.7}$$

The B3 filter is often chosen because it is reasonably smooth and well suited for isolating large image structures, which has historically been a major problem for deconvolution methods. However, for the purpose of spatial resolution enhancement, it is more appropriate to select a Wavelet filter that scales more evenly and can target

smaller scale features more precisely, such as the linear interpolation filter:

$$\psi = \begin{bmatrix} \frac{1}{4} & \frac{1}{2} & \frac{1}{4} \end{bmatrix} \tag{6.8}$$

This is extended into two dimensions by convolving the filter with the transpose of itself, producing the two-dimensional, first-level convolution mask:

$$\psi_1 = \begin{bmatrix} \frac{1}{16} & \frac{1}{8} & \frac{1}{16} \\ \frac{1}{8} & \frac{1}{4} & \frac{1}{8} \\ \frac{1}{16} & \frac{1}{8} & \frac{1}{16} \end{bmatrix} \tag{6.9}$$

This particular Wavelet function operates effectively for resolution enhancement because it is a well-balanced compromise between reconstructing both small and large-scale features. The Wavelet functions for subsequent resolution levels are calculated according to $\frac{1}{2^j}\psi(\frac{x}{2^j}, \frac{y}{2^j})$ where rows and columns are interspersed with zeros in the same manner as described in Chapter 4.

The standard boolean Multiresolution Support is calculated according to the following rules:

$$M(j,x,y) = \begin{cases} 1 \text{ if } w_j(x,y) & \geq & k\sigma_j \\ 0 \text{ if } w_j(x,y) & < & k\sigma_j \end{cases} \tag{6.10}$$

$$\begin{aligned} \text{where} \quad M(j,x,y) &= \text{Multiresolution Support images} \\ k &= \text{threshold} \end{aligned}$$

In deconvolution methods, the threshold k is used to distinguish between the real signal and the noise in the signal. A value of $k = 3$ is generally used to define noise with a probability of 99.7%, assuming a Gaussian distribution. This is because the aim of standard Multiresolution Support is to regularise areas in the imagery that do not contain significant signals. However, for resolution enhancement purposes, the aim is to reconstruct areas in the imagery that contain high-frequency information

and MRE is designed to specifically target these areas. Therefore, it is necessary to dynamically redefine the threshold term, making it dependant on the input image intensity and noise level. This was achieved by inspecting how the image mean, image range, Signal-to-Noise Ratio (SNR) and noise level interact over a range of input values and qualitatively estimating the appropriate output threshold value. By comparing these relationships experimentally, the MRE threshold k was determined:

$$\begin{aligned} k &= \frac{\text{SNR}(O)R(O)}{20\mu(O)} \\ &= \frac{\frac{\mu(O)}{\sigma_I}R(O)}{20\mu(O)} \\ &= \frac{R(O)}{20\sigma_I} \end{aligned} \tag{6.11}$$

$$\begin{aligned} \text{where} \quad \text{SNR}(O) &= \text{Signal-to-Noise Ratio of } O \\ R(O) &= \text{intensity range of } O \\ &= \max(O) \text{ - } \min(O) \\ \mu(O) &= \text{mean of } O \end{aligned}$$

This threshold was found to adequately normalise the Multiresolution Support image calculation. It also leads to MRE being sufficiently robust and capable of accommodating input imagery with variable SNRs and intensity ranges.

The Multiresolution Support images are often too harsh in their filtering and this can potentially introduce discontinuities into the reconstructed signal. This is caused by the boolean definition of Multiresolution Support. It is therefore necessary to impose some form of smoothing on $M(j,x,y)$. Again, the Wavelet function is useful here in gently smoothing the discontinuities contained in $M(j,x,y)$ by adding another convolution operation to Equation 6.6. In this case however, the aim is not to increase the smoothing of the Multiresolution Support images as the resolution becomes coarser. Instead, it is appropriate to convolve each Multiresolution Support image with the first-level Wavelet filter, ψ_1. This adds a subtle smoothing to each

support image ensuring that discontinuities do not interrupt the reconstruction process, while also maintaining the greatest amount of high-frequency content. Figure 6.7 depicts four levels of the redefined Multiresolution Support that have been smoothed with the first-level Wavelet filter.

The regularisation parameter, λ, manages the balance between statistical data fit and high-frequency content reconstruction. Typically, this parameter has been hard to estimate for deconvolution methods, often requiring user input. One of the fundamental advances of Multiscale Entropy deconvolution is its ability to specify a single regularisation value, namely $\frac{\max(\text{PSF})}{2\sigma_I}$, that is consistent across all image types (Pantin and Starck, 1996). This arises from the inclusion of Multiresolution Support into the entropy calculation and significantly improves the operational autonomy of the algorithm. The regularisation parameter, λ, must now also take into account the REF, and can be calculated:

$$\lambda = \frac{\text{REF} \times \max(\text{PSF})}{2\sigma_I} \tag{6.12}$$

As the REF increases, with all other parameters remaining constant, the quantity with which to apply regularisation and high-frequency reconstruction must also increase. This is important because the more a signal is resolution enhanced, the more underdetermined the linear system becomes, requiring a greater amount of regularisation to allow convergence on a stable solution. Hence, the REF simply becomes a linear multiplier contained within the λ parameter.

Since the Multiscale Entropy term has been redefined from a measure based on the noise, as required in deconvolution methods, to a measure based on the input signal range for the application of resolution enhancement, it is also important to make sure that the final MRE calculation scales appropriately with the input signal intensity. Without some form of correction here, enhancing the resolution of an image containing a small average intensity would result in an over-regularised solution, and

(a)

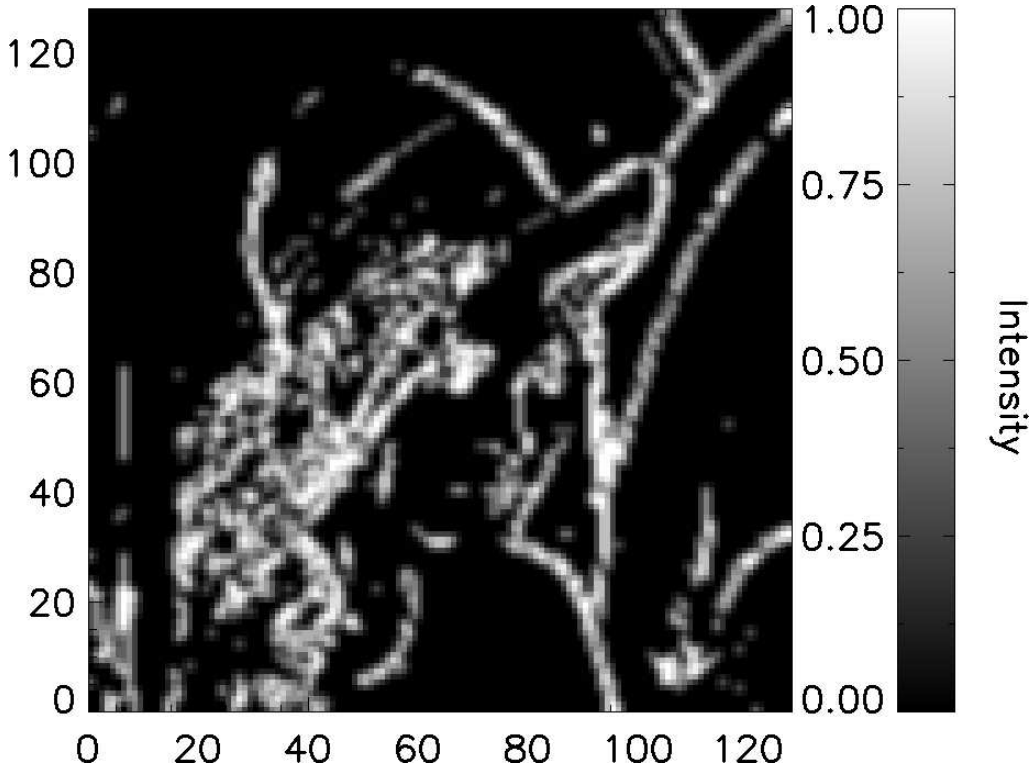

(b)

Figure 6.7: Multiresolution Support decomposition of (a) original standard test image 'Lena' resulting in (b) level 1 Multiresolution Support. Light regions signify areas in which Multiresolution Entropy will be calculated and occur where high-frequency content is present. Dark areas indicate regions where there is no high-frequency content and will not be incorporated into the Multiresolution Entropy calculation.

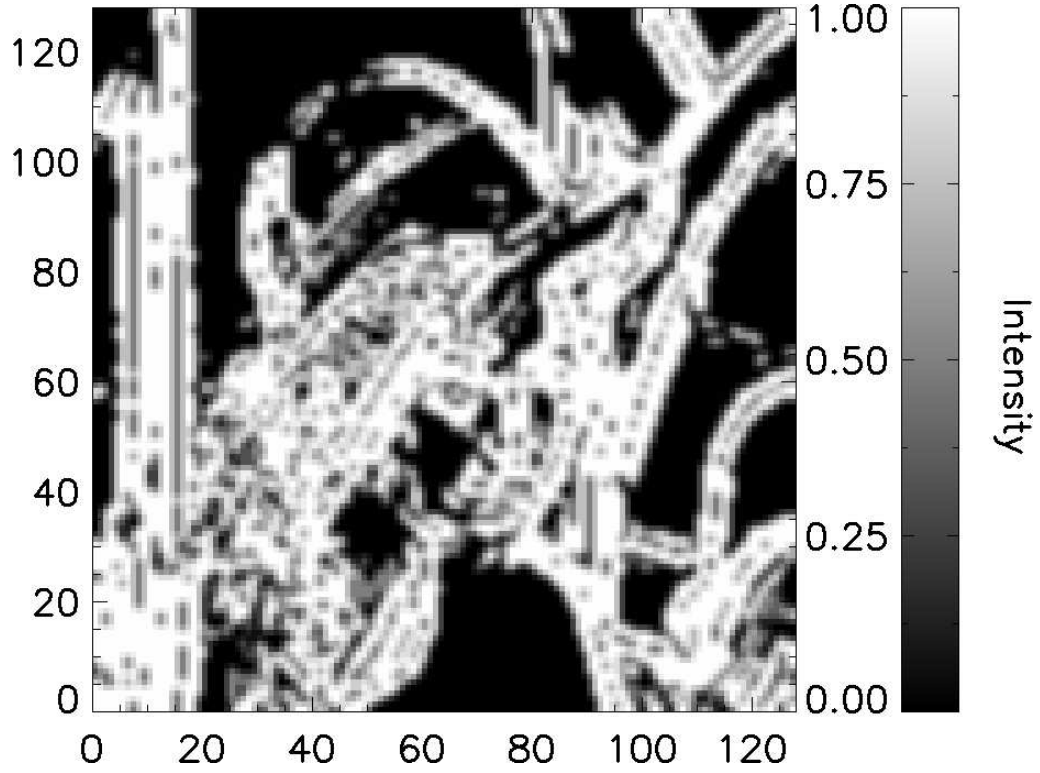

(c)

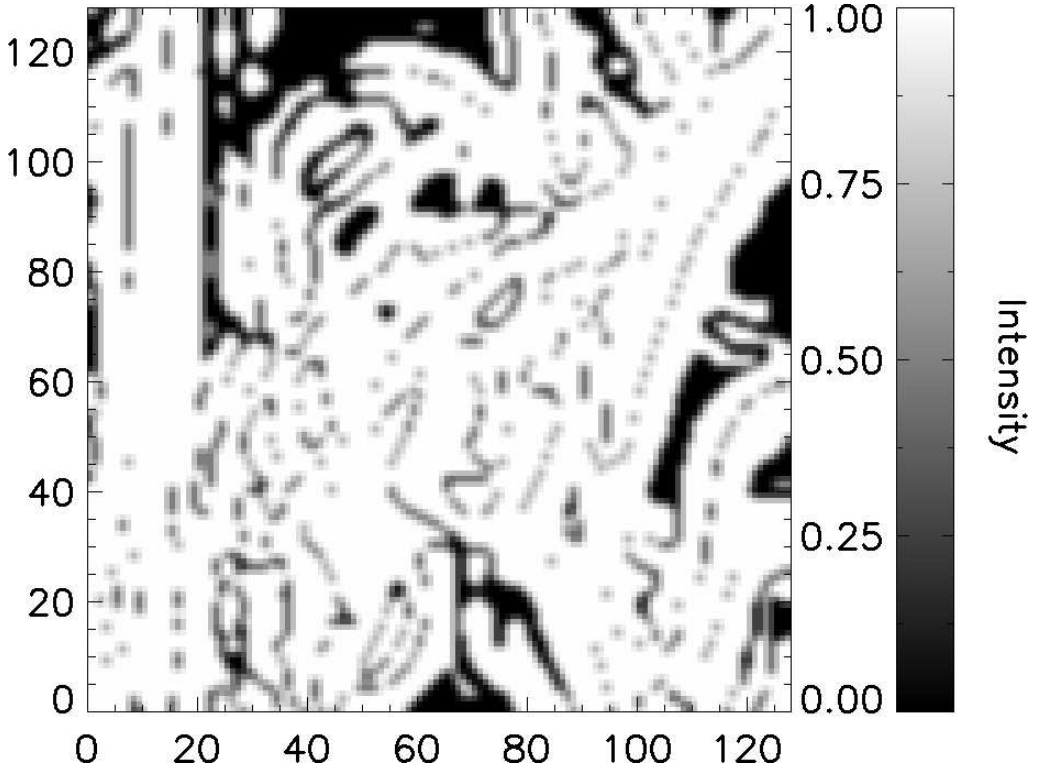

(d)

Figure 6.7 continued: Multiresolution Support decomposition resulting in (c) level 2 Multiresolution Support and (d) level 3 Multiresolution Support. Light regions signify areas in which Multiresolution Entropy will be calculated and occur where high-frequency content is present. Dark areas indicate regions where there is no high-frequency content and will not be incorporated into the Multiresolution Entropy calculation.

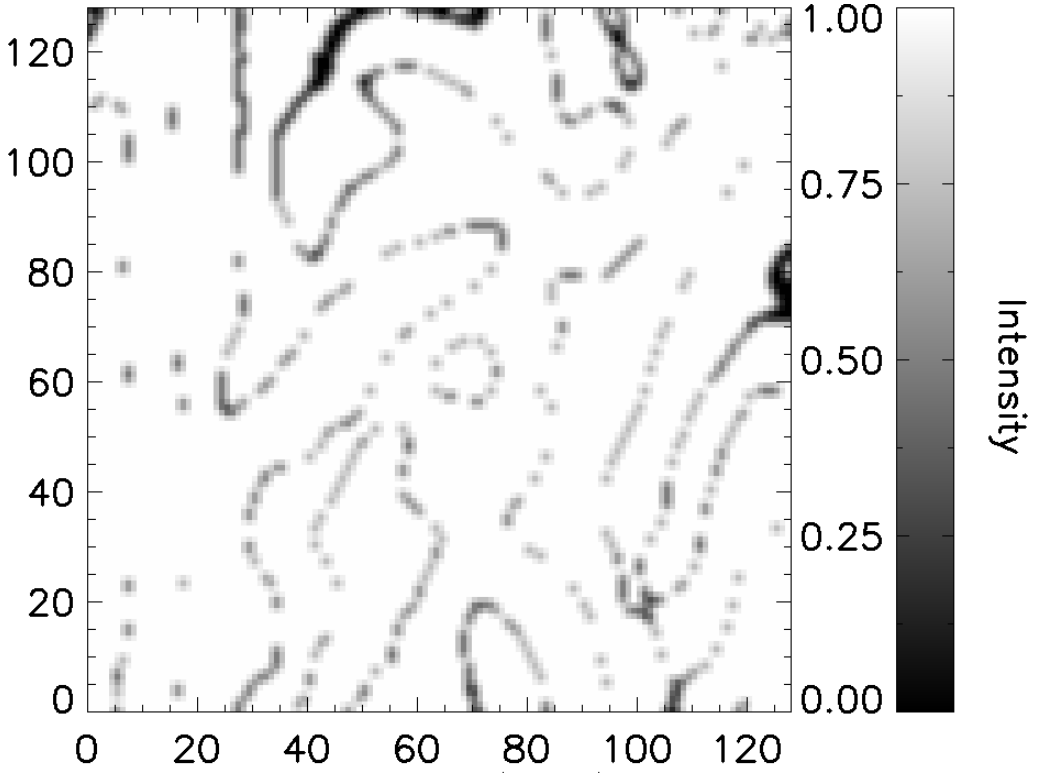

(e)

Figure 6.7 continued: Multiresolution Support decomposition resulting in (e) level 4 Multiresolution Support. Light regions signify areas in which Multiresolution Entropy will be calculated and occur where high-frequency content is present. Dark areas indicate regions where there is no high-frequency content and will not be incorporated into the Multiresolution Entropy calculation.

enhancing the resolution of an image containing a large average intensity would result in an under-regularised solution. A linear scaling factor of $\frac{R}{500}$ was found experimentally to correct any scaling issues, resulting in the gradient equation (Equation 6.6) now becoming:

$$\nabla F(x) = 2A^T(Ax - b) + \lambda^2 \frac{R(O)}{500\,\sigma_I} \sum_{scalesj} [(M(j) * \psi_1)\sigma_j sgn(w_j^{(O)}) \ln(\frac{|w_j^{(O)}|}{m_j})] * \psi_j^T \tag{6.13}$$

For the convolution of the Multiresolution Support images and the Wavelet filter in Equation 6.13, the FFT convolution with Boundary Correction (FBC) method developed in Chapter 3 provides accurate convolution with minimal loss of power.

Without using the FBC method, the resultant operations lose signal intensity and this significantly disrupts the reconstruction algorithm. Therefore, it is critical to renormalise the convolution sum using the FBC method so that no unintended loss of image intensity occurs.

After making all of the described alterations to MRE (Equation 6.4) and its gradient (Equation 6.13), the impact of these changes can be seen by performing the calculations on a standard test image (Figure 6.7(a)). Figure 6.8 shows the logarithmically rescaled response of MRE when applied to Figure 6.7(a) with the pixel summation component of the equation ignored for illustrative purposes. This is remarkably different to the Multiscale Entropy calculated on the same test image in Chapter 4. MRE produces its largest values where high-contrast edges appear in Figure 6.7(a) and this is due to the redefinition of MRE targeting high-frequency content.

The MRE gradient can be viewed by calculating the latter half of Equation 6.13 on Figure 6.7(a). Figure 6.9 shows the MRE gradient response that is used in the search direction of the gradient method. When comparing the MRE gradient with Figure 6.7(a), it is clear that high-frequency edges in the image are targeted which forces the solution in the direction of increased information in these areas.

To find a solution for the linear system, the cost function (Equation 6.5) can be minimised using a one-step gradient method:

$$O^{n+1} = O^n - \gamma \nabla F(x)^n \tag{6.14}$$

This is a gradient descent method that dynamically adjusts the stepping distance for the search direction, $\nabla F(x)^n$, using the step size variable γ. The step size can be determined using any number of stepping estimation techniques (Shi, 2005), but the approach implemented here will use the BB method for its efficiency of convergence and simplicity of use (Barzilai and Borwein, 1988). The BB method

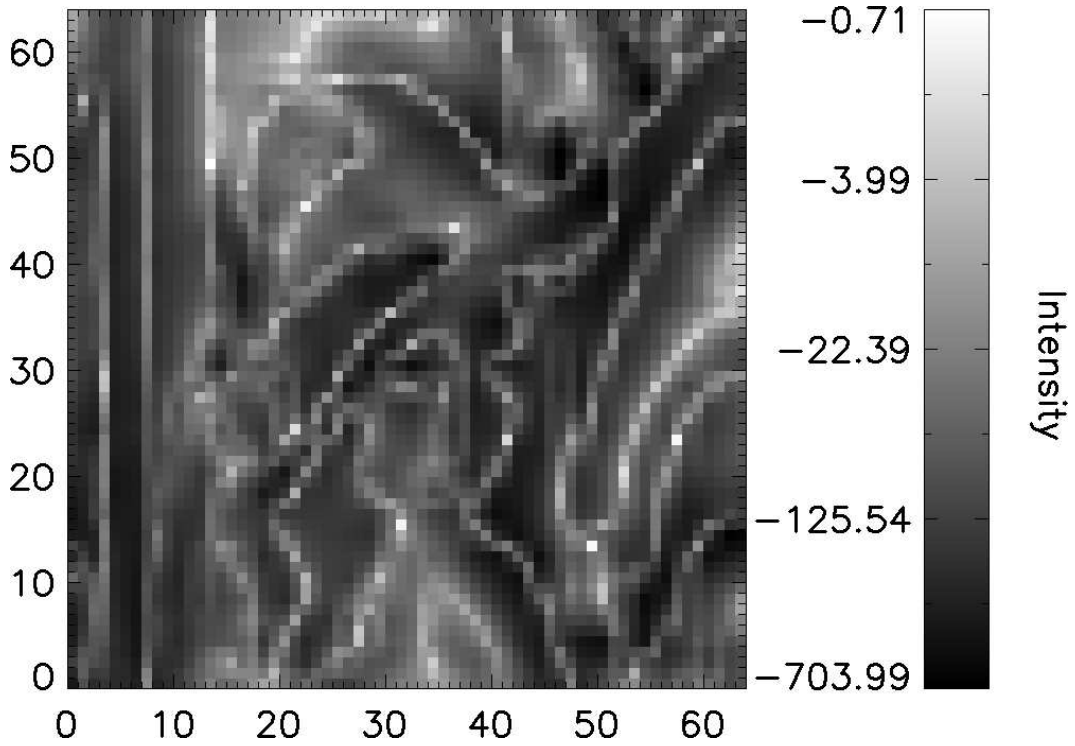

Figure 6.8: Logarithmically rescaled Multiresolution Entropy response to standard test image 'Lena' (Figure 6.7(a)) showing large quantities of entropy in regions of high-frequency content.

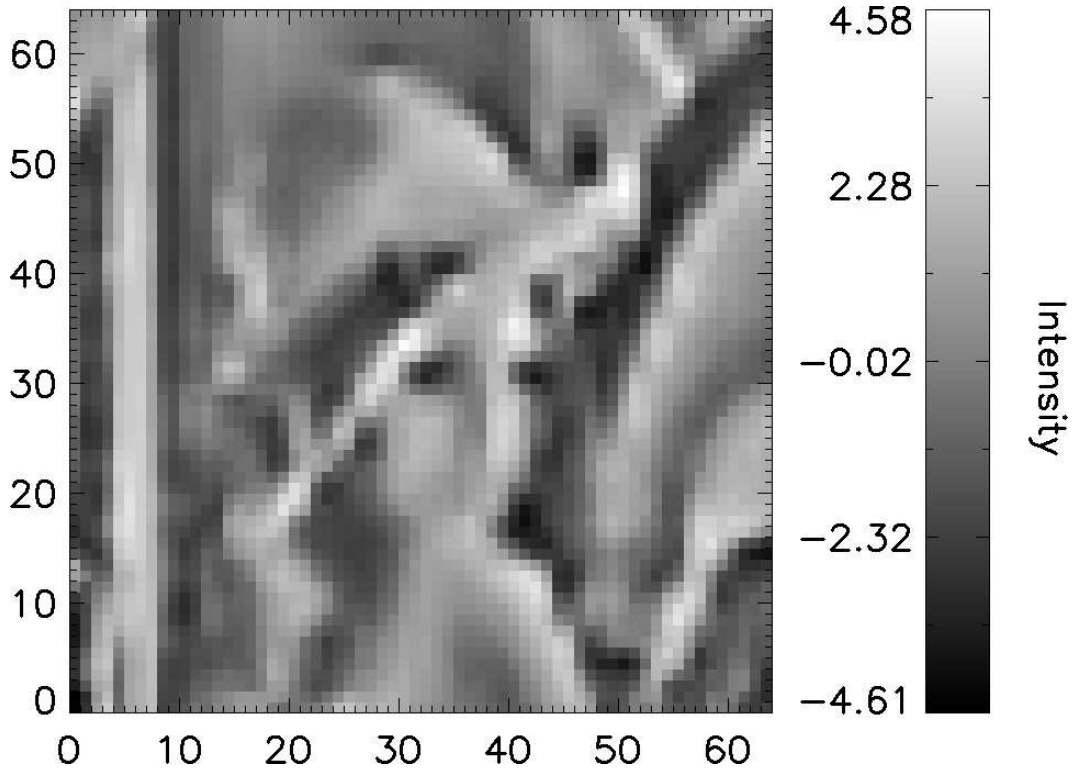

Figure 6.9: Multiresolution Entropy gradient response to standard test image 'Lena' (Figure 6.7(a)) showing the initial MRE search direction for the linear system. High-contrast edges are clearly visible and become iteratively included into the resolution-enhanced solution.

calculates the step size for convergence of the one-step gradient method according to:

$$\gamma = \frac{\sum[(O^n - O^{n-1}) \times (\nabla F(x)^n - \nabla F(x)^{n-1})]}{\sum[\nabla F(x)^n - \nabla F(x)^{n-1}]^2} \tag{6.15}$$

$$\begin{aligned} \text{where} \qquad O^n &= \text{current image} \\ O^{n-1} &= \text{previous image} \\ \nabla F(x)^n &= \text{current search direction} \\ \nabla F(x)^{n-1} &= \text{previous search direction} \end{aligned}$$

Appropriate stopping conditions need to be implemented to determine the convergence of the linear system and find a valid solution. It is typical to limit the number of iterations the gradient method will perform so that the algorithm will not continue indefinitely if the input system is significantly underdetermined. This implementation limits the number of iterations to 60, as convergence can be expected within this threshold, if convergence is indeed possible. It is also important to define the minimum stepping size, *minstep*, so that the algorithm terminates when it is sufficiently close to a stable solution. This can be achieved by checking that the Euclidean norm of the difference between two consecutive iterations is above a critical quantity:

$$\begin{aligned} \text{If } ||\Delta O(x)|| &\geq minstep \times ||O(x)^n||, \text{ then proceed} \\ \text{If } ||\Delta O(x)|| &< minstep \times ||O(x)^n||, \text{ then stop} \end{aligned} \tag{6.16}$$

$$\begin{aligned} \text{where} \qquad \Delta O(x) &= O(x)^{n-1} - O(x)^n \\ minstep &= 1 \times 10^{-6} \end{aligned}$$

Combining all of the discussed elements will produce an operational entropy-based spatial resolution enhancement algorithm capable of regularising underdetermined linear systems. A concerted effort has been placed on the reconstruction of high-frequency content and a convergent solution will produce a statistically stable result that is consistent with the MRE constraints.

6.4 Results

In order to determine the reconstruction accuracy of the MERE algorithm, it is important to build a rigorous experimental design that is free from bias and contamination. A sensible approach is to design a synthetic testing procedure that emulates the processes occurring in the real world with real satellite instruments. To this end, consider the radiance field reflecting off the surface of the Earth immediately before entering the optical system. This radiance field exists free from any instrumental effects and has an extremely high spatial resolution, as previously discussed. A discrete version of this field, O, was defined in Equation 6.1 and a higher-resolution reconstruction of the radiance field, $\uparrow O$, is ultimately what the MERE algorithm is designed to deliver. Figure 6.10 describes the procedure required to simulate the real-world satellite image capture process and is useful as a framework for enhancing image spatial resolution.

The test procedure starts with a Very HR (VHR) truth image to allow for later numerical comparison. The first step is to convolve the input radiance field with a suitably matched VHR PSF. This is the appropriate point at which to apply instrument effects because, as described earlier, the natural convolution process is effectively performed on continuous signals and is best simulated at the highest possible resolution level. The instrumental distortion step is also the point at which VHR information is redistributed within the recorded image, and will still partially exist even after downscaling to a lower resolution. This is precisely the source of information that the MERE algorithm takes advantage of to achieve spatial resolution enhancement. Unless stated otherwise, all results will use a VHR PSF derived from the MODIS Aqua instrumental characterisation model (Meister and McClain, 2010).

The dimensions of the VHR truth image and VHR PSF are selected to be 1088×1088 and 527×527 respectively. These values are chosen specifically because a significant image downscaling is required to simulate the radiance field entering, and being recorded by, the imaging system. The VHR PSF must also be downscaled to the sampling frequency of the desired resolution-enhanced output. However, when the VHR PSF is downscaled to HR, it is critical that the PSFs odd dimensions

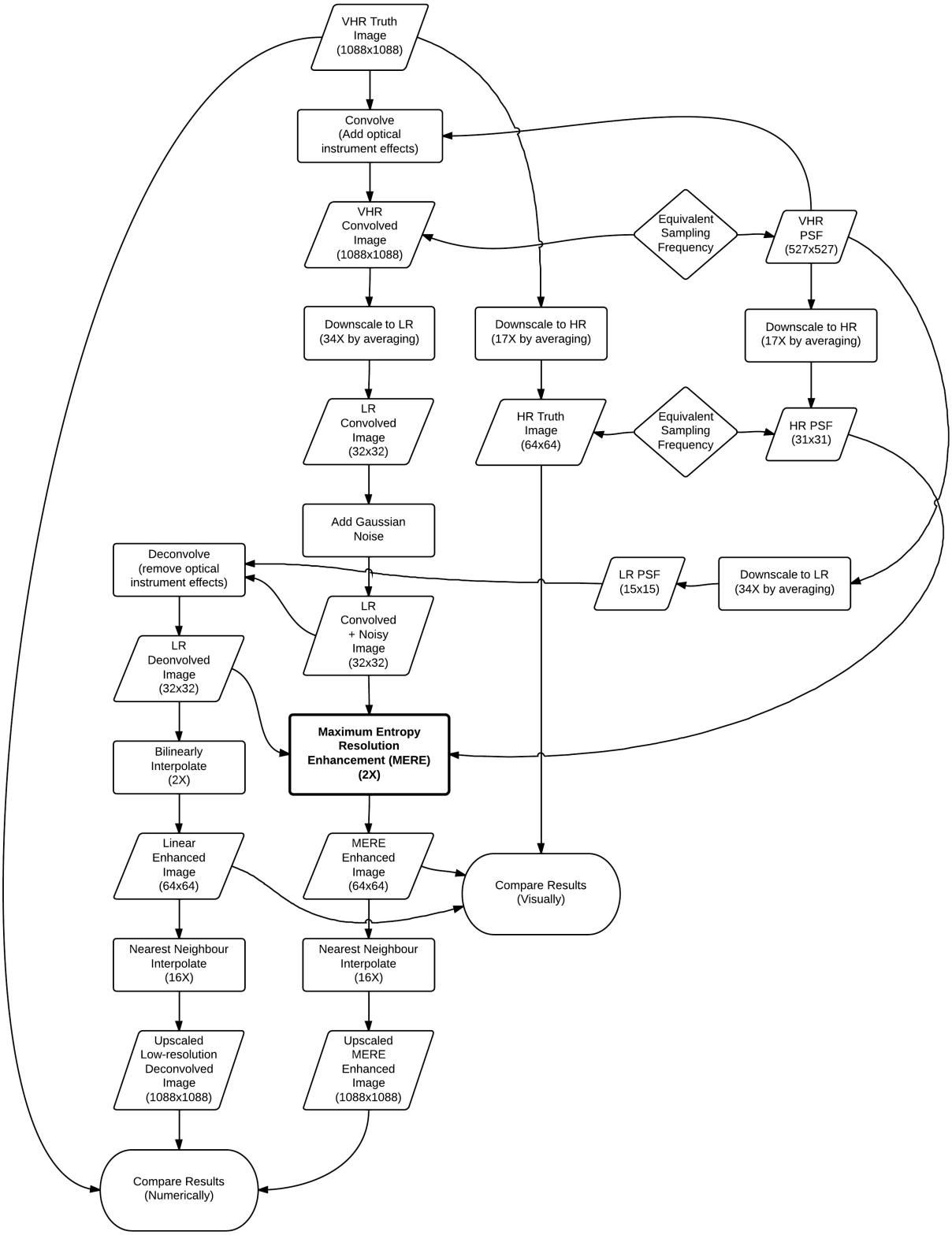

Figure 6.10: Flowchart describing the experimental design procedure for processing synthetic test images, enhancing spatial resolution and comparing the results.

are preserved. This is because instrument PSFs usually have a single peak at a central data point and if the wrong dimensions or downscaling factor are chosen here, then the HR PSF may end up with even dimensions and have its central peak spread across multiple data points. This can introduce inaccuracies into the testing procedure where convolution with the VHR PSF and HR PSF would no longer accurately approximate equivalent operations.

After the VHR convolution is performed, a downscaling operation by a significant factor is required to simulate the digitisation of the input radiance field. In the experimental design, a downscaling factor of 34 is used and the MERE algorithm enhances the image spatial resolution by a factor of 2. The downscaling operations of the test imagery are performed using averaging because this is equivalent to the process occurring when light strikes a satellite detector. That is, as light is reflected off the MODIS scanning mirror and onto an array of detectors, the quantity of light that hits the detector is measured as a voltage, or digital number, averaged over the recording frequency of the detector and finally recorded. Therefore, by using averaging for all of the required downscaling processes, the way light is transformed into information within a satellite optical system is implicitly simulated.

After convolution and downscaling have occurred, an appropriate quantity of Gaussian noise is added to the LR convolved image to simulate the natural detector-based noise process that occurs within the satellite instrument. This is the correct point to add detector noise to the test image because each satellite waveband has a unique noise response that corrupts the recorded image at this resolution. In the experimental design, the original test image is rescaled to have intensity values between 0 and 100 which results in an average image intensity of 46.52. A SNR of 100 is chosen and the standard deviation of the noise in the image, σ_I, can be calculated according to:

$$\sigma_I = \frac{\mu}{\text{SNR}} \tag{6.17}$$

$$\text{where} \quad \mu \quad = \quad \text{mean of the signal}$$

This results in the standard deviation of the added noise being 0.47 for the test image 'Lena', shown in Figure 6.7(a). Additionally, this value is passed into the MERE algorithm and used in many calculations including MRE (Equation 6.4), the modified Multiresolution Support (Equations 6.10 and 6.11), and the MRE gradient (Equation 6.13).

Another input into the MERE algorithm is the LR deconvolved image, and this can be attained by applying a deconvolution technique to the LR convolved and noisy image (Chapter 4). Separately, the original VHR truth image is downscaled to HR by a factor of 17 for later qualitative comparison with the result of the MERE algorithm. The VHR PSF is also downscaled to HR and LR, by factors of 17 and 34 respectively, for input into the MERE and deconvolution algorithms. Again, it is important that downscaling by averaging is used here because this will allow the HR and LR PSFs to approximate the VHR PSF as accurately as possible.

At this point, MERE can be performed with three inputs: the LR convolved and noisy image (32×32); the LR deconvolved image (32×32); and the HR PSF (31×31) sampled at the same frequency of the desired resolution-enhanced output image (64×64). The linear system described in Section 6.2 is now constructed and MRE regularisation is applied to find a unique and stable solution to the system (Section 6.3). The result of the MERE process is a resolution-enhanced image (64×64) that contains high-frequency information extracted from the natural optical PSF convolution process.

Comparing the final MERE result to the original test image will allow the reconstruction accuracy to be assessed. This comparison can be achieved in two ways. The HR MERE result can be directly compared with the HR truth image that was downscaled from the original VHR truth image. This is a good approach for visual comparison and illustration of the resolution-enhanced results. For a numerical comparison, the HR MERE result can be nearest-neighbour interpolated back to the original VHR, with the interpolation process simply replicating pixel values to larger areas and not adding any deterministic information to the result. This is a more appropriate method to derive quantitative results because no inaccuracies are being introduced by downscaling the VHR truth image for comparison. Also, if the

error metric is defined in this way, varying REF results can be compared against each other because all results are compared against the original VHR truth image.

The process depicted in Figure 6.10 was undertaken to enhance the spatial resolution of the standard test image shown in Figure 6.7(a), originally starting at VHR as a 1088×1088 pixel image. Figure 6.11 shows the HR truth image (64×64) downscaled from the original VHR truth image for comparison (Figure 6.11(a)), the LR convolved and noisy image (32×32) (Figure 6.11(b)), and the LR deconvolved image (32×32) (Figure 6.11(c)). Notice that the HR truth image no longer contains an intensity range from 0 to 100, as was defined in the original VHR image. This is because spatially only 1 in every 289 pixel is retained when downscaling by a factor of 17 in two dimensions, which results in a significant loss of information. Therefore, there is a large chance that many of the brightest and darkest pixels will be removed during this process and the resulting downscaled image will undergo a truncation in its intensity range. A more extreme intensity range truncation is encountered to retrieve the LR convolved and deconvolved images. There is not much qualitative difference between these two images (Figures 6.11(b) and 6.11(c)). However, their intensity ranges indicate that the LR deconvolved image contains slightly more extreme intensities than the LR convolved image, as would be expected from a deconvolution process.

Figure 6.12 shows the result of the MERE algorithm having attempted a spatial resolution enhancement by a factor of 2 (Figure 6.12(a)), the difference between the MERE result and the HR truth image (Figure 6.12(b)), and a frequency histogram of the difference image (Figure 6.12(c)). Qualitatively, Figure 6.12(a) appears to contain substantially more information than either the LR convolved or deconvolved images (Figures 6.11(b) and 6.11(c)). The intensity range, which was originally 0 to 100 in the VHR truth image, has been somewhat restored, but the minimum and maximum intensity values appear to have overshot the original values. However, the MERE reconstruction can be considered to be reasonably successful in this respect because the input imagery only contained intensity ranges from approximately 12 to 86. The combination of trying to find the most statistically correct solution and reconstructing high-frequency content using MRE has identified that the brightest

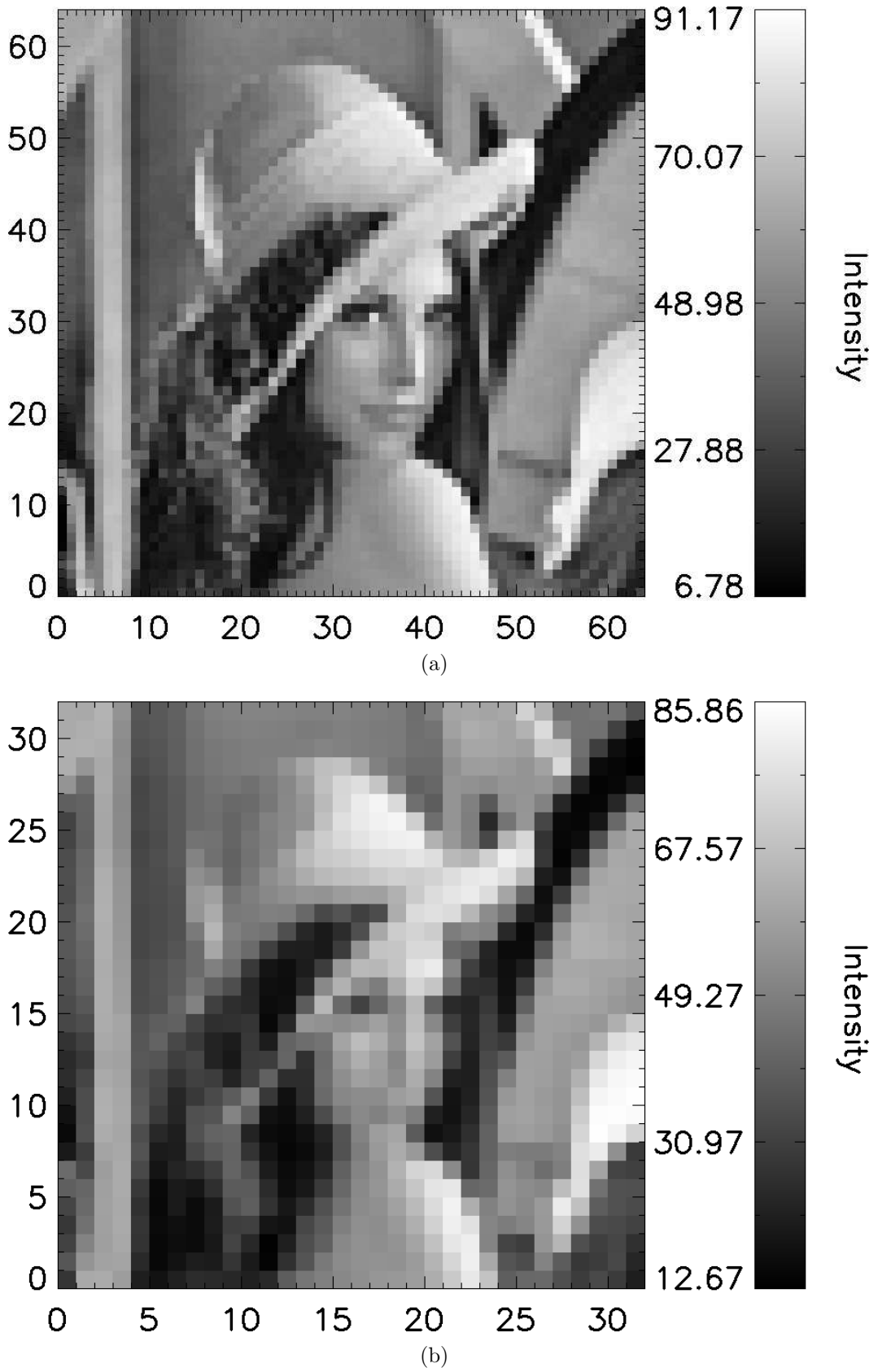

Figure 6.11: Resolution enhancement evaluation procedure showing (a) the high-resolution truth image (64×64) and(b) the low-resolution convolved and noisy image (32×32).

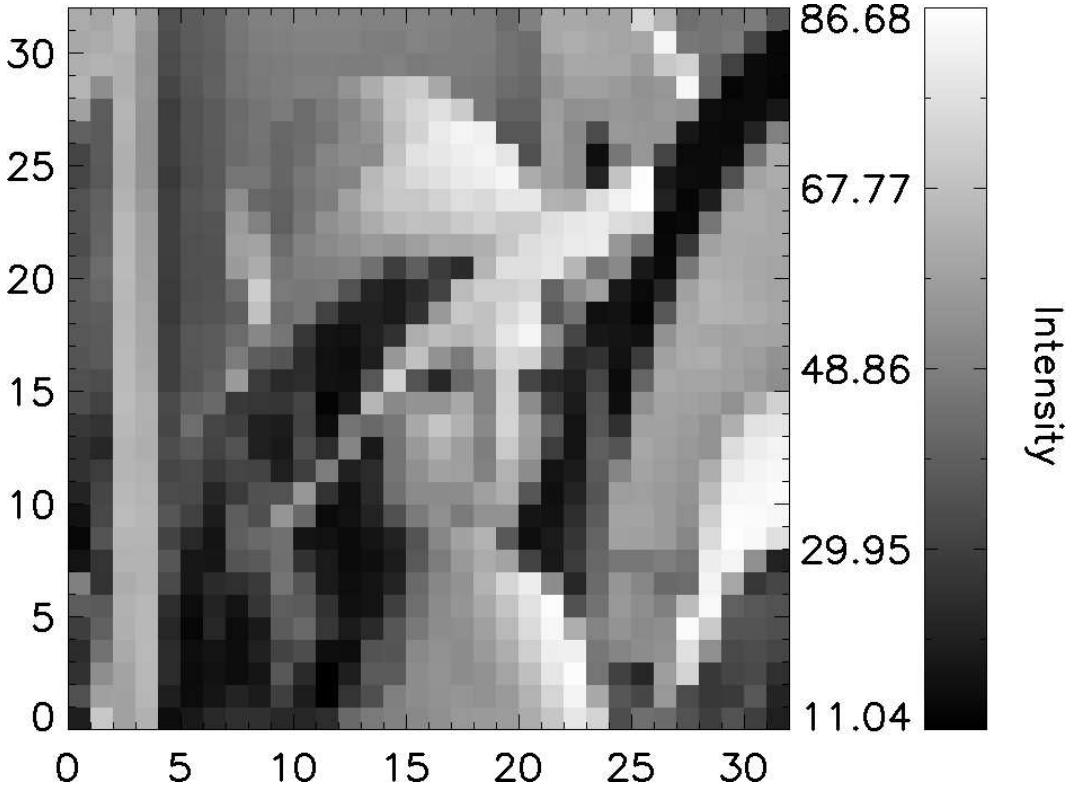

(c)

Figure 6.11 continued: Resolution enhancement evaluation procedure showing (c) the low-resolution deconvolved image (32×32).

and darkest pixels are missing from the LR imagery, and MERE has attempted to reconstruct this missing information.

The difference image highlights areas in which the MERE algorithm has difficulty reconstructing information (Figure 6.12(b)). The smooth areas in the image are reasonably well resolved and the largest differences occur at high-contrast edges. It is not surprising that the MERE algorithm cannot perfectly reconstruct all of the high-frequency information. This is because a significant quantity of information, including high-frequency information, is lost during the downscaling procedure and not all of this information is preserved in the instrumental convolution process. The frequency histogram of the difference image indicates that a large number of pixels are accurately reconstructed and have a difference close to zero, while the number of pixels that contain increasing quantities of reconstruction error becomes rapidly smaller in a trend resembling a power law. The pixels with differences close to zero

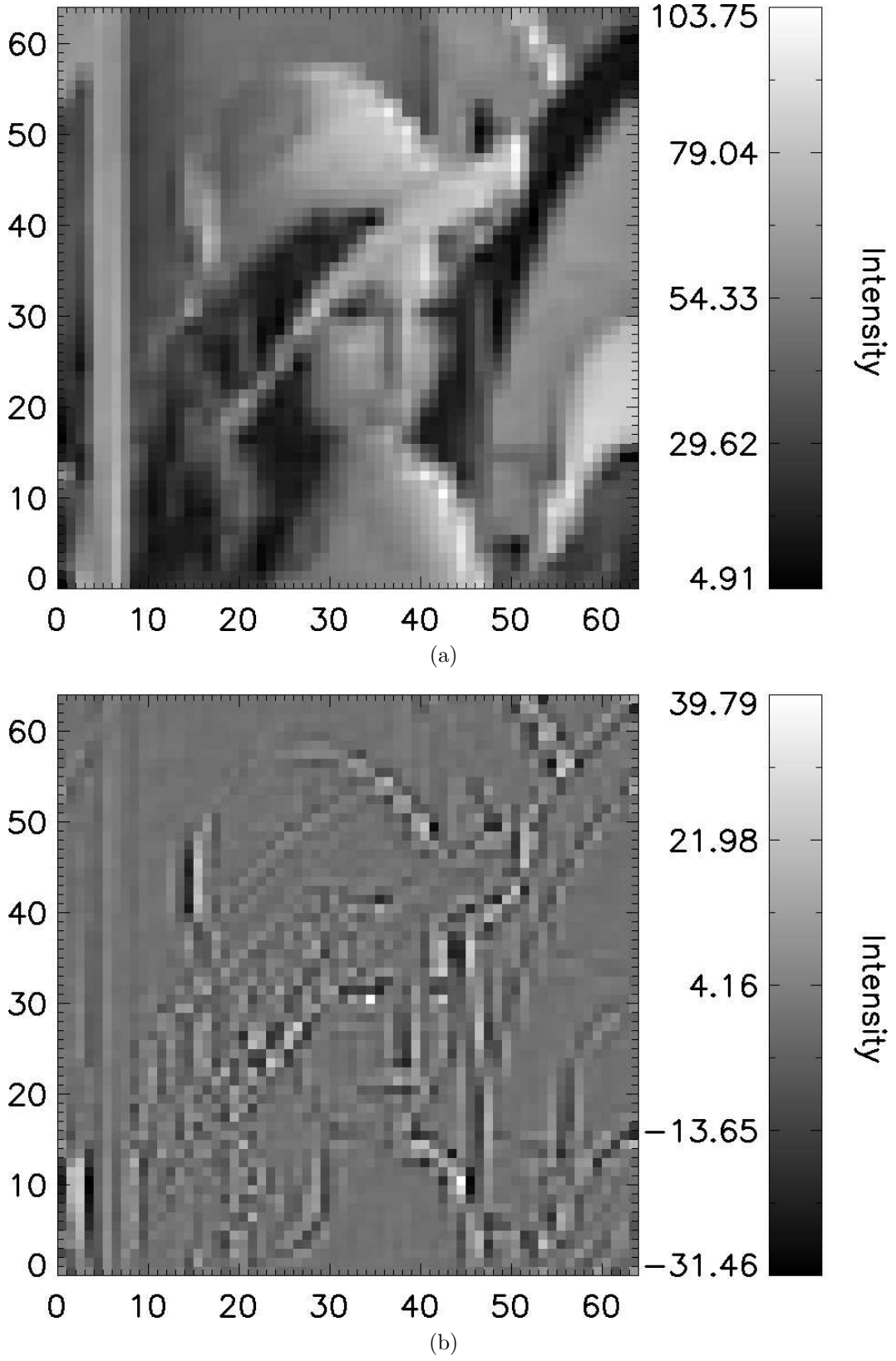

Figure 6.12: MERE results showing (a) the spatially enhanced image (64×64) and (b) the difference between the MERE result and the high-resolution truth image (64×64).

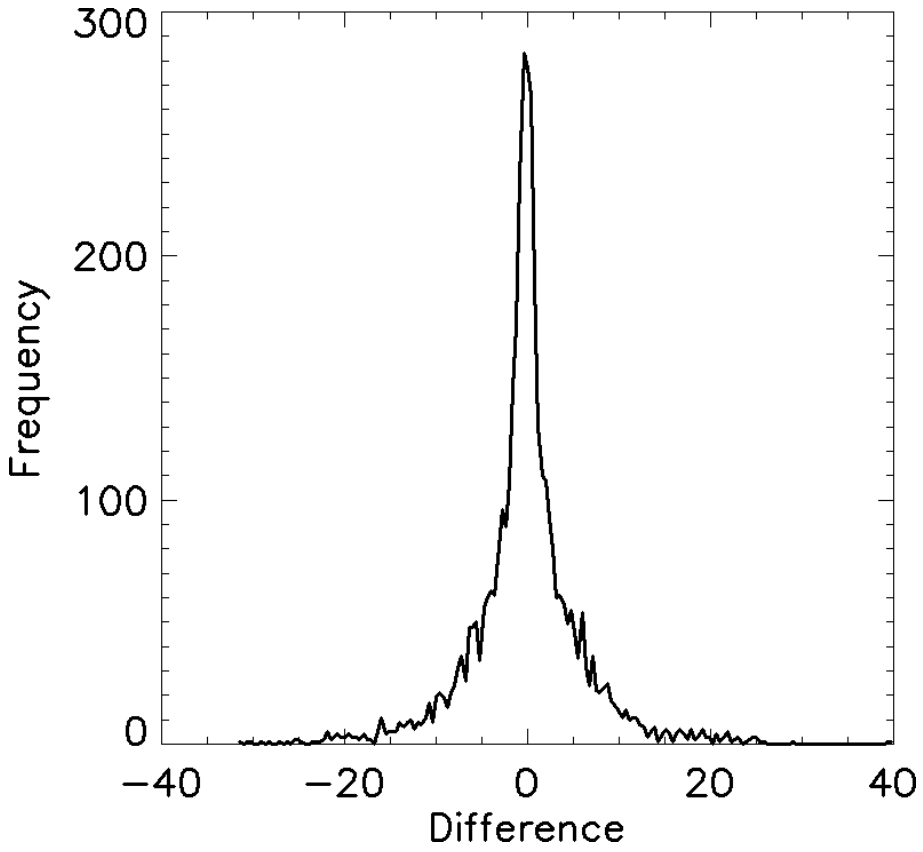

(c)

Figure 6.12 continued: MERE results showing (c) a frequency histogram of the difference image.

are attributed to the well reconstructed smooth areas in the image and pixels with larger errors come from areas in the image that contain high-frequency content (Figure 6.12(b) and 6.12(c)).

Bilinear interpolation is one of the simplest forms of resolution enhancement. It is computationally inexpensive and will act as a benchmark when compared with the MERE result. Figure 6.13 shows the result of bilinearly interpolating the LR deconvolved image (Figure 6.13(a)), the difference between the bilinearly enhanced result and the HR truth image (Figure 6.13(b)), and a frequency histogram of the difference image (Figure 6.13(c)). There appears to be significantly more structure in the bilinearly enhanced difference image than the MERE enhanced difference image (Figures 6.12(b) and 6.13(b)). For instance, extended regions leading up to high-contrast edges in the bilinear difference image contain clear non-zero values, whereas these same regions in the MERE difference image exhibit values closer to

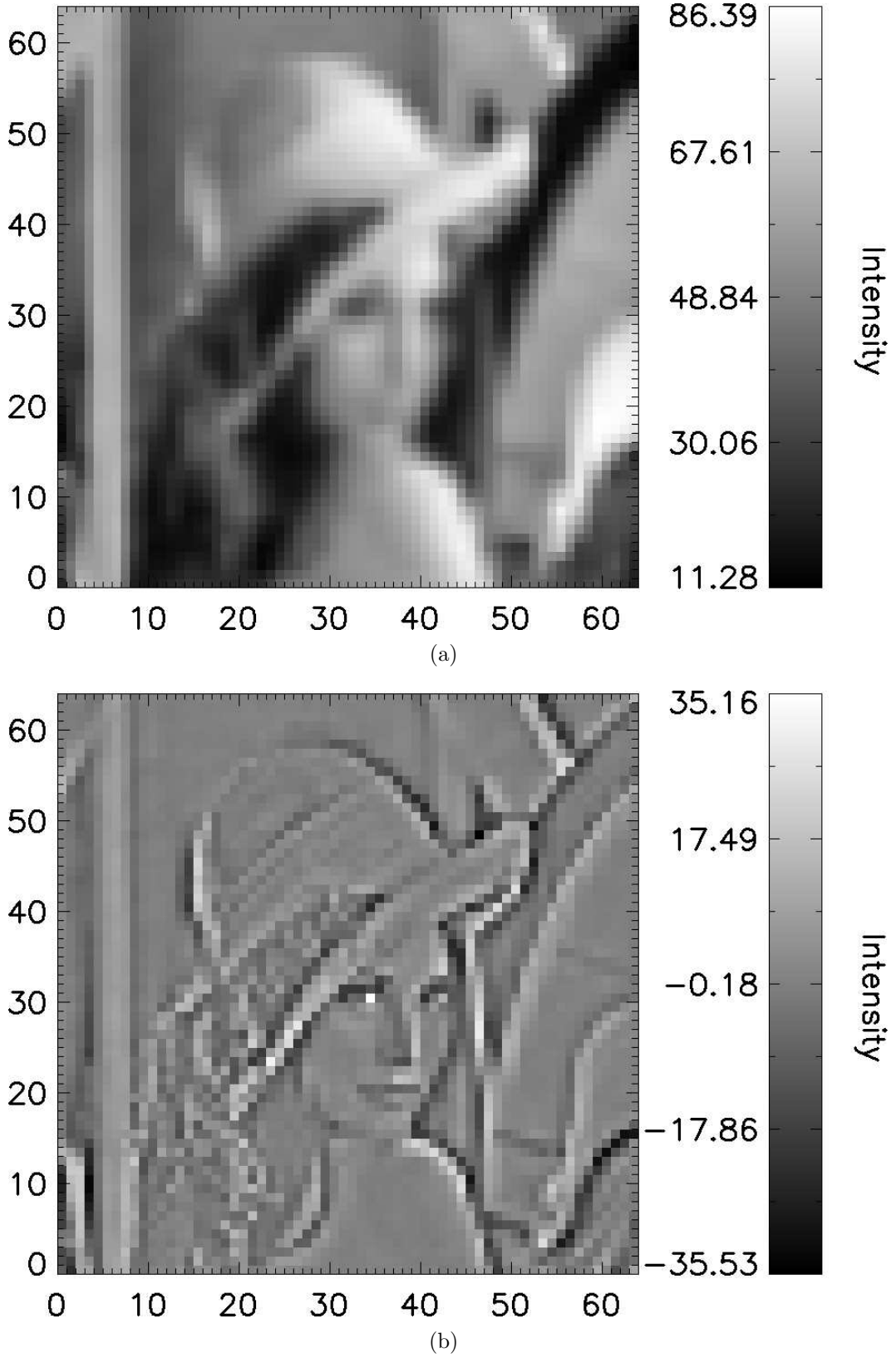

Figure 6.13: Bilinear interpolation results showing (a) the bilinearly enhanced image (64×64) and (b) the difference between the bilinear result and the high-resolution truth image (64×64).

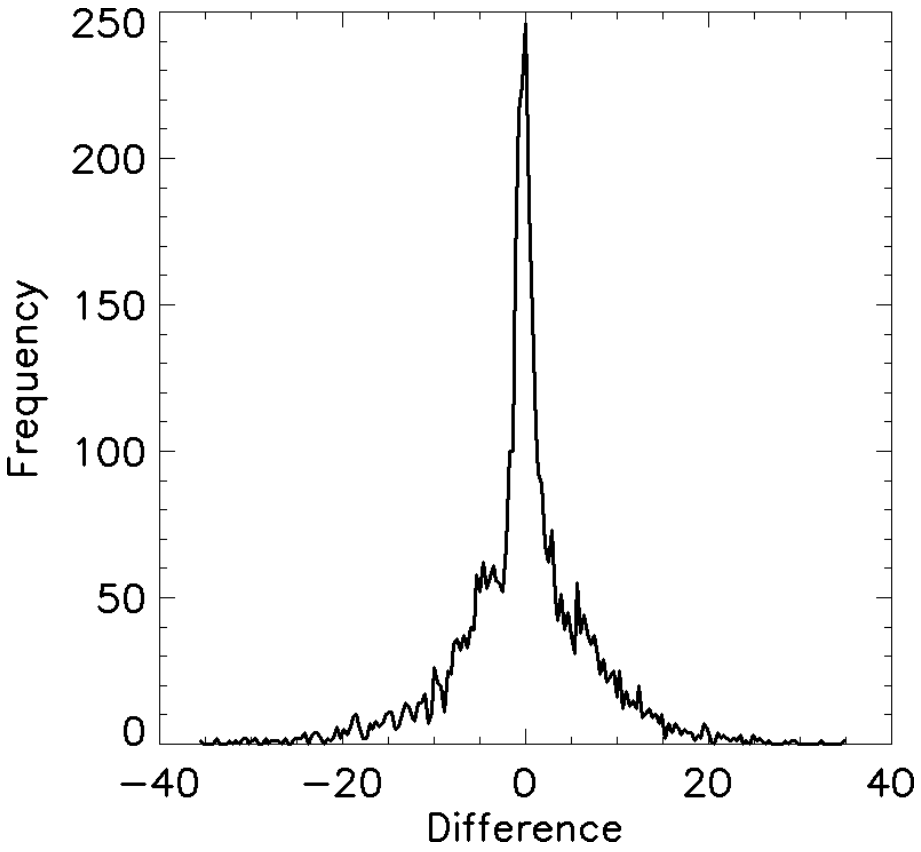

(c)

Figure 6.13 continued: Bilinear interpolation results showing (c) a frequency histogram of the difference image.

zero. This indicates that, while not perfectly reconstructing all the missing high-frequency content, the MERE algorithm performs better than bilinear interpolation in areas not containing extremely high contrast.

To extend this analysis of the MERE algorithm, additional comparisons can be made with bicubic spline interpolation and a Tikhonov regularisation of the constructed linear system. Bicubic spline interpolation is a sophisticated interpolation technique where cubic polynomials are fitted to known data points and the interpolated values are drawn from these fitted curves. This technique can be incorporated into the testing procedure and used for comparison by simply swapping the bilinear interpolation method in Figure 6.10 with a bicubic spline interpolation method. Tikhonov regularisation is a common approach used to solve underdetermined problems (Tikhonov and Arsenin, 1977; Tikhonov et al., 1987). It operates by including a regularisation term into the linear system minimisation:

$$\|Ax - b\|^2 + \lambda^2 \|\Gamma(x - x_0)\|^2 \tag{6.18}$$

$$\begin{aligned} \text{where} \quad \Gamma &= \text{suitably chosen Tikhonov matrix} \\ x_0 &= \text{initial starting point} \end{aligned}$$

The identity matrix is often chosen as the Tikhonov matrix and will be used here. This limits smoothing and gives preference to solutions with smaller residuals. Applying Tikhonov regularisation to the linear system constructed in Section 6.2 will allow for a comparison of MRE regularisation and a common regularisation technique. That is, using an alternative regularisation method on the linear system will highlight whether the problem formulation or the MRE constraint has the most impact on the accuracy of the resolution-enhanced results. Tikhonov regularisation for resolution enhancement can be implemented by swapping the MERE method in Figure 6.10 with a standard Tikhonov linear system solver (Hansen, 1994). A Generalised Cross-Validation (GCV) method can be used to determine the regularisation parameter, λ. GCV is designed to find a regularisation quantity such that if an arbitrary element of b is removed, then the corresponding regularised solution would predict this observation well (Wahba, 1990).

Figure 6.14 shows the result of Tikhonov resolution enhancement (Figure 6.14(a)), the difference between the Tikhonov enhanced result and the HR truth image (Figure 6.14(b)), and a frequency histogram of the difference image (Figure 6.14(c)). The Tikhonov resolution-enhanced result successfully produces a solution, but is affected by severe artefact creation (Figure 6.14(a)). The intensity range is less accurately restored when compared with the MERE result and high-frequency edges in the image are also not as accurately reconstructed. The difference image shows that the difference structure is now overwhelmed by erroneous artefacts (Figures 6.12(b) and 6.14(b)). This is because linear methods for underdetermined problems generally struggle with the treatment of noise, as discussed in Chapter 2. The Tikhonov method, in particular, often overly-smooths the solution and this can be problematic around image features. The frequency histogram reflects these errors with a smaller number of differences with values of zero, and an increase in the

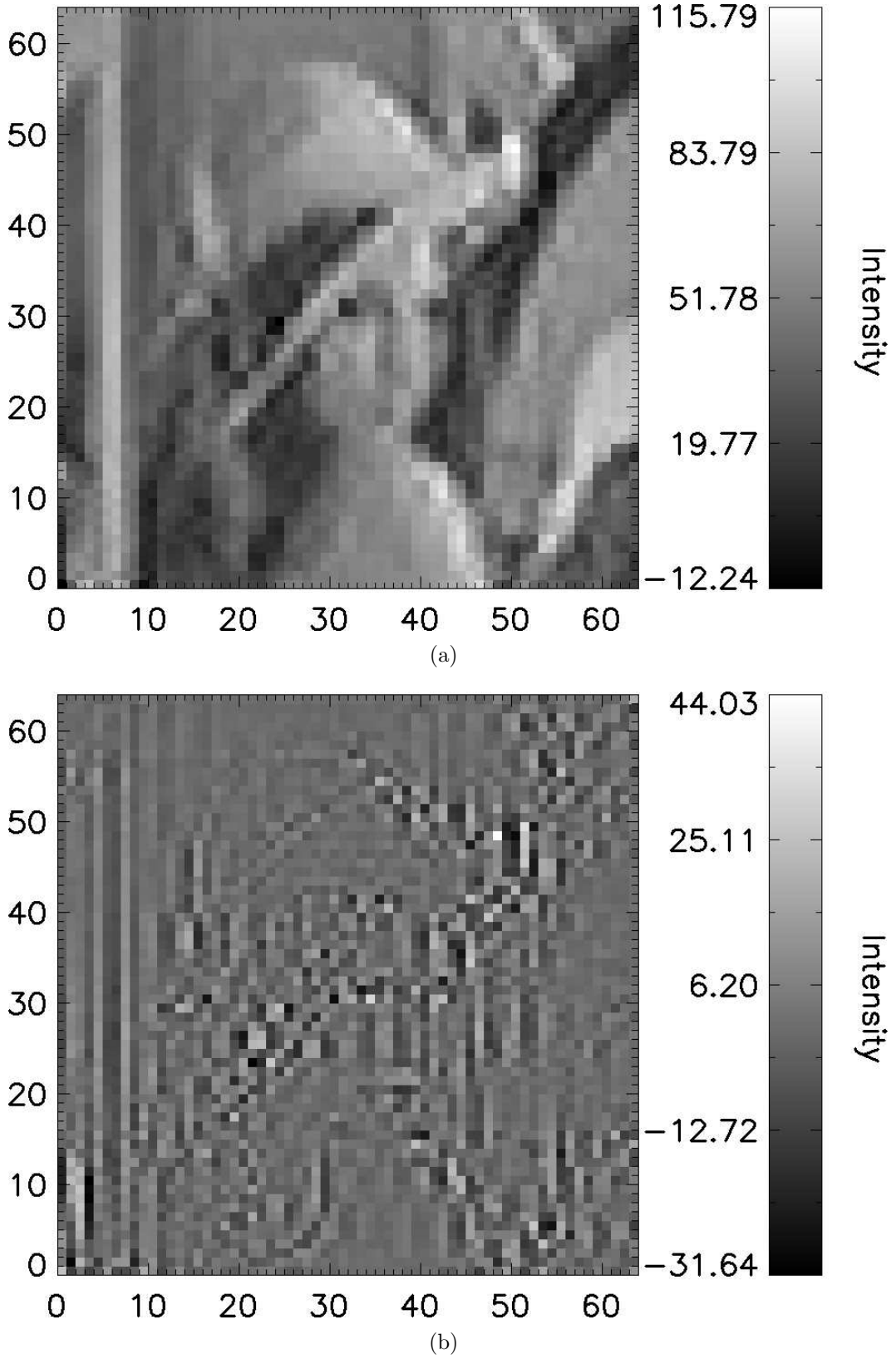

Figure 6.14: Tikhonov resolution enhancement results showing (a) the Tikhonov enhanced image (64×64) and (b) the difference between the Tikhonov result and the high-resolution truth image (64×64).

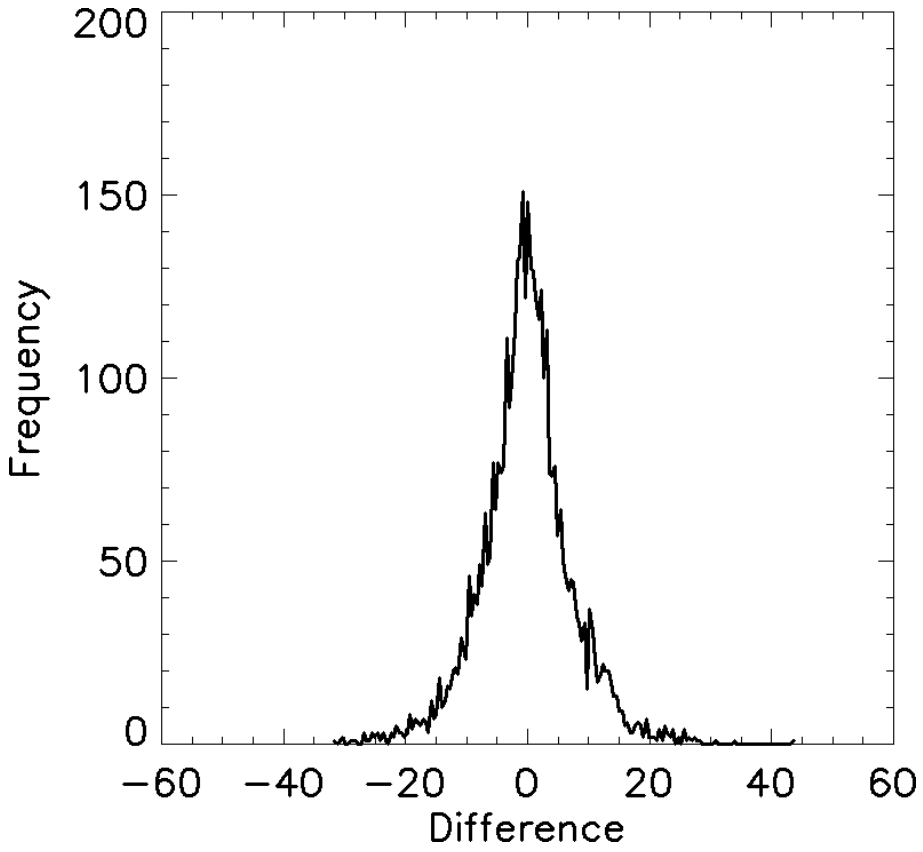

(c)

Figure 6.14 continued: Tikhonov resolution enhancement results showing (c) a frequency histogram of the difference image.

quantity of differences with non-zero values (Figure 6.12(c) and 6.14(c)). This result indicates that finding an accurate resolution-enhanced solution not only relies on the correct problem formulation, or construction of the linear system in this case, but also the appropriate selection of applied constraints. With this in mind, MRE has been specifically crafted to reconstruct high-frequency content and appears to provide a superior solution when applied to the problem of resolution enhancement.

Figure 6.15 shows the result of bicubic spline interpolation of the LR deconvolved image (Figure 6.15(a)), the difference between the bicubic interpolation enhanced result and the HR truth image (Figure 6.15(b)), and a frequency histogram of the difference image (Figure 6.15(c)). As with bilinear interpolation, bicubic spline interpolation produces similarly smooth results. The intensity ranges have been reasonably well restored and the only other significant difference between the two interpolation methods is highlighted in the difference image, where bicubic spline

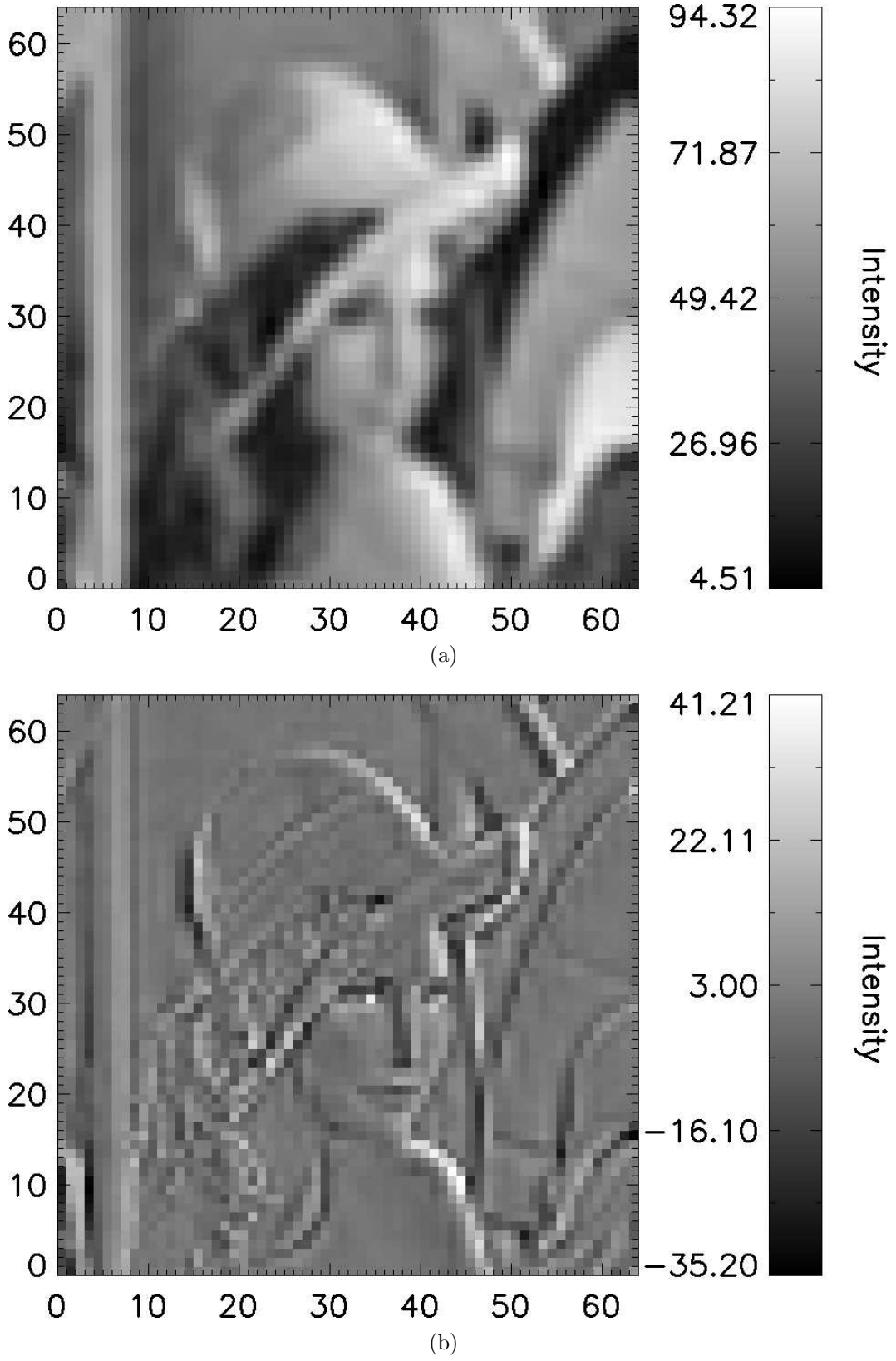

Figure 6.15: Bicubic interpolation results showing (a) the bicubic interpolation enhanced image (64×64) and (b) the difference between the bicubic result and the high-resolution truth image (64×64).

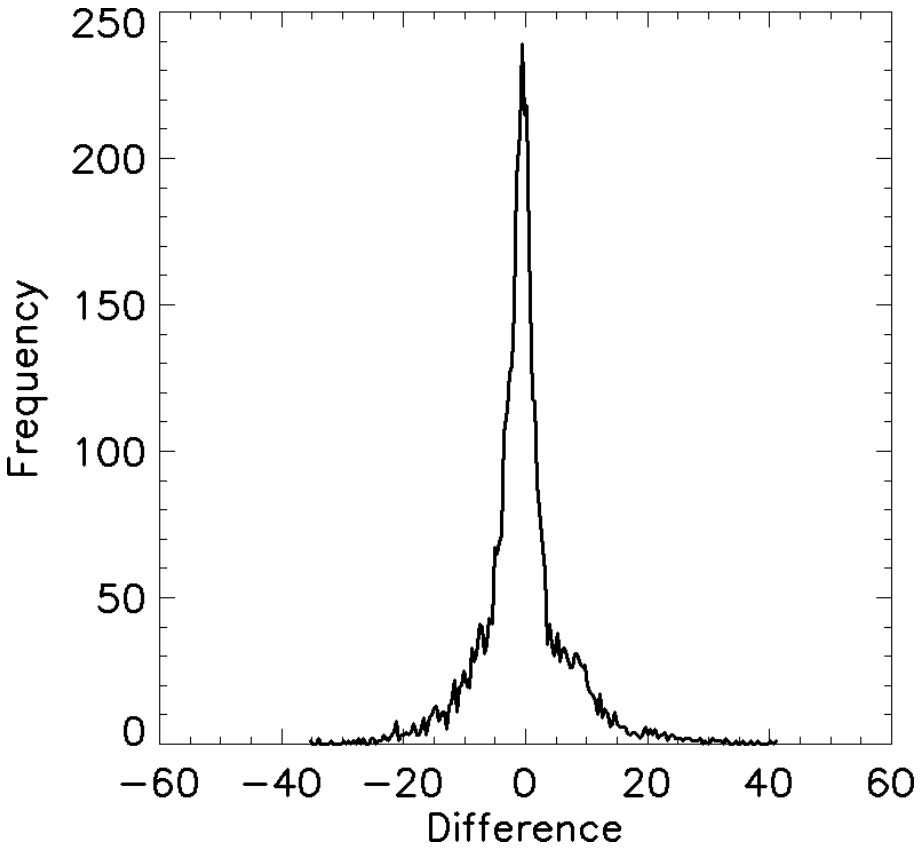

(c)

Figure 6.15 continued: Bicubic interpolation results showing (c) a frequency histogram of the difference image.

interpolation shows interesting curved structures near high-contrast edges (Figures 6.13(b) and 6.15(b)).

In addition to a qualitative comparison, it is important to numerically quantify the performance of the MERE reconstruction against the other resolution enhancement techniques. A useful method here is to calculate the Euclidean norm of the difference image. The Euclidean norm of image vector x is defined:

$$\|x\| = \sqrt{\sum_{i=1}^{n} x_i^2} \tag{6.19}$$

$$= \sqrt{x_1^2 + \cdots + x_n^2}$$

When applied to a difference image, this technique produces a single number

that represents the sum total over all pixels of the difference between the HR reconstruction and the truth solution. This is because the Euclidean norm effectively interprets every pixel difference as a positive distance from the ideal solution. The summation of these positive differences is a good representation of the overall error in the reconstructed image. This comparison metric will be termed the Euclidean difference norm and its result will be referred to as the reconstruction error. Additionally, this error method allows results with varying REFs to be compared, as long as the experimental design is followed and the results are nearest-neighbour interpolated to the original VHR (1088×1088) for comparison.

Having already compared the four resolution enhancement techniques using the standard test image 'Lena' (Figure 6.7(a)), it is important to extend the evaluation by comparing results from a range of different real and synthetic test images. Figure 6.16 shows the real and synthetic test images chosen to investigate the resolving power of the four resolution enhancement methods under different conditions. Figure 6.17 shows a comparison of results for the first test image (Figure 6.16(a)) including each of the four resolution enhancement methods. Figures 6.18, 6.19 and 6.20 follow this same layout for the remaining three test images (Figures 6.16(b), 6.16(c) and 6.16(d)), and indicate how each resolution enhancement method performs over a range of different input imagery. Table 6.1 presents the reconstruction errors for each resolution enhancement method calculated using the Euclidean difference norm method and averaged over 5 trials for each test image.

In the synthetic image evaluation of Figures 6.17 and 6.18, every resolution enhancement method except bilinear interpolation over-reconstructs the image intensity range. Bilinear interpolation can not reconstruct beyond the input intensity range because it is simply calculating weighted averages of surrounding pixels. In terms of reconstructing the desired intensity range, synthetic imagery provides an unrealistic example because there are many data points that contain both the smallest and largest values in Figures 6.17 and 6.18. Natural images are much more likely to contain only a single data point with the minimum and maximum value, which would readily be discarded in the downscaling process. For this reason, bilinear interpolation appears to perform well on synthetic imagery with many data points

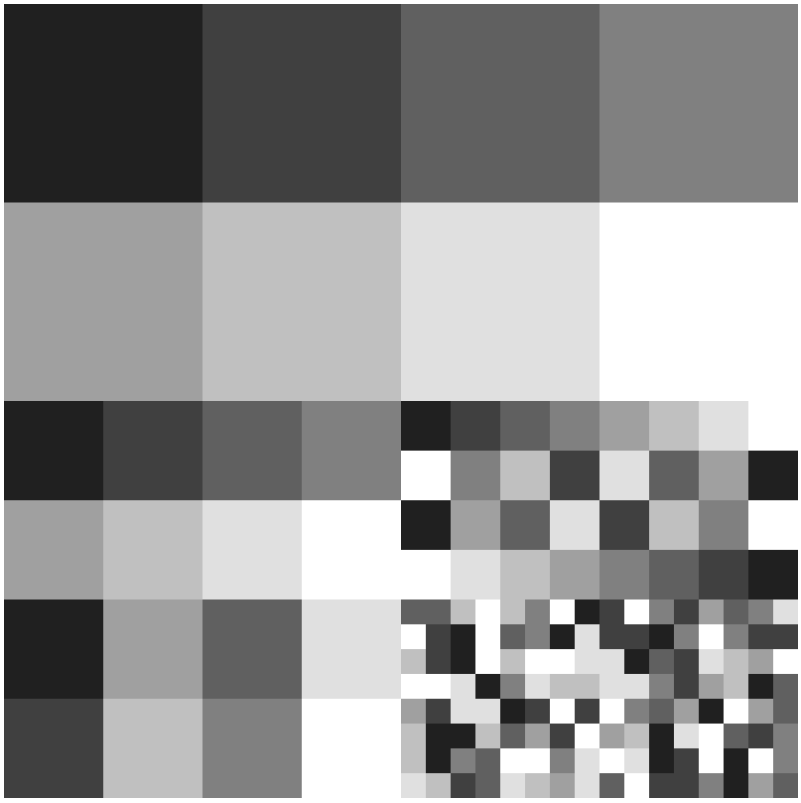

(a)

(b)

Figure 6.16: Test images showing (a) a standard USC texture mosaic #2 comprising various sized blocks of uniform intensity and (b) a standard USC texture mosaic #3 comprising more complicated regions of uniform intensity.

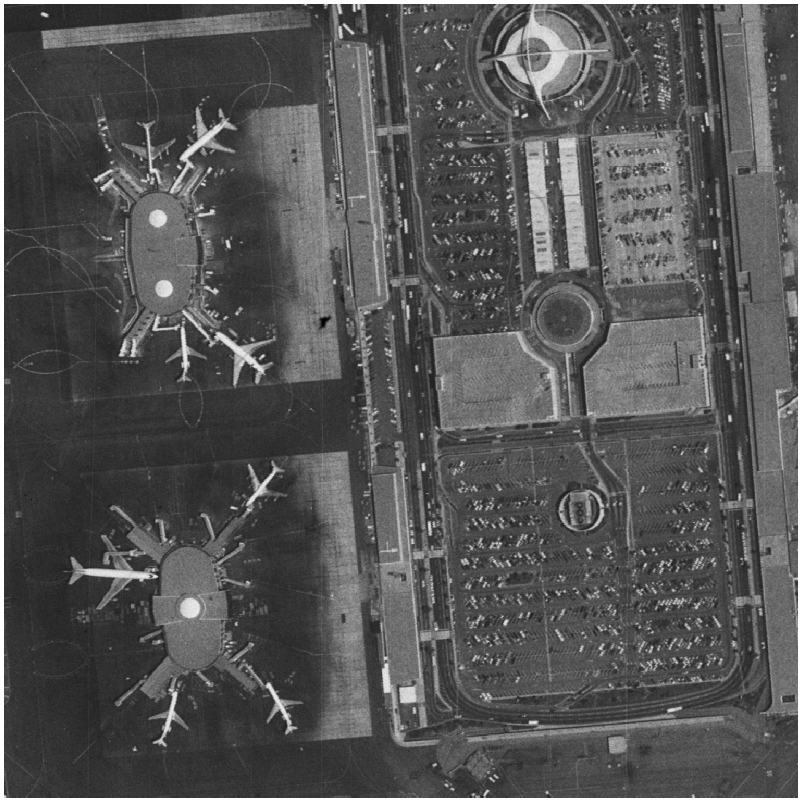

(c)

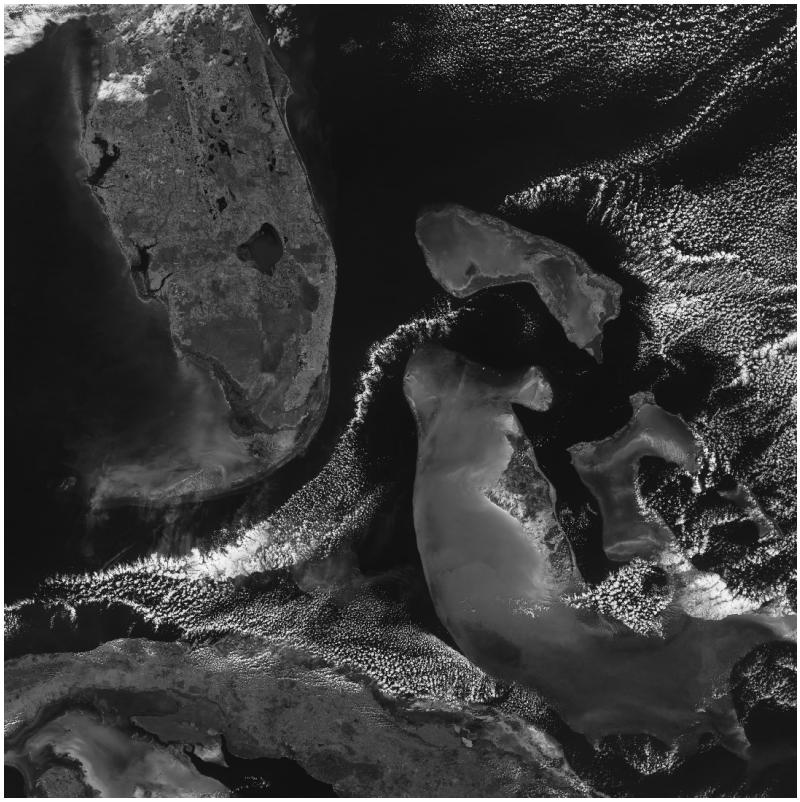

(d)

Figure 6.16 continued: Test images showing (c) a standard real test image of an airport and (d) a MODIS image of Florida and Bahamas (Captured on 24 January 2003, 1805 UTC.

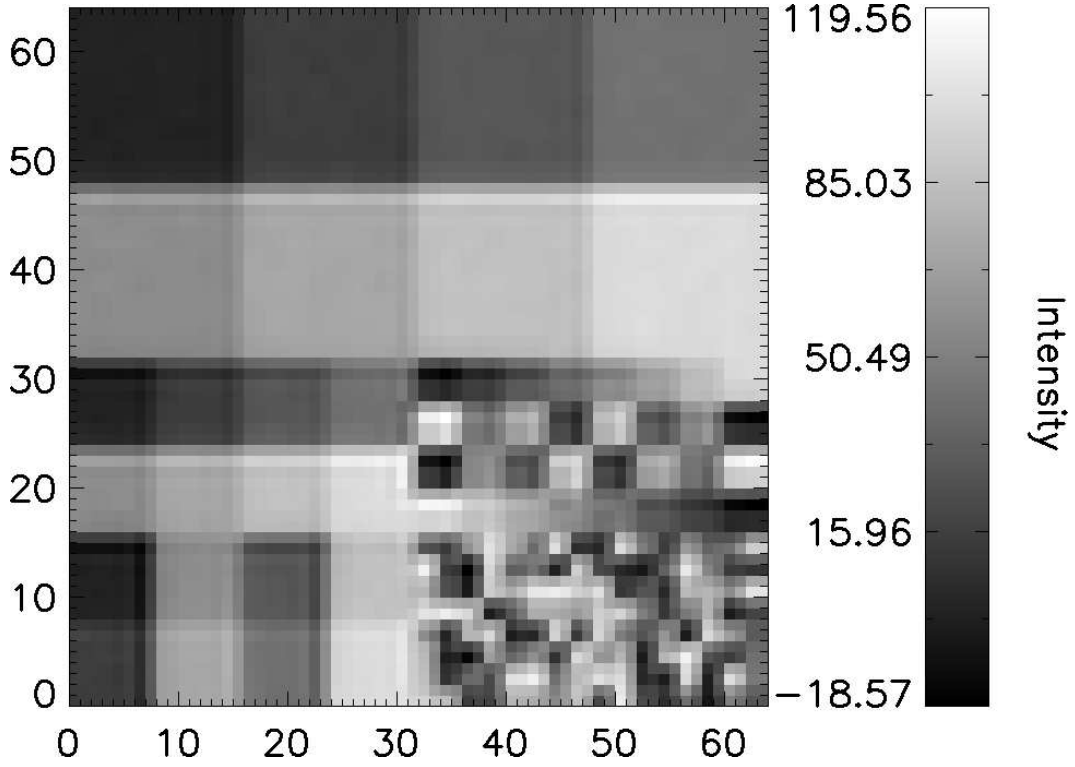

(a) MERE

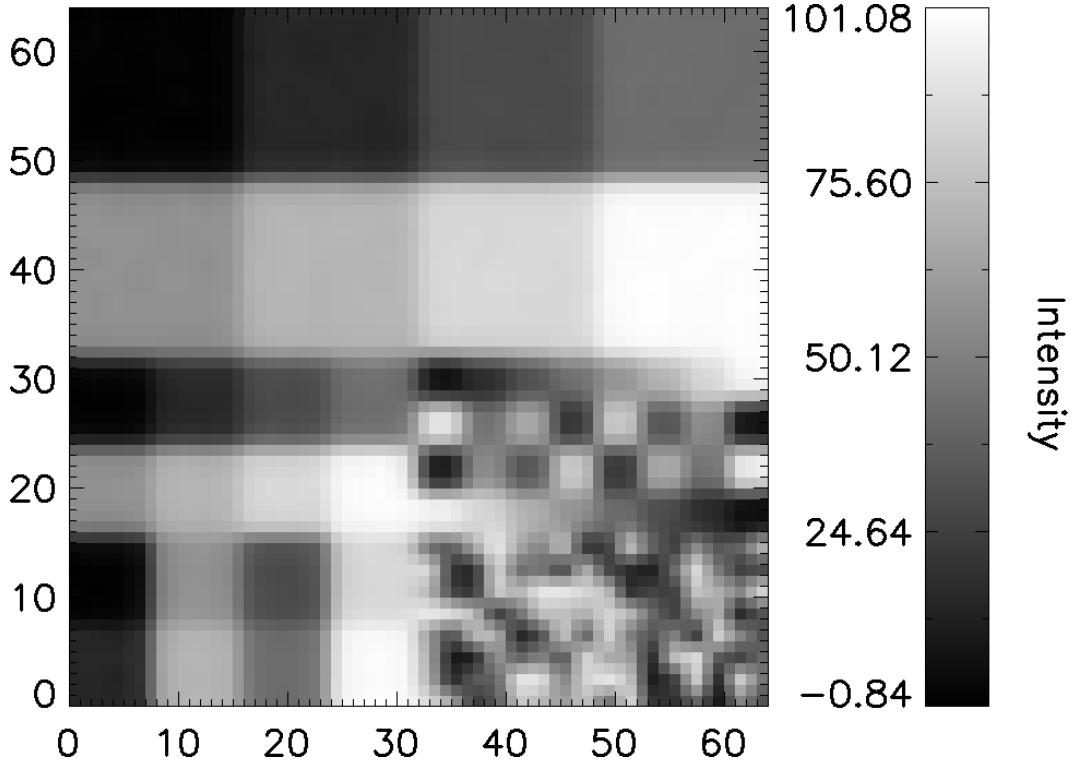

(b) Bilinear interpolation

Figure 6.17: Resolution-enhanced result comparison for USC texture mosaic #2 (Figure 6.16(a)) showing (a) the MERE reconstructed result and (b) the bilinearly interpolated result.

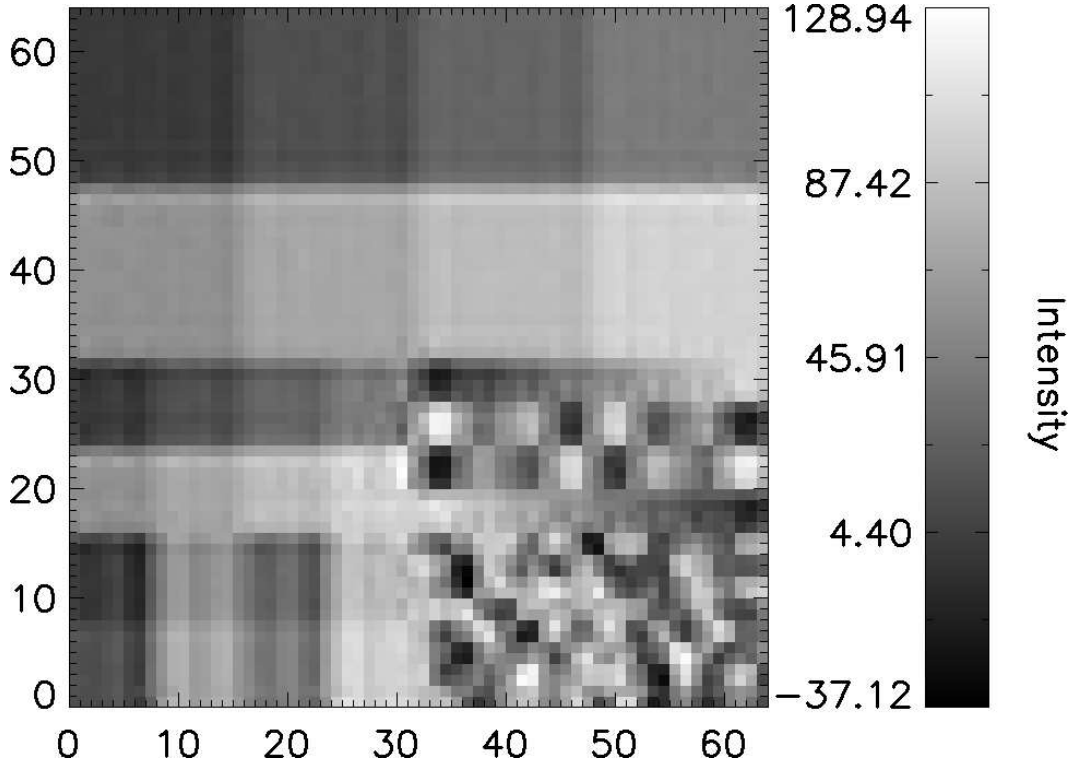

(c) Tikhonov enhancement

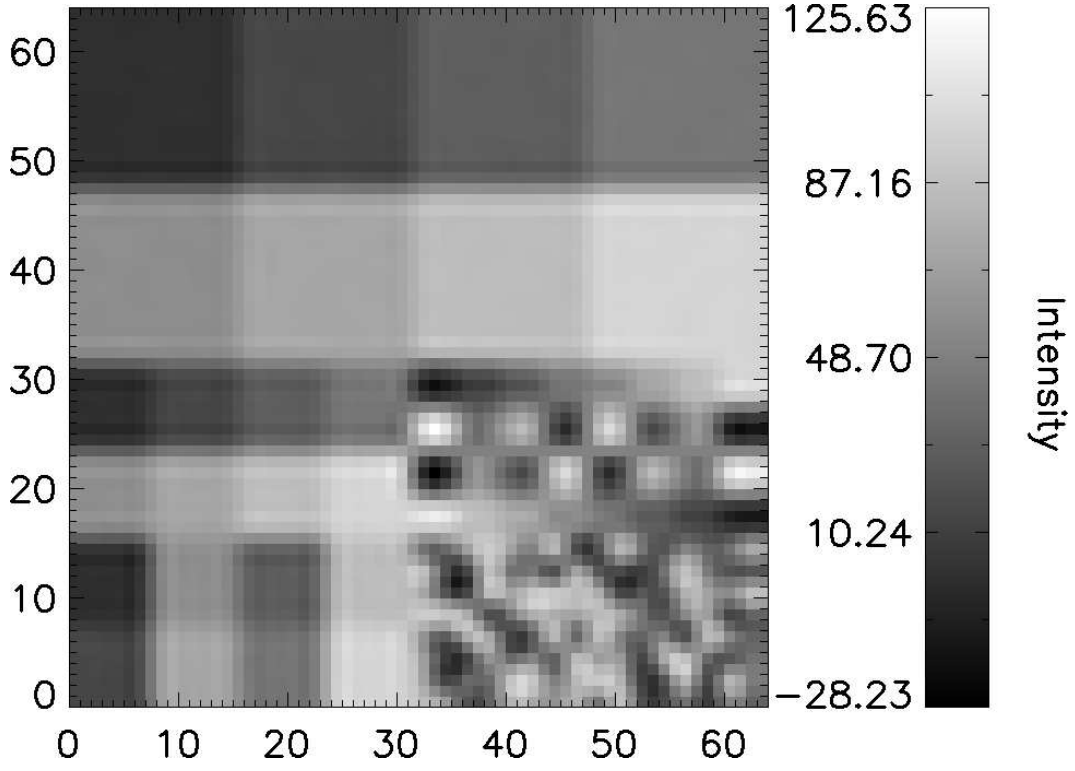

(d) Bicubic interpolation

Figure 6.17 continued: Resolution-enhanced result comparison for USC texture mosaic #2 (Figure 6.16(a)) showing (c) the Tikhonov resolution enhancement result and (d) the bicubic interpolated result.

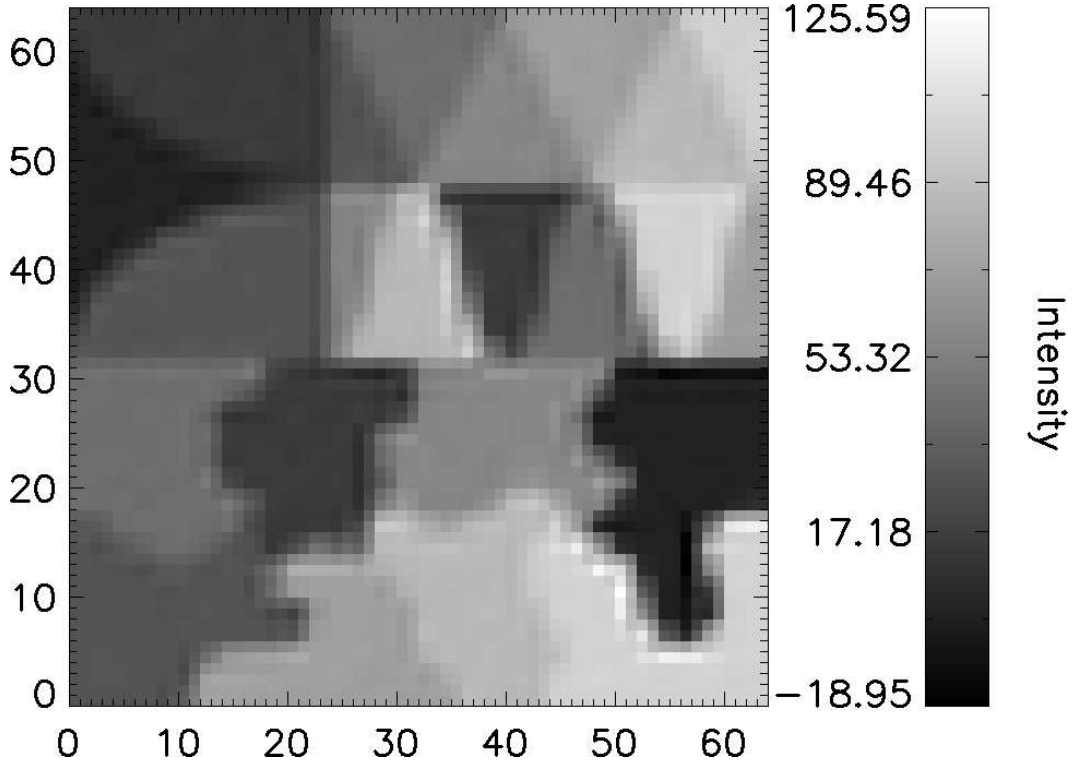

(a) MERE

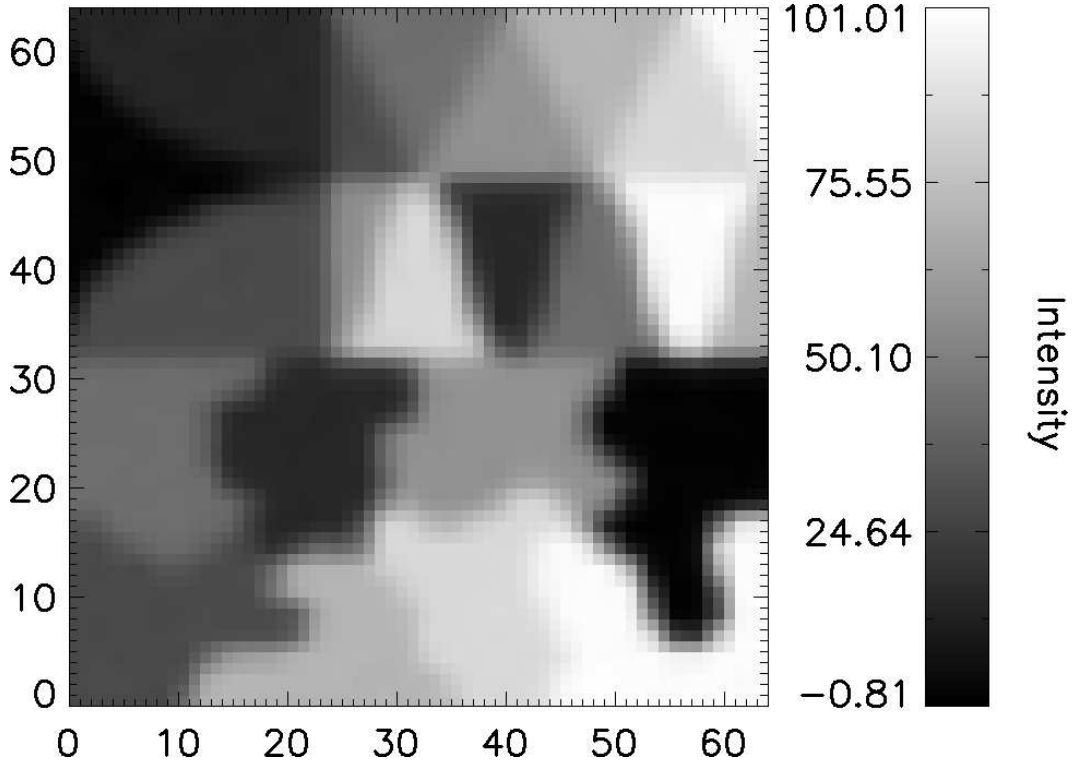

(b) Bilinear interpolation

Figure 6.18: Resolution-enhanced result comparison for USC texture mosaic #3 (Figure 6.16(b)) showing (a) the MERE reconstructed result and (b) the bilinearly interpolated result.

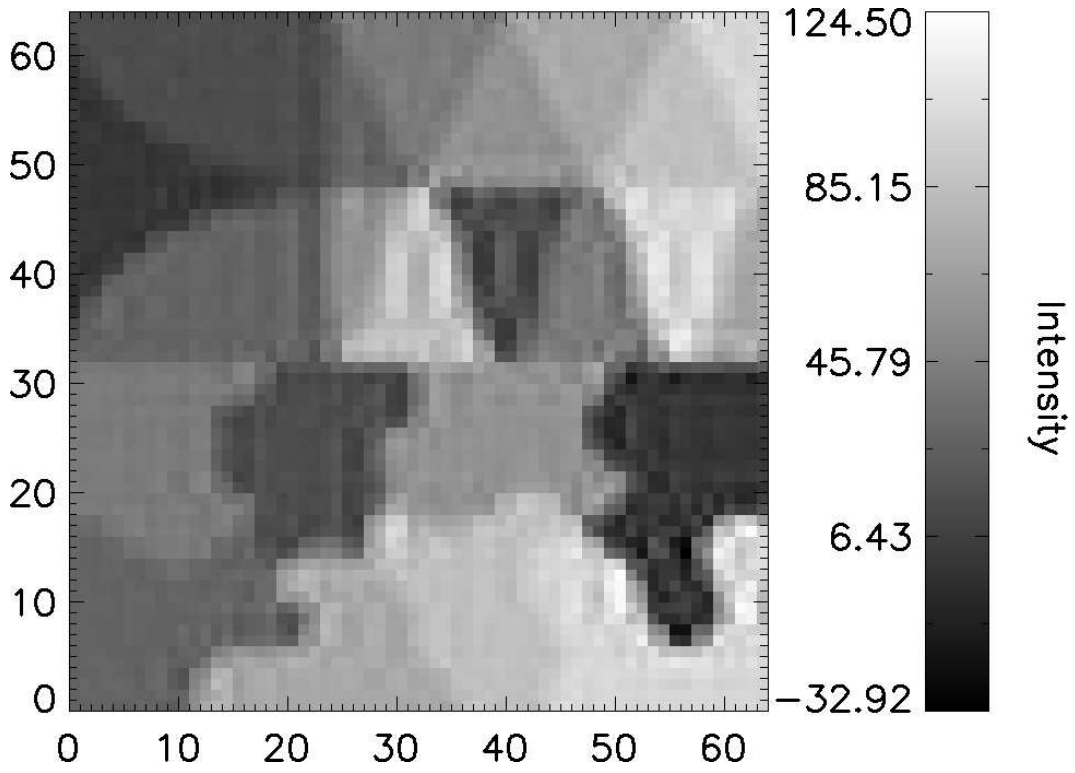

(c) Tikhonov enhancement

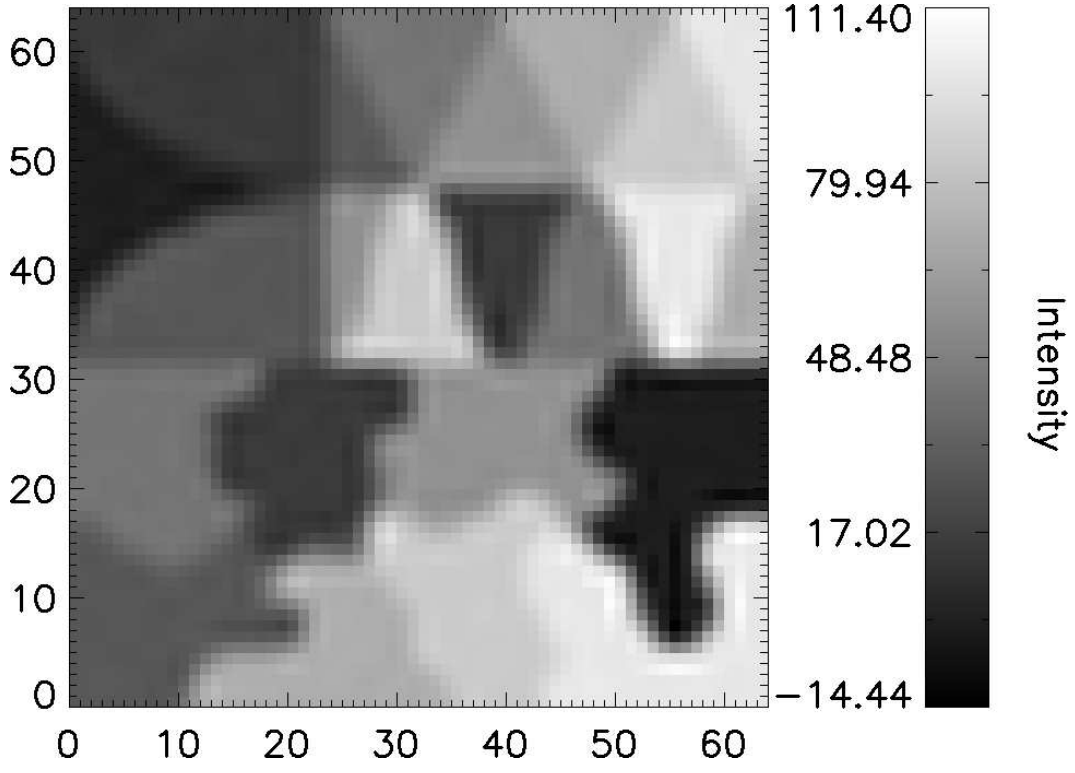

(d) Bicubic interpolation

Figure 6.18 continued: Resolution-enhanced result comparison for USC texture mosaic #3 (Figure 6.16(b)) showing (c) the Tikhonov resolution enhancement result and (d) the bicubic interpolated result.

containing the minimum and maximum values. However, it is incapable of restoring the desired resolution-enhanced intensity range in natural images as seen in Figures 6.19 and 6.20.

Synthetic imagery does, however, allow for a comparison of how the four resolution enhancement methods reconstruct uniform high-contrast edges. Bilinear interpolation operates as expected and blurs high-contrast edges. MERE, Tikhonov resolution enhancement, and bicubic interpolation over-reconstruct opposing sides of the discontinuities, often producing lines of darker and brighter pixels on the darker and brighter sides of the discontinuities respectively. Again, this effect is encountered most with synthetic imagery and is not as severe in natural imagery. Tikhonov resolution enhancement visibly increases artefact creation in the images (Figures 6.17(c) and 6.18(c)). MERE visually and quantitatively appears to produce the most accurate result (Table 6.1). The high-frequency component of Figure 6.17 provides an interesting challenge for the resolution enhancement methods. This can be considered one of the hardest signals to recover for resolution enhancement because it simultaneously contains high-frequency and high-contrast information. Both interpolation techniques significantly blur this region of the test image while the MERE and Tikhonov methods restore the high-frequency content more accurately (Table 6.1).

The natural imagery in Figures 6.19 and 6.20 provide a more realistic example and it is clear that Tikhonov resolution enhancement continues to be affected by spurious artefact creation. MERE appears to reconstruct more high-frequency information than the interpolation techniques and individual planes are almost recognisable (Figure 6.19). Figure 6.20 depicts a typical remote sensing image containing shallow and deep waters, as well as land and clouds. Again, the MERE algorithm appears to provide a superior reconstruction without overly smoothing the result. The Tikhonov resolution enhancement method quantitatively produces the most accurate results for this particular image, even including its artefact creation issues (Table 6.1). However, when averaged over all of the test images, the MERE algorithm provides the best reconstruction accuracy out of the resolution enhancement techniques included in this comparison.

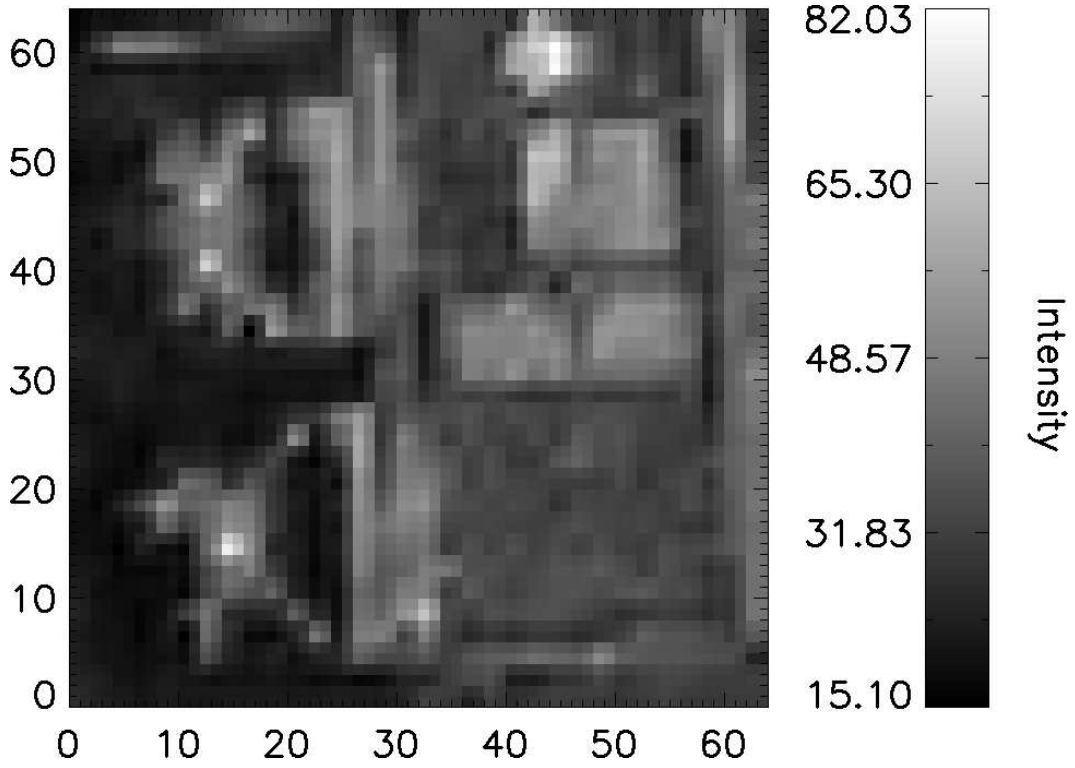

(a) MERE

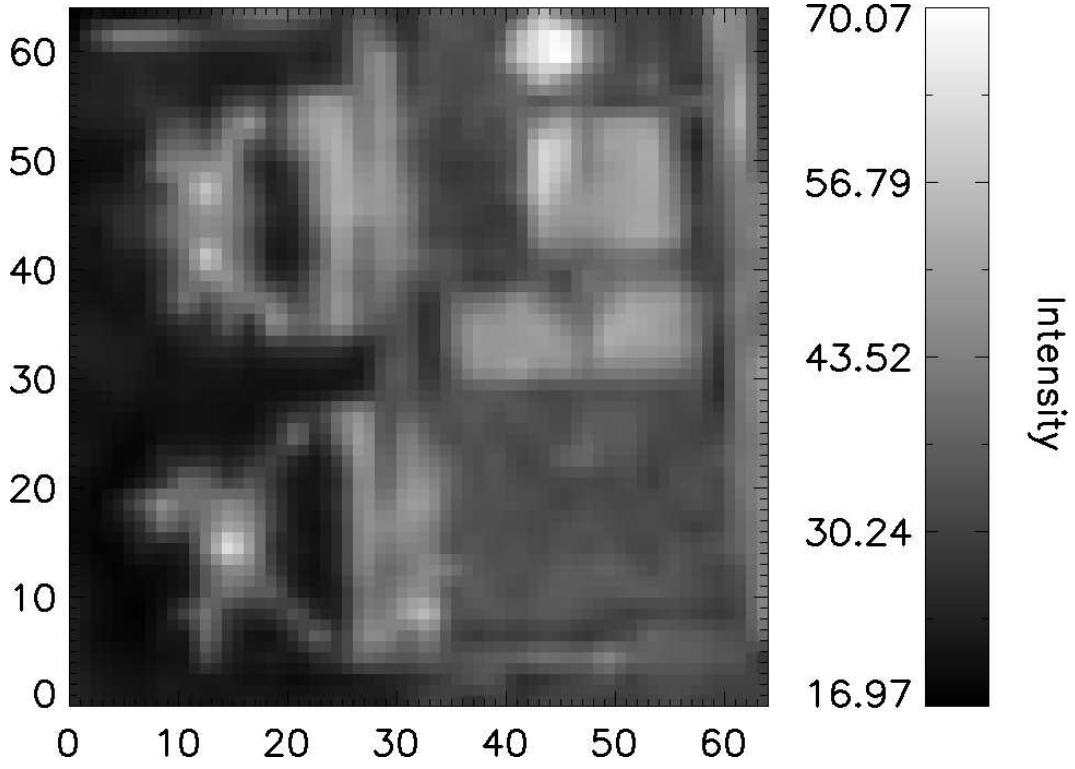

(b) Bilinear interpolation

Figure 6.19: Resolution-enhanced result comparison for standard airport test image (Figure 6.16(c)) showing (a) the MERE reconstructed result and (b) the bilinearly interpolated result.

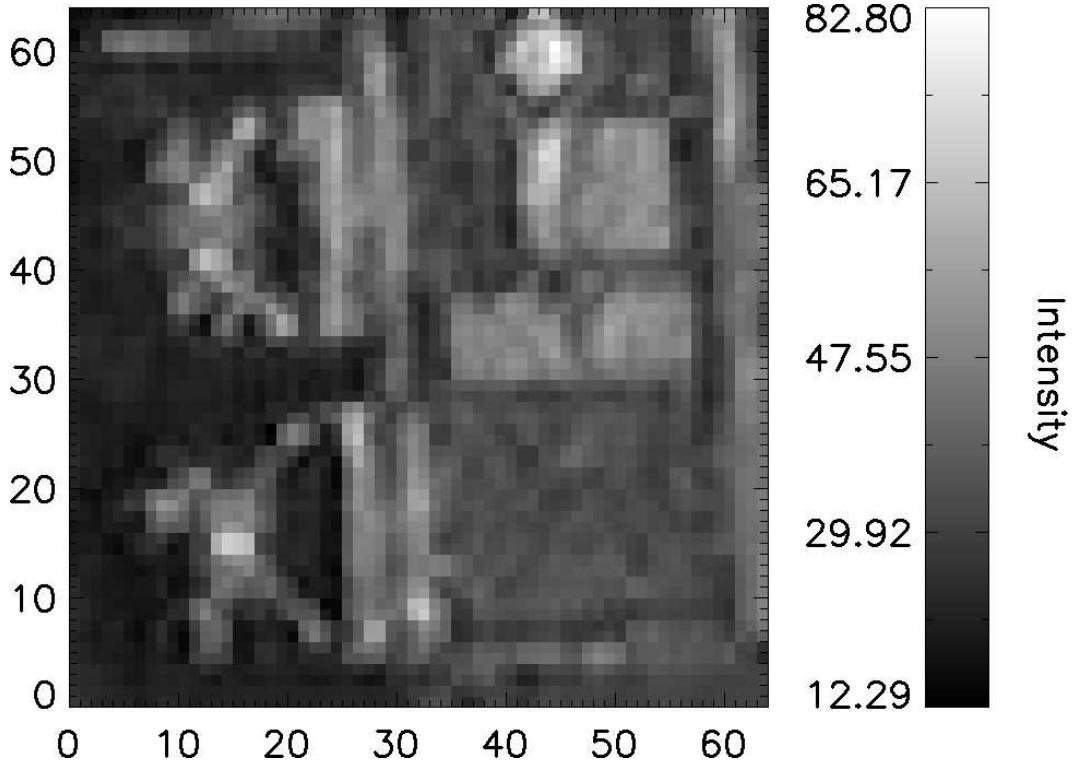

(c) Tikhonov enhancement

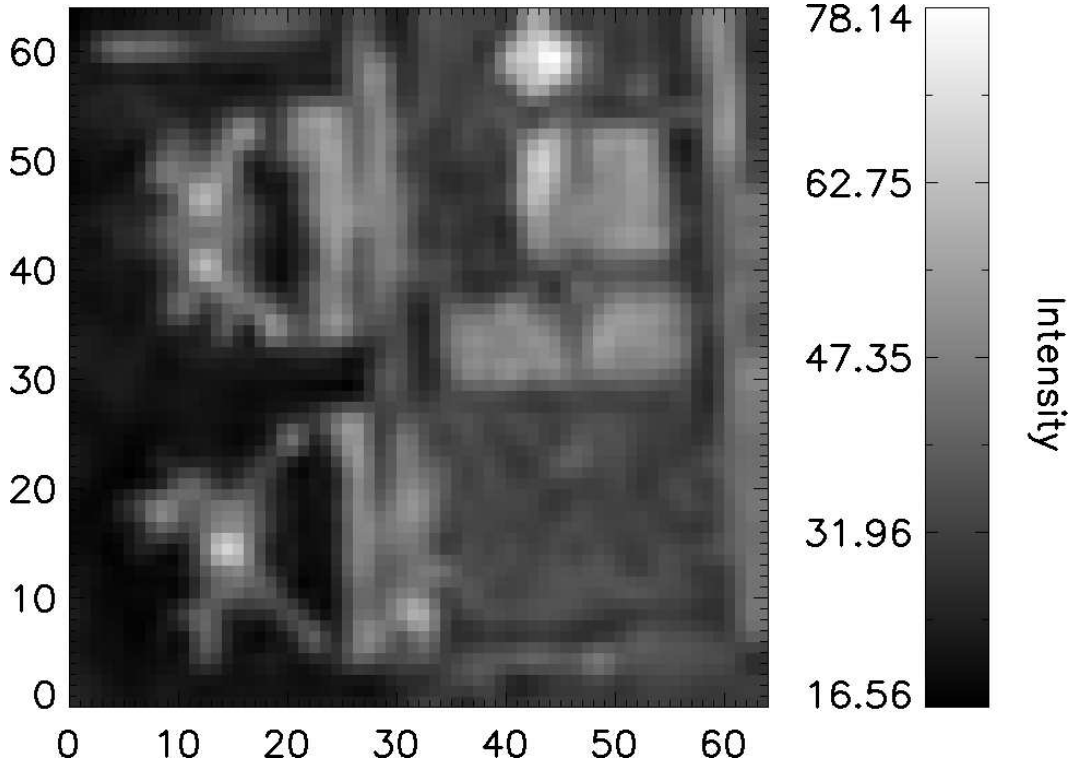

(d) Bicubic interpolation

Figure 6.19 continued: Resolution-enhanced result comparison for standard airport test image (Figure 6.16(c)) showing (c) the Tikhonov resolution enhancement result and (d) the bicubic interpolated result.

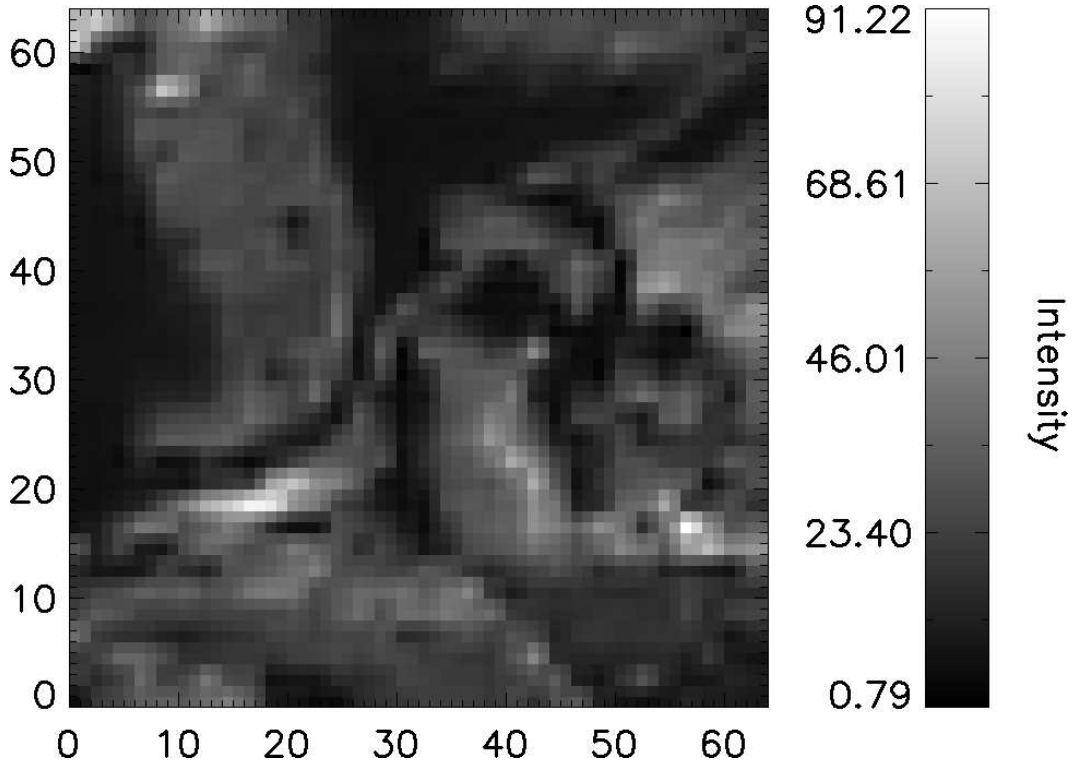

(a) MERE

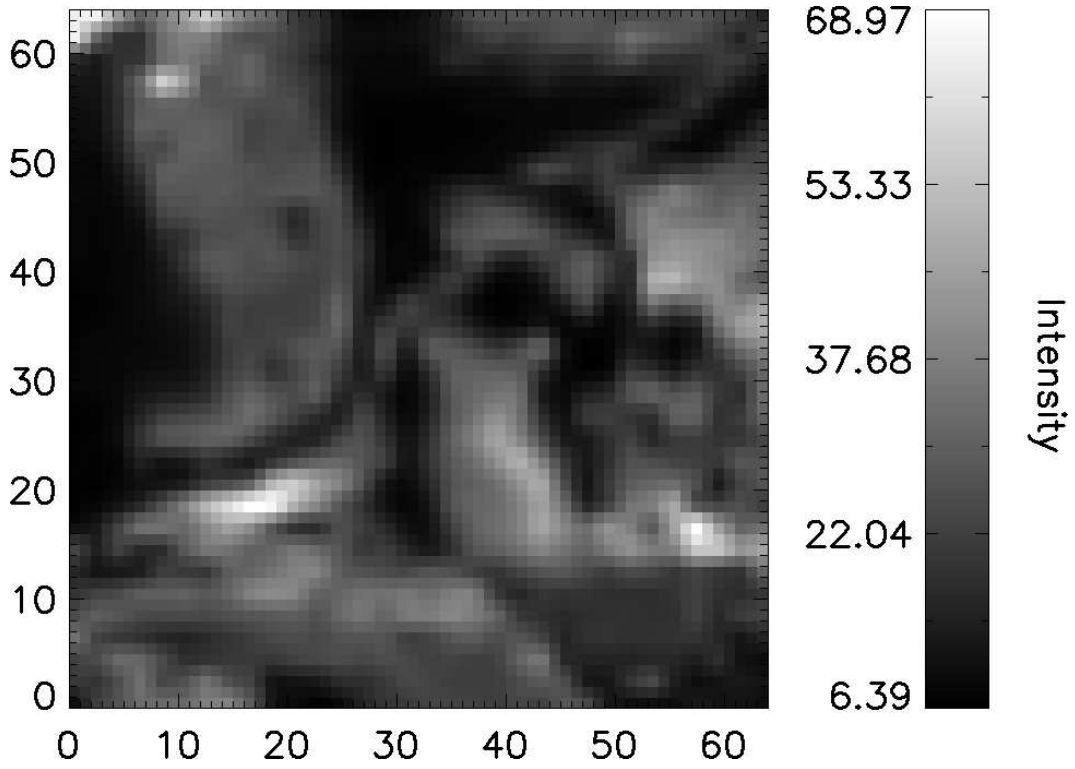

(b) Bilinear interpolation

Figure 6.20: Resolution-enhanced result comparison for MODIS test image (Figure 6.16(d)) showing (a) the MERE reconstructed result and (b) the bilinearly interpolated result.

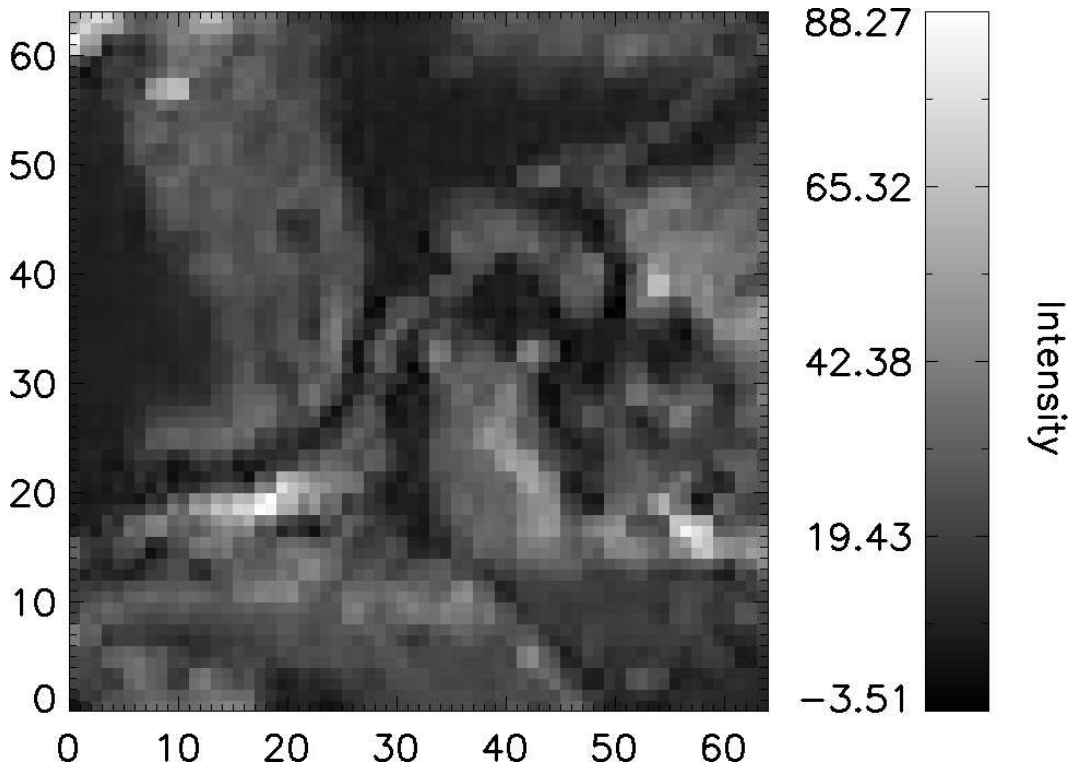

(c) Tikhonov enhancement

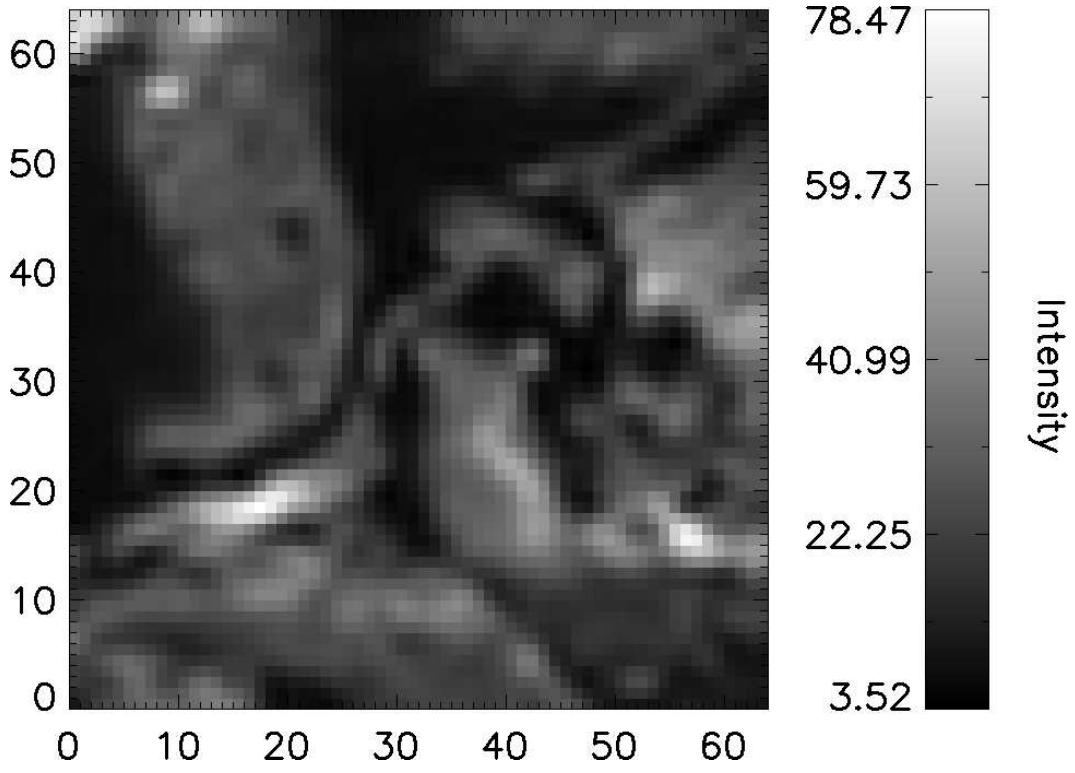

(d) Bicubic interpolation

Figure 6.20 continued: Resolution-enhanced result comparison for MODIS test image (Figure 6.16(d)) showing (c) the Tikhonov resolution enhancement result and (d) the bicubic interpolated result.

Table 6.1: Reconstruction errors calculated using the Euclidean difference norm method for each test image and resolution enhancement method. Bold numbers indicate the smallest reconstruction errors and therefore the most accurate resolution enhancement method for each test image.

Test image	MERE	Bilinear	Tikhonov	Bicubic
1 - USC #2	**3811.31**	6291.74	5583.42	6786.59
2 - USC #3	**2922.11**	3441.88	3068.71	3675.05
3 - Airport	**2927.25**	2930.44	3172.35	3089.34
4 - MODIS	2308.94	2422.31	**2226.25**	2453.35
5 - Lena	**3316.64**	3437.84	3783.85	3608.25
Average	**3057.25**	3704.84	3566.92	3922.52

6.4.1 Solution Quality Analysis

Having identified that the Tikhonov method visibly amplifies artefacts in the solution, it is important to objectively quantify that this is the case. Wang and Bovik (2004) developed an objective Structural SIMilarity (SSIM) index that compares local patterns of pixel intensities, normalised for luminance and contrast, between two images. If one of the input images is the original distortion-free image, then the SSIM index represents the quality of the second input image. A SSIM index of 1 indicates an ideal solution with no distortion and an index of 0 represents severe distortion and image degradation. The results of applying this technique to the resolution enhancement methods for each test image are reported in Table 6.2, where the two image inputs are the original VHR truth image and the nearest-neighbour interpolated resolution-enhanced result for each method. In every case, the Tikhonov result produces the smallest SSIM index values. This quantitatively indicates that the Tikhonov method amplifies the creation of spurious artefacts and can be discarded as producing unreliable results for this reason.

Overall, the MERE algorithm compares favourably with the other resolution enhancement methods qualitatively and quantitatively across the selected range of test images. The average reconstruction errors and SSIM indices over all of the test images indicate that MERE outperforms the other methods and visually MERE

produces the most compelling results.

6.4.2 Gradient Step Size

Returning to the operation of the MERE algorithm, Figure 6.21 displays the gradient step size, γ, at each iteration of the resolution enhancement process (Equation 6.15). The stability of the step size variable is determined by the balanced combination of the data fidelity and regularisation terms (Equation 6.5). If λ is selected to be too large and MRE overpowers the search direction, γ is repeatedly calculated to be very small and the gradient method ultimately fails to find a stable solution, terminating after exhausting the maximum number of iterations. This is because there is no step size quantity, positive or negative, to move in the direction of the gradient that would result in minimising the cost function and finding a stable solution. Alternatively, if λ is selected to be too small and the data fidelity term overpowers the search direction, then γ will typically be very small for several iterations and then be extremely large for a single iteration. This is because not enough regularisation has been applied to the problem and the solution space is relatively flat. When extremely large steps are taken, severe artefacts are created around discontinuities contained in the image and the final result becomes undesirable. Here again, the gradient method fails to converge on a unique solution and terminates after reaching the maximum iteration limit. Ideally, γ needs to slowly converge to 0. This would indicate that the reconstruction has moved in the direction of the gradient (Equation 6.13) and minimised the cost function (Equation 6.5), successfully becoming close enough to the unique solution to be convergent and terminate the reconstruction process. This case is exemplified in Figure 6.21. The convergence of the gradient method is directly related to the successful evaluation of the λ parameter for resolution enhancement (Equation 6.12). The fluctuations seen in γ correspond to the gradient method attempting to minimise the cost function by moving in the direction of the steepest slope. The magnitude of the fluctuations are a result of the ill-posed nature of the resolution enhancement problem and can be expected to become larger as the REF is increased. While some fluctuations in γ occur, the overlying trend appears to converge to 0. This particular MERE operation managed to find a unique solution

Table 6.2: Structural similarity index values calculated for each test image and resolution enhancement method. A structural similarity index of 1 indicates an ideal solution with no distortion and an index of 0 represents severe distortion and image degradation. Bold numbers indicate the smallest structural similarity index value and therefore the most distorted and degraded resolution-enhanced image.

Test image	MERE	Bilinear	Tikhonov	Bicubic
1 - USC #2	0.8762	0.8329	**0.7876**	0.7982
2 - USC #3	0.8630	0.8643	**0.8112**	0.8548
3 - Airport	0.6494	0.6500	**0.6415**	0.6449
4 - MODIS	0.7204	0.7164	**0.7072**	0.7129
5 - Lena	0.7403	0.7412	**0.6853**	0.7361
Average	0.7699	0.7610	**0.7266**	0.7494

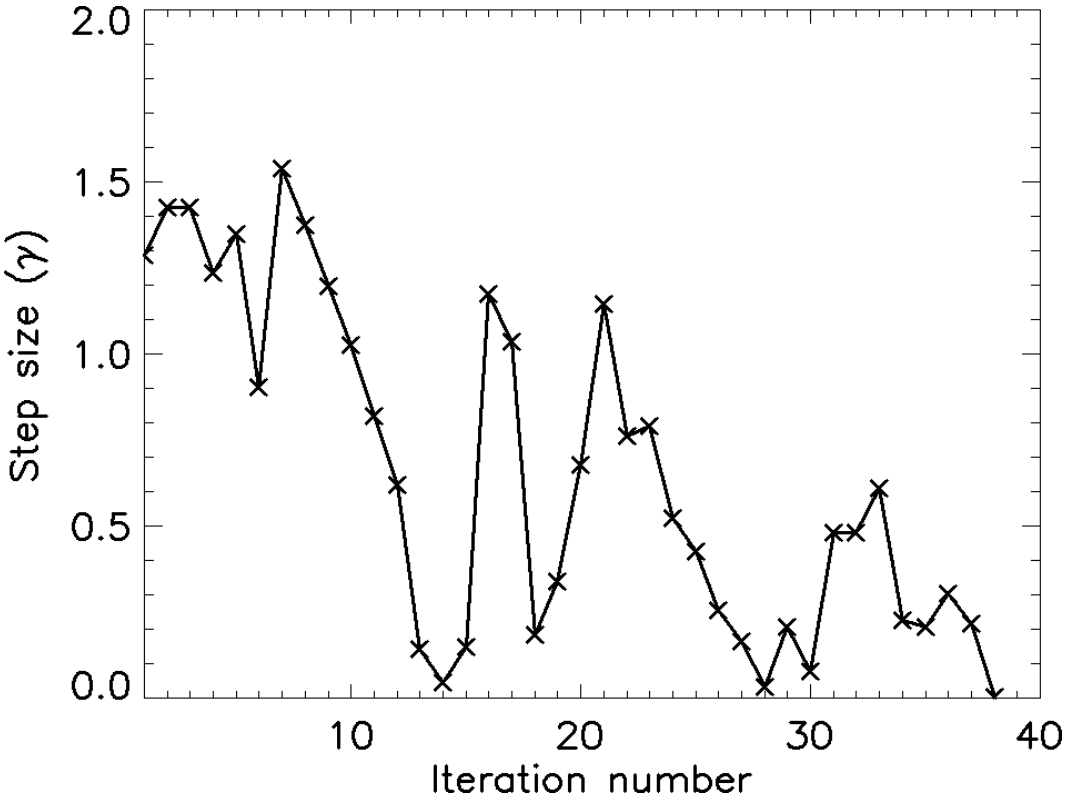

Figure 6.21: Gradient step size, γ, at each iteration of the MERE algorithm. The gradient step size contains some minor fluctuations, slowly converging to 0 as a unique and stable solution is approached and successfully terminating the reconstruction at iteration 39.

that is sufficiently stable to become convergent and terminate the reconstruction at iteration 39.

6.4.3 Computational Complexity

Comparing the computational complexities of the four resolution enhancement methods will help determine if the quantitative benefits of the MERE approach come at a reasonable operational cost. Let n be the width and height of the square LR image to undergo resolution enhancement. The REF is a scalar multiplier of the image size n and is therefore irrelevant for the purpose of computational complexity analysis. The computational complexities of interpolation methods have been well established and are reported in Table 6.3 (Goshtasby, 2005).

Table 6.3: Computational complexities of nearest-neighbour, bilinear, bicubic convolution and bicubic spline image resamplings of an $n \times n$ pixel image.

Type of Resampling	Computational Complexity
Nearest-Neighbour	$O(n^2)$
Bilinear Interpolation	$O(n^2)$
Bicubic Convolution	$O(n^2)$
Bicubic Spline, Direct Computation	$O(n^4)$
Bicubic Spline, Using FFT	$O(n^2 \, log \, n)$

From the three bicubic interpolation methods reported in Table 6.3, bicubic convolution is selected for implementation because it provides the same interpolation results as the direct computation and FFT methods, but at reduced computational cost. Therefore, bicubic and bilinear interpolation both have the same computational complexity, but practically, bicubic interpolation takes longer to compute because it performs more calculations within this order of complexity. This computational complexity analysis can be extended to include the MERE and Tikhonov resolution enhancement methods by tracing the operational code and identifying the most computationally significant calculations. MERE is a non-linear resolution enhancement method that has the potential to converge at any iteration number. Therefore, a worst case scenario is assumed and the code is analysed with the

maximum number of algorithm iterations in mind. An inspection of the operation code revealed the computational requirements for each component in the MERE and Tikhonov algorithms reported in Table 6.4.

Table 6.4: Computational complexities of the components required to enhance spatial resolution using MERE and Tikhonov resolution enhancement.

Algorithm Component	Computational Complexity
Linear system construction	$O(n^4)$
MERE solver	$O(n^4)$
MERE Total	$O(n^4)$
Singular Value Decomposition (SVD)	$O(n^6)$
Generalised Cross-Validation (GCV)	$O(n^4)$
Tikhonov solver	$O(n^6)$
Tikhonov Total	$O(n^6)$

The complete MERE algorithm consists of building the linear system and finding a solution using the MERE solver. The linear system is built by stepping through each data point in the HR input image ($O(n^2)$) and performing a response function calculation which has a further cost of $O(n^2)$. Therefore, the linear system construction has a total computational complexity of $O(n^4)$. The most computationally complex calculation in the MERE solver is a matrix multiplication of a $n^2 \times n^2$ and $1 \times n^2$ matrix which results in an $O(n^4)$ operation. The total MERE algorithm also has the computational complexity of $O(n^4)$ as none if its components exceed this complexity order.

The Tikhonov resolution enhancement method is a combination of the construction of the linear system, a Singular Value Decomposition (SVD), a Generalised Cross-Validation (GCV) calculation that determines the regularisation parameter λ, and the Tikhonov solver. A SVD operation is known to have a computational complexity of $O(m^2n + n^3)$, where m and n are the dimensions of the input matrix A (Golub and Loan, 1996). Considering a square image where m and n are of equal length, the computational complexity of a SVD operation now becomes $O(n^3)$, where constants can be discarded and only the highest complexity

order is relevant. The construction of the linear system results in the A matrix having dimensions $(REF \times n)^2 \times n^2$, which, for the purposes of computational complexity analysis, can be simplified to $n^2 \times n^2$. Therefore, n^2 must be substituted into the previous computational complexity for a SVD calculation to account for the size of the resolution enhancement A matrix. This results in the overall computational complexity for a SVD calculation now becoming $\mathrm{O}(n^6)$. The GCV method operates at $\mathrm{O}(n^4)$ complexity which is dominated by a $n^2 \times n^2$ and $1 \times n^2$ matrix multiplication. The most complex calculation in the Tikhonov solver is a matrix multiplication of two $n^2 \times n^2$ matrices, which also results in a computational complexity of $\mathrm{O}(n^6)$.

It should also be noted that an increase in the input image size results in rapid growth of the A matrix dimensions. In fact, as the square input image dimension n becomes larger, the A matrix increases at a rate of n^4. This represents extreme growth and results in the MERE algorithm quickly exhausting the maximum accessible RAM capacity in a single computer. For this reason, the analysis of the MERE algorithm is limited to resolution-enhanced image sizes no greater than 64×64 pixels and REFs no greater than 4.

6.4.4 PSF Structure

Another avenue for investigation is how PSF shape affects the performance of the MERE algorithm. Since the natural convolution process is the step that redistributes VHR information, it is conceivable that the ability to enhance image resolution could be quite sensitive to fluctuations in the PSF. Figure 6.22 shows the reconstruction errors encountered when the Full-Width Half-Maximum (FWHM) of a VHR Gaussian PSF is increased from 1 to 150 pixels, following the experimental design in Figure 6.10. A VHR PSF FWHM of 1 is a reasonably accurate scenario for satellite instruments because they are designed to be precise, free from aberration and therefore produce minimal blurring. As the PSF FWHM increases up to approximately 28, the ability of MERE to enhance spatial resolution is immediately improved. This is an interesting region where the increase in blurring benefits the reconstruction accuracy and is not too severe that it completely eliminates high-

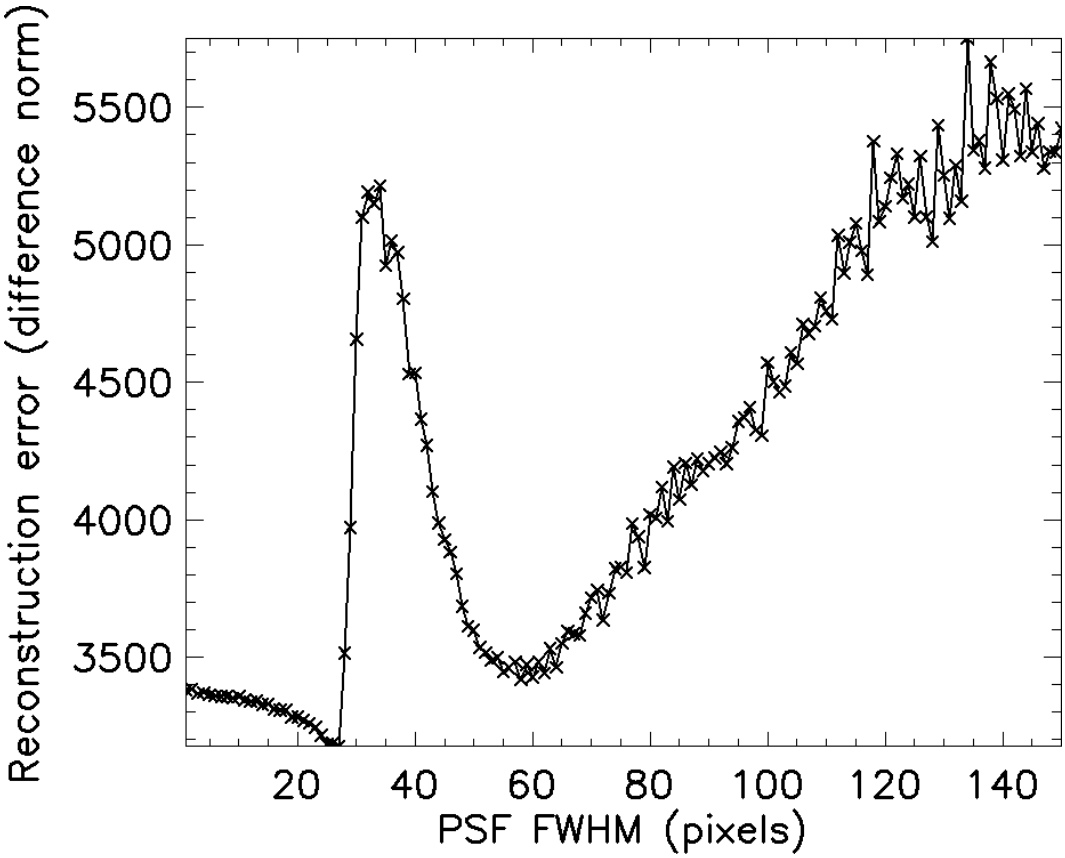

Figure 6.22: Resolution-enhanced reconstruction error calculated using the Euclidean difference norm method as a function of PSF FWHM.

frequency content. However, a region of reconstruction difficulty is encountered with the FWHM ranging from approximately 28 to 50. This effect is a result of the experimental design and signal discretisation. To gather all of the inputs to the MERE algorithm, deconvolution must be performed at LR and the LR PSF should ideally have odd dimensions. As the FWHM of the VHR PSF approaches the downscaling factor of 34, the equivalent LR PSF becomes an inaccurate representation of the VHR PSF. This is because with a small FWHM, the LR PSF will have its peak at a single central pixel. But as the FWHM becomes larger, the LR PSF begins to misrepresent the VHR PSF and have its peak spread out over a larger area. This inaccuracy manifests itself by degrading the quality of the deconvolution process with the FWHM between 28 and 50, which in turn affects the quality of the resolution-enhanced reconstruction. This effect is unavoidable because the entire experimental design is reliant on discrete signals. Disregarding this region of PSF inaccuracy, the remaining trend indicates that resolution enhancement

becomes more difficult as the FWHM is increased. This is an understandable result because the original VHR truth image gets progressively blurred as the FWHM is increased and greater quantities of high-frequency content are removed. This, in turn, limits the availability of information with which to construct the linear system and ultimately restricts the resolution enhancement abilities of the MERE algorithm.

6.4.5 Signal-to-Noise Ratio Analysis

The SNR of the input imagery is another important factor that will determine how well the MERE reconstruction performs. This can be investigated by increasing the quantity of Gaussian noise added at the LR stage of the experimental design (Figure 6.10) and then proceeding with the spatial resolution enhancement and comparison. The reconstruction error response to an increasing SNR is shown in Figure 6.23. It is clear that at small SNRs, where the signal is only approximately as large as the noise, it is difficult to enhance spatial resolution. However, as the SNR becomes larger and the size of the real signal begins to dominate the noise, the performance of MERE dramatically improves until levelling off. Ultimately, the SNR reaches a threshold at approximately 4, above which the noise has very little impact on reconstruction accuracy. For comparison, the MODIS Aqua detector SNR averaged over all of the ocean colour bands is approximately 791 (Xiong et al., 2005). Therefore, this result indicates that the MERE algorithm operates robustly with respect to realistic quantities of detector-based noise.

6.4.6 Varied Resolution Enhancement Factors

Thus far, a REF of 2 has been investigated and analysed. However, each of the four resolution enhancement methods are capable of larger integer-based REFs. This can be achieved by following the experimental design depicted in Figure 6.10 and altering the REF at the interpolation and MERE stages. The resolution-enhanced results for varying REFs must still be nearest-neighbour interpolated back to the original VHR so that direct comparisons can be made.

Figure 6.24 shows the reconstruction error of each resolution enhancement

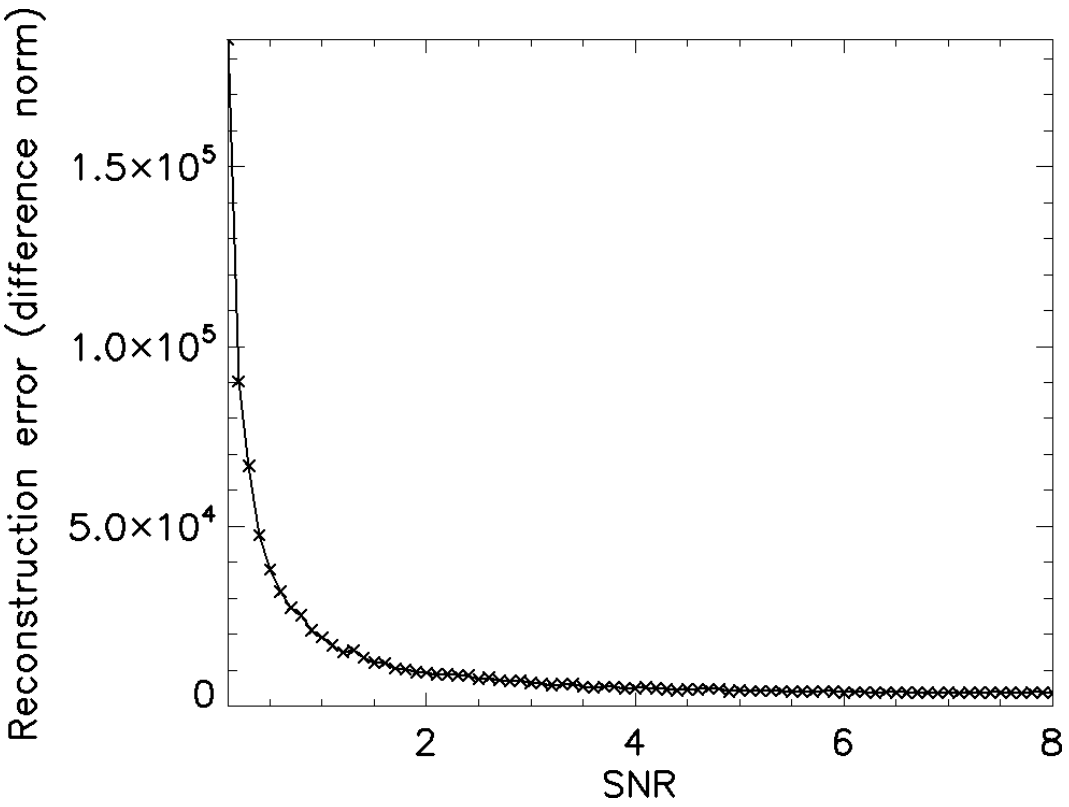

Figure 6.23: Resolution-enhanced reconstruction error calculated using the Euclidean difference norm method as a function of detector-based SNR.

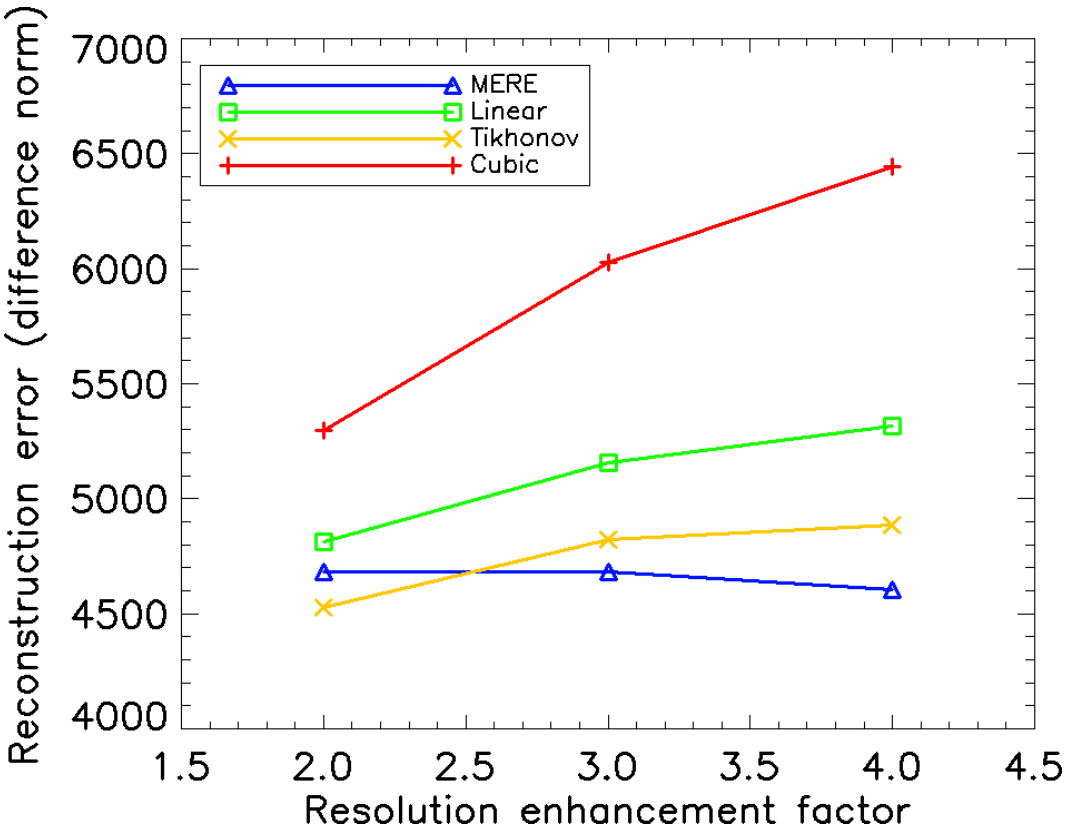

Figure 6.24: Resolution-enhanced reconstruction error calculated using the Euclidean difference norm method as a function of the resolution enhancement factor.

method as the REF is increased. The REFs of 2, 3 and 4 were selected for analysis since any REF above these values overwhelm the memory capacity of a single machine. Both interpolation and Tikhonov methods encounter larger reconstruction errors as the REF increases. This is due to a combination of the amount of high-frequency information preserved in the convolved image during the instrument convolution process, and the specific abilities of the resolution enhancement methods to extract this information. The interpolation methods are not designed to recapture this information and bicubic interpolation produces significantly worse results than bilinear interpolation. The Tikhonov method performs well at a small REF but also begins to produce larger reconstruction errors as the REF increases. Surprisingly, the MERE algorithm produces less total reconstruction error as the REF is increased. This suggests that the MRE constraint at the core of the MERE algorithm is beneficially restricting the linear system such that the reconstruction error improves for the analysed REFs. It also indicates that, while the Tikhonov constraint successfully minimises the residuals to determine the statistically best result, more than just a statistical measure is required to find a desirable solution to the linear system. This result indicates that structural information contained in two-dimensional imagery is vital and must be taken into account when attempting spatial resolution enhancement, a concept at the foundation of the MERE approach. It would be expected that the MERE algorithm would not continue to produce increasing reconstruction accuracy at higher REFs.

It is also important to visually inspect the reconstruction results using different REFs. Figures 6.25 and 6.26 show the resolution-enhanced reconstructions with varying REFs for the MERE and Tikhonov methods respectively. Using these REFs, a single LR pixel becomes a 2×2, 3×3 or 4×4 group of pixels and this is represented by the subfigures within Figures 6.25 and 6.26 being displayed at different sizes. The MERE results show a qualitatively reasonable solution for a REF of 2 (Figure 6.25(a)), but begin to exhibit mild square-shaped discontinuities at larger REFs (Figures 6.25(b) and 6.25(c)). This is largely due to the power-conserving constraint implemented in the construction of the linear system where groups of HR pixels are restricted to conform to the intensity of the corresponding

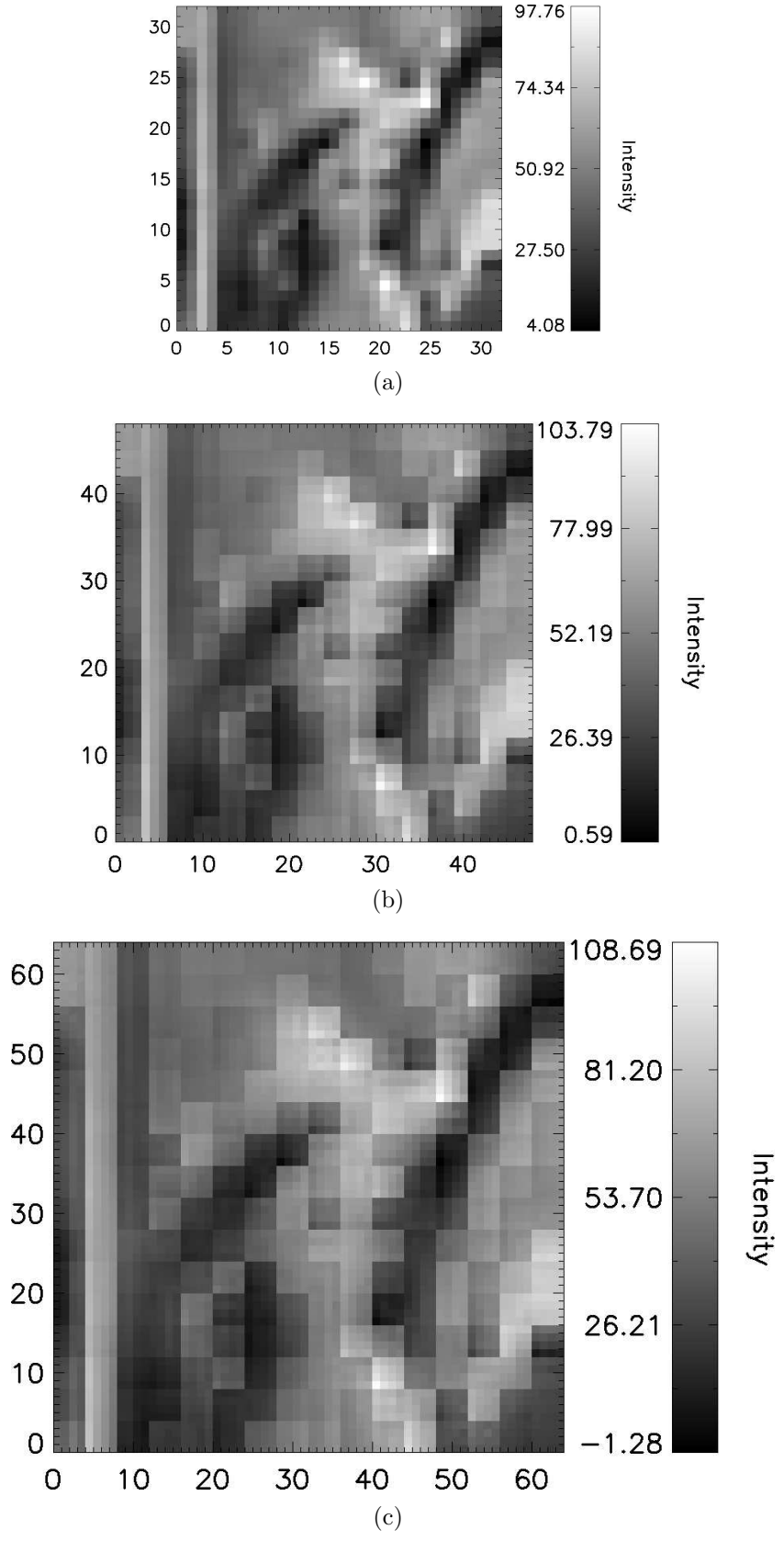

Figure 6.25: Resolution-enhanced reconstructions with resolution enhancement factors of (a) 2, (b) 3 and (c) 4 using the MERE algorithm.

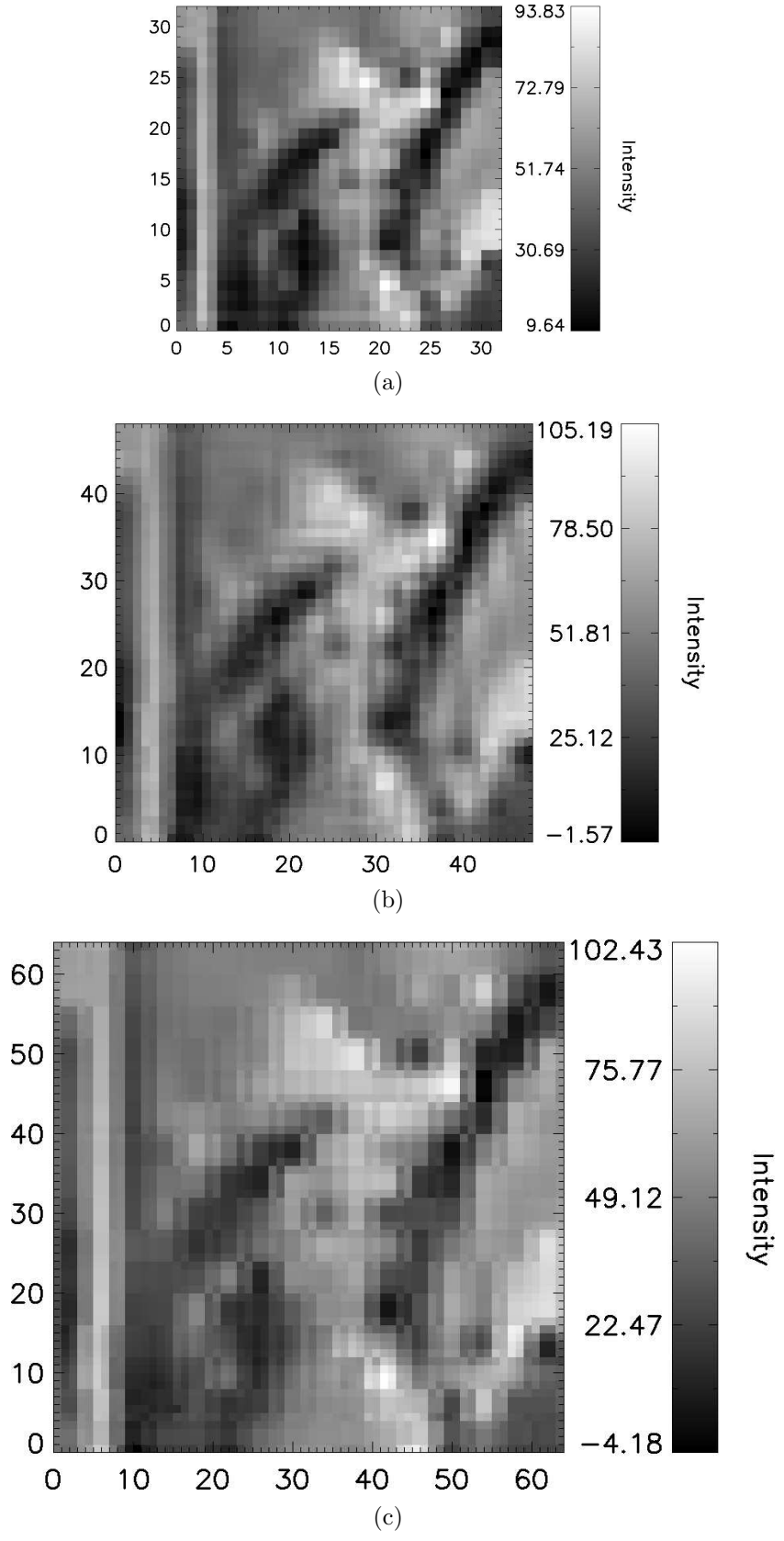

Figure 6.26: Resolution-enhanced reconstructions with resolution enhancement factors of (a) 2, (b) 3 and (c) 4 using the Tikhonov method.

LR pixel (Section 6.2). There are some possible techniques that could be employed to minimise these discontinuities, such as adding an offset power-conserving constraint to the linear system. However, there is no real-world physical process in the satellite optical system that calls for such a constraint, and any additional constraints would just serve to improve the qualitative results. As such, no further constraints to the linear system will be investigated. It is interesting to note that, even with the square-shaped discontinuities, the MERE results with larger REFs produce smaller overall reconstruction errors when compared with the original VHR image (Figures 6.24 and 6.25). The Tikhonov method produces a reasonable reconstruction at a REF of 2, but begins to produce irregularities when pushed to larger REFs (Figure 6.26). In fact the Tikhonov REF of 2 result (Figure 6.26(a)) quantitatively outperforms the other resolution enhancement methods (Figure 6.24). This can happen occasionally depending on the specific properties of the input system, as has been seen previously in Table 6.1.

6.4.7 Future Work

There are some practical limitations to the MERE method. The current implementation of the MERE algorithm requires that the HR PSF dimensions be at most half the size of the LR image dimensions in order to calculate the renormalised point-wise PSF response required by the construction of the linear system. This limitation causes no unintended effects, but could potentially be replaced with an alternative method that does not contain the same limitation.

There is also the possibility to extend the MERE and Tikonov algorithms to incorporate non-integer REFs. The current implementation has been designed to provide proof-of-concept that spatial resolution enhancement is indeed possible through modelling a HR PSF convolution process and solving a linear system. This has been carried out for the simple case of integer REFs. However, it is highly likely that the optimum REF will be a non-integer value. Therefore, non-integer REF compatibility would be desirable. There are several changes that must be made to the current MERE implementation to allow for non-integer REF support. Firstly, the LR convolved and deconvolved imagery must be interpolated by the desired

non-integer REF. For instance, if a REF of 2.5 was selected, each LR pixel would be interpolated to cover a 2.5×2.5 pixel area. The 0.5 of the original LR pixel that crosses the border would account for 50 percent of the value of the new HR pixel, with the other 50 percent coming from the adjacent 0.5 LR pixel, as calculated using interpolation by averaging. The HR PSF convolution process could then be modelled on a per-pixel basis at HR rather than a per-pixel-group basis, effectively removing the concept of a HR composite convolution. This would result in a greater number of constraint equations in the linear system, but may not necessarily improve the ill-posed nature of the problem. The power conserving constraint could then be constructed, but would not appear as well-structured as the previous definition. The interpolation step would generate new pixel values for every HR pixel that crosses a LR pixel border. The power constraints could be simplified into single equations where multiple adjacent pixels contain the same value, but there would still be individual constraint equations containing a variable number of elements. All of these changes would culminate in the MERE algorithm supporting non-integer REFs.

It is also the case that the operational MERE code has not been optimised. There is not a great deal of opportunity to improve the computational complexity of the MERE algorithm for computation on a single machine because the calculation is dominated by a $n^2 \times n^2$ and $1 \times n^2$ matrix multiplication, resulting in an $\mathrm{O}(n^4)$ operation. However, this calculation could be parallelised and computed on GPUs with significant gains in computational speed (Ohshima et al., 2007; Cui et al., 2009). The CUDA and OpenCL frameworks both provide parallel computing capabilities that are compatible with the MERE algorithm and could offer an attractive implementation opportunity (NVIDIA, 2009; Khronos OpenCL Working Group, 2008). Such an implementation would be executable across heterogeneous platforms. The increased speed of computation from parallel calculations would make the MERE algorithm practical to use. Algorithm parallelisation is beyond the scope of this work, but is noted as potential future work. The construction of the linear system could also be further optimised, which would affect the performance of the MERE algorithm. Currently, the linear system is built using a brute-force approach,

but could conceivably be optimised by implementing a convolution PSF response operation. This improvement would have no effect on the results of the MERE method, but may slightly improve the overall runtime of the technique.

6.5 Summary

A novel approach to spatial resolution enhancement has been established and is shown to successfully extract high-resolution content from a range of test imagery under a maximum entropy framework named MERE (Maximum Entropy Resolution Enhancement). This technique involves the creation of a system of linear equations that relate Low-Resolution (LR) convolved data points to LR deconvolved data points using a High-Resolution (HR) Point Spread Function (PSF). This critically requires the PSF of the optical system to be sampled at the same frequency as the intended final resolution-enhanced output image. In this way, a HR underdetermined linear system is constructed and can be solved using additional Multiresolution Entropy and power-conserving constraints.

Results show that the MERE algorithm provides a superior resolution enhancement when compared with bilinear interpolation, bicubic interpolation, and an alternative linear system solver incorporating a Tikhonov constraint. In particular, MERE produced the best reconstruction accuracy over a range of real and synthetic test imagery, improved reconstruction accuracy as the resolution enhancement factor increased over a limited range, and had a robust response to increases in detector-based noise.

The developments made in this chapter contribute to existing methods. The approach taken to achieve spatial resolution enhancement is entirely original and provides proof-of-concept that resolution enhancement can be achieved by modelling a HR PSF convolution process and solving an underdetermined linear system. The Multiresolution Entropy constraint builds on robust entropy techniques. The appropriate selection of Wavelet filter for image decomposition and the customisation of Multiresolution Support images enable high-frequency content to be targeted. These techniques are all distinct research contributions that together

allow spatial resolution enhancement to be realised.

A computational complexity analysis showed that the current MERE algorithm has moderately unfavourable scaling properties and quickly exhausts the hardware of a single machine as the input image size increases. A range of limitations of the current MERE system have been discussed and some potential improvements have been highlighted. Overall, the MERE algorithm has been demonstrated to operate beneficially to the problem of spatial resolution enhancement and could be highly valuable for many marine research disciplines.

Chapter 7

Conclusion

The aim of this thesis was to develop a range of computational techniques to increase the accuracy of satellite data and improve monitoring capabilities for marine environments. This involved an in-depth analysis of the physical instrumental distortion process that is inherent in a convolution operation. Removing these instrumental effects at the beginning of the satellite image processing chain reduces errors from being propagated and amplified by subsequent processing stages. Although the correction is small in a lot of cases, it is well quantified provided the relative detector gain is corrected during calibration. With a deep understanding of how instrumental convolution affects recorded imagery, several approaches were undertaken to increase the quality of satellite products. While the techniques developed in this thesis were applied to marine satellite imagery, they are also widely applicable in many other fields.

An entropy-based deconvolution technique was developed to remove instrumental distortion from MODIS Aqua imagery. One of the fundamental calculations within the deconvolution process is a convolution operation. To perform these convolution operations, an accurate and efficient convolution method was developed that uses a renormalisation approach to minimise boundary contamination effects. Two validation methods were undertaken to quantify the radiometric improvement that deconvolution has on a range of MODIS products. Finally, a novel spatial resolution enhancement technique was developed to extract high-frequency information from recorded imagery that has undergone natural instrumental convolution.

7.1 Research Contribution

Each of the major research components in this thesis contains distinct contributions that have advanced the knowledge in unique ways. The FFT convolution with Border Correction (FBC) method developed in Chapter 3 combined Fast Fourier Transform (FFT) convolution with a post-convolution border renormalisation correction factor to reduce boundary effects. While FFT convolution and a similar boundary condition had both been identified previously, the combination of these two techniques had not been documented. Hence, this represents an important contribution to convolution literature. The FBC method has an extensive range of applications. Convolution is a fundamental technique in digital signal processing and is also used in probability theory, statistics and deconvolution problems. The FBC method can potentially be applied in all of these research areas to provide a useful improvement over other common convolution boundary condition methods.

The Multiscale Entropy deconvolution algorithm for MODIS Aqua imagery developed in Chapter 4 included several substantial research contributions. A multi-detector convolution process was created to simulate the physical MODIS detector layout. This resulted in all convolution calculations accurately representing the MODIS Aqua instrumentation and allowed successful deconvolution to be achieved. The critical problem of detector saturation for ocean colour bands was solved by developing a method to estimate the radiometric response of saturated measurements using alternative MODIS bands. In this way, the correct quantity of instrumental distortion is removed during deconvolution. The combination of these methods along with efficient computational techniques including Wavelet image decomposition, Multiresolution Support images and the FBC method provide an accurate and robust algorithm for removing instrumental distortion and restoring image quality.

Throughout the validation process undertaken in Chapter 5, two measurement comparison techniques were developed. A high-order polynomial fitting method was created that used typical Baltic Sea reflectance spectra to appropriately constrain an in-situ spectral measurement fitting process. This allowed the direct comparison of in-situ and MODIS spectral measurements and can be useful when aligning

measurements from different remote sensing instruments. A coincident satellite data comparison method was developed to allow MODIS Aqua measurements to be directly compared with high-resolution QuickBird imagery. This comprised appropriate radiometric correction, spatial measurement location mapping and measurement coverage estimation. The result of this method allows high-resolution comparisons to be conducted and represents a new research contribution for satellite validation techniques.

The Multiscale Entropy Resolution Enhancement (MERE) algorithm developed in Chapter 6 represents a significant contribution to the field of image processing. A new entropy-based constraint named Multiresolution Entropy was created to regularise an underdetermined system of linear equations, focus on high-frequency content and reconstruct high-resolution features. The appropriate selection of a Wavelet filter for image decomposition and customisation of the Multiresolution Support definition are also important research contributions that allow high-frequency content to be accurately targeted and reconstructed. The MERE algorithm represents an entirely new approach to spatial resolution enhancement and is a considerable research contribution.

7.2 Summary of Results

The boundary condition concept that underpins the FBC method was described and compared with other common boundary condition methods. Situations in which a border renormalisation approach would be useful were highlighted and the reasons why this can be an improvement on common techniques were discussed. The convolution border renormalisation approach was developed for calculation in the spatial and frequency domains. A comparison of convolution results using both methods over a range of synthetic and real test signals showed that the two methods perform equivalent convolution operations. As a result, efficient convolution with boundary renormalisation can be achieved using the FBC method.

The impact MODIS instrument effects have on recorded imagery was analysed and shown to produce radiometric errors greater than 1% up to 20km away from

highly reflective features. Multiscale Entropy deconvolution successfully removed instrumental distortion from convolved test imagery. High-contrast regions were correctly restored and instrument effects were removed down to the level of detector-based noise. In one example, the maximum individual pixel error was reduced from 90.01% down to 0.34%. When applied to typical MODIS images, the restored maximum individual pixel error ranged between approximately 20% and 115% for various contrasting features. These successful deconvolution results critically rely on multiresolution analysis techniques that decompose the input imagery into a range of spatial frequencies and incorporate two-dimensional structural information into the deconvolution process.

In-situ validation of the Multiscale Entropy deconvolution algorithm proved to be inconclusive in comprehensively characterising the effects of deconvolution. This was due to a limited number of comparable in-situ sample points and their limited spatial extent and contrast. A secondary validation approach compared coincident high-resolution QuickBird imagery with MODIS overpass measurements containing a high-contrast Antarctic ice edge. The results indicated that deconvolution improved the radiometric quality of MODIS measurements in the blue-bands. However, not enough comparable measurements were available for the green and red wavelengths to conclusively determine any improvement from deconvolution in these regions of the spectrum. It is expected that successful validation for a range of MODIS ocean colour bands can be achieved with a more appropriate coincident high-resolution QuickBird scene selection.

The results of the MERE algorithm provide proof-of-concept that spatial resolution enhancement can be achieved by modelling a high-resolution point spread function convolution process, applying appropriate constraints and solving an underdetermined system of linear equations. MERE outperformed a range of other resolution enhancement techniques including two interpolation methods and an alternative Tikhonov constraint for the MERE linear system. The redefined Multiresolution Support helps the Multiresolution Entropy constraint to accurately target high-frequency content and improve image reconstruction in high-contrast areas. The algorithm stepping size selection operates well and successfully guides the

regularisation process to a convergent solution. This is directly related to the correct calculation of the regularisation parameter that was redefined to accommodate spatial resolution enhancement. The MERE reconstruction error quantitatively scales well at integer resolution enhancement factors up to 4 and clearly outperforms the other resolution enhancement techniques. MERE is very robust in the presence of detector-based noise and can perform accurately at relatively small signal-to-noise ratios.

7.3 Limitations and Further Work

The FBC method is limited to power of 2 signal padding to maintain the most efficient FFT convolution operations. This can add a moderate computational overhead as input image sizes grow and are padded to subsequent powers of 2. A potential improvement could be realised by swapping the FFT convolution routine that is called by the FBC method with a mixed-radix FFT convolution method. With the availability of smaller mixed-radix padding dimensions, this could reduce the severity of padding and increase the speed of computation. The FBC method may not be suitable for all forms of signal convolution. Due to the renormalisation approach of the FBC method, convolution kernels that contain negative components can result in disruption or sensitivity reduction near signal boundaries. For this reason, the FBC method is not appropriate for applications such as derivative or edge-detection calculations.

The Multiscale Entropy deconvolution algorithm for MODIS Aqua imagery could be improved to reduce inaccuracies caused by the bow-tie effect of scanning-based instruments. The left and right edges of level 1A MODIS scenes contain duplicate measurements that introduce small errors during deconvolution. These errors do not affect the centre of MODIS scenes, but increase towards the edges. The algorithm could be improved by implementing a mask-based method that intelligently accounts for duplicate measurements prior to deconvolution. This would eliminate contamination from bow-tie effects. The Multiscale Entropy deconvolution algorithm also has the potential to be multi-threaded. This would allow certain

components of the algorithm to be processed concurrently and would provide a substantial improvement in compute time.

Recent work has shown that effective deconvolution can also be achieved with total variance methods and proximal operators (Babacan et al., 2009; Li et al., 2012; Dupé et al., 2009, 2012). A comparative study between these new techniques and the method developed in Chapter 4 would be interesting future work which would contribute further to the literature.

The current implementation of the MERE algorithm is limited to integer resolution enhancement factors. It is highly likely that the optimum resolution enhancement factor for specific input imagery has a non-integer value. A possible implementation strategy was discussed in Chapter 6 and would significantly advance the flexibility and operation of the MERE algorithm. Several elements of the MERE algorithm also have the opportunity to be parallelised and computed on a GPU. The scaling properties of the MERE linear system are quite extreme and parallelisation may be an efficient way to allow for resolution enhancement of large image sizes.

Further work on spatial resolution enhancement could include a comprehensive comparison of the technique developed in Chapter 6 with recently published super-resolution research featuring dictionary learning, sparse representation and total variation regularisation (Pan et al., 2013; Jia et al., 2013; Jung et al., 2013). Such a comparison may highlight the strengths and weaknesses of these computational techniques and uncover further research directions in achieving spatial resolution enhancement of higher accuracy and efficiency.

This thesis has investigated and developed several computational techniques to improve the quality of satellite data. The FBC method minimises convolution boundary effects, Multiscale Entropy deconvolution accurately removes instrumental distortion and the MERE algorithm provides a mechanism to enhance the spatial resolution of satellite imagery. The combination of these three techniques results in substantial improvement to the accuracy and quality of satellite data and can increase the ability to monitor and manage coastal marine and open-ocean environments.

References

Achard, F., Eva, H. D., Stibig, H. J. and Mayaux, P., 2002, 'Determination of deforestation rates of the world's humid tropical forests', *Science*, vol. 297, pp. 999–1002.

Acharya, T. and Ray, A. K., 2005, *Image processing: principles and applications*, Wiley-Interscience, New Jersey.

Airy, G. B., 1835, 'On the diffraction of an object-glass with circular aperture', *Transactions of the Cambridge Philosophical Society*, vol. 5, p. 283.

Anscombe, F. J., 1948, 'The transformation of Poisson, binomial and negative-binomial data', *Biometrika*, vol. 35, no. 3-4, p. 246.

Antoine, D. and Morrel, A., 2005, 'MERIS ATBD 2.7: Atmospheric correction of the MERIS observations over ocean case 1 waters', Tech. Rep. 5, Laboratory of Oceanography, Villefranche.

Australian Bureau of Statistics, 2002, *Regional Population Growth 2001-02*, Australian Bureau of Statistics, Australia and New Zealand.

Babacan, S. D., Molina, R. and Katsaggelos, A. K., 2009, 'Variational Bayesian blind deconvolution using a total variation prior', *IEEE Transactions on Image Processing*, vol. 18, no. 1, pp. 12–26.

Baker, J., 1990, *Planet earth: the view from space*, Harvard University Press, Cambridge.

Baker, S. and Kanade, T., 2002, 'Limits on super-resolution and how to break them', *IEEE Transactions on Pattern Analysis and Machine Intelligence*, vol. 24, no. 9, pp. 1167–1183.

Barbieri, R., 1997, 'Draft of the MODIS level 1B algorithm theoretical basis document version 2.0', *SAIC/GSC MCST Document*.

Barnes, W. L., Pagano, T. S. and Salomonson, V. V., 1998, 'Prelaunch characteristics of the Moderate Resolution Imaging Spectroradiometer (MODIS) on EOS-AM1', *IEEE Transactions on Geoscience and Remote Sensing*, vol. 36, no. 4, pp. 1088–1100.

Barzilai, J. and Borwein, J. M., 1988, 'Two-point step size gradient methods', *IMA Journal of Numerical Analysis*, vol. 8, no. 1, pp. 141–148.

Begin, I. and Ferrie, F. P., 2004, 'Blind super-resolution using a learning-based approach', In 'Proceedings of the 17th International Conference on Pattern Recognition', IEEE, pp. 85–89.

Behrenfeld, M. J., O'Malley, R. T., Siegel, D. A., McClain, C. R., Sarmiento, J. L., Feldman, G. C., Milligan, A. J., Falkowski, P. G., Letelier, R. M. and Boss, E. S., 2006, 'Climate-driven trends in contemporary ocean productivity', *Nature*, vol. 444, no. 7120, pp. 752–755.

Belton, J. S. and Gandhi, A., 1988, 'Application of the CLEAN algorithm to cometary light curves', In 'Bulletin of the American Astronomical Society', vol. 20, p. 836.

Bettens, E., van Dyck, D., den Dekker, A. J., Sijbers, J. and van den Bos, A., 1999, 'Model-based two-object resolution from observations having counting statistics', *Ultramicroscopy*, vol. 77, no. 1, pp. 37–48.

Bishop, C. M., Blake, A. and Marthi, B., 2003, 'Super-resolution enhancement of video', In 'Proceedings of the Ninth International Workshop on Artificial Intelligence and Statistics', CiteSeer, vol. 2.

Bom, M. and Wolf, E., 1980, 'Principles of optics', *Pergamon Press*, vol. 6, p. 188.

Bontekoe, T. R., Koper, E. and Kester, D. J. M., 1994, 'Pyramid maximum entropy images of IRAS survey data', *Astronomy and Astrophysics*, vol. 284, no. 3, pp. 1037–1053.

Borman, S. and Stevenson, R. L., 1998, 'Super-resolution from image sequences-a review', *Circuits and Systems*, pp. 374–378.

Bracewell, R. N., 2000, *The Fourier transform and its applications*, McGraw-Hill, New York.

Bracewell, R. N. and Roberts, J. A., 1954, 'Aerial smoothing in radio astronomy', *Australian Journal of Physics*, vol. 7, no. 4, pp. 615–640.

Brando, V. E. and Dekker, A. G., 2003, 'Satellite hyperspectral remote sensing for estimating estuarine and coastal water quality', *IEEE Transactions on Geoscience and Remote Sensing*, vol. 41, no. 6, pp. 1378–1387.

Brigham, E. O., 1986, *The fast Fourier transform and its applications*, McGraw-Hill, New York.

Burg, J. P., 1975, *Maximum entropy spectral analysis*, PhD thesis, Stanford University.

Capel, D. P. and Zisserman, A., 2001, 'Super-resolution from multiple views using learnt image models', In 'Proceedings of the 2001 IEEE Computer Society Conference on Computer Vision and Pattern Recognition', IEEE, pp. 627–634.

Carlund, T., Hakansson, B. and Land, P., 2005, 'Aerosol optical depth over the Baltic Sea derived from AERONET and SeaWiFS measurements', *International Journal of Remote Sensing*, vol. 26, no. 2, pp. 233–245.

Chander, G., Mishra, N., Helder, D. L. and Aaron, D. B., 2013, 'Applications of Spectral Band Adjustment Factors (SBAF) for cross-calibration', *IEEE Transactions on Geoscience and Remote Sensing*, vol. 51, pp. 1267–1281.

Clark, B. G., 1980, 'An efficient implementation of the algorithm 'CLEAN'', *Astronomy and Astrophysics*, vol. 89, p. 377.

Cooley, J. W. and Tukey, J. W., 1965, 'An algorithm for the machine calculation of complex Fourier series', *Mathematics of Computation*, vol. 19, no. 90, p. 297.

Cristina, S. V., Goela, P. and Icely, J. D., 2009, 'Assessment of water-leaving reflectances of oceanic and coastal waters using MERIS satellite products off the southwest coast of Portugal', *Journal of Coastal Research*, vol. 2009, no. 56, pp. 1479–1483.

Cui, X., Chen, Y. and Mei, H., 2009, 'Improving performance of matrix multiplication and FFT on GPU', In '15th International Conference on Parallel and Distributed Systems', IEEE, pp. 42–48.

Darecki, M. and Stramski, D., 2004, 'An evaluation of MODIS and SeaWiFS bio-optical algorithms in the Baltic Sea', *Remote Sensing of Environment*, vol. 89, no. 3, pp. 326–350.

Daubechies, I., 1992, *Ten lectures on wavelets*, Society for Industrial Mathematics, Philadelphia.

Dekker, A. G., 1993, *Detection of optical water quality parameters for eutrophic waters by high resolution remote sensing*, Vrije Universiteit, Amsterdam.

Dempster, A. P., Laird, N. M. and Rubin, D. B., 1977, 'Maximum likelihood from incomplete data via the EM algorithm', *Journal of the Royal Statistical Society. Series B (Methodological)*, vol. 39, no. 1, pp. 1–38.

den Dekker, A. J. and van den Bos, A., 1997, 'Resolution: a survey', *Journal of the Optical Society of America A: Optics, Image Science, and Vision*, vol. 14, no. 3, pp. 547–557.

Deshpande, A. A., 1996, 'Application of 'CLEAN' in the power spectral analysis of non-uniformly sampled pulsar timing data', *Journal of Astrophysics and Astronomy*, vol. 17, no. 1, pp. 7–16.

Dhawan, A. P., Rangayyan, R. M. and Gordon, R., 1985, 'Image restoration by Wiener deconvolution in limited-view computed tomography', *Applied Optics*, vol. 24, no. 23, pp. 4013–4020.

DigitalGlobe, 2006, *QuickBird Imagery Products*, Product Guide.

Dorband, J. E. and Hollis, J. M., 1992, 'Super-resolution of imagery using the Maximum Entropy Method', In 'Astronomical Data Analysis Software and Systems I', vol. 25, p. 200.

Dupé, F. X., Fadili, J. M. and Starck, J. L., 2009, 'A proximal iteration for deconvolving Poisson noisy images using sparse representations', *IEEE Transactions on Image Processing*, vol. 18, no. 2, pp. 310–321.

Dupé, F. X., Fadili, M. J. and Starck, J. L., 2012, 'Deconvolution under Poisson noise using exact data fidelity and synthesis or analysis sparsity priors', *Statistical Methodology*, vol. 9, no. 1, pp. 4–18.

Farsiu, S., Robinson, D., Elad, M. and Milanfar, P., 2004a, 'Advances and challenges in super-resolution', *International Journal of Imaging Systems and Technology*, vol. 14, no. 2, pp. 47–57.

Farsiu, S., Robinson, M. D., Elad, M. and Milanfar, P., 2004b, 'Fast and robust multiframe super resolution', *IEEE transactions on image processing*, vol. 13, no. 10, pp. 1327–1344.

Ficek, D., Zapadka, T. and Dera, J., 2011, 'Remote sensing reflectance of Pomeranian lakes and the Baltic', *Oceanologia*, vol. 53, no. 4, pp. 959–970.

Freeman, W. T., Pasztor, E. C. and Carmichael, O. T., 2000, 'Learning low-level vision', *International journal of computer vision*, vol. 40, no. 1, pp. 25–47.

Frieden, B. R., 1975, 'Image enhancement and restoration', *Picture processing and digital filtering*, vol. 6, pp. 177–248.

Fu, G., Baith, K. S. and McClain, C. R., 1998, 'SeaDAS: The SeaWiFS Data Analysis System', In 'Proceedings of the 4th Pacific Ocean Remote Sensing Conference', pp. 28–31.

Golub, G. H. and Loan, C. F. V., 1996, *Matrix computations*, Johns Hopkins University Press, Baltimore.

Gordon, H. R., 1978, 'Removal of atmospheric effects from satellite imagery of the oceans', *Applied Optics*, vol. 17, no. 10, pp. 1631–1636.

Gordon, H. R. and Clark, D. K., 1980, 'Remote sensing optical properties of a stratified ocean: an improved interpretation', *Applied Optics*, vol. 19, no. 20, pp. 3428–3430.

Gordon, H. R. and Voss, K. J., 1999, 'MODIS normalized water-leaving radiance algorithm theoretical basis document', Tech. Rep. Mod 18.

Goshtasby, A. A., 2005, *2-D and 3-D image registration: for medical, remote sensing, and industrial applications*, John Wiley & Sons, New Jersey.

Gottlieb, D. and Shu, C. W., 1997, 'On the Gibbs phenomenon and its resolution', *Society for Industrial and Applied Mathematics Review*, vol. 39, no. 4, pp. 644–668.

Guenther, B. and Barnes, W. L., 1996, 'MODIS calibration: a brief review of the strategy for the at-launch calibration approach', *Journal of Atmospheric and Oceanic Technology*, vol. 13, no. 2, pp. 274–285.

Gull, S. F. and Skilling, J., 1991, *Quantified Maximum Entropy MemSys5 user's manual*, Version 1.2, Maximum Entropy Data Consultants, Suffolk.

Hanisch, R. J. and White, R. L., 1994, 'The restoration of HST images and spectra-II', In 'Proceedings of a workshop held at the Space Telescope Science Institute', vol. 1.

Hansen, P. C., 1994, 'Regularization tools: A Matlab package for analysis and solution of discrete ill-posed problems', *Numerical algorithms*, vol. 6, no. 1, pp. 1–35.

Hassanieh, H., Indyk, P., Katabi, D. and Price, E., 2012, 'Nearly optimal sparse fourier transform', In 'Proceedings of the 44th symposium on Theory of Computing', ACM Press, New York, 1, p. 563.

Helstrom C.W., 1964, 'The detection and resolution of optical signals', *IEEE Transactions on Information Theory*, vol. 74, pp. 233–243.

Helstrom C.W., 1969, 'Detection and resolution of incoherent objects by a background-limited optical system', *Journal of the Optical Society of America*, vol. 59, no. 2, pp. 164–175.

Helstrom C.W., 1970, 'Resolvability of objects from the standpoint of statistical parameter estimation', *Journal of the Optical Society of America*, vol. 60, no. 5, pp. 659–666.

Higurashi, A. and Nakajima, T., 2000, 'A study of global aerosol optical climatology with two-channel AVHRR remote sensing', *Journal of Climate*, vol. 13, no. 12, pp. 2011–2027.

Högbom, J. A., 1974, 'Aperture synthesis with a non-regular distribution of interferometer baselines', *Astronomy and Astrophysics Supplement*, vol. 15, no. 3, pp. 417–426.

Holschneider, M., Kronland-Martinet, R., Morlet, J. and Tchamitchian, P., 1989, 'A real-time algorithm for signal analysis with the help of the wavelet transform', In 'Wavelets. Time-Frequency Methods and Phase Space', vol. 1, p. 286.

Ikeda, M. and Dobson, F. W., 1995, *Oceanographic applications of remote sensing*, CRC Press, Florida.

Irani, M. and Peleg, S., 1991, 'Improving resolution by image registration', *CVGIP: Graphical models and image processing*, vol. 53, no. 3, pp. 231–239.

Jähne, B., 2002, 'Digital image processing', *Measurement Science and Technology*, vol. 13, no. 9, p. 1503.

Jansson, B. O., 2003, 'The Baltic Sea'.

Jaynes, E. T., 1957, 'Information theory and statistical mechanics', *Physical review*, vol. 108, no. 2, pp. 171–190.

Jia, K., Tang, X. and Wang, X., 2013, 'Image Transformation Based on Learning Dictionaries across Image Spaces', *IEEE Transactions on Pattern Analysis and Machine Intelligence*, vol. 35, no. 2, pp. 367–380.

Johnson, R. W. and Shore, J. E., 1980, 'Axiomatic derivation of the principle of maximum entropy and the principle of minimum cross-entropy', *IEEE Transactions on information theory*, vol. 26, no. 1, pp. 942–943.

Johnson, R. W. and Shore, J. E., 1983, 'Comments on and correction to 'Axiomatic derivation of the principle of maximum entropy and the principle of minimum cross-entropy'', *Information Theory, IEEE Transactions*, vol. 29, no. 6, pp. 942–943.

Jung, C., Ju, J., Jiao, L. and Yang, Y., 2013, 'Enhancing dictionary-based super-resolution using nonlocal total variation regularization', *Optical Engineering*, vol. 52, no. 1, pp. 17005–17005.

Justice, C. O., Vermote, E. F., Townshend, J. R. G., Defries, R., Roy, D. P., Hall, D. K., Salomonson, V. V., Privette, J. L., Riggs, G. and Strahler, A. H., 1998, 'The Moderate Resolution Imaging Spectroradiometer (MODIS): land remote sensing for global change research', *IEEE Transactions on Geoscience and Remote Sensing*, vol. 36, no. 4, pp. 1228–1249.

Kaufman, Y. J., 1989, *Theory and applications of optical remote sensing*, In The atmospheric effect on remote sensing and its correction, John Wiley & Sons, New York, pp. 336-428.

Kaufman, Y. J., Tanré, D. and Boucher, O., 2002, 'A satellite view of aerosols in the climate system', *Nature*, vol. 419, pp. 215–223.

Khronos OpenCL Working Group, 2008, 'The OpenCL specification', Tech. rep., Version 1.0.

Kosarev, E. L., 1990, 'Shannon's superresolution limit for signal recovery', *Inverse problems*, vol. 6, p. 55.

Krantz, S. G., 1999, *Handbook of complex variables*, Birkhauser, Boston.

Kratzer, S., Brockmann, C. and Moore, G., 2008, 'Using MERIS full resolution data to monitor coastal watersA case study from Himmerfjärden, a fjord-like bay in the northwestern Baltic Sea', *Remote Sensing of Environment*, vol. 112, no. 5, pp. 2284–2300.

Kratzer, S., Hakansson, B. and Sahlin, C., 2003, 'Assessing Secchi and photic zone depth in the Baltic Sea from satellite data', *AMBIO: A Journal of the Human Environment*, vol. 32, no. 8, pp. 577–585.

Kratzer, S. and Tett, P., 2009, 'Using bio-optics to investigate the extent of coastal waters: A Swedish case study', *Hydrobiologia*, vol. 629, no. 1, pp. 169–186.

Kratzer, S. and Vinterhav, C., 2010, 'Improvement of MERIS level 2 products in Baltic Sea coastal areas by applying the Improved Contrast between Ocean and Land processor (ICOL)-data analysis and validation', *Oceanologia*, vol. 52, no. 2, pp. 211–236.

Krause, K., 2005, 'Radiometric use of QuickBird imagery', *Technical Note*, pp. 1–18.

Landweber, L., 1951, 'An iteration formula for Fredholm integral equations of the first kind', *American Journal of Mathematics*, vol. 73, no. 3, p. 615.

Lee, Z., Carder, K. L., Mobley, C. D., Steward, R. G. and Patch, J. S., 1999, 'Hyperspectral remote sensing for shallow waters: 2. Deriving bottom depths and water properties by optimization', *Applied optics*, vol. 38, no. 18, pp. 3831–3843.

Lee, Z. P., Darecki, M. and Carder, K. L., 2005, 'Diffuse attenuation coefficient of downwelling irradiance: An evaluation of remote sensing methods', *Journal of Geophysical Research: Oceans*, vol. 110, no. C02017.

Li, W., Li, Q., Gong, W. and Tang, S., 2012, 'Total variation blind deconvolution employing split Bregman iteration', *Journal of Visual Communication and Image Representation*, vol. 23, no. 3, pp. 409–417.

Lin, Z., He, J., Tang, X. and Tang, C. K., 2008, 'Limits of learning-based superresolution algorithms', *International journal of computer vision*, vol. 80, no. 3, pp. 406–420.

Liu, C., Shum, H. Y. and Freeman, W. T., 2007, 'Face hallucination: theory and practice', *International Journal of Computer Vision*, vol. 75, no. 1, pp. 115–134.

Livesey, A. K. and Skilling, J., 1985, 'Maximum entropy theory', *Acta Crystallographica Section A: Foundations of Crystallography*, vol. 41, no. 2, pp. 113–122.

Lucy, L. B., 1974, 'An iterative technique for the rectification of observed distributions', *The astronomical journal*, vol. 79, no. 6, pp. 745–754.

Lucy, L. B., 1992a, 'Resolution limits for deconvolved images', *The Astronomical Journal*, vol. 104, pp. 1260–1265.

Lucy, L. B., 1992b, 'Statistical limits to super resolution', *Astronomy and Astrophysics*, vol. 261, p. 706.

Madden, F. N., Godfrey, K. R., Chappell, M. J., Hovorka, R. and Bates, R. A., 1996, 'A comparison of six deconvolution techniques', *Journal of Pharmacokinetics and Pharmacodynamics*, vol. 24, no. 3, pp. 283–299.

Magain, P., Courbin, F. and Sohy, S., 1998, 'Deconvolution with correct sampling', *The Astrophysical Journal*, vol. 494, p. 472.

McNally, J. G., Karpova, T., Cooper, J. and Conchello, J., 1999, 'Three-dimensional imaging by deconvolution microscopy', *Methods*, vol. 19, no. 3, pp. 373–85.

Meister, G. and McClain, C. R., 2010, 'Point-spread function of the ocean color bands of the Moderate Resolution Imaging Spectroradiometer on Aqua', *Applied optics*, vol. 49, no. 32, pp. 6276–6285.

Meister, G., Zong, Y. and McClain, C. R., 2008, 'Derivation of the MODIS Aqua Point-Spread Function ocean color bands', In 'Proceedings of Society of Photo-Optical Instrumentation Engineers', Spie, vol. 7081, pp. 70811F–1.

Mendel, J. M., 1983, *Optimal seismic deconvolution: an estimation-based approach*, Academic Press, California.

Merino, M. T. and Nunez, J., 2007, 'Super-resolution of remotely sensed images with variable-pixel linear reconstruction', *IEEE Transactions on Geoscience and Remote Sensing*, vol. 45, no. 5, pp. 1446–1457.

Mobley, C. D., Stramski, D., Bissett, W. P. and Boss, E., 2004, 'Optical Modeling of Ocean Waters: Is the Case 1-Case 2 Classification Still Useful?', *Oceanography*, vol. 17, no. 2, pp. 60–67.

Moré, J. J., 1978, 'The Levenberg-Marquardt algorithm: implementation and theory', In 'Numerical analysis', Springer, pp. 105–116.

Morel, A. and Prieur, L., 1977, 'Analysis of variations in ocean color', *Limnology and Oceanography*, vol. 22, no. 4, pp. 709–722.

Mueller, J. L., 2000, 'SeaWiFS algorithm for the diffuse attenuation coefficient, K (490), using water-leaving radiances at 490 and 555 nm', *SeaWiFS postlaunch calibration and validation analyses*, vol. 3, no. 11, pp. 24–27.

NASA, 1993, *Hubble Images of M100 Before and After Mirror Repair*, NASA, Photograph.

Nishihama, M., Wolfe, R., Solomon, D., Patt, F., Blanchette, J., Fleig, A. and Masuoka, E., 1997, 'MODIS level 1A earth location: algorithm theoretical basis document version 3.0', *SDST-092, MODIS Science Data Support Team*.

NOAA, 2010, *Advanced Very High Resolution Radiometer - AVHRR*, http://noaasis.noaa.gov/NOAASIS/ml/avhrr.html, viewed 29/05/2010.

NVIDIA, 2009, *NVIDIA CUDA*, programming guide, version 2.3.

Ohshima, S., Kise, K., Katagiri, T. and Yuba, T., 2007, 'Parallel processing of matrix multiplication in a CPU and GPU heterogeneous environment', In 'Proceedings of the 7th international conference on high performance computing for computational science', pp. 305–318.

Pan, Z., Yu, J., Huang, H., Hu, S., Zhang, A., Ma, H. and Sun, W., 2013, 'Super-Resolution Based on Compressive Sensing and Structural Self-Similarity for Remote Sensing Images', *IEEE Transactions on Geoscience and Remote Sensing*, vol. 51, no. 9, pp. 4864–4876.

Pantin, E. and Starck, J. L., 1996, 'Deconvolution of astronomical images using the multiscale maximum entropy method', *Astronomy and Astrophysics Supplement Series*, vol. 118, no. 3, pp. 575–585.

Park, S. C., Park, M. K. and Kang, M. G., 2003, 'Super-resolution image reconstruction: a technical overview', *IEEE Signal Processing Magazine*, vol. 15, no. 2, pp. 21–36.

Pijpers, F. P., 1999, 'Unbiased image reconstruction as an inverse problem', *Monthly Notices of the Royal Astronomical Society*, vol. 307, no. 3, pp. 659–668.

Piles, M., Camps, A., Vall-llossera, M. and Talone, M., 2009, 'Spatial-resolution enhancement of SMOS data: a deconvolution-based approach', *IEEE Transactions on Geoscience and Remote Sensing*, vol. 47, no. 7, pp. 2182–2192.

Platt, T., Hoepffner, N., Stuart, V. and Brown, C., 2008, 'Why Ocean Colour? The Societal Benefits of Ocean-Colour Technology', Tech. rep., International Ocean-Colour Coordinating Group, Dartmouth, Canada.

Qiu, S., Godden, G., Wang, X. and Guenther, B., 2000, 'Satellite-Earth remote sensor scatter effects on Earth scene radiometric accuracy', *Metrologia*, vol. 37, p. 411.

Qui, Y., Liu, Z., Lu, R. and Ke, L., 2000, 'The application of CLEAN algorithm to astronomical image reconstruction working in spatial domain', *Publications of the Yunnan Observatory*, vol. 2, pp. 1–9.

Richardson, W. H., 1972, 'Bayesian-based iterative method of image restoration', *Journal of the Optical Society of America*, vol. 62, pp. 55–59.

Riedmiller, M. and Braun, H., 1993, 'A direct adaptive method for faster backpropagation learning: The RPROP algorithm', In 'IEEE International Conference on Neural Networks, 1993', IEEE, pp. 586–591.

Ruhl, C. A. and Schoellhamer, D. H., 2001, 'Combined use of remote sensing and continuous monitoring to analyse the variability of suspended-sediment concentrations in San Francisco Bay, California', *Estuarine, Coastal and Shelf Science*, vol. 53, no. 6, pp. 801–812.

Rydén, L. and Karlsson, I., 2012, *Rural development and land use*, Baltic University Press, Uppsala.

Sathyendranath, S., 2000, 'Remote sensing of ocean colour in coastal, and other optically-complex waters', Tech. rep., International Ocean-Colour Coordinating Group, Dartmouth, Canada.

Shahram, M., 2004, 'Imaging below the diffraction limit: a statistical analysis', *Image Processing, IEEE Transactions*, vol. 13, no. 5, pp. 677–89.

Shannon, C. E., 1949, 'A mathematical theory of communication', *M.D. computing: computers in medical practice*, vol. 14, no. 4, pp. 306–17.

Shen, H., Ng, M. K., Li, P. and Zhang, L., 2008, 'Super-resolution reconstruction algorithm to MODIS remote sensing images', *The Computer Journal*, vol. 52, no. 1, pp. 90–100.

Shensa, M. J., 1992, 'The discrete wavelet transform: wedding the a trous and Mallat algorithms', *IEEE Transactions on Signal Processing*, vol. 40, no. 10, pp. 2464–2482.

Shi, Z. J., 2005, 'Step-size estimation for unconstrained optimization methods', *Computational & Applied Mathematics*, vol. 24, no. 3, pp. 399–416.

Singleton, R., 1969, 'An algorithm for computing the mixed radix fast Fourier transform', *IEEE Transactions on Audio and Electroacoustics*, vol. 17, no. 2, pp. 93–103.

Skilling, J. and Bryan, R. K., 1984, 'Maximum entropy image reconstruction-general algorithm', *RAS Monthly Notices*, vol. 211, pp. 111–124.

Smith, R. C. and Baker, K. S., 1981, 'Optical properties of the clearest natural waters (200-800 nm)', *Applied optics*, vol. 20, no. 2, pp. 177–184.

Smith, S. W., 2003, *Digital signal processing: a practical guide for engineers and scientists*, Newnes, Burlington.

Starck, J. L., 1995, 'Multiresolution support applied to image filtering and restoration', *Graphical Models and Image Processing*, vol. 57, no. 5, pp. 420–431.

Starck, J. L., 1996, 'Multiscale maximum entropy images restoration', *Vistas in Astronomy*, vol. 40, no. 4, pp. 563–569.

Starck, J. L. and Bijaoui, A., 1994, 'Filtering and deconvolution by the wavelet transform', *Signal Processing*, vol. 35, no. 3, pp. 195–211.

Starck, J. L., Murtagh, F. and Gastaud, R., 1998, 'A new entropy measure based on the wavelet transform and noisemodeling [image compression]', *IEEE*

Transactions on Circuits and Systems II: Analog and Digital Signal Processing, vol. 45, no. 8, pp. 1118–1124.

Starck, J. L., Pantin, E. and Murtagh, F., 2002, 'Deconvolution in astronomy: a review', *Publications of the Astronomical Society of the Pacific*, vol. 114, no. 800, pp. 1051–1069.

Stumpf, R. P. and Tomlinson, M. C., 2005, 'Remote sensing of harmful algal blooms', In 'Remote Sensing of Coastal Aquatic Environments', Springer Netherlands, Dordrecht, pp. 277–296.

Sun, J., Zheng, N. N., Tao, H. and Shum, H. Y., 2003, 'Image hallucination with primal sketch priors', In 'IEEE Computer Society Conference on Computer Vision and Pattern Recognition', Published by the IEEE Computer Society, vol. 2, pp. 729–736.

Tao, S., Zhigao, Y., Liyu, L. and Qianqing, Q., 2006, 'Single-Frame Remote Sensing Image Superresolution Reconstruction with Sub-blocks Noniterative Scheme', In 'IEEE International Conference on Geoscience and Remote Sensing Symposium', IEEE, pp. 1382–1385.

Thuillier, G., Hersé, M. and Foujols, T., 2003, 'The solar spectral irradiance from 200 to 2400 nm as measured by the SOLSPEC spectrometer from the ATLAS and EURECA missions', *Solar Physics*, vol. 214, no. 1, pp. 1–22.

Tikhonov, A. N. and Arsenin, V. Y., 1977, 'Solutions of ill-posed problems', *WH Winston, Washington, DC*.

Tikhonov, A. N., Goncharsky, A. V. and Bloch, M., 1987, *Ill-posed problems in the natural sciences*, vol. 53, Mir Publishers, Moscow.

Trott, M., 2004, *The Mathematica guidebook for programming*, Springer, New York.

USGS, 2009, *Landsat Thematic Mapper Data (TM)*, http://eros.usgs.gov/#/Guides/landsat_tm, viewed 29/05/2010.

Vermote, E. F., El Saleous, N. Z. and Justice, C. O., 2002, 'Atmospheric correction of MODIS data in the visible to middle infrared: first results', *Remote Sensing of Environment*, vol. 83, no. 1-2, pp. 97–111.

Wahba, G., 1990, *Spline models for observational data*, vol. 59, Society for Industrial Mathematics, Philadelphia.

Wakker, B. P. and Schwarz, U. J., 1988, 'The Multi-Resolution CLEAN and its application to the short-spacing problem in interferometry', *Astronomy and Astrophysics*, vol. 200, no. 1-2, pp. 312–322.

Wang, M., 2010, 'Atmospheric Correction for Remotely-Sensed Ocean-Colour Products', Tech. rep., International Ocean-Colour Coordinating Group, Dartmouth, Canada.

Wang, Z. and Bovik, A. C., 2004, 'Image quality assessment: from error visibility to structural similarity', *IEEE Transactions on Image Processing*, vol. 13, no. 4, pp. 600–612.

White, R. L. and Allen, R. J., 1991, 'The restoration of HST images and spectra', In 'Proceedings of a workshop held at the Space Telescope Science Institute', vol. 1.

Wiener, N., 1949, 'Extrapolation, interpolation, and smoothing of stationary time series: with engineering applications'.

Wright, J. and Huang, T. T., 2008, 'Image super-resolution as sparse representation of raw image patches', In 'IEEE Conference on Computer Vision and Pattern Recognition', Ieee, pp. 1–8.

Xiong, J., Toller, G., Chiang, V., Sun, J., Esposito, J. and Barnes, W. L., 2005, 'MODIS level 1B algorithm theoretical basis document', Tech. rep., NASA, Washington D.C.

Xiong, X. and Barnes, W. L., 2006, 'An overview of MODIS radiometric calibration and characterization', *Advances in Atmospheric Sciences*, vol. 23, no. 1, pp. 69–79.

Xiong, X., Chiang, K., Sun, J., Barnes, W. L., Guenther, B. and Salomonson, V. V., 2009, 'NASA EOS Terra and Aqua MODIS on-orbit performance', *Advances in Space Research*, vol. 43, no. 3, pp. 413–422.

Yang, H. and Gordon, H. R., 1997, 'Remote sensing of ocean color: assessment of water-leaving radiance bidirectional effects on atmospheric diffuse transmittance.', *Applied Optics*, vol. 36, no. 30, pp. 7887–7897.

Yang, J., Wright, J., Huang, T. and Ma, Y., 2008, 'Image super-resolution as sparse representation of raw image patches', In 'IEEE Conference on Computer Vision and Pattern Recognition, 2008', IEEE, pp. 1–8.

Yang, J., Wright, J., Huang, T. S. and Ma, Y., 2010, 'Image super-resolution via sparse representation', *IEEE Transactions on Image Processing*, vol. 19, no. 11, pp. 2861–2873.

Zhang, W. and Cham, W. K., 2008, 'A single image based blind super-resolution approach', In '15th IEEE International Conference on Image Processing', pp. 329–332.

Zibordi, G., Holben, B. and Mélin, F., 2010, 'AERONET-OC: an overview', *Canadian Journal of . . .*, vol. 36, no. 5, pp. 488–497.

Zibordi, G., Mélin, F., Berthon, J. F., Holben, B., Slutsker, I., Giles, D., DAlimonte, D., Vandemark, D., Feng, H., Schuster, G., Fabbri, B. E., Kaitala, S. and Seppälä, J., 2009, 'AERONET-OC: a network for the validation of ocean color primary products', *Journal of Atmospheric and Oceanic Technology*, vol. 26, no. 8, pp. 1634–1651.

Zibordi, G., Ruddick, K. and Ansko, I., 2012, 'In situ determination of the remote sensing reflectance: an inter-comparison', *Ocean Science Discussions*, vol. 8, no. 4, pp. 567–586.